UNIVERSITY OF LIVERPOOL

Selective hydrogenation of 5-hydroxymethylfurfural (HMF) to 2, 5-dimethylfuran (DMF) over Ru, Ni, and Co mono and bimetallic catalysts supported on carbon and carbon nanotube.

Thesis submitted in accordance with the requirements of the University of Liverpool for the degree of Doctor in Philosophy

by

Nor Azam Bin Endot

February 2017

Abstract

The main objective of this thesis is to develop better catalysts for the hydrogenation of 5-hydroxymethylfurfural, HMF into high quality liquid fuel 2, 5- dimethylfuran (DMF) or partly hydrogenating compounds. This could be achieved by exploiting the support effect and using CNTs to improve activity and developing mono- and bimetallic systems utilising less expensive metals like Nickel, Cobalt or Iron compared to noble metals like ruthenium and rhodium. Succeeding at this could be an economic incentive for the scale-up production of DMF. In addition, we envisaged the opportunity to be able to produce the metal catalyst and support in one simple step using a sugar and the metal salt and we studied the utilisation of carbon synthesised hydrothermally from glucose as a catalyst support using microwave techniques. The physical and chemical properties of the catalysts were characterised using such techniques as X-ray diffraction (XRD), temperature programmed reduction (TPR), inductively coupled plasma emission spectroscopy (ICP), hydrogen and carbon monoxide chemisorption, transition electron microscopy (TEM) and x-ray photoelectron spectroscopy (XPS).

Hydrogenation of HMF to DMF was examined over monometallic and bimetallic Ru, Ni and Co supported on carbon and CNT at 150 °C (20 bar of H_2). Among the monometallic catalysts supported on carbon, Ru catalysts exhibited the highest DMF yield up to 80 % in 3 hours followed by Ni and Co catalyst. This is because Ni and Co are not as good as Ru in the hydrogenolysis step in order to get to DMF. As a comparison to carbon, CNT as a support shows a remarkable improvement in the HMF conversion and DMF yield in a shorter reaction time. The effect is consistence for all the catalysts. A control test with only CNT showed a negligible activity which confirms that the enhancement is due to the presence of metal catalyst. HMF conversion of 100 % with 84 % DMF yield in 1 hr was achieved over 5 wt % Ru/CNT. The improvement of reactivity is attributed to the electronic effect of CNT derived from the curvature shape of CNT. This consequently enhanced the electron density of metal thus improving the adsorption of C=O bonds resulting in higher reactivity. We found that the promoting effect of the CNT support was universal to all catalyst tested, so that reasonably good Co and Ni catalysts could be obtained, particularly for the initial step of the reaction.

The bimetallic system of RuCo and RuNi with specific molar ratios showed a significant improvement in reactivity compared to their monometallic counterparts, particularly considering the lower loading used. High yield of DMF was obtained even at low Ru content in a bimetallic catalyst without losing much DMF yield. 3.5 % RuCo/C 1:5 (0.6 % Ru) and 3.2 % RuNi 1:3 (0.7 % Ru) have better specific DMF yield as compared to 5% Ru/C and 5 % Ru/CNT. 4.2 % RuCo/CNT 1:2 with only 0.2 % loading of Ru showed the highest specific DMF yield. This finding is a positive outcome in order to reduce the dependent on the expensive noble metal without compromising the activity and the yield of desired product, in our case DMF. This proved the synergistic effect of this system. The only difference when different supports were used was that CNT improved the reaction rates however this is also lead to the formation of ring hydrogenation and ring opening products. Carbon has lower reaction rate however it gives better DMF yield. Finally, we demonstrated that one step microwave assisted synthesis of carbon supported catalysts is a promising technique to simultaneously synthesise catalyst as well as hydrothermal carbon in a shorter amount of time compared to the conventional hydrothermal and incipient wetness impregnation method.

Acknowledgements

I would like to thank Majlis Amanah Rakyat (MARA) for sponsoring my PhD studies, my supervisor Professor Jose Antonio Lopez-Sanchez for giving me the opportunity to study within his group and his kind support and guide during my study will be always appreciated. Not to be forgotten Prof. Nick Greeves for his input and advice for my project.

My deepest gratitude to my beloved parents, Mr Endot bin Saad and Mrs Zaition Hasshim for their prayers, support and encouragement for me to pursue my dream. Not to be forgotten my siblings, especially my little sister Miss Norasmihan Endot for her endless support and motivation.

I would also like to say special thanks to the postdocs in my group for their constant help and enthusiasm during this project. Especially Dr Peter Priecel, Dr Thomas Davies and Dr Piera Demma Cara for the TEM and SEM measurements. I would like to thanks to all members of the chemistry department especially Dr Konstantin Luzyanin for the ICP analysis, Microbiorefinery (MBR) and Centre of Materials Discovery (CMD) for access to state of the art facilities.

I would like to acknowledge everybody who has help me at some point during my research and say thanks to all my friends especially my dear friend Monica Lomeli and Dr Zulkiflie Idris for always be there for me. Not to be forgotten the member of JALS research group; brother Ali Bashal, Dr Joel Mcglone, Nadiah and my Spanish and Mexican friends for making my time at the University enjoyable and wish them all the best for the future.

Contents

Figures

Tables

Schemes

Chapter 1 Introduction

1.1 Biomass

The growth in demand for fossil feedstocks as the main source of chemical and energy, together with their fast depletion has increased the need for the development of a new and sustainable source of energy and platform chemicals. At the moment, fossils fuels contribute to nearly 92 % of the commodity chemicals produced and 82 % of energy source in the United Kingdom. This is expected to change and a large part of it can be generated from biomass in the near future.[1] Biomass is the fit candidate for the alternative feedstock given that it is abundant and the only widely available carbon source apart from oil and coal. In addition, the use of biofuels derived from biomass contributes to the mitigation of greenhouse gas emission; provide a clean and therefore sustainable energy source.[2] Biomass consists of carbohydrates, lignin, fatty acids, lipids, protein, and others.[3]

1.1.1 Introduction to Biomass

Lignocellulose is a polymeric material that is a widely accessible resource; it is abundant and low in cost`. Recent efforts to develop a biomass technology for producing fuels and chemicals are directed towards the utilisation of non-edible lignocellulosic biomass.[4] The sources of non-edible lignocellulose are mostly from plants which can be from agricultural waste, forest residue, wood and energy crops.[5]

Lignocellulose contains three different monomer units namely, cellulose, hemicellulose, and lignin. Figure 1.1.1 displays the structure of lignocellulosic biomass with cellulose, hemicellulose, and lignin. Among them, cellulose is the biggest fraction, making up 40-50 % of lignocellulose. It is a linear homo-polymeric material consisting of glucose monomers linked by *β*-(1-4)-glycosidic linkages with inter- and intra-molecular hydrogen bonds which make it fibrous and crystalline structure. Hemicellulose comprises 15-30 % of lignocellulose. Hemicellulose is non-linear polysaccharides with a low degree of polymerization and amorphous structure. Due to this, hemicellulose is hydrolyzed at a faster rate than crystalline cellulose and it can be removed under milder conditions, usually in diluted acid.

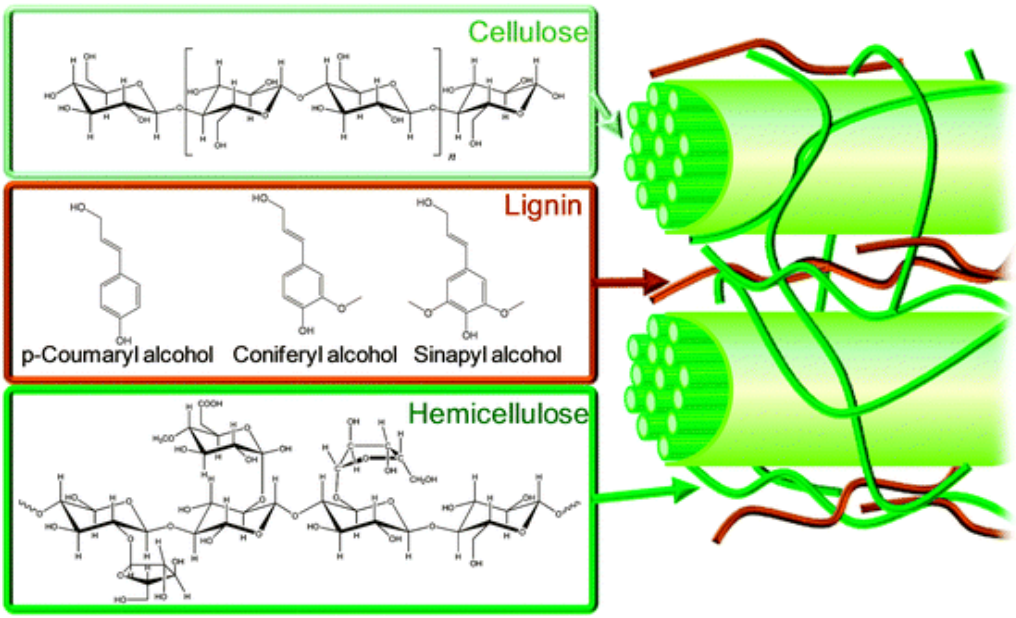

Figure 1.1.1 structure of lignocellulosic biomass with cellulose, hemicellulose, and lignin.[6] Reproduced by permission of The Royal Society of Chemistry.

Depending on the source of the lignocellulose, the structure of hemicellulose varies and may consist of pentose, hexose, and uronic acids. Lastly, lignin comprises 15-30 % of lignocellulose. Like hemicellulose, lignin is a three-dimensional amorphous polymer consisting of methoxylated and phenylpropane structures.[7] In plant cell wall, lignin fills the spaces between cellulose and hemicellulose and it acts like a resin that holds the lignocellulose matrix together. It is widely accepted that lignin is made up of polymerization of three monolignols, which are three different units of phenylpropane namely, *p*-Coumary alcohol, coniferyl alcohol, and sinapyl alcohol, that make it rich in aromatics functionality.[8]

Owing to the different properties of each lignocellulose component, each one requires different treatment or method of depolymerization into its monomeric units which in turn, can be converted via fermentation or chemical routes to platform chemicals that can be used to produce fine chemicals, bio-derived monomers or fuels.[9] Examples of such platform chemicals are d-glucose (from the depolymerisation of cellulose), 5- hydroxymethylfurfural, HMF (from dehydration of d-fructose) from which 2, 5 dimethylfuran, DMF, 2, 5-furandicarboxylic acid, FDCA and levulinic acid, LA are originated, furfural (from dehydration of C5 sugars).[10] The conversion of biomass

into platform chemicals, also known as building block chemicals, will be discussed in the following sub-chapter.

1.1.2 Conversion of biomass

The catalytic conversion of biomass and derivatives to chemicals has been the theme of intense research efforts during the past decade, with 20 % annual increase in the number of publications on this topic.[11] Many publications focus on the large variety of biomass feedstocks and the reaction type. In 2004, the US Department of Energy, DOE identified twelve building block chemicals that can be subsequently produced from sugars via biological or chemical conversions.[12] The twelve building blocks then can be further converted to a number of high-value biobased chemicals or materials. **Table 1.1.1** listed the twelve identified building blocks chemical by the DOE.

Table 1.1.1 Identified building blocks chemical for high value added chemicals.[12]

Building Blocks
1,4 succinic, fumaric and malic acids
2,5 furan dicarboxylic acid
3 hydroxy propionic acid
aspartic acid
glucaric acid
glutamic acid
itaconic acid
levulinic acid
3-hydroxybutyrolactone
glycerol
sorbitol
Xylitol/arabinitol

Depending on the target products, hemicellulose and cellulose fractions are either processed together or separately. The simultaneous processing such as gasification or pyrolysis offers the benefits of a simple separation, while the

fractionation of hemicellulose and cellulose allows the processing of each fraction to be tailored to the advantage of the different physical and chemical properties of each fraction. Biomass consists of molecules typically highly functionalised and this allows for many different chemicals to be produced, however, this also results in difficulties in controlling selectivity during the upgrade as many parallel and consecutive reactions can appear and, particularly, the degradation of the desired product or intermediate in the reaction medium.[13] Therefore, one of the most effective ways to process lignocellulosic biomass is through sequential steps which allow oxygen to be partially removed in the first step to reducing the reactivity of the feedstock. The second step is where the remaining functionality is modified to enable the upgrade to more valuable chemicals or fuels.[14]

As illustrated in **Figure 1.1.2**, biomass can be upgraded into a variety of platform chemicals as well as fuels from C_5 and C_6 sugars. Chemical methods are usually employed to process hemicellulose and cellulose after the fractionation considering the different reactivity of C_5 and C_6 sugars. For example, the conversion of C_5 sugars like xylose into furfural, or the conversion of C_6 sugar, glucose into HMF, levulinic acid, and formic acids. Among the chemicals obtained from xylose, the production of furfural has received major attention due to its potential to be converted into high value-added chemicals, such as furfuryl alcohol, tetrahydrofuran, or tetrahydro furfuryl alcohol. Furfural is also used in oil refining, pharmaceutical, plastics, and agrochemical industries.[15] In addition, furfural can be upgraded to platform chemicals and fuel precursors such as levulinic acid and levulinic esters through the intermediate of furfuryl alcohol. Like furfural, HMF is a promising platform chemical derived from sugars but from the C_6 fraction. This will be discussed in detail in subchapter 1.2.

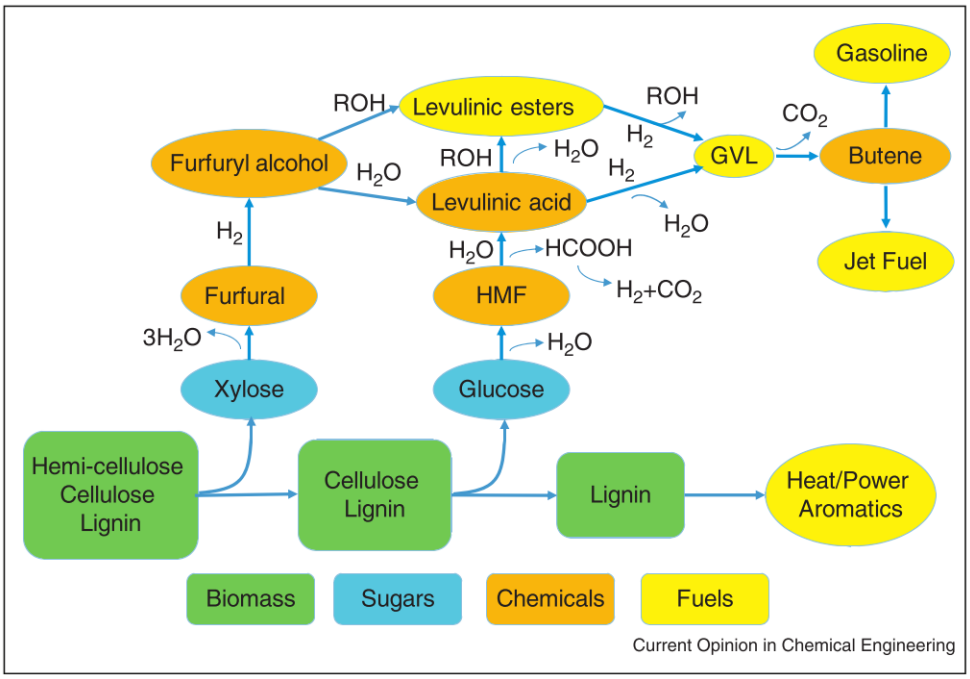

Figure 1.1.2 Roadmap for conversion of lignocellulosic biomass (green) to fuels (yellow) and chemicals (orange) passing through the intermediate formation of furfural and levulinic acid from C5 and C6 sugars (blue). Adapted from [16] by permission of Elsevier publication.

The main drawback of biomass as a feedstock and, particularly carbohydrates, is the high content of oxygen within their molecular structures. Removing oxygen increases the energy density if the product is for fuel use. **Figure 1.1.3** shows that selective removal of oxygen atoms from hexose (fructose) to produce DMF. It does not only reduces the boiling point but also reaches the lowest water solubility and research octane number, RON of mono-oxygenated C_6 compounds which are suitable for liquid fuels.[17] There are three main options for lowering the oxygen content in carbohydrates. The first option is the removal of small and highly oxidised carbon molecules such as CO_2, formaldehyde, and formic acid. Fermentative conversion of carbohydrates into ethanol, butanol and CO_2 is one of the examples. The second option is through hydrogenolysis, which is the removal of oxygen from the molecule by forming water. The third option is the removal of water by dehydration of carbohydrates into a variety of interesting compounds especially furans and levulinic acid.[17]

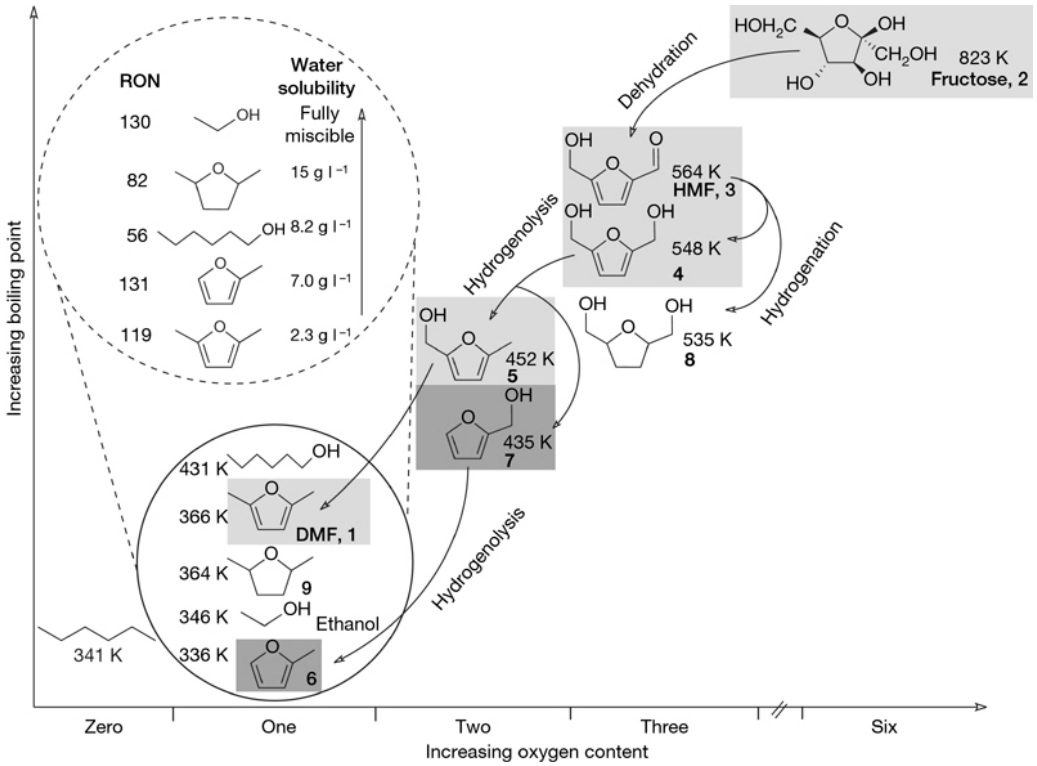

Figure 1.1.3 Normal boiling points of representative C_6-hydrocarbons formed by removal of oxygen atoms from hexoses, compared to the normal boiling point of ethanol. Reproduced by permission of Nature Publishing Group's. [17]

1.1.3 Biomass pretreatment

Biomass pretreatment is essential in the conversion of lignocellulosic biomass into fuels or chemicals.[18] It helps to hydrolyze cellulose easily by removing the hemicellulose, increasing the surface area and reducing the crystallinity of cellulose.[9, 19] As mention in subchapter 1.1.1, due to high crystallinity and fibrous structure of glucose, it is recalcitrant to hydrolysis. Upon addition of water, glucose is liberated due to the cleaving of β-(1-4) - glycosidic linkage. These cellulose fibrils are covered by hemicellulose, which is a randomly branched polymer consisting of xylose monomer and other C5 and C6 sugars. The differences in the structural and chemical properties of hemicellulose and cellulose lead to differences in reactivities and physical properties.

Biomass pre-treatment methods can be classified into several groups; physical, chemical, biological and multiple or combinations pre-treatment. In combinatorial pre-treatment methods, physical parameters such as temperature or pressure or a

biological step are combined with chemical pre-treatments and are termed as a physicochemical or biochemical method. These pre-treatments are generally more effective in enhancing the biomass digestibility. Some example of biomass pre-treatments typically employed are hydrolysis, ammonia fibre explosion,[20] steam explosion,[21] organoslv,[22] hot water [23] and ionic liquid pre-treatment.[24] Several extensive reviews on biomass pre-treatment have been published in the literature.[19, 23, 25]

1.2 HMF as a versatile compound

5-Hydroxymethylfurfural (HMF) is a versatile and multifunctional furanic compound derived from dehydration of hexose sugars. It is yellow in colour and highly soluble in water. It is currently utilised as feedstock for the production of industrial solvents and a good platform chemical for the synthesis of the precursor in pharmaceuticals, thermal resistant polymers, and macrocyclic compounds and mostly for the synthesis of di-aldehydes, ethers, amino alcohols and various organic intermediates. This potentially leads to the numerous chemical products such as solvents, surface active agents, phytosanitary products, and resins.[26, 27]

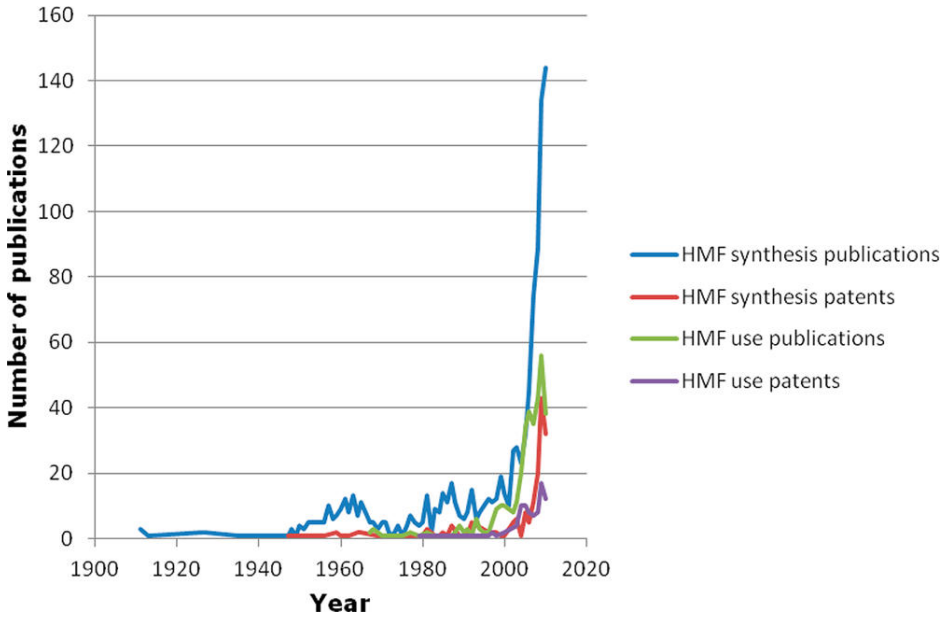

Figure 1.2.1 Number of publications on HMF per year, as registered by web of science. Taken from [28]

Figure 1.2.1 shows an extraordinary increase in the number of publication on HMF in recent years. The number of HMF synthesis publication and patent, as well as HMF used publication and patents increased sharply from mid-2000. Comprehensive reviews on HMF as versatile platform chemical have been published [3, 28-30]

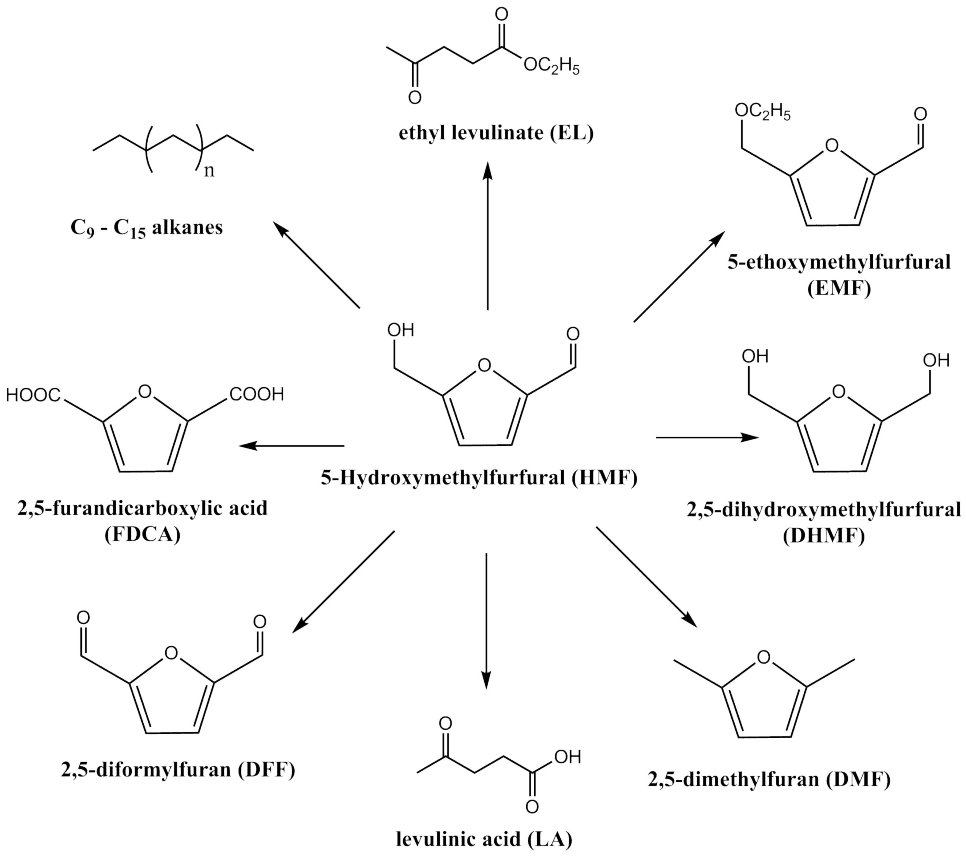

Figure 1.2.2 Intermediates with high industrial potential produced from HMF. Adapted from [31]

HMF has received a lot of attention due to its potential as precursor for fuel production such as ethyl levulinate (EL), 5-ethoxymethylfurfural (EMF), 2, 5-dimethylfuran (DMF), C9-C15 alkanes and high value chemicals such as levulinic acid (LA), 2,5-dihydroxymethylfurfural (DHMF), 2,5-diformylfuran (DFF), and 2,5-furandicarboxylic acid (FDCA).[10] **Figure 1.2.2** illustrated the intermediates with high industrial potential produced from HMF.

The presence of functional groups such as furan, primary hydroxyl, and formyl allows HMF to be transformed to various other target molecules through selective oxidation and reduction processes. FDCA is an oxidation product of HMF which has the

potential to replace terepthalic, isopthalic and adibic acids in the manufacture of polyamides, polyesters, and polyurethanes.[32] Oxidation of HMF also leads to DFF which is a versatile compound with applications as a starting material for the synthesis of pharmaceuticals, anti-fungal agents and as a component for foundry sand binders.[33] DHMF is also a valuable product in the furan family that it is potentially used as an intermediate in the synthesis of drugs, crown ethers and the manufacture of polyurethane foams.[34]

1.2.1 Production of HMF

The synthesis of HMF is based on the acid catalysed triple dehydration of hexoses mainly glucose and fructose. Although disaccharides or polysaccharides such as sucrose, cellobiose, inulin or cellobiose, as well as converted industrial wastes, can be used as HMF source but hydrolysis is necessary for the depolymerization (**Figure 1.2.3**).[29]

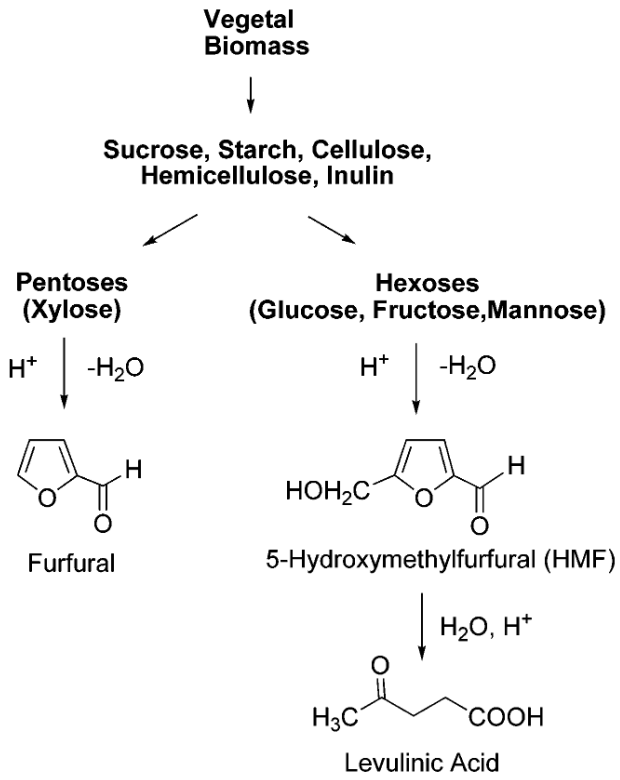

Figure 1.2.3 Products obtained from dehydration of Monosaccharides.

Besides HMF, the acid catalysed dehydration reaction leads to at least traces of various other dehydration products such as levulinic and formic acid and polymeric side products called humines or humic acids.[30, 35] In order to prevent these side reactions and obtain a high yield of HMF, the proper design of catalysts selective to HMF is crucial. The utilisation of multifunctional catalyst based on transition metals with solid/base catalysts is expected to allow several reaction steps to be finished in one reactor, and avoid the costly intermediate separation process.[36] In addition, the recycling of the catalyst and the efficient separation of the target product would also contribute to the efficient production of HMF.

The mechanism of HMF formation from fructose and sucrose has been described by Antal et al.[37], Van Dam [38] and Kuster.[39] They concluded that the dehydration could occur via two possible pathways as shown in **Figure 1.2.4**; (i) based on acyclic compounds and (ii) based on the transformation of ring systems. This also demonstrated that the chemistry of the formation of HMF is very complex due to many reactions involves besides dehydration. For example, a series of side reactions such as isomerization, fragmentation, and condensation will influence strongly the yield of the product. The production of HMF from dehydration process is more efficient and selective from fructose than from glucose due to a low degree of glucose enolization, owing to the stable ring structure of glucose compared to fructose. Enolization also known as tautomerization is a structural isomer in which a hydrogen atom is transferred from one carbon to another as shown in **Figure 1.2.4**. Since enolization is the determining step of HMF formation, glucose will react slower than fructose. Moreover, glucose can condense to form oligosaccharides which can react with HMF resulting in cross polymerised materials. Nonetheless, glucose is still used as a feedstock for HMF production due to its lower cost.

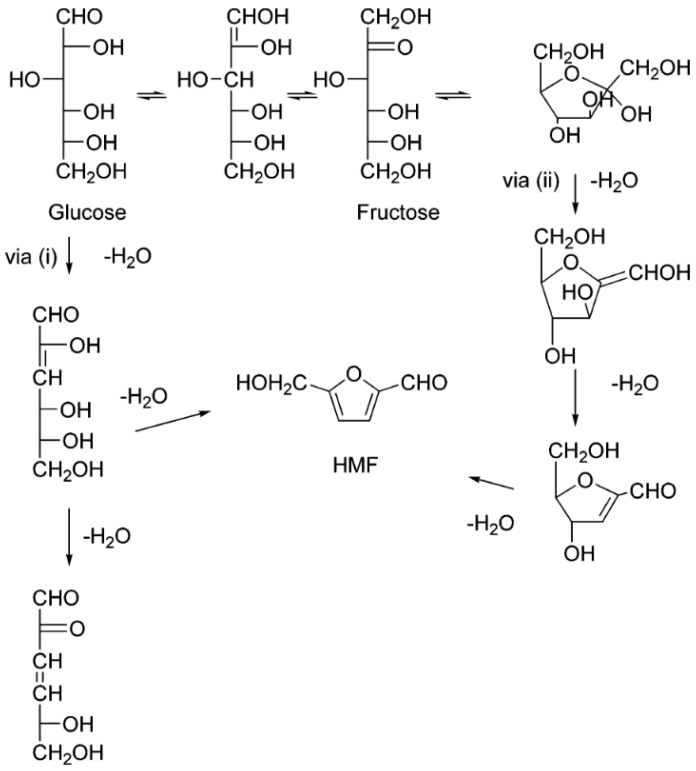

Figure 1.2.4 Pathways for the dehydration of Hexoses to HMF.

Reviews of HMF production and the kinetic studies of the dehydration reaction had been published.[10, 28-30, 39]The most convenient method of obtaining HMF is the acid-catalyzed dehydration of fructose. Fructose can be obtained by acid-catalysed hydrolysis of sucrose and inulin or by selective isomerization of glucose to fructose. Dehydration of hexoses to HMF has been carried out using a variety of catalysts such as organic acid (oxalic, maleic acids), inorganic acids (H_2SO_4, HCL), organic and inorganic salts and solid acids, Lewis acids ($ZnCl_2$, $AlCl_3$) and other (ion exchange resins, zeolites).[40]

1.3 DMF as alternative fuel

2, 5-Dimethylfuran (DMF) among other furan derivatives such as 2-methylfuran (MF) and furan is a promising biomass-derived renewable fuel candidate to reduce the consumption of fossil fuel and engine emissions. This is due to its comparable combustion properties to those of commercial gasoline and the sustainable

productivities from lignocellulosic raw materials. The utilisation of biofuels such as methanol and ethanol that have been blended with gasoline as transportation fuels in many countries could greatly reduce the dependence on fossil fuels.[41] However, methanol and ethanol have the lower heating value that increases the transportation costs and furthermore, their high solubility in water poses a threat to water security. These fundamental disadvantages limit the practical utilisation of bioethanol.[42, 43]

DMF has received significant attention due to its high energy density (30 MJ/L), high research octane number (RON = 119), low oxygen content (O/C = 0.17) and ideal boiling point (92-94 °C). In addition, DMF is nearly immiscible in water and thus easier to blend with gasoline than ethanol. Moreover, DMF has a low latent heat of vaporisation (0.30 kJ cm^{-3}) which means lower energy consumption during purification through distillation compared to bioethanol.[44] A comparison of the fuel properties of DMF to that of ethanol and gasoline is shown in **Table 1.3.1**.

Table 1.3.1 Comparison of the fuel properties of DMF versus gasoline and ethanol. Adapted from [45]

Property	DMF	Ethanol	Gasoline
Molecular formula	C_6H_80	C_2H_5O	C_5-C_{12}
O/C	0.16	0.5	0
Gravimetric oxygen content [%]	16.7	34.8	0
Density at 20 °C [kgm^{-3}]	889.7	790.9	744.6
Water miscibility at 25 °C [gL^{-1}]	2.3	miscible	immiscible
Boiling point [°C]	93	78	32-200
Energy density [MJ/L]	30	23.4	31
RON	119	110	95.8
Auto-ignition temperature [°C]	286	423	257

Recently, DMF-blended gasoline has been tested on a single cylinder gasoline direct injection gasoline engine against the benchmark of standard gasoline. The test results revealed that DMF has satisfactory combustion, ignition and emission characteristics comparable to commercial gasoline.[46, 47] A detailed review on the fundamental combustion characteristic of DMF and furan derivatives has been published by Xu et al.[46]

DMF has the potential for mass production from an abundant raw material such as lignocellulose biomass.[48] Furthermore, it is possible to obtain high efficiency in the conversion of DMF from biomass, which allows DMF to be used as alternative fuel candidate.[49] Recently DMF has been recognised as a source of bio-based ρ-xylene production via Diels-Alder cycloaddition with ethylene and subsequent dehydration (**Figure 1.3.1**).[50-52]

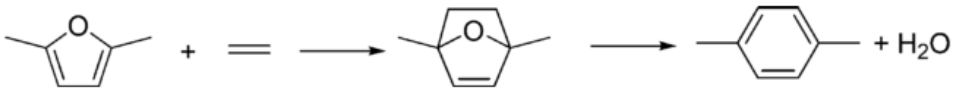

Figure 1.3.1 production of ρ-xylene production via Diels-Alder cycloaddition with ethylene and subsequent dehydration

1.3.1 Production of DMF

The first process for the production of DMF was reported in 1980 by Shunichi.[45] It involves two step processes where firstly, HMF was reduced to 2-methylfurfural alcohol (MFA) using hydrazine (N_2H_4), then followed by hydrodeoxygenation using Pd/C and cyclohexene as a hydrogen source to produce 27 % DMF at 80 °C. Since then, this technology has not been explored until the emerging of DMF as a sustainable biofuel was established. Many researchers have now developed catalytic routes to produce DMF selectively and this has recently been reviewed.[45]

The typical processes to acquire upgraded biofuels or chemical platforms require the use of homogeneous, heterogeneous or biological (enzymes, microorganisms, and yeasts) catalysts. [3] The chemical process of transforming lignocellulose into DMF is a multi-steps process. The first step typically involves the pretreatment of lignocellulose into glucose, followed by acid catalysed dehydration of the glucose isomer, fructose into HMF. The next step is the catalytic hydrodeoxygenation (HDO) of HMF into DMF. [53] **Figure 1.3.2** illustrated the pathway of DMF preparation from biomass.

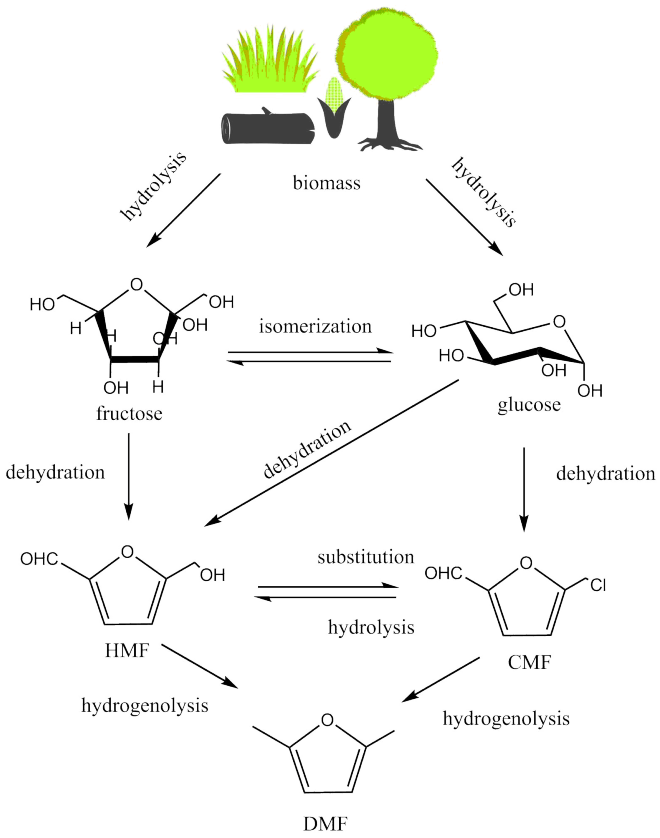

Figure 1.3.2 Pathway of DMF preparation from biomass. Adapted from.[54]

Recently, Dutta et al. have demonstrated that DMF can be produced from 5-chloromethyl furfural, CMF instead of HMF over Pd/C (2:1 N, N-dimethylformamide/acetic acid solvent mixture, room temperature, 3 atm H_2, 1.25 h).[55] CMF is produced under mild conditions and in a high yield from sugars, cellulose or directly from cellulosic biomass hydrochloric acid treatment in a biphasic system.[56]

A thermodynamic study by Verevkin et al. revealed that hydrogenation of HMF to DMF is feasible through hydrogenation of HMF to DHMF and subsequent hydrogenolysis of DHMF to DMF, given the equilibrium constant completely shifted to the desired reaction product even at 25 °C.[57]

1.3.2 Conversion of DMF from sugar

Recent advances have allowed the production of DMF from a different source of HMF by acid-catalyzed hydrolysis of cellulose into sugar component, for instant glucose and fructose. Dumesic et al. performed a synthesis of DMF with 71 % yield by

hydrogenation-hydrogenolysis of HMF from fructose using Cu-Ru/C catalyst. [17]Binder and Raines used untreated corn stover to synthesise DMF [48]. They used $CrCl_3$-HCl catalyst to transform corn stover into HMF, followed by hydrogenation-hydrogenolysis of HMF into DMF with Cu-Ru/C catalyst under H_2.

Production of DMF from fructose via one-pot synthesis has been investigated by Sudipta et al. with a maximum yield of 32 % DMF. [58] The reaction progressed via HMF synthesis using formic acid as a catalyst for fructose and N, N-dimethylacetamide (DMA) catalyst for glucose and untreated biomass in the first step. In the subsequent steps, HMF was converted to DMF by hydrogenation and hydrogenolysis reactions using Ru/C catalyst and formic acid as H_2 source. **Scheme 1** illustrated the integrated reaction pathway for the transformation of Biomass-derived carbohydrates into DMF.

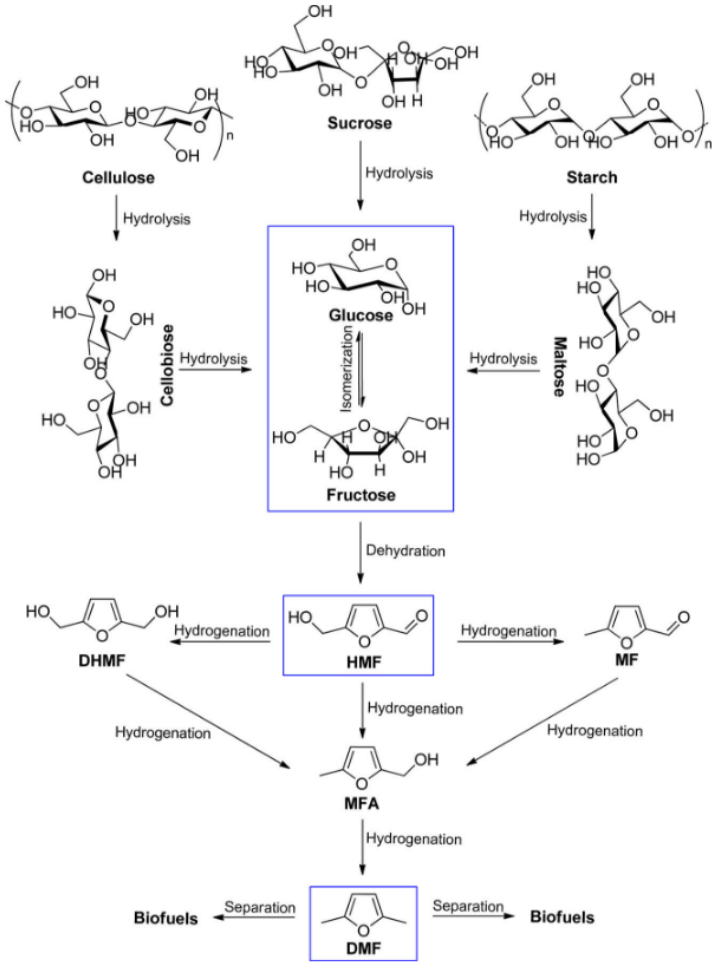

Scheme 1 Integrated reaction pathway for the transformation of Biomass-derived carbohydrates into DMF (taken from [59]).

1.3.3 Catalytic Conversion of HMF to DMF

As one of the versatile compounds, HMF is the key for the production of DMF. The conversion of HMF into DMF has been widely studied and the recent progress is summarised in **Table 1.3.2**.

Table 1.3.2 Overview of DMF production from HMF in the literature.

Entry	Catalyst	Condition					HMF conv. (%)	DMF Yield (%)	Ref.
		Solvent	H_2 donor	Temp.(°C)	Time (h)	Pressure (Bar)			
1	$CuCrO_4$	1-butanol	H_2	220	10	6.8	100	61	[17]
2	CuRu/C	1-butanol	H_2	220	10	6.8	100	71	[17]
3	Ru/C	1-butanol	H_2	260	1.5	-	99.8	60.3	[60]
4	Pd/C	[EMIM]Cl	H_2	120	1	62	47	15	[61]
5	$Pd/C/H_2SO_4$	THF	Formic Acid	70	15	-	100	95	[62]
6	Cu-PMO	methanol	methanol	300	0.75	-	100	34	[63]
7	Ru/C	Isopropyl alcohol	Isopropyl alcohol	190	6	-	100	81	[64]
8	Pd/C	Water:CO_2	H_2	80	2	10	100	100	[65]
9	Ru/K-OMS-2	1-butanol	H_2	220	6	10	90	33	[66]
10	Ru/Co_3O_4	THF	H_2	130	24	7	99	93.4	[67]
11	Ru/C	THF	Formic acid	75	15	-	-	32	[58]
12	PtCo@HCS	1-butanol	H_2	180	2	10	100	98	[68]
14	Ru/C	THF	H_2	200	2	20	100	94.7	[31]
15	PdAu/C	THF	H_2	60	6	atm	100	96	[69]
16	$Ni\text{-}W_2C/AC$	THF	H_2	180	3	40	100	96	[70]
17	Pd/Fe_2O_3	2-propanol	2-propanol	180	-	15[a]	98	72	[71]
18	Pd/C	Dioxane	Formic acid	120	15	-	100	>95	[72]
19	Cu-Ru-PMO	ethanol	H_2	220	6	50	100	79[b]	[73]
20	Pd/C/Zn	THF	H_2	150	8	8	>99	85	[74]
21	Ru/Hydrotalcites	2-propanol	H_2	220	4	10	100	58	[75]
22	Ni/Co_3O_4	THF	H_2	130	24	10	99	76	[76]
23	$Ni\text{-}Al_2O_3$	Dioxane	H_2	180	4	12	100	92	[77]
24	Cu-Co@C	ethanol	H_2	180	8	50	100	99.4	[78]
25	Pt/rGO	1-butanol	H_2	120	2	30	100	73.2	[79]
26	Pt-Ni/C	1-propanol	H_2	200	5[c]	33	100	98	[80]
27	Ni-Fe/CNT	n-butanol	H2	200	3	30	100	91.3[d]	[81]
28	Ru/HT	2-propanol	H_2	220	5	10	100	58	[75]
29	Ru/NaY zeolite	THF	H_2	220	1	15	100	78	[82]

30	CuZn	CPME	H_2	220	6	20	100	97[b]	[83]

[a] N_2 pressure was used. [b] DMF + DMTHF.[c] continuous flow reactor [d] selectivity

Among the work on HMF hydrogenation reported in the literature, it can be seen that most of the catalysts utilised consist of a noble metal such as Pd, Ru, and Pt, apart from transition metal catalysts based on Cu, Ni and Co supported on metal oxides and carbon. The addition of secondary metal from transitional metal to noble metal have also been employed by many researchers. Apart from the different type of metal, it was also observed that reaction conditions namely type of solvent, H_2 donor, reaction temperature, reaction time and H_2 pressure play an important role in influencing the HMF conversion and DMF yield. This will be discussed in details in the next section.

Dumesic et al. were able to produce a reasonable DMF yield using $CuCrO_4$ and CuRu/C catalysts under a batch condition in 1-butanol at 220 °C and 6.8 bar H_2 in 10 hours [entry 2]. It was observed that addition of Ru to Cu supported on carbon increased the DMF yield from 61 to 71 % under the same reaction condition. Although Ru/Co_3O_4 [entry 10] catalysed reaction achieved a high DMF yield (93 %) at a relatively low pressure at temperature, a high catalyst loading (40 wt. % with respect to HMF) and long reaction time (24 hr) are needed. Pd/C in supercritical carbon dioxide leads to 100 % yield of DMF in 2 hours, however, the reaction requires the specific combination of water and supercritical CO_2 [entry 8].

DMF production by catalytic transfer hydrogenation have also been investigated using formic acid (FA),[58, 62] methanol,[63] isopropyl alcohol (IPA) [64],[71] Thananatthanachon et al. demonstrated the conversion of HMF to DMF using $Pd/C/H_2SO_4$ (2 mmol HMF in THF,0.4 g catalyst) with 95 % yield of DMF in 15 hours at 120 °C .[62] However, this requires the addition of H_2SO_4. Dutta et al. performed the same reaction using Ru/C, however, lower DMF yield was obtained (30 %).[58]

Jae et al. have investigated catalytic transfer hydrogenation, CTH of HMF into DMF with 2-propanol as a hydrogen donor over Ru/C and RuO_2 [84]. They found out that the catalyst for the CTH of HMF to DMF is a bifunctional material consisting of both Ru

and RuO_2. It was suggested that the synergy of Ru and RuO_2 was responsible for the selective production of DMF.

1.3.4 Mechanism of HMF hydrogenation to DMF

There have been many types of catalytic reaction mechanisms proposed by researchers for the selective hydrogenation of HMF to DMF, but they always involve three consecutive steps as summarised by Hu et al [59] (**Scheme 2**). The first step involving the hydrogenations of the C2-aldehyde group and C5-hydroxyl group in HMF into 2,5-dihydroxymethylfurfural, DHMF, and 5-methylfurfural, MF respectively. The presence of the conjugated field on the furan ring stabilise the ring and the electron withdrawing effect of oxygen on the aldehyde group make the C2-aldehyde group and C5-hydroxyl groups unstable. Conjugation allows a delocalization of pi electrons across the adjacent p orbitals which in general may lower the overall energy of the molecule and increase stability.[85] Furan is a five-membered ring with two alternating double bonds and an oxygen in position 1. Oxygen has two lone pairs, one of which occupies a p-orbital on that position, thereby maintaining the conjugation of that five-membered ring. Nishita et al. found that the conversion of HMF into DHMF is more prominent compared to HMF into MF using Ru-K-OMS-2 catalyst [66]. This is due to the selective adsorption of HMF through carbonyl group which resulted in the formation of DHMF. Then both DHMF and MF are subsequently hydrogenated into the same intermediate 5-methylfurfuryl alcohol, MFA. The last step is the hydrogenation of MFA into targeted product 2,5 dimethylfuran, DMF.

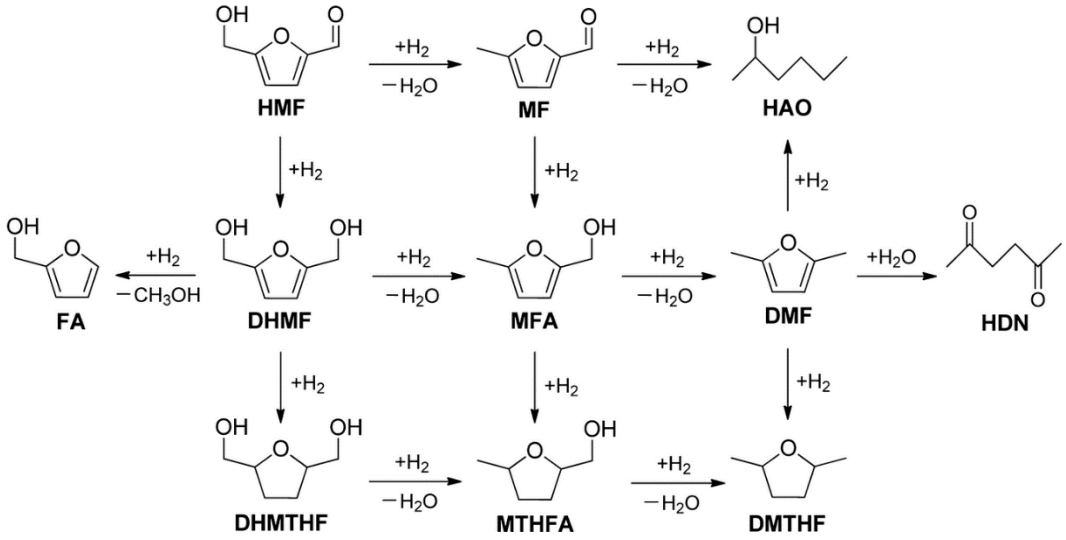

Scheme 2 Possible reaction mechanism for the hydrogenation of HMF into DMF, adapted from [59]

Although from the thermodynamic point of view the C=C bond is easily hydrogenated compared to C=O, the presence of the conjugated furan ring makes the hydrogenation of the C=O bond relatively easier than C=C bond in the selective hydrogenation of HMF into DMF. Thus it is possible to obtain high selectivity towards DMF. However many other possible byproducts and intermediates can be generated due to the high reactivity of HMF such as furfuryl alcohol (FA), 2-5-dihydroxymethyltetrahydrofuran (DHMTHF), 5-methyltetrahydrofurfuryl alcohol (MTHFA), 2,5-dimethyltetrahydrofuran (DMTHF), 2,5-hexanedione (HDN), and 2-hexanol (HAO). Under appropriate conditions such as reaction temperature, H_2 pressure, time of reaction and catalyst the formation of this byproduct are less favourable.

A recent study by Hu Lei et al. shows that various parameters play important roles in the formation of high DMF yield.[31] Among the metals supported on carbon (Pd, Pt, Rh), Ru exhibited excellent reactivity with 80.6 % yield after 2 hours. 5 mol % Ru/C loading was found to be the optimum loading for high DMF yield [31, 72]. As for the reaction time, 2 hours was found to give the highest DMF yield. When the reaction time was prolonged the yield of DMF decreased which demonstrated the formation of undesired byproducts. Increasing the H_2 pressure raised the solubility of H_2 in a solvent, thus facilitated the hydrogenation of HMF into DMF. However, at low H_2 pressure, the

yield of DMF is low due to incomplete hydrogenation of HMF into DMF which is possibly resulting in the formation of intermediates like DHMF and MF. Too high H_2 pressure might promote further hydrogenation and the opening of DMF resulting by-product like DMTHF and MFUR.

A study by Mitra et al. found that product distribution is highly dependent on reactant concentration and catalyst loading [72]. Increasing the concentration of HMF by 4-fold led to decrease in ring hydrogenation products and improve the selectivity of DMF. Catalyst loading also influencing the selectivity of hydrogenation/hydrogenolysis of the ring. Decreasing catalyst loading from 10 to 5 mol %, decreased the tendency for the ring hydrogenation prior to the hydrogenolysis as confirmed by the absence of DHMTHF in the reaction.

1.4 Heterogeneous catalysis

Catalysts have been used by humankind for over 2000 years. The first observed uses of catalysts were in the making of wine, cheese, and bread.[86] Today, catalysis plays a prominent role in our society with the majority of all chemicals and fuels produced within the chemical industry are involving catalysts. In fact, catalysis has become vital in controlling environmental pollution, with selective catalytic routes replacing the rigid stoichiometric process that produces waste. This is due to catalyst is a substance that affects the rate of reaction but emerges from the process unchanged.[86] A catalyst usually facilitates the reaction rate by providing alternative pathways with lower activation energy than without the presence of a catalyst.

Generally, the field of catalysis can be divided into three categories, heterogeneous, homogeneous and enzymatic catalysis. Heterogeneous catalysts are present in a phase different from that of the reactants; typically the reactants are in the gas or liquid phase, whereas the catalyst is a solid material. Homogeneous catalysts operate in the same phase as the reactants and enzyme catalysts are a specialised protein that is folded into complex shapes that allow smaller molecules to fit into them. The place where these substrate molecules fit is called the active site.

Heterogeneous catalysts have the desirable property that can easily be separated from the reactants and products. This is a key factor why industry prefers heterogeneous catalysts over homogeneous catalysts especially when it involves high-volume products.[87] For heterogeneous catalysts, the chemical reactions take place on the surface of the materials. For that reason, typically heterogeneous catalysts are typically very porous materials in order to maximise the surface area. In some cases, a support is used to stabilise nanoparticles (2-20 nm) of the active material. The heterogeneous catalyst should consist of small particles with a high fraction of surface atoms. This is usually achieved by dispersing particles on porous supports such as silica, alumina, titania or carbon. Examples of unsupported industrial heterogeneous catalysts are iron catalysts for ammonia synthesis and CO hydrogenation, mixed metal oxide catalysts used in the production of acrylonitrile from propylene and ammonia and Raney nickel catalyst for hydrogenation reactions.[88]

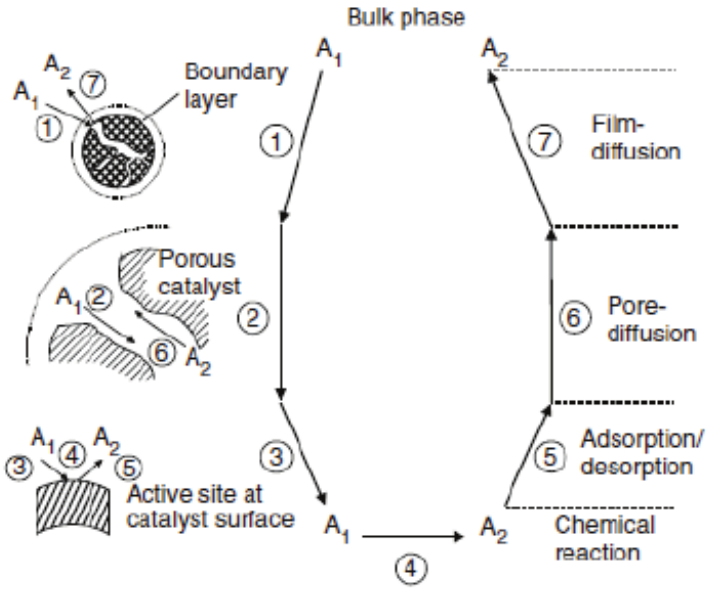

Figure 1.4.1 catalytic steps in heterogeneous catalyst (fluid-solid reaction $A_1 \rightarrow A_2$) Adapted from [89]

Traditionally, the catalytic reaction in heterogeneous catalyst consist of seven key steps (**Figure 1.4.1**); (1) diffusion of the reactants from the bulk phase (boundary layer) to the external surface of catalyst granule (film diffusion), (2) diffusion of the reactant from the pore mouth through the catalyst pores to the active sites on the interior surface (pore diffusion), (3) adsorption of the reactant, (4) chemical reaction at specific

active sites on the catalyst surface, (5) desorption of the product from inner surface, (6) diffusion of the products from the interior to the pore mouth at the external surface, and (7) diffusion of the products from the external surface of catalyst to the bulk fluid phase.

Transitional metals or mixed oxides such as Fe, Co, Ni, Cu, Ru, Rh, Pd, Ir, Pt, Au, etc are typically employed as metal active catalysts due to their ability to catalyse chemical transformation. This is owing to their unique property of changing oxidation states by donating or accepting electrons which resulted in making or breaking of bonds on the surface, enabling the catalytic activity. The classic reactions involving this process are hydrogenation, oxidation and dehydrogenation reaction.[90] Extensive reviews and discussion on the catalyst structure and electronic factor in heterogeneous catalysis have been published by Narskov et al.[91, 92]

1.4.1 Bimetallic catalysts

Bimetallic catalysts contain two different metals, which either can be miscible or immiscible as macroscopic bulk alloys. The combination of an active and inactive metal [e.g., Ni and Cu (miscible) or Os and Cu (immiscible)] dilutes the active metal on the particle surface. Therefore the catalytic performance of reactions requiring assemblies of several active metal atoms rather than a single isolated atom is influenced.[93, 94] [93]Selectivity of catalytic processes can thus be optimised due to the change in the geometric and electronic structure of the bimetallic catalysts which will affect the adsorption of the substrate.[95] Generally, the surface composition of binary alloys differs from that of bulk. The component having the lower surface energy free energy is enriched in the surface layer. For instance, Cu is largely enriched at the surface of Cu-Ni alloys, even at the lowest concentration. Furthermore, the surface compositions of binary alloys may be altered by the reaction atmosphere.

In bimetallic materials, there are four types of possible types of where the two metals can be mixed in patterns.[96] Firstly, the core-shell structure where a core metal atoms are surrounded by a shell of metal atoms of a different type.[97] Secondly,

segregated nano-alloys structures can be formed, where the two metal components have a pseudo-planar interface between them. However, this pattern is less commonly reported in the literature. Thirdly, homogeneously mixed alloys where the two metals are intimately mixed in either an atomically ordered or a statically random manner which normally called as ordered nanoalloys and random nanoalloys respectively. Among these two sub-patterns, random nanoalloys are more commonly found compared to the ordered one.[98, 99] Finally, multi-shell nanoalloys can be formed in which there is more than one concentric shell covering the core metal to form an "onion –like" structure. This kind of patterns typically occurs in some bimetallic and trimetallic catalyst system.[100, 101] **Figure 1.4.2** shows the schematic representation of some of possible mixing patterns of bimetallic systems.

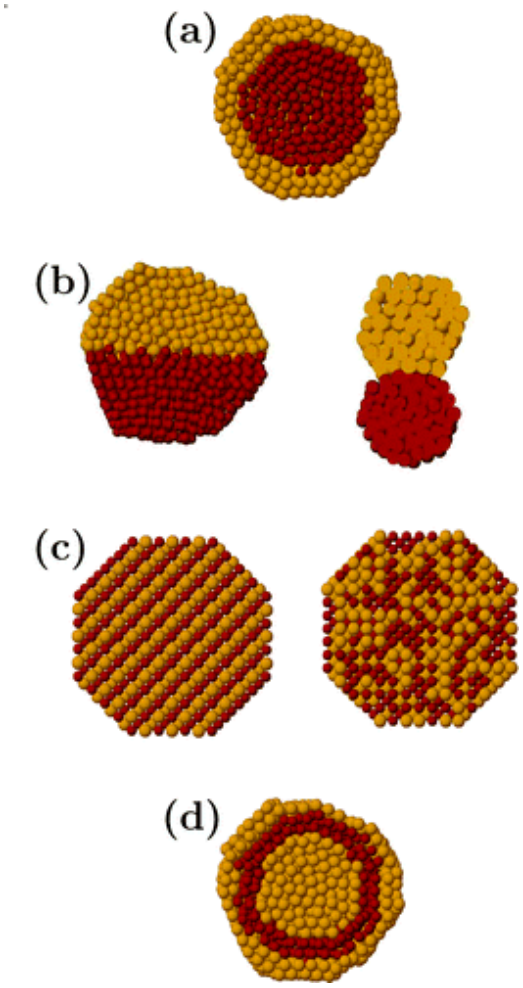

Figure 1.4.2 Schematic representation of cross-sections of the clusters of some possible mixing patterns; (a) core-shell, (b) sub-cluster segregated, (c) mixed, (d) multi-shell. Adapted with permission from.[96]

The factors influencing the type of mixing in bimetallic system include [96];(a) the relative strength of the bond between the two different metals as compared to the two component pure metals; if the alloy bond strength is greater, intimate mixing is favoured while if it is lower, segregation of the two metals is favoured (b) the surface energy of the two metals, the metals with lower surface energy tends to move to the surface of the alloy forming the shell (c) relative atomic size, smaller atoms tends to occupy the core compared to the bigger atoms (d) charge transfer, electron transfer between less to more electronegative elements favours mixing (e) stabilizer ligand, the metals that forms a stronger bond to the stabilizer ligand prefer to form a shell in the case of stabilised nanoalloys and (f) specific electronic/magnetic effects than can stabilise a specific structure between the two metals based on the electronic shell structure or electron spin interactions.

The secondary metal may act either as poison or promoter with respect to three effects[102]; site blocking, functionality, and ligand effect. The effects of poisoning and promotion can affect both the activity and the selectivity of a catalyst. For example, the addition of Au to Ni attenuates the formation of carbonaceous deposits due to the lower reactivity of Au/Ni alloy surface compared to pure Ni. However, the addition of Au to Ru does not form an alloy and lead to the segregation of Au to the steps. Since the step sites are more reactive than the terrace sites towards the dissociation of nitrogen, the presence of sufficient amount of Au poison the reactivity of Ru for NH_3 production by poisoning the active sites.

Promotion can occur due to the added metal changes the electronic structure of the mixture as compared with the pure metals. This is also known as ligand effect which is the same as co-adsorption of electronegative and electropositive atoms on pure metals. The shifts in the d-bands lead to the changes in binding energies and activation energies which are reflected in catalytic activity and selectivity. The ligand effects are most likely to occur when an alloy is formed.[102]

The bi-functionality effect is where each metal contributes as a function of the overall chemical mechanism, which is the sum of at least two parallel steps that occur at different sites. The presence of islands of one metal form on top of the other metal gives rise to the possibility that each metal will act much like the pure metals. Thus for

example, if one is good at dissociating one molecule while the other has a particularly well suited binding energy for the other reactant, the combination of the favourable properties of both pure metals can lead to a catalyst that is more effective than the sum of its parts. For instance, the electro-catalytic oxidation of CO in an aqueous solution on a Pt electrode promoted with Ru, CO is bound at sites on Pt surface, whereas OH is formed from the dissociation of water on Ru islands. Oxidation occurs at an appropriate voltage when CO diffuses from the Pt sites to the edge sites of the Ru islands.[103]

1.4.2 The role of Support

The catalyst support also plays an important role in the selectivity of hydrogenation reactions. The supports are usually metal oxides or carbon with the goal of maximising the specific surface area thus gives a better dispersion of the active phase. Most common support included various types of silica, alumina, and carbon. However, the use of microporous support typically involves mass transfer issue due to diffusion limitation. In porous catalysts particles, the reacting molecules diffuse first through the fluid film surrounding the particles surface and then diffuse into the pores of the catalyst to the active sites. In a similar way, the reaction products are diffusing out of the catalyst grains. As an outcome of the pore diffusion in the most common reaction kinetics, the reaction rates inside the pore is lower than with the concentration level of the main bulk.

Carbon materials have been one of the most widely studied as a support for the catalyst preparation owing to its advantages.[104] Other than being low in cost, carbon also gives better dispersion due to high surface area compared to other support such as Al_2O_3 and SiO_2. Moreover, the carbon surface is relatively inert, preventing from any unwanted reactions catalysed by the support surface or the reaction of the support with the active phase. Most importantly carbon can minimise poisoning issues due to hydrophobic nature of carbon. For example, it leads to a weaker interaction between the catalyst and the solvent. However, the chemical nature of their surface can be modified chemically to decrease the hydrophobic character by oxidising treatment.[104]

For example, the treatment with hydrogen peroxide and nitric acid introduced the oxygen surface groups which responsible for the improvement of hydrophilic character of carbon surface.

Ricardo et al. reported that Ru supported on materials with a high isoelectric point (basic) such as ceria, magnesia-zirconia and ɣ-alumina resulted in a high yield of DHMTHF as compared to low isoelectric point (acidic) support such as SiO_2 for selective hydrogenation of HMF.[105] This demonstrated that the basicity of the catalyst support favours the formation of ring hydrogenation of DHMF to (DHMTHF). On the other hand, the acidic support favours the formation of ring opening product such as 1, 2, 5-hexanetriol.

The effect of different supports on Palladium catalyst for the hydrogenation of HMF has been studied by Cai et al.[106] The acidic Pd/ɣ-Al_2O_3 and Pd/SiO_2 shows a similar activity as that of Pd/C apart from the selectivity towards DHMTF, which is higher than those of Pd/C, suggesting that the acidity of the support is influencing the product's selectivity. When the reaction is prolonged to 3 h, the final product is mainly DHMTHF due to the saturation of the C=C bond in DHMF (Scheme 2). As for Pd/TiO_2, DHMF was the main product even when the reaction time was prolonged. It was speculated that, by dispersing metal on the reductive support (TiO_2), metal catalyst demonstrates the potential for selectively hydrogenating the carbonyl group without affecting the C=C bond. [106] In the case of Pd/HT catalyst, the basic HT support was found to restrain the dehydration reaction and inhibits the hydrogenation activity of Pd. It's also reported that HT could induce ring opening, C-O dissociation reaction, and other side reactions.[107]

1.4.3 Carbon

Among the different type of supports used in heterogeneous catalysis, carbon materials are one of the most studied supports in many hydrogenation reactions. Although these materials do not possess any electronic effect that can enhance the selectivity towards certain compounds, like partially reducible oxides or graphite, owing to its high surface area it is very beneficial in catalyst preparation.[108] Apart from

that, there are many specific characteristics of carbon which makes them popular as a support for heterogeneous catalysis over other traditional catalyst support; carbon surface is resistance to both acidic and basic media, the structure is stable at high temperatures, the pore structure can be tailored to obtain the pore size distribution needed for given application, porous carbon can be prepared with a variety of macroscopic shapes (e.g., granules, powder, fibres, cloths, pellets, monoliths, disk), the surface chemical properties of carbon can be modified to control the polarity and hydrophobicity, the active phase which usually the precious metals can be recovered easily from the spent catalysts by burning away the carbon support and finally carbon supports are usually cheaper than other conventional catalysts supports.[104] The use of carbon as a catalyst support relies primarily on the relative inertness of its surface, which facilitates the interaction between active phases or between active phases and promoters, thus enhancing the catalytic behaviour. This makes porous carbons an excellent choice as catalyst support in a great number of reactions.

A large variety of carbon materials has been heavily utilised as catalyst supports. The most significant are granular and powdered activated carbons (prepared from thermal activation and chemical activation) and carbon blacks (produced by partial combustion or pyrolysis of hydrocarbon); however, there is increasing interest in related material such as activated carbon fibres and cloths, nanotubes and nanofibers (CNFs).[109] Comprehensive reviews of the use of these materials as support as well as a catalyst have been published by several researchers. [110-112].

The different pores have different meanings for the catalytic reaction. Micropores are responsible for the strong adsorption of small molecules and therefore play an important role in the adsorption of small molecules for water purification. As they are smaller than 2 nm, they are sometimes not accessible for larger molecules. Pham Huu et al. reported that CNF-supported catalyst exhibited high catalytic activity compared to activated carbon in liquid phase hydrogenation of the C=C bond in cinnamaldehyde.[113] This was due to a large number of micropores on activated carbon led to the diffusion problems which affect the catalytic rate. The mesopores are typically considered as the part of the catalyst where the actual catalytic reaction takes place. The macropores are useful for the transport of molecules between the liquid

phase and the mesopores. The porosity needs to be adjusted for optimum catalyst performance.

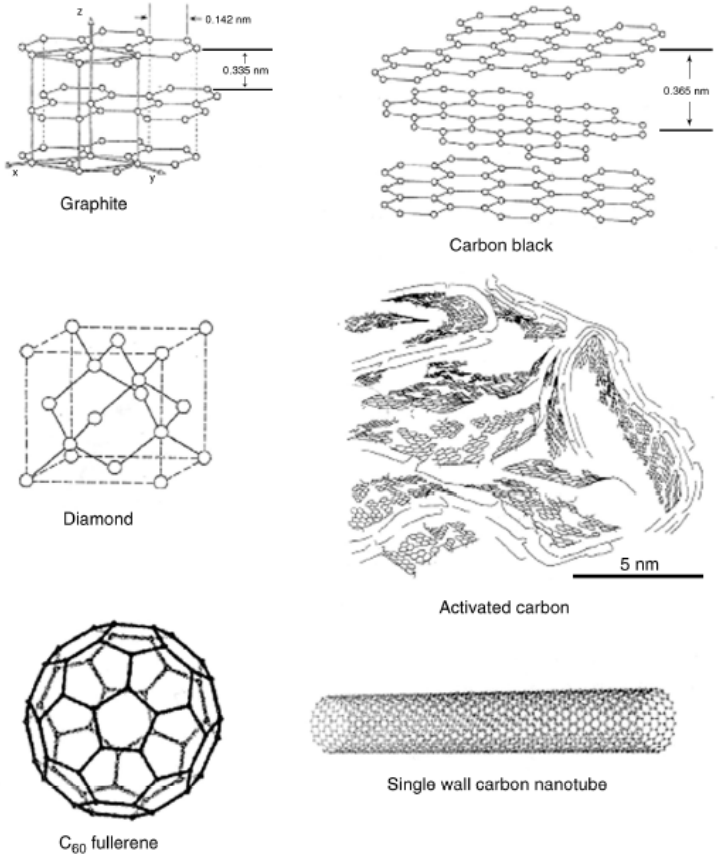

Figure 1.4.3 Approximate structure of industrial carbons. Taken from [113]

1.4.4 Carbon Nanotube, CNT

The scientific interest in CNT received a boost in the 1990s after the publication of two key articles by Japanese microscopists showing that CNT is either multiwalled or single-walled and, are formed during the synthesis of fullerenes by arc discharge.[114] Since then, CNT has become one of the most active research topics in nanoscience and nanotechnology due to its exceptional properties that make them suitable for many possible applications such as polymer reinforcements for composites, breakthrough materials for energy storage, electronics, and catalysis.[110, 115, 116] **Figure 1.4.4** lists the elements that have been deposited on CNT and carbon nanofiber, CNF. One can notice that precious metals like Pt and Pd supported on CNT and CNF has been extensively

studied due to the possible application in the fine chemical industry[112], while the emerging of Pt and Pt-Ru systems are mostly due to the potential of CNT and CNT as supports for fuel cell electrocatalysts.[117]

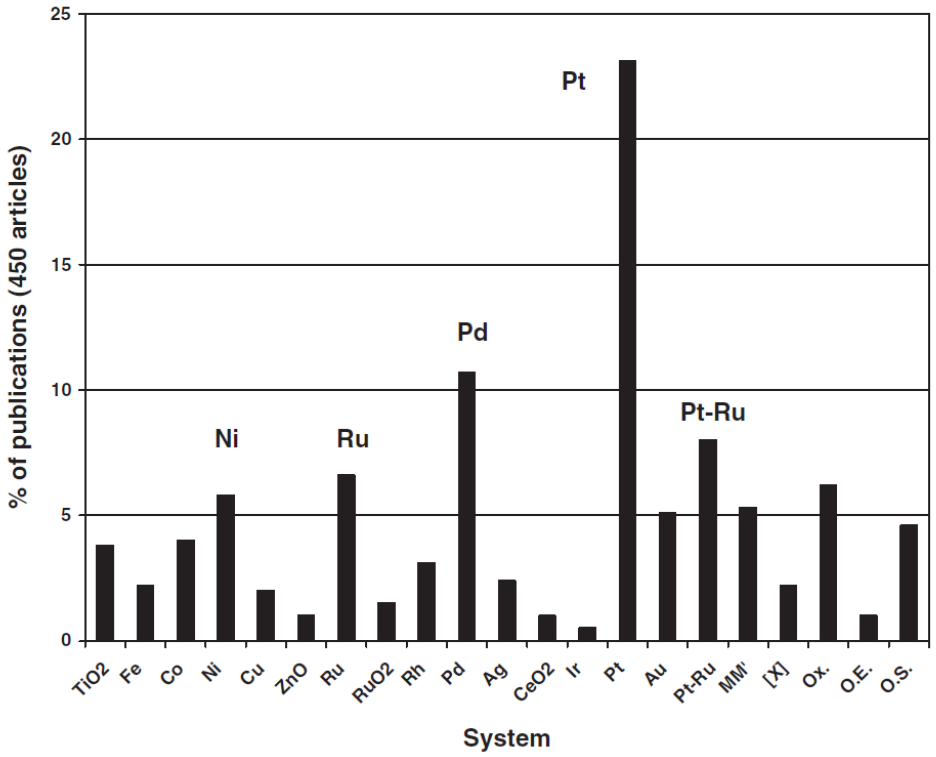

Figure 1.4.4 Elements that have been deposited on CNTs or CNFs. MM1; bimetallic systems; [x] molecular complexes; Ox, oxides; O.E., other elements; O.S., other systems. taken from[104]

CNTs have been drawing a lot of attentions in catalysis lately mostly due to the fact that it could enhance some catalytic activity. This is due to their unique properties such as uniform pore size distribution, high length to diameter aspect ratio which provides them with a high external surface area. These special properties could influence the metallic particle size distribution, dispersion, metal oxidation state but also can reduce mass transfer limitation which leads to a high catalytic performance in comparison with other conventional support.[118] In addition, the three-dimensional nanoscale structure of rolled up graphene layers allows a transfer of electronic density from the support to the deposited metallic nanoparticles. This could affect the properties of the metallic phase and their catalytic behaviour.[119] Moreover, the

curvature of the CNT could induce an extra modification on the molecular adsorption on the metallic phase thus affecting the catalytic activity.[120]

CNT consists of a rolled up graphite sheet and available as single-walled (SWCNT) and multiwalled nanotubes (MWCNT). Typically, CNTs is prepared by arc discharge, laser ablation, and catalytic chemical vapour deposition. CNTs can be readily dispersed in a solvent using ultrasound; however, they can quickly aggregate and precipitate due to its strong van der Waals forces.

Typically, several pre-treatment on CNT are essential in order to obtain a high dispersion of metallic phase by introducing the functional group on the surface of CNT as CNT do not possess a lot of functional groups on their surface apart from surface defects (vacancies, dangling bonds at open ends) and re-hybridization defects (ability of carbon to hybridize between sp^2 and sp^3) can be considered as an anchoring site for metals.[121, 122] The most common methods used for the pre-treatment are acid oxidation, gas-phase oxidation by air or CO_2 or oxidation by oxidising agents such as hydrogen peroxide, ozone, permanganate and physical methods such as ball milling or sonication.[104]

In addition, these pre-treatments can also modify the CNT towards wetting and the capability of the precursor to be reduced on the support. For examples, HNO_3- oxidised CNTs is hydrophilic in contrast to untreated CNTs which are hydrophobic. The presence of oxygenated groups can also inhibit the reduction of the metal on the support due to strong metal support interaction [104]

1.4.5 Confinement and electronic effects on CNT

Carbon nanotubes can be divided into two categories; single-walled, SWNT and multiwalled, MWCNT. Ideally, single wall CNT is made of a perfect graphene sheet which is a poly-aromatic monoatomic layer made of hexagonal displays of Sp^2 hybridised carbon atoms, rolled up into a cylinder and closed by two caps (semi-

fullerenes). The internal diameter of CNT can vary between 0.4 and 2.5 nm and the length ranges from few micros to several millimetres.

MWCNT is a concentric SWCNT with increasing diameter and coaxially disposed. The number of walls present can vary from two to several tens so that the external diameter can reach 100 nm. The concentric walls are typically spaced by 0.34 nm similar to the inter-graphene distance evidenced in turbostratic graphite materials (there is quenched rotational dis-alignment between adjacent graphene sheets, i.e. one sheet is rotated with respect to its neighbour). It is also worth to note that residual metallic particles such as Fe, Co originate from the production process can be found in the inner cavity of MWCNT.

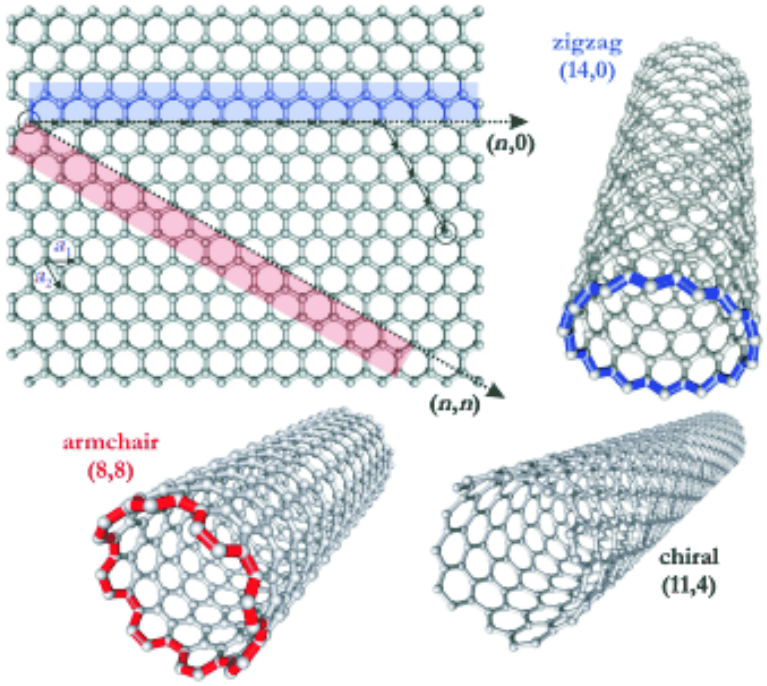

Figure 1.4.5 Roll-up of a graphene sheet leading to three different types of CNT.[116]

Extensive studies concerning the electronic properties of CNT has been published in the literature.[110, 120, 123-125] Electronic properties are mainly governed by two factors; the tube diameter and the helicity which is defined by the way in which the graphene layer is rolled up for example armchair, zigzag or chiral as showed in **Figure 1.4.5**. This curvature of the graphene sheet induces strong modification of the electronic properties and compared to graphite, CNT shows a modification of the π

electron cloud.[126, 127] The curvature can be expected to alter the bonding features on CNT as a result of the curvature-induced rehybridization of carbon bonding orbitals (non- planar sp^2 configuration)(**Figure 1.4.6**).[128] The prehybridization process including a certain amount of σ character in a π-type orbital change both its chemical and physical characteristics.[129]

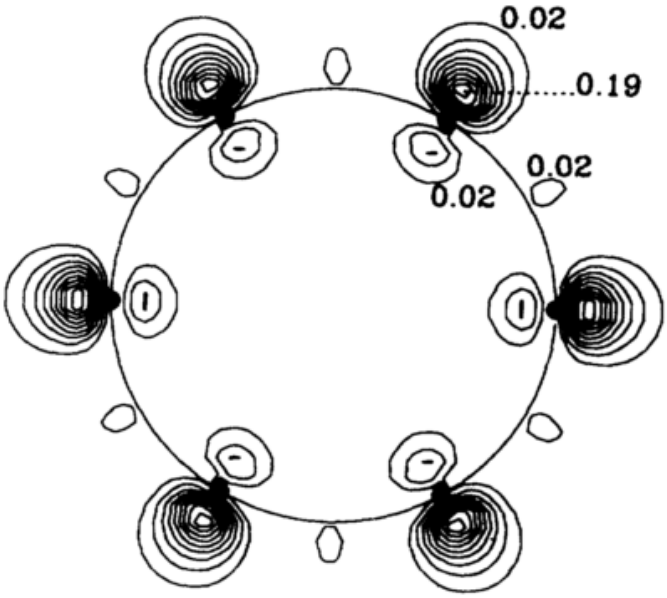

Figure 1.4.6 the effect of curvature induced rehybridization in CNT. taken from[128]

Studies on the electronic properties of MWCNT discovered that they behave like an ultimate carbon fibre. The arrangement of carbon atoms determines the surface and electronic properties of CNTs. According to the theoretical prediction; the geometry of the ring structures imparts either a metallic or semi-metallic nature to CNT. The armchair nanotube exhibits a metallic behaviour (finite value of charge carriers in the density of state (DOS) at the Fermi energy) while the zigzag nanotube is a small gap semiconductor (no charge carriers in the DOS at Fermi energy).[130] This naturally influences the properties of metals loaded onto the support. When used in catalysis, these conductive properties of CNT as a supports shows clear differences with respect to activated carbon, and recent theoretical study related to the interaction of transition metal atom with CNT and graphite indicates major differences.[131] It has been demonstrated that the binding sites are depending on the structure of the support; the studies performed over Ni show a sensible variation of the stability of anchoring sites

between graphite and CNT. This is due to the different curvature of the surface where the active species can be deposited. The curvature also affects the value of magnetic moments on the Ni atoms on CNT wall and the charge transfer direction between Ni and carbon can be inverted. This leads to a possibility of peculiar metal support interaction that has to be taken into consideration.[131] Duca et al. examined the combined properties of graphite versus CNT with Pd_9 clusters by a computational method (density functional theory, DFT).[132] It was found that Pd_9 clusters may have a stronger interaction with a CNT compared to flat graphite sheets due to the curvature of CNT which has an effect on its metallic properties. This was proved by the atomic orbital overlap occurring between the cluster and the nanotube.

1.4.6 The role of Solvent

The medium of reaction also plays an important role in determining the reactivity or the product yield in a chemical reaction especially hydrogenation of HMF.[133] Usually, solvent like water is preferable since it's a green solvent and no extra precaution is needed to handle it as a waste. However, not all reaction is suitable with water as the solvent. In general, solvent can be categorised into three different categories including polar protic, polar aprotic and nonpolar. Polar protic solvents are often displayed hydrogen bonding and have acidic hydrogen. These solvent have high dielectric constant and polarity for instant water, formic acid, methanol, butanol and propanol. These types of solvent are most likely to participate in the reaction. Polar aprotic solvents are lack of hydrogen bond and have moderately to high dielectric constants. They do not participate in the reaction as they are relatively free in solution and making them more reactive. Common examples of this solvent are acetone, acetonitrile, THF and DMSO. Non-polar solvents are solvent like hexane, benzene and toluene which have low dielectric constants and not a good solvent for a charged species.

Recent study by Chatterjee et al.[134] shows that solvent with negative δ values which are capable of accepting electrons shows a higher conversion of HMF. However, as the δ value increase the conversion of HMF is decreased. They suggested that the solvent adsorption leads to the partial blocking of metal active sites. In addition, a neutral

medium was preferred over basic or acidic medium. Water was also found to be superior to other organic solvents used for the conversion of HMF and the production of BHMF [134].

The study of the effect of solution phase acidity on the selectivity for hydrogenation of HMF performed by Alamillo et al [105]. Treatment of the HMF feed with resin led to increasing of over 20 % in the selectivity of DHMTHF using Ru catalyst. The treatment with resin resulted in an increase in pH and the increment in pH suggest that the minor impurities of acid mixed with HMF decreased the selectivity to DHMTHF. The influence of addition of specific types of acid on hydrogenation of HMF has also been studied. [105] Levulinic acid and H_2SO_4 were added to the reaction mixture and addition of levulinic acid led to decrease in DHMTHF yield while H_2SO_4 resulted in significant decline in DHMTHF selectivity from 76 % to 9 %. Tt was suggested that HMF and DHMF undergo acid catalysed degradation thus lead to low selectivity.[105]

The study of hydrogenation of HMF using different solvent was also been carry out by Alamillo et al. using water-1-butanol biphasic system, water, a mixture of THF and water and THF-alcohol [105]. It was found that HMF and DHMF were completely converted in each of reactions. The selectivity of DHMTHF is decreased when pure water was used indicating the presence of additional degradation pathways in the presence of water.

1.5 Hydrogenation

1.5.1 Introduction

Hydrogenation reactions are the most important in reduction conversion reactions and important in fat and oil industry. In hydrogenation reactions taking place over the surface of metal catalysts, the metal surface activates hydrogen molecules to form active hydrogen species, which then attack the double bond of the substrate adsorbed on the catalyst surface. One of the most important themes on designing

hydrogenation catalyst is the control of the relative activity in C=O and C=C hydrogenation (**Figure 1.5.1**).

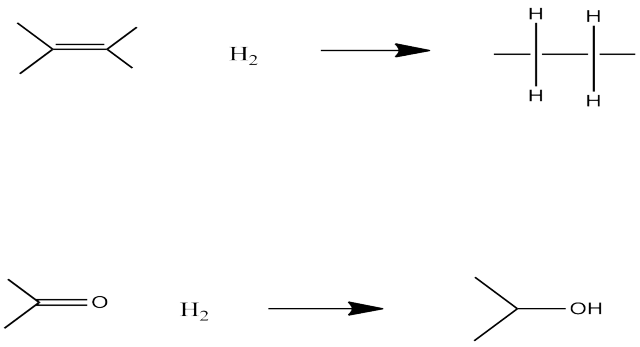

Figure 1.5.1 Hydrogenation of C=C and C=O bonds

The bonding strength between hydrogen and metal surfaces increases with an increase in d-orbitals. If the bonding is too strong, the products are not readily released thus maximum catalytic activity will not be achieved. Therefore, the maximum catalytic activity will occur when there is approximately one vacant of d-orbital per atom.[86] The typical active metals comprise noble metals and some transition metals like Rh, Ru, Os, Pd, Ir, Pt, Cu, Ni, and Co.[135] On the other hand, metals like V, Cr, Cb, Mo, Ta and W, each has a large number of vacant d orbitals, are relatively inactive due to strong adsorption for the reactants or the products or both. Usually, Ir and Os catalysts show moderately high selectivity to C=O hydrogenation, while Pt, Ru, and Co possess moderate selectivity and Pd, Rh and Ni are unselective or poorly selective to unsaturated alcohol.

Several properties like adsorption geometry on the catalyst surface, nature of the hydrogen species and acid-base properties do play an important role in affecting the selectivity in hydrogenation. [133] Experimental and theoretical studies show that catalytic performance is critically affected by the adsorption structures of the substrates on the metal surface. In general, the atoms directly bonded to the surface of the metal atom are more likely to react.[136] However, too strong adsorption can rather decrease the reactivity. For example, hydrogenation of propenal over Pt catalyst

primarily produced propanol due to C=C hydrogenation, as the Pt metal surface strongly adsorbs propenal at the carbon atoms in the C=C bond (**Figure 1.5.2 a**).[137] However, the presence of a substituent on the C=C bond, for example, a methyl group, can affect the adsorption geometry via steric hindrance and make the adsorption of both C=C and C=O possible (**Figure 1.5.2 b**). In the case of HMF, selective hydrogenation of C=O is easier compared to C=C since C=O is located on the metal surface and the localised effect on furan ring favours the hydrogenation at C=O bond (**Figure 1.5.2 c**). Other than that, temperature and surface coverage may change the adsorption structure. Higher temperature or higher surface coverage leads to the dissociation of weak bonds and changes the adsorption mode.

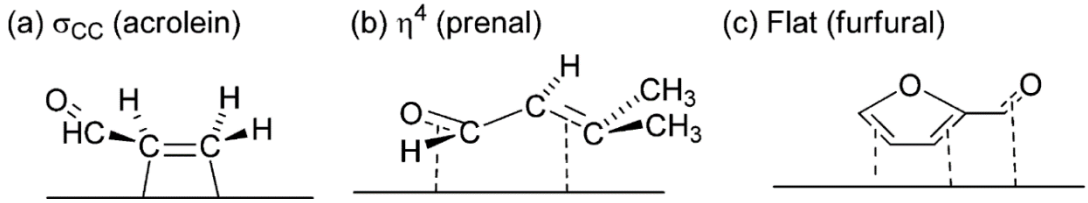

Figure 1.5.2 Typical adsorption modes of α,β-unsaturated aldehydes on Pt (111) surface.[137-139]

Figure 1.5.3 illustrated the adsorption structure of furfural on the catalyst surface proposed by Nakagawa et al. [140] It was believed that the addition of Ir may promote the adsorption of C=O site on furfural and weaken the adsorption on the furan ring in the case of Pd-Ir/SiO_2 catalyst. This was demonstrated by comparing the selectivity of furfural and furfuryl alcohol on Pd-Ir alloy to monometallic Pd and Ir. The high reactivity of furan ring hydrogenation was observed on monometallic Pd. In the presence of furfural, the hydrogenation of furfuryl alcohol over Ir was suppressed, suggesting the strong adsorption of C=O on the surface of Ir.

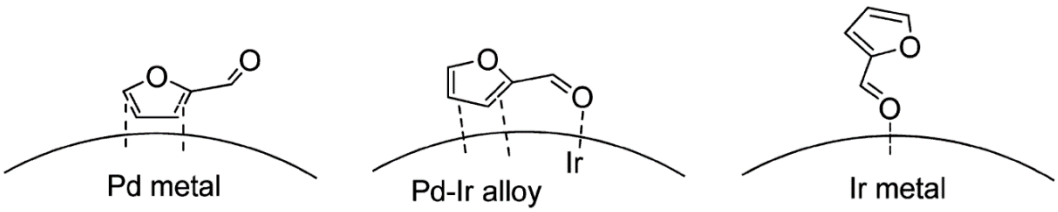

Figure 1.5.3 The proposed adsorption structure of furfural on the catalyst surface.[140]

The property of the adsorption of the substrate on the catalyst can be changed by the addition of a secondary metal, particularly an oxophilic metal (electropositive element) like Sn. Vetere et al. [141] studied the chemoselective hydrogenation of Furaldehyde using monometallic Pt, Ni, Rh and bimetallic catalyst with Sn supported on SiO_2. They found that addition of Sn showed significant in conversion for Pt and increase in selectivity towards furfuryl alcohol with Ni. **Figure 1.5.4** shows the promotion effect of an oxophilic metal on substrate adsorption at the C=O bond.[138, 142, 143] The presence of an oxophilic metal or cation on the noble metal surface induce the hydrogen species formed on the noble metal to be transferred to the C=O bond to achieve selective hydrogenation.

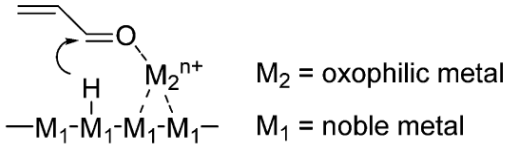

Figure 1.5.4 Effect of the oxhophilic metal promoter.

The nature of the active hydrogen species may affect the overall reductive conversion of reactants. Hydride is the anion of hydrogen, H- or more commonly, it is a compound in which one or more hydrogen centres have nucleophilic, reducing or basic properties. The hydrogen atom in hydride compounds bonded to a more electropositive element or group.[144] For an instant, homogeneous reactions of unsaturated aldehydes with $NaBH_4$, where the active hydrogen species is a hydride, the hydride anion attacks the positively charged C atom in the C=O bond (**Figure 1.5.5**).

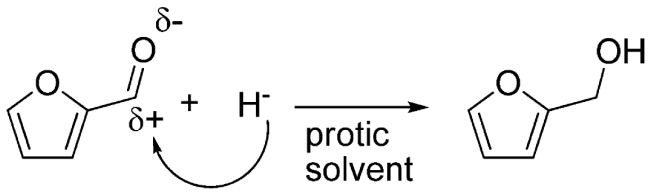

Figure 1.5.5 Effect of Hydrides species on reductive conversions of substrates

Hydrides like species have also been suggested as active species in direct C-O hydrogenolysis. For example hydride like species formation due to heterolytic dissociation of H_2 to H^+ and H^- species leading to high activity and selectivity toward unsaturated alcohol in the hydrogenation of unsaturated aldehyde over Ir-ReO_x/SiO_2.[145]

1.5.2 Hydrogenations with Noble metal catalysts

Typical processes to acquire upgraded biofuels or chemical platforms require the use of homogeneous, heterogeneous or biological (enzymes, microorganisms, and yeasts) catalysts. [3] This process normally involving acid catalysed reaction.

As the conversion of HMF to DMF is a hydrogenation/hydrogenolysis process, catalysts employed for this reaction are hydrogenation catalysts, commonly noble metals such as Pd, [65] Ru[58, 66, 67], Pt[68] and others, which are generally supported on carbon in some form. This combination provides high reactivity and good dispersion on sustainable and tuneable supports with high surface area and easy to modify porosity and surface properties.

However, noble metals may be deactivated in water, which is commonly used in these hydrogenations. Moreover, their price is high and unsustainable. Only in the case of low concentrations and high catalyst lifetime can these catalysts be considered as those of future for biomass transformations. However, they possess high reactivity even at low hydrogen pressures and it was shown that it is possible to obtain 100 % HMF conversion and 98 % DMF yield after 2 hours at 180 °C and 10 bar H_2 over Pt-Co in hollow carbon nanospheres.[68] In another study, Ru/Co_3O_4 catalyst exhibited 93.4 %

DMF yield at 130 °C and 7 bar H_2.[67] Further still, transfer hydrogenation with 2-propanol as a hydrogen donor was carried out by Jae and co-workers, who used Ru/C and achieved 100 % HMF conversion and 81 % DMF selectivity after 6 hours at 190 °C under 20 bar N_2.[64] With the same catalyst, Ru/C in the presence of THF as the solvent yielded 94.7 % DMF at 200 °C under 20 bar H_2 for 2 hours. [31]

1.5.3 Hydrogenation reactions with transitional metal catalyst

Up to now, most of the catalysts being used in the transformation of HMF into DMF involved precious metals such as Ru, Pt, and Pd. [45] Thus an alternative catalytic system based on non-precious metals (Co, Ni, Cu, and Fe) is crucial from the economic point of view since they are cheaper.

Ni and Co are the typically active metals for hydrogenation processes since both metals can hydrogenate C=C and C=O bonds.[77, 133] Raney nickel catalyst, for example, has been used in a wide range of hydrogenation reaction, such as in the hydrogenation of nitro compounds, alkenes, carbonyl compounds, nitriles, alkynes and aromatic compounds.[146] Recently, Iriondo et. al. has demonstrated that Cu catalyst supported on ZrO_2 had the best selectivity towards DMF among other compared metals such as Pt and Ru.[147] Ni supported on Co_3O_4 has also shown good activity as an additive to Co_3O_4 in converting HMF into DMF, since both of the elements have good ability to break C-O bonds.[76] 76 % yield of DMF was achieved under relatively mild reaction conditions (130 °C, 10 bar H_2, 24 hr). Ni supported on Al_2O_3 from Kong et al. shows that Ni is promising for HMF hydrogenation with a high yield of DMF, DMTHF, and DHMTHF.[77] The modulation of the surface metal-acid bifunctional site via calcination temperatures and control reaction conditions resulted in a high yield of DMF (91.5 %), DMTHF (97.4 %) and DHMTHF (96.2 %).

Catalysts based on Ni and Co were also used in the chemoselective hydrogenation of furfural. Furfural hydrogenation is pretty much similar to HMF

hydrogenation, apart from having less methyl and a hydroxyl group.[141] Ni/SiO_2 was reported to have better reactivity than Rh/SiO_2 for hydrogenation of furfural and selectivity to furfuryl alcohol.[141] **Figure 1.5.6** shows the schemes proposed by Nakagawa et al. for hydrogenation mechanism of furfural and furfural alcohol over Ni/SiO_2 catalyst. Based on the kinetic analysis they reported that adsorption of furfural on a Ni/SiO_2 catalyst is much stronger than that of furfural alcohol, FOL under the hydrogenation conditions, suggesting that furfural is adsorbed at the C=O group.[148]

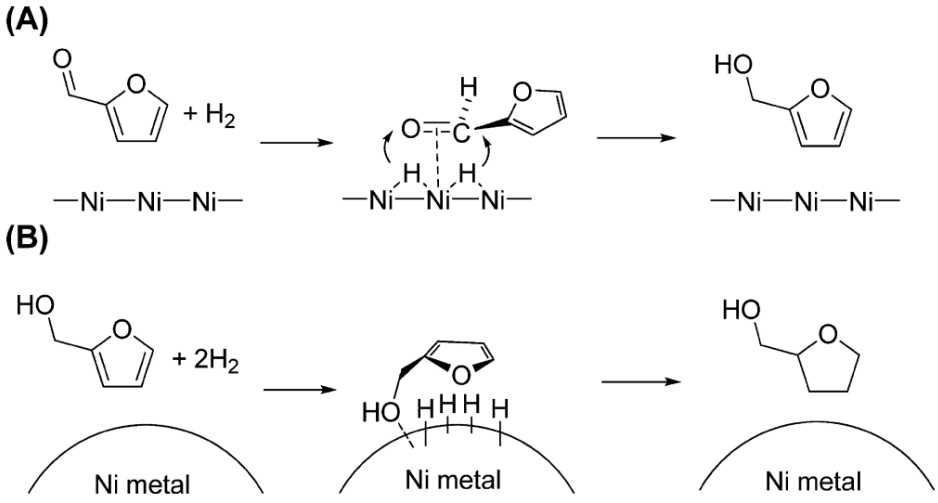

Figure 1.5.6 Proposed mechanisms for the hydrogenation of (A) furfural and (B) FOL over Ni/SiO_2.[148]

The utilisation of new and cheap metals for hydrogenation of HMF to DMF should be explored more since this could be beneficial as an alternative for the precious metal. Apart from the transitional metal being used as a monometallic catalyst for hydrogenation, the combination of these metals with other transitional metal or noble metals were also getting more attention.[45] However, this will be discussed in sub-chapter 1.5.4.

1.5.4 Hydrogenation reactions with bimetallic catalyst

Bimetallic catalysts have been received a lot of attention in selective oxidation [149], Fischer-Tropsch [150] and hydrogenation catalytic reactions. [151]. This is due to positive synergistic effects emerging upon alloying that result in structures and properties which are distinct from that pure element as discussed in sub-chapter 1.4.1. The

chemical and physical properties may be tuned by varying the amount of composition and atomic ordering as well as the size of the clusters. In fact, bimetallic metal nanoparticles may display not only magic sizes but also the magic compositions at which the alloy present a special stability that may determine the chemical reactivity especially catalytic activity.[152] For instant in benzene hydrogenation, Yoon et al. [153] have synthesised bimetallic catalyst of Pd-Rh/CNT via a microemulsion method and it was found that this combination exhibited the highest TOF compared to its monometallic analogues. Another example was shown by Zhu et al., that showed that Ru-Ni/C (0.024 wt. % Ru, 1.00 wt. % Ni) shows the highest TOF for hydrogenation of benzene compared to monometallic of Ni/C and Ru/C. [151] The authors suggested that this is due to the efficient synergistic effect between Ru, Ni and NiO sites stemming from the nanostructure of Ru on Ni/NiO nanoparticles. It is also speculated that the additional metals can improve the size and the morphology of active particles as well as the catalysts selectivity. [154]

In the hydrogenation of glucose to sorbitol, the addition of the metalloids; elements that have properties of both metals and non-metals such as boron, B as the promoter to Ni demonstrated an improvement in activity. The authors have found that the higher activity of this alloy catalyst is due to the combination of the structural features and the surface electronic state.[155] EXAFS analyses of the samples revealed that the amorphous catalyst has lower Ni coordination number and shorter Ni-Ni bond distance compared to a crystalline catalyst which has been calcined. This was considered to be responsible for the active catalyst which is beneficial for the hydrogenation reactions. Furthermore, the addition of B to Ni makes it electron rich and as a consequence, the glucose adsorption through the C=O group is weakened. This means that more H_2 could be adsorbed on the Ni-B catalysts and hence a higher hydrogenation activity is observed.[155]

Besides improving the reactivity of the reaction, the bimetallic system also can help in reducing the depending on noble metals by incorporating some non-noble metal like Ni and Co. Not only they are cheaper but in certain molar ratios, it could result in better reactivity than the noble metals itself. [156]

As for the hydrogenation of bio-derived furan derivatives like furfural and HMF, many Ni, Co or Cu based bimetallic catalysts have been utilised.[71] Recently Chen et al. demonstrated that carbon coated Cu-Co bimetallic nanoparticles show an excellent performance in selective hydrogenolysis of HMF to DMF with 99.4 % yield of DMF at 180 °C, 50 bar H_2 in 8 hrs. [78] XPS analysis revealed that the coexistence of cobalt oxide species which responsible for the synergistic effect between cobalt species and copper. While Luo et al. reported that (10 wt. %) Pt-Ni alloyed nano-crystals supported on carbon with ratio 3:1 exhibited high yield of DMF compared to other composition and its monometallic catalysts. [80] Ni-Fe/CNT (10 % wt.) also displayed high selectivity towards DMF and DHMF depending on the temperature. This was attributed to the formation of Ni-Fe alloys species that is beneficial to the C-O bond cleavage. [81] The bimetallic of non-noble metals were also been demonstrated by Giovanni et al. High yield of the mixture of both DMF and DMTHF were obtained when Cu-Zn nanoalloy was used in HMF hydrogenation.[83] The author proposed that the synergistic effect between active Cu^0 sites with Lewis acidic ZnO sites was responsible for the high reactivity based on the previous study.[157]

After the recent increased interest in biomass related transformations, the challenges for the catalysis chemist reside in the complex structure and functionalities of biomass. The challenge in designing catalyst to facilitate the new transformations is to prepare catalysts than can selectively remove functional group and break specific chemical bonds in the biomass-derived feedstock. Thus, bimetallic catalysts systems seem to be promising due to the synergistic effects between two combination metals.

1.6 Objective and thesis outline:

The core objective of this thesis is to develop better catalysts for the hydrogenation of HMF into DMF or partly hydrogenating compounds. This could be achieved by using exploiting the support effect and using CNTs to improve activity and developing bimetallic systems. Moreover, the utilisation of less expensive metals like Nickel and Cobalt compared to noble metals like ruthenium and rhodium could be an economic incentive for the production of DMF.

The physical and chemical properties of the catalysts were characterised using such techniques as XRD, TPR, inductively coupled plasma emission spectroscopy (ICP), hydrogen and carbon monoxide chemisorption, TEM and XPS. The thesis contains seven chapters and it is organised as follows:

Chapter 1, *Introduction,* explains the current state of arts regarding biomass as an alternative source for fuels and chemical platforms in addition to a brief introduction to heterogeneous and bimetallic catalysis and the role of carbon and CNT as the support for heterogeneous catalysis. The literature on the production of DMF from biomass especially HMF is reviewed, particularly the catalyst used and the reaction conditions involved.

Chapter 2, *Methodology***,** provides a description of the methods used in the catalyst preparation as well as the procedures for the HMF hydrogenation to DMF. It also describes the qualitative and quantitative techniques used for the product analysis. Additionally, the techniques of catalyst characterization and a brief theory of the techniques are described.

Chapter 3 discussed the optimum conditions for HMF hydrogenation over Ru catalyst supported on carbon. The characterization of Ru supported on carbon and carbon nanotube catalysts are elucidated. The result of HMF hydrogenation over Ru supported on carbon and the improvement in the catalytic activity of carbon nanotube as the support is also discussed. The reaction pathways are suggested.

Chapter 4 discussed the effect of transitional metals catalysts supported on carbon particularly cobalt, nickel, copper, and iron on HMF hydrogenation as a comparison to noble metal, ruthenium. The effect of CNT as the support for HMF hydrogenation is also examined. Moreover, the characterization of each catalyst is also elucidated.

Chapter 5 investigated the effect of bimetallic catalyst ruthenium-cobalt and ruthenium-nickel with the certain composition on HMF hydrogenation to DMF. The characterizations of bimetallic catalyst are also discussed. Finally, the effect of CNT as the support in comparison to carbon is described. This chapter also highlights the

reactivity of bimetallic catalysts over the monometallic catalyst and the possible reason are discussed.

Chapter 6 reports the investigation on the preparation of hydrothermal carbon, HTC derived from sugar (glucose) as a possible support for a catalyst to be used in HMF hydrogenation to DMF. The effect of microwave assists techniques in the synthesis of HTC as a comparison to the conventional hydrothermal method is also explained. Furthermore, one step preparation of supported catalyst on HTC using the microwave is introduced as an alternative to conventional incipient wetness impregnation. Finally, the activity of HMF hydrogenation using as-synthesized catalysts supported on HTC is reported.

Finally, **Chapter 7** draws the conclusions from the result of the catalytic study on HMF hydrogenation into DMF and the characterization of the catalyst.

Chapter 2 Experimental

2.1 Introduction

This chapter describes the materials and the experiments performed including catalyst preparation, characterization techniques as well as catalytic testing and product analysis. The characterization techniques were used to identify the properties of a catalyst such as metal loading, surface area, particle size, reduction profile, a number of active sites as well as dispersion. In the catalytic testing, the steps and how the reactions were performed and products analysed were discussed in detail. The equations used for calculating conversion, yield, and turnover frequency (TOF) have also been described.

2.2 Materials

5-Hydroxymethylfurfural (HMF) (99.0 %), 2,5-dimethylfuran (DMF) (99.0 %), 5-methylfurfural (MF) (99.0 %), 5-methylfurfuryl alcohol (MFA) (99.0 %), 2-methylfuran (MFUR) (99.5 %), 2,5-dihydroxymethylfurfural (97.0 %) (DHMF), 2,5-dimethyltetrahydrofuran (DMTHF) (96 %), 2-hexanol (99.0 %), 1,2-hexanediol (99.0 %), 5 % Ru/C, $RuCl_3.xH_2O$ (99.98 %), $Co(NO_3)_2.6H_2O$ (98.0 %), $Cu(NO_3)_2{\cdot}3H_2O$, $Fe(NO_3)_3{\cdot}9H_2O$ (99.9 %), dioxane (> 99.5 %), tridecane (99.0 %), D-glucose (99.5 %) and multi-walled carbon nanotubes (CNT) (10 nm × 4.5 nm × 4 µm , 82 % carbon content) were purchased from Sigma-Aldrich. 2,5 dihydroxylmethyltetrahydrofuran (DHMTHF) (98.0 %) was purchased from Carbosynth. $Ni(NO_3)_2.6H_2O$ (99.9 %) was purchased from Alfa Chemicals.

2.3 Catalyst preparation

All catalysts were prepared via incipient wetness impregnation with 2-3 ml of water unless otherwise stated. CNT was washed with deionized water to remove the remaining of amorphous carbon and Ni catalysts during CNT synthesis and dried in vacuum oven overnight.[158] All the catalysts are reduced under pure H_2 (N4.5 ,99.995 %) before catalytic testing. As for the synthesis of hydrothermal carbon (HTC), hydrothermal carbonisation with was employed using the microwave and conventional heating autoclave reactors. Catalysts comprising of metals supported on HTC were synthesised via both, incipient wetness impregnation and, one step microwave-assisted carbonisation of glucose.

2.3.1 Preparation of monometallic catalysts supported on carbon and CNT

The catalysts were prepared by incipient wetness impregnation of the metal salts solution using Carbon Norit SX plus and CNT as supports. During incipient wetness impregnation, the aqueous solution of the metal salt was impregnated into the support via capillary force. Typically, for 5 wt % loading of Ru, 103 mg of $RuCl_3.xH_2O$ was dissolved in 2 ml of deionized water. The metal solution was then added dropwise to 1 g of support. The mixture was mixed via a mechanical step using mortar and pestle before dried in the vacuum oven at 60 °C overnight. The catalysts were then reduced under H_2 (60 ml min^{-1}) at 400 °C (heating rate of 5 °C min^{-1}) for 4 hours in a tube furnace. The same procedures were employed for the different ruthenium loadings (1 and 3 %) with the adjustment of the amount of $RuCl_3.xH_2O$ corresponding to the metal loadings. For 5 % (Ni, Co, Cu, Fe) supported on Carbon and CNT, the same procedures were employed using $Ni(NO_3)_2.6H_2O$, $Co(NO_3)_2.6H_2O$, $Cu(NO_3)_2.3H_2O$ and $Fe(NO_3)_3{\cdot}9H_2O$ as the metal precursors.

2.3.2 Preparation of bimetallic catalysts supported on carbon and CNT

The bimetallic catalysts were prepared by incipient wetness impregnation of metal salts solution with Carbon Norit SX plus and CNT. During incipient wetness impregnation the aqueous solution of metal was impregnated into the support via capillary force. Typically, a specific amount of metal salts corresponding to the metal loading were dissolved in 2 ml of deionized water. The aqueous solution of metals salts was then added dropwise to the support. The mixture was then mixed using mortar and pestle before dried it in the vacuum oven at 60 °C overnight. The catalysts were then reduced under pure H_2 (60 ml min^{-1}) at 400 °C (heating rate of 5 °C min^{-1}) for 4 hours in a tube furnace.

2.3.3 Preparation of 5 wt. % Ru supported inside of CNT

Catalysts were prepared according to the procedures described in the literature aiming at predominantly diffuse the metal inside the CNTs and so prepare the metal nanoparticles predominantly on the inner surface of the nanotube.[120, 159] As described

in the literature, the extended stirring was necessary to drive metal salts into the channel due to the concentration difference accompanied by the slow evaporation. Typically, 103 mg of $RuCl_3.xH_2O$ were dissolved in 10 ml of acetone, followed by addition of 1 g of CNT. The mixture was dispersed to form a homogeneous solution by ultrasound. Acetone was then evaporated from the mixture at room temperature under continuous stirring. The resulting solid was dried at 110 °C in a vacuum oven overnight. The sample was labelled as Ru/CNT (I). The catalyst was reduced under H_2 flow (60 ml min^{-1}) at 400 °C (heating rate of 5 °C min^{-1}) for 4 hours in a tube furnace before the catalytic testing was performed.

2.3.4 Preparation of 5 wt % Ru supported outside of CNT

Catalysts were prepared according to the procedures described in the literature to preferentially deposit the metal on the outer surface of the nanotube.[120, 159] The key step for the preparation of Ru loaded outside CNTs is the protection of inner channels by inducing a medium as a temporary blocker during impregnation with a solution containing metal salts. In this case, acetone was used as the blocker. It was speculated that the limited diffusion of metal salts into acetone which was already filled in the channel was responsible for the decoration of Ru outside the CNTs. Once the metal salts were added into the CNTs-dispersed solution, acetone was completely evaporated within one hour thus there was no enough time to drive the metal salts into the channels sufficiently. In addition, parts of the metal salts diffused into the channels were expelled out through the fast thermal motion of acetone.

Typically, 1 g of CNT was dispersed in 10 ml of acetone using an ultrasonic bath before the addition of acetone solution of $RuCl_{3.3}H_2O$. The mixture was heated at 60 °C under continuous stirring to evaporate the acetone within 1 hr. Subsequently, the solid was subjected to the same drying and reduction treatment as above and labelled as Ru/CNT (O). The catalyst was reduced under H_2 flow (60 ml min^{-1}) at 400 °C (heating rate of 5 °C min^{-1}) for 4 hours in a tube furnace before the catalytic testing was performed.

2.4 Synthesis of hydrothermal carbon microspheres (HTC) from glucose

The synthesis of hydrothermal carbon (HTC) was performed via two different methods; hydrothermal carbonisation with autoclave[160] and microwave-assisted hydrothermal carbonisation.[161] [162]

2.4.1 Conventional hydrothermal carbonisation with autoclave

13.5 ml of a deionized water solution containing 1.5 g glucose were sealed in an autoclave (45 ml) and hydrothermally reacted in a pre-heated oven at 180 °C for the desired reaction time (24 and 48 hours). After the reaction, the autoclave was cooled to room temperature in an ice bath before a black solid powder was separated from the aqueous solution via centrifugation. The resulting solid was washed several times with deionized water and methanol then dried in a vacuum oven at 80 °C overnight.

2.4.2 Microwave-assisted hydrothermal carbonisation

Hydrothermal carbon was synthesised using a CEM Discover SP microwave with an auto-sampler. In a typical process, 2.5 g of glucose were dissolved in deionized water (23 ml). The solution was sealed in 35 ml glass vessel and heated to 200 °C for 6 hours using the microwave. The product was collected by filtration, washed with deionized water and alcohol before being dried in the vacuum oven at 80 °C overnight. In additional experiments, the same synthesis was followed but the concentration of glucose, time and synthesis temperature were varied.

2.4.3 Preparation of Ru supported on HTC via Incipient Wetness Impregnation

HTC was pre-treated under N_2 (60 ml min^{-1}) at 550 °C for 4 hr (heating rate of 2 °C min^{-1}). 103 mg of $RuCl_3.xH_2O$ was dissolved in 2 ml of deionized water. Ru salt solution was added by dropwise to the pre-treated HTC before dried in the oven at 60 °C overnight. The catalysts were then reduced under H_2 (60 ml min^{-1}) at 400 °C (heating rate of 5 °C min^{-1}) for 4 hours in a tube furnace prior to the catalytic test.

2.4.4 One step Microwave assisted carbonisation of Ru supported on HTC

Ru, Co, and Ni supported on HTC with 5 % metal loading were synthesised using the microwave in one single step during the formation of the carbon support. In a typical process, for Ru/HTC, 2.5 g of glucose and a specific amount of metal salts (70.8 mg $RuCl_3.xH_2O$, 170 mg $Co(NO_3)_2.6H_2O$, 171 mg $Ni(NO_3)_2.6H_2O$) were dissolved in deionized water (23 ml). The solution was sealed in a 35 ml glass vessel and heated to 200 °C for 6 hours using the microwave. The product was collected by filtration, washed with deionized water and alcohol before being dried in a vacuum oven at 60 °C. For the rest of catalysts supported on HTC with this one step method, the steps were the same apart from varying the concentration of glucose, time and synthesis temperature.

2.4.5 Microwave

Microwave technology is a great option to conventional heating methods owing to its rapid heating capability. The microwave heating occurs through the conversion of electromagnetic energy into heat within the irradiated material.[163] This offers a number of advantages over the conventional heating for example; non-contact heating, energy transfer instead of heat transfer, rapid heating, selective material heating, volumetric heating, quick start up and stopping, heating from the interior of the material body and higher level of safety and automation. [164]

In this work, a CEM Microwave equipped with an auto-sampler as shown in **Figure 2.4.1** was used for the preparation of hydrothermal carbon, HTC from glucose as well as the synthesis of catalysts supported on HTC.

Figure 2.4.1 CEM Microwave –Discover SP.

2.5 Catalysts Characterization

2.5.1 Inductively Coupled Plasma- Optical Emission Spectroscopy, ICP-OES

Inductively coupled plasma – optical emission spectroscopy (ICP-OES) is an analytical technique used for the measurement of elemental composition for trace and minor components in liquid samples. A liquid is vaporised into argon plasma at ca. 5500 K which excites and ionises the atom in the sample. The intensity of the light emitted is measured using optical detection at the wavelengths characteristic of the element of interest and compared to a calibration curve of a respective elemental standard. Many elements can be analysed at different wavelengths that are chosen on the basis the of sensitivity, resolution, and to avoid interference from other elements.[165]

The catalyst was digested using aqua regia (3:1 ratio of HCL to HNO_3) before being treated in the microwave at 180 °C for 15 min. Samples were diluted to 2 % (v/v) before ICP analysis. The instrument used for ICP analysis is Agilent 5110 ICP-OES available in the Chemistry Department of University of Liverpool as shown in Figure **2.5.1**

Figure 2.5.1 Agilent 5110 ICP-OES.

2.5.2 Powder X-ray diffraction (XRD)

XRD is the main characterization tool whenever solid crystalline materials are synthesised as it provides important information about crystalline phases and micro-structural properties such as crystallite sizes and bulk defect types and concentration as well as the presence or absence of doping elements in the lattices.[166]

During the experiment, incident x-rays that scattered by the atoms in an ordered lattice interfere constructively in a direction given by Bragg's law. If one measures the angles, 2θ, under which constructively interfering X-rays leave the crystal, the Bragg relation gives the corresponding lattice spacing, which are characteristic for a particular compound as illustrated in **Figure 2.5.2**.[167]

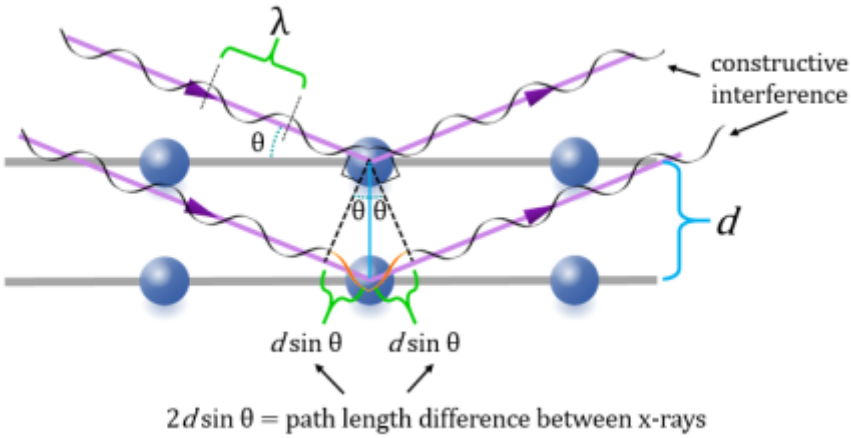

Figure 2.5.2 Constructive interference according to Bragg equation.

$$n\lambda = 2d \sin\theta \qquad \textbf{Equation 2.5-1}$$

where λ is the wavelength of the x-rays, d is the distance between the two lattice planes, θ is the angle between the incoming X-rays and the normal to the reflecting lattice plane, n is an integer called the order of the reflection.

The X-ray diffraction (XRD) patterns were recorded on a Panalytical X'Pert PRO HTS X-ray diffractometer using Cu-Kα radiation (λ = 0.154 nm) over the range of 4-90° 2θ to determine crystal phases of the prepared catalysts.

2.5.3 Temperature Programmed Reduction (TPR)

TPR provides useful information about the temperatures needed for the complete reduction of a catalyst.[168] For bimetallic catalysts, TPR patterns often indicate if the two metals are mixed or not. If the bimetallic combination reduces largely in the same temperature range, it indicates that both components are well mixed in the fresh catalyst. The reduction of a metal oxide, MO_n by H_2 can be described by the equation:

$$MO_n + nH_2 \rightarrow M + nH_2O \qquad \textbf{Equation 2.5-2}$$

Thermodynamics predicts under which conditions a catalyst can be reduced; as with every reaction, the reduction will proceed when the change in the Gibbs free energy, ΔG has a negative value. Reduction reactions of metal oxides by hydrogen start with the dissociative adsorption of H_2. Depending on how fast or slow the dissociative

adsorption is with respect to the subsequent reduction reactions, comprising diffusion of atomic hydrogen into the lattice, reaction with oxygen and removal of hydroxyl species formed.

TPR profiles were obtained with a Micromeritics AutoChem II 2920 Instrument equipped with a thermal conductivity detector (TCD). For TPR experiments, 0.05 g of the sample was placed in a U-shaped quartz tube located inside an electric furnace and heated at 10 °Cmin^{-1} to 800 °C under a 5 vol. % H_2 flow diluted in N_2 (total flow rate of 60 cm^3min^{-1}, STP). The TCD signal automatically recorded the H_2 consumption.

2.5.4 Chemisorption

Pulse H_2 and CO Chemisorption analysis were used to determine the metal active sites and percent metal dispersion by applying measured doses of reactant gas to the sample.[169] The injected gas chemically reacts with the active site until all of the active sites have reacted. The first few injections may be totally consumed and no change in signal from the detector will be recorded. A calibrated thermal conductivity detector (TCD) monitors the quantity of adsorptive that is not taken up by the active metals. As the sample approached saturation, peaks representing the concentration of unreacted molecules appear. **Figure 2.5.3** shows the typical pulse chemisorption profile. The quantity of molecules chemisorbed is the difference between the total amount of reactant gas injected and the sum of the amount that did not react with the active sites.[170] The area under each peak is proportional to the quantity of the injection that was not adsorbed. From the known quantity of each injection, the fraction of each injection that was not adsorbed and the mass of the sample material, the number of moles of adsorptive gas taken up by each gramme of sample is determined.[171] The volume of the active gas chemisorbed is calculated using the volume injected, V_{inj} and from the area under the peaks as follows;

$$\mathbf{V_{ads}}\left(\mathbf{STP}, \frac{\mathbf{cm^3}}{\mathbf{gm}}\right) = \frac{\mathbf{V_{inj}}}{\mathbf{m}} \times \sum_{\mathbf{i=1}}^{\mathbf{n}}\left[\,\mathbf{1} - \frac{\mathbf{A_i}}{\mathbf{A_f}}\,\right] \quad \textbf{Equation 2.5-3}$$

where m is the mass of the sample, A_i is the area of the peak, and A_f is the area of the last peak.

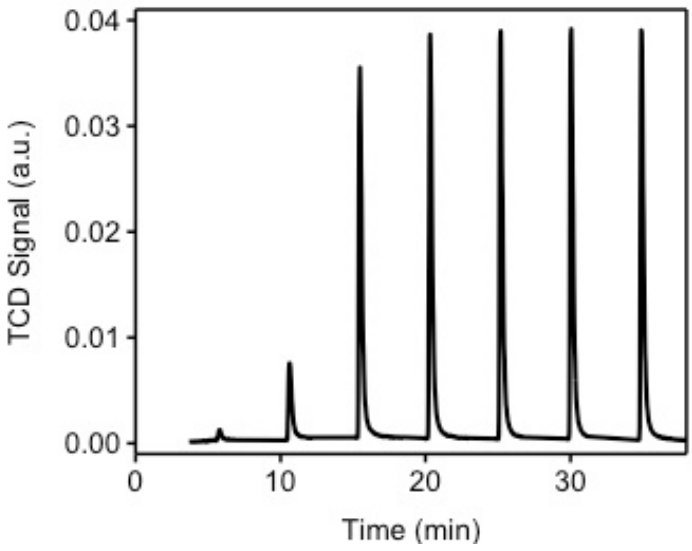

Figure 2.5.3 Typical pulse chemisorption profile.

The percent of metal dispersion, D (%) was calculated based on the following formula:

$$\boldsymbol{D}\ (\%) = \frac{\mathbf{SF.MW.CHS}}{\mathbf{100}.\boldsymbol{L}} \qquad \textbf{Equation 2.5-4}$$

Where SF is the chemisorption stoichiometric factor, MW is the atomic mass of metal, CHS is the amount of chemisorbed gas and L is the metal loading.

The amounts of chemisorbed hydrogen and CO on the catalysts were measured using a Micromeritics AutoChem II 2920 equipped with TCD signal (**Figure 2.5.4**). A sample amount of 0.05 g was reduced under hydrogen flow at 400 °C for 4 h and then cooled to 30 °C with flushing of N_2 to remove the excess H_2 from the system. 10-20 pulses of H_2 or CO were injected in the flow at 2 min intervals until the catalyst was saturated with H_2 or CO.

Figure 2.5.4 Micromeritics AutoChem II 2920.

The turnover frequency, TOF was used to measure the catalytic activity. TOF is simply the number of times that the overall catalytic reaction takes place per catalytic site per unit time for a fixed set of reaction conditions such as temperature, pressure or concentration, reactant ratio and extent of reaction. TOF can be expressed as the following formula[172]

$$\mathrm{TOF} = \frac{\text{number of molecules of a given product}}{\text{number of active sites} \times \text{time}} \quad \textbf{Equation 2.5-5}$$

For most of the heterogeneous reactions involving the catalytic transformation of small molecules in the temperature ranges 100 - 500 °C and the pressure up to a few bars, the turnover frequencies typically fall between 10^{-2} and 10^{2} s^{-1}.[94]

2.5.5 Scanning Electron Microscopy, SEM

Scanning electron microscopy was used to study the morphology of synthesised hydrothermal carbon. The technique uses a beam of high-energy target electrons, which then bombard the surface of a specimen under a vacuum environment. The

bombardment process ejects electrons from atoms of the specimen. The ejected electrons are called secondary electrons, SE. A secondary electron detector, a component of SEM, then captures the SE which are then processed to give micrographs. **Figure 2.5.5** illustrates the schematic view of SEM. The main difference between SEM and TEM is that SEM sees contrast due to the topology and composition of a surface while TEM projects all information on the mass it encounters in a two-dimensional image in subnano-meter resolution. [173] SEM is mainly used to characterise particle sizes in the range of 10^{-7}-10^{-4} m for example oxide, sulphide, zeolite, carbon and unsupported metals.

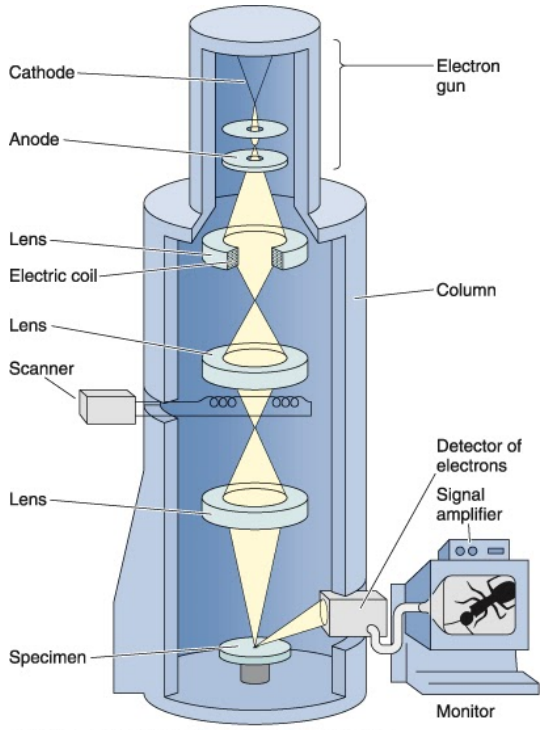

Figure 2.5.5 Schematic view of a scanning electron microscope (SEM)

Sample specimens for SEM studies were prepared by ultrasonic dispersion of the catalyst in methanol. The suspensions were then transferred onto a silicon wafer and the subsequently dried and gold coated before the study. SEM images were acquired on JEOL 2100 SEM instrument microscope available in Chemistry Department of the University of Liverpool. Approximately 100-200 particles were randomly counted to determine the particle size distribution.

2.5.6 Transmission Electron Microscopy, TEM

The morphology of small nanoparticles on supports was observed using TEM. In TEM, the instrument is in a sense similar to an optical microscope, if one replaces optical lenses with electromagnetic lenses. The primary electron beam of high energy and intensity passes through a condenser to produce parallel rays, which impinge on the sample. As the attenuation of the beam depends on the density and the thickness of the samples, the transmitted electrons form a two-dimensional projection of the sample mass, which later magnified by the electron optics to produce bright field image. The lighter areas of the image represent those areas of the sample that more electrons were transmitted through (thinner or less dense). The darker areas of the image represent the areas of the sample that have fewer electrons transmitted which are normally thicker or denser. **Figure 2.5.6** illustrates the schematic diagram of TEM. Typical operating conditions of a TEM instrument are 100 to 200 keV electrons, 10-6 mbar vacuum, 0.3 nm resolutions and a magnification of 3. 10^5 to 10^6.[173]

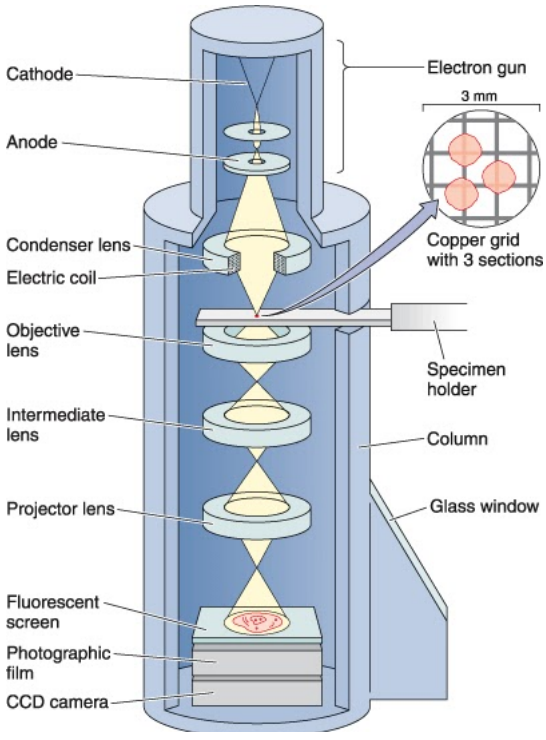

Figure 2.5.6 Schematic view of a transmission electron microscopy (TEM).

Sample specimen for TEM studies were prepared by ultrasonic dispersion of the catalyst in methanol. The suspensions were dropped onto a holey carbon-coated copper grid (300 mesh). TEM images were acquired on JEOL 2100 TEM instrument microscope (**Figure 2.5.7**) operated at 200 kV. Approximately 100-200 particles were randomly counted to determine the particle size distribution.

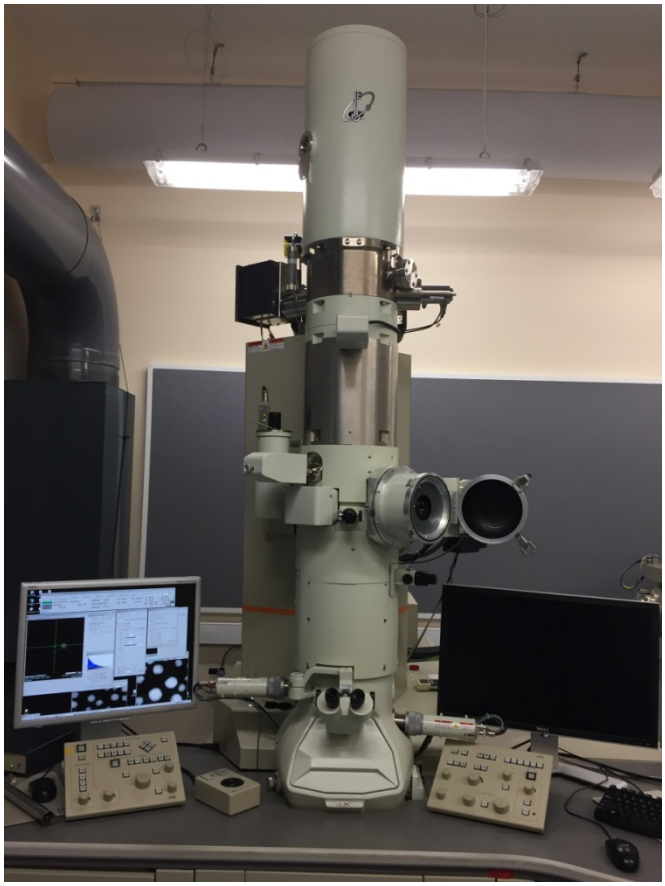

Figure 2.5.7 JEOL 2100 TEM instrument.

2.5.7 X-ray Photoelectron Spectroscopy, XPS

Photoelectron spectroscopy, XPS is a very useful technique for the study of the surface chemistry of the catalyst as it provides information on the elemental composition, the oxidation state of the elements and in favourable cases, on the dispersion of one phase over another. XPS is based on photoelectric effect, whereby an atom absorbs a photon of energy, hv, after which a core or valence electron with binding energy E_b is ejected with kinetic energy.[174]

$$E_k = h\upsilon - E_b - \phi \quad \textbf{Equation 2.5-6}$$

Where;

Ek is the kinetic energy of the photoelectron;

h is Planck's constant;

υ is the frequency of the exciting radiation;

Eb is the binding energy of the photoelectron with respect to the Fermi level of the sample;

ϕ Is the work function of the spectrometer

In XPS, an incident X-ray photon is absorbed and a photoelectron is emitted. Measurement of its kinetic energy allows to calculate the binding energy of the photoelectron. The atom stays behind is unstable ion with a hole in one of the core levels. The excitation ion relaxes by filling the core hole with an electron from the higher shell. The energy released by this transition is taken up by another electron, the Auger electron, which leaves the sample with an element specific kinetic energy. Routinely used X-ray sources are Mg Kα (1253.6 eV) and Al Kα (1486.3 eV). The XPS spectrum is usually a plot of the intensity of the photoelectrons detected as a function of binding energy. Photoelectron peaks are labelled according to the quantum numbers of the levels from which the electron originates. Spin orbit-splitting as well as the binding energy of particular electron level increasing with atomic number. One can determine the oxidation state of the element due to every element not only have specific binding energy and but also contain chemical information. This is because the energy levels of core electrons depend slightly on the chemical state of the atom. The binding energy goes up with the oxidation state due to higher attractive force from the nucleus.[174]

XPS measurements of each sample were carried out on a high-resolution angle-resolved K-Alpha™+ X-ray Photoelectron Spectrometer (XPS) (**Figure 2.5.8**) using monochromatic Al Kα radiation (1486.6 eV). The CASA XPS program with Shirley background was employed to deconvolute the XPS spectra. The XPS analysis was kindly performed by Nexus, University of Newcastle (project ID 16-142).

Figure 2.5.8 K-Alpha™+ X-ray Photoelectron Spectrometer (XPS) System.

2.5.8 C-H-N-S Elemental Analysis

Elemental analysis was used to determine the carbon content in hydrothermal carbon support sample. This method provides rapid determination of carbon, hydrogen, nitrogen and sulphur in organic materials. This technique relies on the combustion process, where carbon is converted into carbon dioxide, hydrogen to water, nitrogen to nitrogen gas/oxides of nitrogen and sulphur to sulphur dioxide. The absorbent is used to remove these additional combustion products before they are swept out of the combustion chamber by inert carrier gas over a high purity copper. Copper is used to remove oxygen and to convert any oxides of nitrogen to nitrogen gas. The gases are then passed through traps and detected by the detector.[175]

This analysis was carried out on Thermo Flash EA 112 series analyser with thermal conductivity detector (TCD) in the chemistry department at University of Liverpool.

2.5.9 Thermo Gravimetric Analysis, TGA

Thermogravimetric analysis was performed to study the changes in sample weight as a function of temperature or time as the sample specimen is subjected to a controlled temperature program in a controlled atmosphere.[176] TGA consists of a sample pan that is supported by a precision balance. That pan resides in a furnace and is heated or cooled during the experiment. The mass of the sample is monitored during the experiment. A sample purge gas controls the sample environment.

TGA was carried out on Perkin-Elmer TGA 7 instrument under nitrogen flow at the ramp of 10 °C/ min from room temperature to 550 °C.

2.5.10 Surface Area Measurements

The surface area of the support used was determined by physisorption. The most common method used for this is to measure how much N_2 is adsorbed onto a certain amount of material. The uptake is measured at a constant low temperature as a function of N_2 pressure and very well described by the Brunauer-Emmet-Teller (BET) isotherm.[177]

$$\frac{\mathbf{p}}{\mathbf{V}\,(\mathbf{p_0}-\mathbf{p})} = \frac{\mathbf{1}}{\mathbf{V_m C}} + \frac{\mathbf{c}-\mathbf{1}}{\mathbf{V_m C}} . \frac{\mathbf{p}}{\mathbf{p_0}} \qquad \textbf{Equation 2.5-7}$$

Where V is the volume of gas adsorbed, p is the pressure of gas, p_0 is the saturated vapor pressure of the liquid at the operating temperature and V_m is the volume equivalent to an adsorbed monolayer, while C is the BET constant. A plot of $p/V(p_0-p)$ versus p/p_0 is usually linear in the range of p/p_0 from 0.05 to 0.35 and the slope and intercept of this plot yields both C and the monolayer volume V_m.

The BET method can be expressed by the following equation;

$$\mathbf{A_s} = (\mathbf{V_m}/22414)\,\mathbf{N_a}\,\sigma \qquad \textbf{Equation 2.5-8}$$

Where A_s is the surface area, and N_a is the Avogadro number (6.022×10^{23} mol^{-1}), σ is the area covered by one nitrogen molecule (0.162 nm^2) and the constant number 22414 is the molar volume of N_2 (ml mol^{-1}) under standard conditions.

The Surface area measurements were carried out using Quantachrome Nova 4200 available in the chemistry department of the University of Liverpool (**Figure 2.5.9**). Typically, 100 mg of sample was used for the analysis and degassed overnight under vacuum at 120 °C. Five points measurement were taken between pressures (P/P_0) of 9.5 $x10^{-2}$ and 2.98 $x10^{-1}$ at 77.3 K.

Figure 2.5.9 Quantachrome Nova 4200.

2.6 Hydrogenation of HMF and product analysis

2.6.1 Catalytic testing

The hydrogenation of HMF as carried out in a stainless steel 50 ml Parr reactor equipped with the head stirrer (**Figure 2.6.1**) under H_2 atmosphere (10-40 bar) at 130-200 °C. The temperature in the reactor was controlled by temperature controller using a thermocouple. The catalyst was pre-reduced at 400 °C for 4 hours before the reaction. 60 mg of catalyst was transferred into the reactor vessel together with 30 ml of stock solution of HMF in dioxane (40 mM). The reactor was then sealed and purged with N_2 three times. When the reaction temperature was reached, the reactor was

pressurised with H_2. Samples were taken around 0.5- 1ml at specific times via a sampling valve for time online studies. The products were separated from the catalyst via centrifugation (5 min at 1300 rpm) and 0.22 µm syringe membrane filter before being analysed with gas chromatography, GC.

Figure 2.6.1 50ml Parr reactor from Parr Instrument.

2.6.2 Gas Chromatography, GC

A gas chromatograph (Agilent 7890A GC system) (**Figure 2.6.2**) equipped with flame ionisation detector (FID) and SUPELCOWAX 10 capillary column (30 m x 0.32 mm x 0.25 µm) were used for qualitative and quantitative product analysis.

Figure 2.6.2 Agilent 7890A GC system.

The product identification was performed by separating the compounds in the products mixture by converting them into volatile phase. A mobile phase, containing the volatile mixture together with carrier gas usually an inert gas such as He, Ar, N_2 or H_2, travels through a column consisting of a stationary phase which normally consists of a microscopic layer of liquid or polymer on an inert solid support. Upon their displacement through the column, analyte molecules are partitioned between the carrier gas and the stationary phase to an extent which depends mainly on their chemical structure or boiling point. At the end of the separation section, the molecule reaches a detection system in which a specific physical property gives rise to an electric signal which is proportional to a number of molecules of the same identity. A data system then processes these data to produce a chromatogram which is a graph of detector signal with time.[178] **Figure 2.6.3** Schematic diagram of typical GC system.illustrated the schematic diagram of typical GC system.

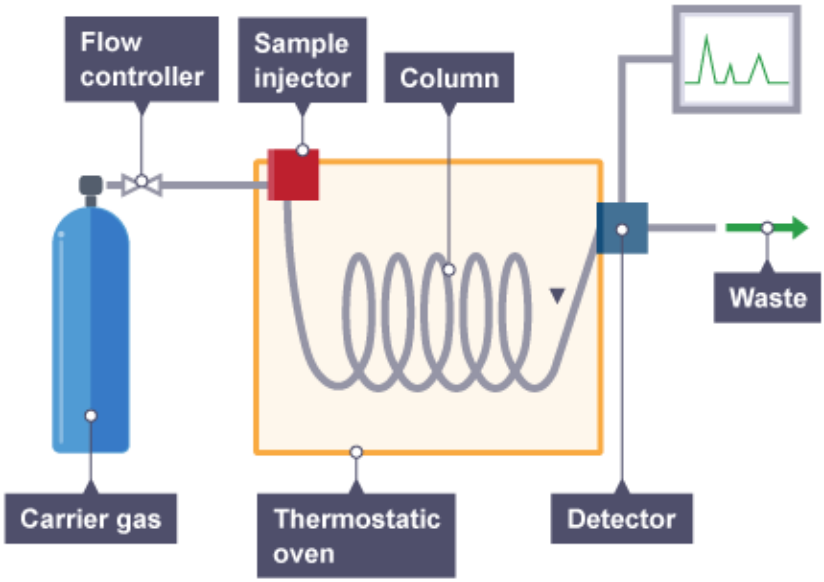

Figure 2.6.3 Schematic diagram of typical GC system.

2.6.2.1 Quantitative analysis of products with GC

There are several types of quantification method commonly used. The five most common are area percent, single point external standard, multiple points of an external standard, single point internal standard and multiple points of the internal standard. In this work, the multiple points of internal standard were used to quantify all the compounds, the reactant, and the expected products.[179] This method depends on the addition of a constant concentration of a chosen standard to a different concentration of analyte that has been diluted in a solvent. A calibration is performed by plotting the area of the internal standard on the x-axis and the concentration of internal standard on the y-axis. The calibration factor, K is determined from the plot. The concentration of the analyte can then be calculated using the following equation:

$$\text{Concentration} = A/A_i \times K \qquad \text{Equation 2.6-1}$$

Where A/A_i is the peak area ratio of analyte to a standard and K is the calibration factor derived from the linear plot of the calibration curve. Tridecane was used as an internal standard to calibrate the reactant and products and dioxane was used as the solvent.

DMF conversion, product yield, mass balance and specific yield were calculated using the following equations. The mass balance does not influence the validity of the data

since the stoichiometry of the reaction is 1:1 and there are no changes in the carbon number.

$$\textbf{Conversion}\ (\%) = \frac{\boldsymbol{Moles\ of\ substrate\ reacted}}{\boldsymbol{initial\ mole\ of\ substrate}} \times \mathbf{100} \qquad \text{Equation 2.6-2}$$

$$\textbf{Product yield}\ (\%) = \frac{\textbf{Moles of product}}{\textbf{initial moles of substrate}} \times \mathbf{100} \qquad \text{Equation 2.6-3}$$

$$\textbf{Mass balance}\ (\%) = \frac{\textbf{total mole of products and unreacted substrate}}{\textbf{initial moles of substrate}} \times \mathbf{100} \qquad \text{Equation 2.6-4}$$

$$\textbf{Specific yield} = \frac{\textbf{moles of product}}{\textbf{mole of metal in the catalyst}} \qquad \text{Equation 2.6-5}$$

Table 2.6.1 Retention times with Supelcowax, HP5 and HP5-GCMS column for the reactant and products for HMF hydrogenation.

Compounds	Retention time (min)		Response factors
	SupelCowax10	HP-5 GCMS	
HMF	14.4	5.20	1.1232
DMF	4.9	1.955	0.7208
DHMF	14.6	5.076	1.2068
MF	9.783	3.432	0.6558
MFA	10.4	3.353	0.7959
DMTHF	4.144 + 4.327	1.618	0.5927
2 Hexanol	7.139	2.170	0.5465
1,2 hexanediol	11.1	4.13	0.8000
DHMTHF	12.9	4.88	1.024
MTHFA	8.9	-	-

Typical GC chromatograms for hydrogenation of HMF are shown in **Figure 2.6.4**, while the conditions of the column and detector are represented in **Figure 2.6.5**. The initial column temperature of 40 °C was held for 2 min, and then the temperature was ramped at 20 °C min^{-1} until 260 °C was reached and held for 2 min. The injection volume was 1 µL with a split ratio of 1:10, the injector temperature was 270 °C and the carrier gas was N_2 with a flow rate of 1 mL min^{-1}. Real samples were used for the determination of the reaction products as well as quantification.

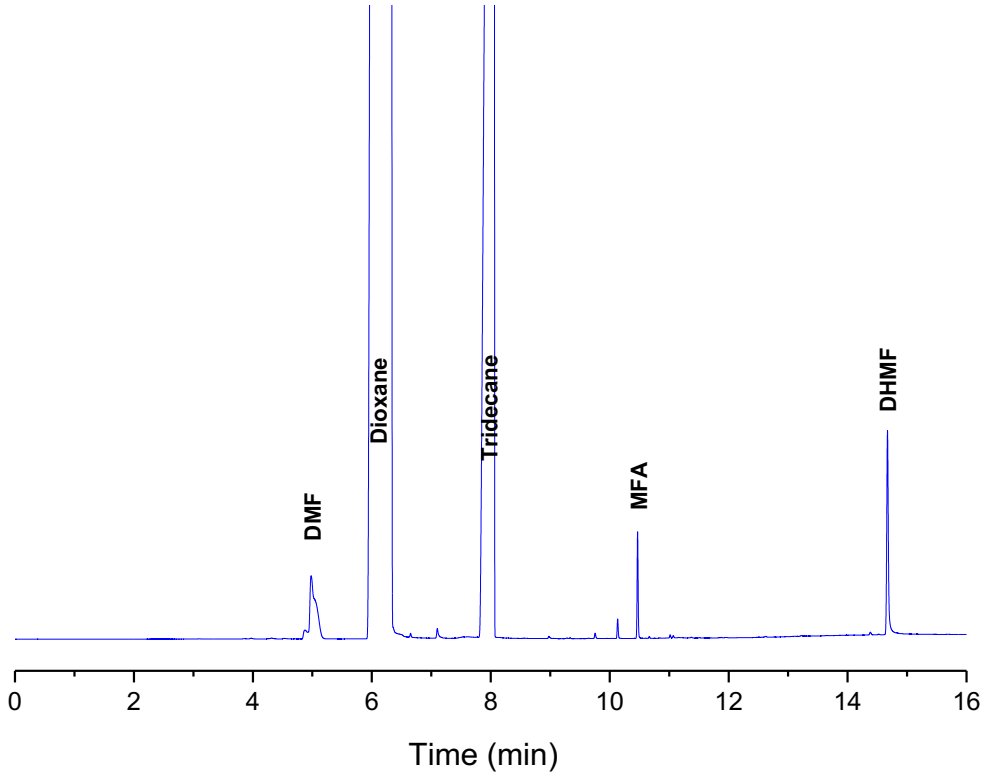

Figure 2.6.4 Typical GC chromatogram for HMF hydrogenation over 5 % Ru/C sigma using Supelcowax Column.

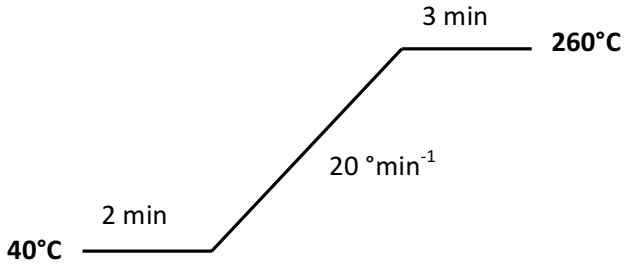

Injection temperature = 270 °C

Detector temperature = 280 °C

Flow = 1 mLmin-1, N_2

Figure 2.6.5 GC analysis conditions of Supelcowax10 column and detector of GC for HMF hydrogenation.

2.6.2.2 Gas chromatography –mass spectroscopy (GC-MS)

GC-MS was utilised to corroborate the products present and ensure unequivocal assignment of the GC peaks observed during quantification of reaction testing. Mass spectrometric detector (MSD) is the most common used detector which allows obtaining the fingerprint of the molecule, i.e., its mass spectrum. Mass spectra provide information on the molecular weight, elemental composition and in a high resolution mass spectrometer (MS), functional groups present and the geometry and spatial isomerism of the molecule can be obtained. In this technique, a substrate is vaporised under high vacuum before being bombarded by a beam of high-energy electrons. The volatile substrate then undergoes fragmentation and forms an arrangement of ions of different sizes. The equation below displays the ionisation of the substrate, M upon bombarded by the high energy electron, e^- resulting in positively charged ionised molecular radical, M^+.[178]

$$\boldsymbol{M} + \boldsymbol{e}^- = \boldsymbol{M}^+ + \mathbf{2}\boldsymbol{e}^- \quad \text{Equation 2.6-6}$$

The resulting ions are measured by first accelerating them in an electric field and subsequently deflecting them in a magnetic field, where the deflection can be interpreted in terms of their mass/charge ratio (m/z).

Figure 2.6.6 Agilent Technologies 5975 series MSD.

In this work, GC-MS analysis was performed using Agilent Technologies 5975 series MSD (**Figure 2.6.6**) equipped with a HP-5 capillary column (30 m x 0.32 mm x 0.25 µm) and equipped with flame ionisation detector (FID). The conditions of the column and detector are represented in **Figure 2.6.7**. The initial column temperature of 50 °C was held for 1 min, and then the temperature was ramped at 25 °C min-1 until 280 °C was reached and held for 2 min. The injection volume was 1 µL with a split ratio of 1:30, the injector temperature was 270 °C, the ion source temperature was 200 °C and the carrier gas was H_2 with a flow rate of 1 mL min^{-1}.

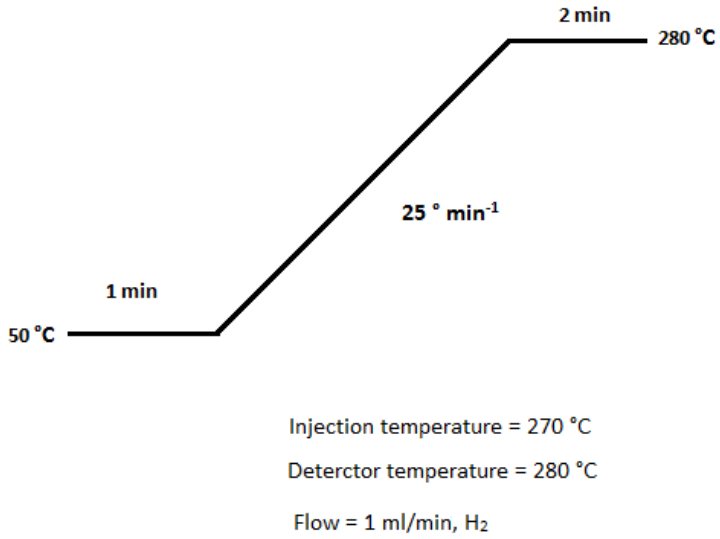

Figure 2.6.7 GC analysis conditions of HP5 column and detector of GC-MS for HMF hydrogenation.

Chapter 3 HMF hydrogenation over Ru supported on carbon and CNT catalyst

3.1 Introduction

Ruthenium has been extensively used as a catalyst in many reactions namely ammonia synthesis [180], electrolysis [181], carbon monoxide oxidation [182] and hydrogenation of aromatics [183, 184]. As for hydrogenation reactions, Ru has been utilised for several decades [185]. Ru nanoparticles supported on various supports such as carbon, zeolite, alumina, titanium oxides and silicas have been reported to be highly reactive for various reactions. [105]

The hydrogenation of HMF to DMF is a complicated reaction since HMF contains an aldehyde group, hydroxyl group, and reactive furan ring. The need to control which functional group will be hydrogenated and which should not be hydrogenated is crucial for the product selectivity. Thus, it is very important to choose the suitable catalyst to fit on the reaction mechanism in order to get high selectivity towards the desired product.

The presence of the conjugated furan ring, a hydroxyl group and the electron withdrawing effect of oxygen on the aldehyde group makes the C2-aldehyde group and C5-hydroxyl groups unstable. Hydrogenation of the hydroxyl group will produce methylfurfural, MF while hydrogenation of aldehyde group will end up with DHMF. Although from the thermodynamic point of view the C=C bond is easily hydrogenated compared to C=O, the presence of the conjugated furan ring makes the hydrogenation of the C=O bond relatively easier than the C=C bond in the selective hydrogenation of HMF into DMF.[57] Thus it is possible to get high selectivity of DMF. However many other possible byproducts and intermediates would be generated due to the reactivity of HMF such as furfuryl alcohol (FA), 2-5-dihydroxymethyltetrahydrofuran (DHMTHF), 5-methyltetrahydrofurfuryl alcohol (MTHFA), 2,5-dimethyltetrahydrofuran (DMTHF), 2,5-hexanedione (HDN), and 2-hexanol (HAO) as illustrated in **Scheme 3**.

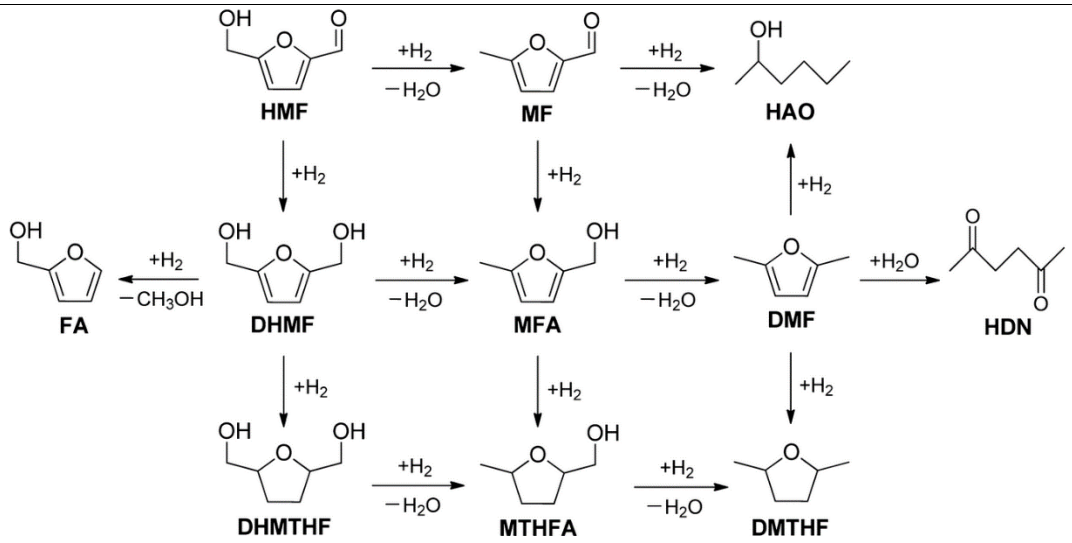

Scheme 3 Reaction scheme in HMF hydrogenation

The studies regarding the effect of metal species on product selectivity in HMF hydrogenation were carried out by Cai et al. using carbon supported Ru, Pd, Ir, Pt and Ni [106]. It was found that using Ru/C and Pd/C, the conversion of HMF is high but the product distribution is different. The deep hydrogenated product DHMTF is the main product with Pd/C while DHMF is the major product for Ru/C. HMF conversion for Pt/C was similar to Ir/C, however, the selectivity towards furan-diols was the lowest for Pt/C. Ni/C displays the poorest result in HMF conversion and the yield of diols which might result from the large particle size of Ni in Ni/C. The specific reactivity of the metals in HMF hydrogenation was as follows: Pd = Ru >Ir > Pt >Ni. Lei et al [31] demonstrated that Ru exhibited an excellent catalytic activity in HMF hydrogenation to DMF when compared to other metal catalysts such as Raney-Ni, Pd/C, Pt/C and Rh/C.

The effect of metal component on the selectivity of HMF hydrogenation was studied by Alamillo et al. [105] It was found that the majority of the HMF was converted to an unidentified product when palladium or platinum was used as the catalyst but not when using higher loading of 10 % Pd. In terms of DHMF hydrogenation palladium and platinum catalyst were less active compared to the ruthenium catalyst [105]. The lower selectivity towards DHMTHF using Pt might be due to Pt being able to catalyse both hydrogenation and C-C scission reaction to produce ring opening products. [105]

Based on the literature, it is agreed that Ru is the best candidate for the selective hydrogenation of HMF to DMF.[64, 67, 74, 75, 82, 84, 186] Along with the type of metal, reaction temperature, H_2 pressure, catalyst quantity and Ru loading also play significant roles in the catalytic activity of the catalyst. Hu et al. have done an extensive study on the reaction conditions for HMF hydrogenation and show that the type of solvent and support used play a vital role in the selectivity towards DMF. [31, 59] Recent studies found that the solvent profoundly affects the catalytic activity in HMF hydrogenation [82]. Solvents like dimethyl sulfoxide, DMSO, acetonitrile, and toluene have lower activity as result of competitive adsorption between solvent and reactant molecules on the active sites. In our study, dioxane was chosen as a solvent since it results in good activity in HMF conversion as well as DMF yield. [72] [77]

CNT has been drawing a lot of attention in catalysis lately mostly due to the fact that it could enhance some catalytic activity. This is due to their unique properties such as uniform pore size distribution, high length to diameter aspect ratio which provides them with a high external surface area. These special properties could influence the metallic particle size distribution, dispersion, metal oxidation state but also can reduce mass transfer limitation which leads to a high catalytic performance in comparison with other conventional support.[118] CNTs are inherently mesoporous structures and this allows for diffusion, reaction and desorption of chemical species better than conventional microporous carbon. In addition, the three-dimensional nanoscale structure of rolled up graphene layers allows a transfer of electronic density from the support to the deposited metallic nanoparticles. This could affect the properties of the metallic phase and their catalytic behaviour.[119] Moreover, the curvature of the CNT could induce an extra modification on the molecular adsorption on the metallic phase thus affecting the catalytic activity.[120]

However, there is not much literature focusing on hydrogenation of HMF over CNT supported catalysts. Recently, Yu et al.[81] demonstrated that Ni-Fe based catalyst supported on CNT showed higher HMF conversion (86 %) compared to carbon supported catalysts (47 %) at 100 C, 30 bar H_2 in 0.5 hr. It was suggested that the smaller metal particle size on CNT were responsible for the high conversion

In this chapter, we report how CNTs are a much better support than conventional carbon for supported Ru nanoparticles and study the optimum reaction conditions for HMF hydrogenation.

3.2 Results and Discussion

Results of characterization of the prepared Ru catalysts as well as the hydrogenation tests will be discussed in this subchapter.

3.2.1 Characterization of Catalyst

The prepared catalysts were characterised using X-ray diffraction (XRD), temperature programmed reduction (TPR), chemisorption, Transmission electron microscopy (TEM) and Inductive Coupled Plasma- Optical Emission Spectroscopy, ICP-OES. The catalyst preparations are as described in experimental section (Chapter 2).

3.2.1.1 Inductive Coupled Plasma- Optical Emission Spectroscopy, ICP-OES

ICP-OES of prepared catalyst was done to determine the actual metal loading of the catalysts. The results are shown in **Table 3.2.1**. It can be seen that the loading from ICP is close to the theoretical loading except for Ru/C IW. This could be due to the experimental error during. The ICP test was performed 3 times in the beginning in order to ensure the result is consistence. The actual loading from ICP will be used in the characterization analysis such as chemisorption as well as TOF calculation.

Table 3.2.1 ICP-OES results of prepared Ru catalysts.

Entry	Catalysts	Theoretical loading (%)	ICP loading
1	Ru/C IW	5	3.0
2	Ru/CNT	5	4.8
3	Ru/C Sigma	5	5.2

3.2.1.2 X-ray diffraction, XRD

Powder XRD was recorded of the reduced catalysts to identify the presence of impregnated metal on the support. **Figure 3.2.1** shows the XRD patterns for reduced carbon, 5 % Ru/C, 3 % Ru/C and 1.5 % Ru/C in the range of 15 to 90°. The diffraction

peaks at 20.8 °, 26.6 °, 44.2 °, 50.3 ° and 59 ° can be indexed to carbon which is matched with JCPDS no 00-022-1069. XRD analysis of most carbon catalysts did not reveal any peak of the metal phase of Ru on carbon; this is probably due to the low concentration of metal in these catalysts, but also that the particle is too small and suggests that the active component was loaded on the support with high dispersion as reported in previous literature. [2, 7]

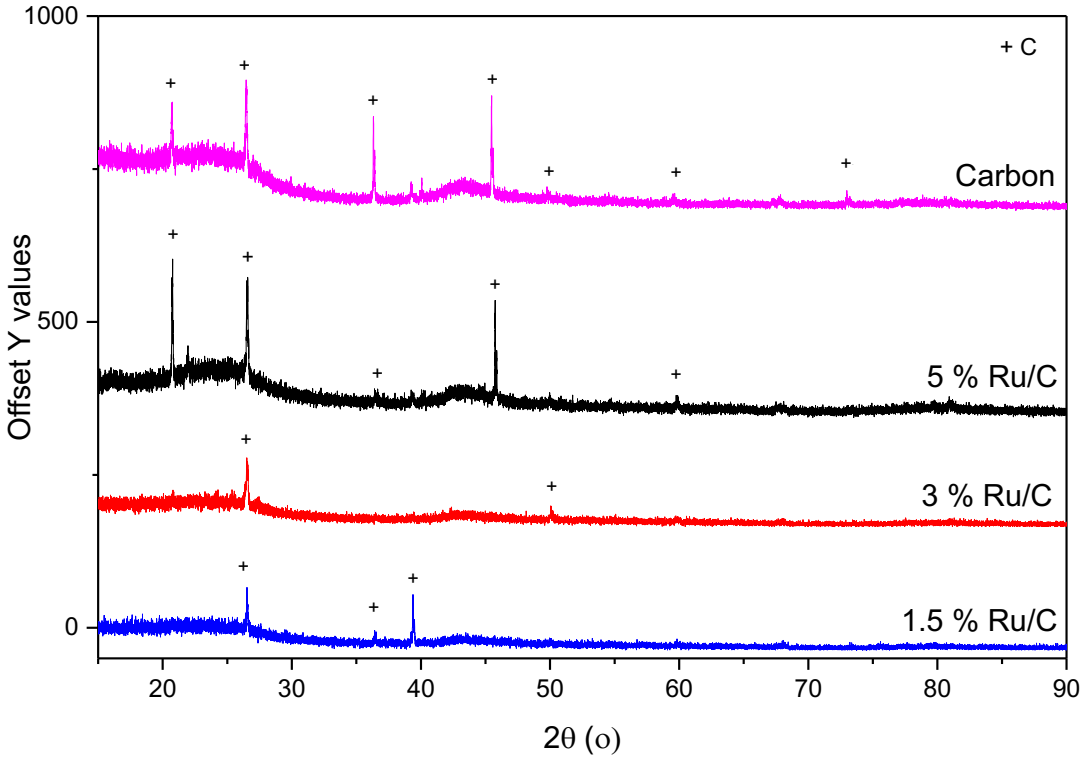

Figure 3.2.1 XRD patterns (Cu Kα radiation) for reduced carbon, 5 % Ru/C, 3 % Ru/C and 1.5 % Ru/C.

XRD patterns for Ru/CNT showed no change in terms of the present of the peaks of the metal phase of Ru apart from 5% Ru/CNT as shown in **Figure 3.2.2**. The XRD peaks at 2θ = 26°, 44° correspond to the graphite reflection of CNT. The XRD patterns of the catalysts are overshadowed by the peaks of CNT. This could be due to the interaction of Ru species with oxygen surface groups (OSGs) during H_2 reduction, which results in some doping by carbon.[120] The absence of the Ru peaks in the catalyst could be due to the small particle size which is beyond the detectable limit of XRD which is usually about 2 nm.[166] This is in agreement with TEM results, which showed

the particle size of Ru/CNT to be 1.5±0.5 nm. So that both techniques indicate that Ru is supported on CNT with good dispersion.

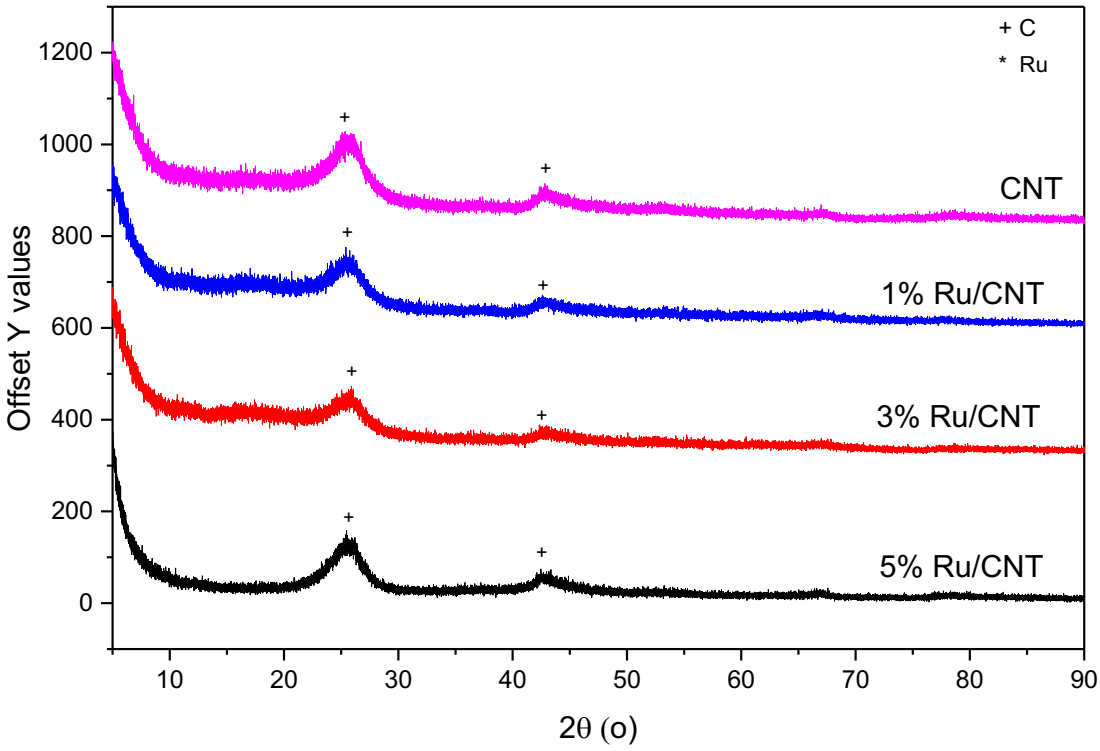

Figure 3.2.2 XRD patterns (Cu Kα radiation) for reduced carbon nanotubes, 5 % Ru/CNT, 3 % Ru/CNT and 1 % Ru/CNT.

3.2.1.3 Temperature Programmed Reduction, TPR

Temperature programmed reduction (TPR) studies help to understand the activation of catalysts as well as reduction profiles of catalysts under H_2 atmosphere. **Figure 3.2.3** shows the TPR profiles for carbon supported metal catalysts. 5 % wt. Ru/C catalyst exhibited two peaks at 100 °C and 170 °C respectively. It is well known that the reduction temperature of a bulk $RuCl_3$ was higher than the reduction of dispersed supported $RuCl_3$. This could be why Ru^{3+} species on Ru/C sigma catalyst started to decompose to Ru^0 at 50 °C, while on Ru/C IW and Ru/CNT the reduction started at 70 °C. The temperature difference could be attributed to the crystalline size of metal salts precursors as reported in the literature.[187-189] The second peak can be assigned to the reduction of Ru^{3+} to Ru^{x+}. [8][188, 190] Therefore, reduction of Ru/C under H_2 at 400 °C should be able to reduce Ru into its metallic state (Ru^0). It was reported that the broader peak in Ru/C around 500 °C to 700 °C can be attributed to the methanation of the support which is common with carbon as previously reported for other ruthenium

supported carbon catalysts. [9][185, 187, 191, 192] It is worth to point out that the second reduction peak of Ru/CNT is lower than Ru/C which suggested a weak metal support interaction between Ru species with CNT. According to Tavasoli et al. who synthesised Co supported on CNT via impregnation technique, the reduction temperature of cobalt oxide species shifted to lower temperature and enhanced the reducibility of the catalyst. The author suggested that by using a CNT support, the interaction between cobalt surface species decreased greatly.[193]

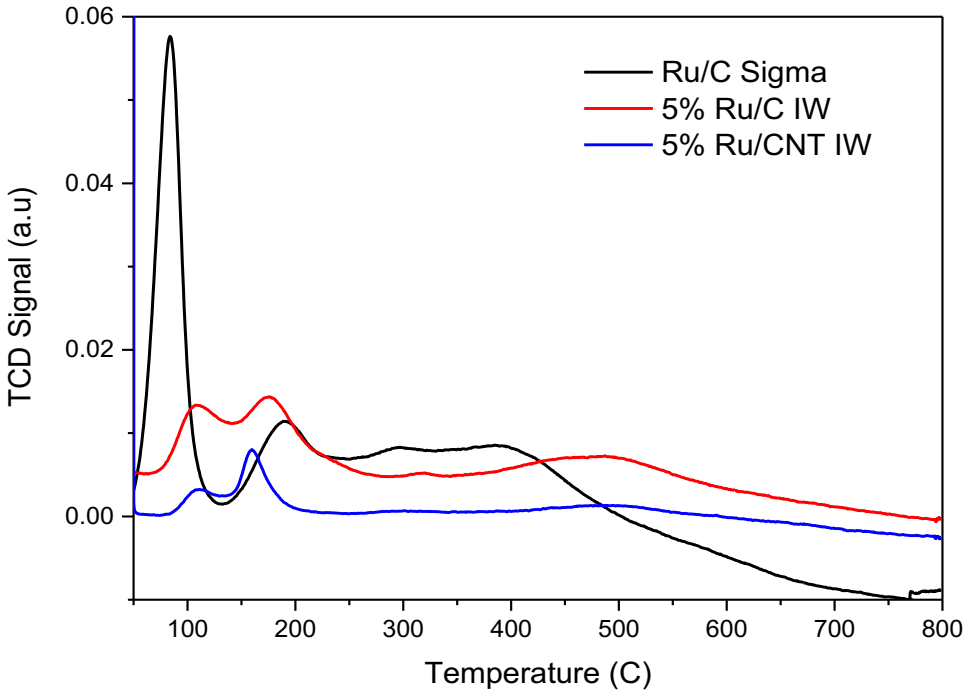

Figure 3.2.3 TPR profiles for carbon and CNT supported Ru catalysts.

3.2.1.4 Chemisorption

The quantification of active metal sites and dispersion were investigated by H_2 and CO chemisorption as shown in

Table 3.2.2.

Table 3.2.2 Results from Chemisorption of H_2 and CO for Ru/C and Ru/CNT.

entry	Catalyst	H_2 Chemisorption (µmol/g)	D^a (%)	CO chemisorption (µmol/g)	D^a (%)
1	5% Ru/C	5.4	2	66	13

2	5% Ru/CNT	1.3	0.52	40	8

[a] metal dispersion.

H_2 and CO uptakes were used to determine the metal dispersion, D, by assuming that either one hydrogen atom or CO molecule is chemisorbed on the surface of Ru atom. The Ru catalyst exhibited much lower adsorption ability for hydrogen than for CO. This is possibly due to the well-established character of the activated process that exhibits the H_2 adsorption on Ru.[194] In addition, multiple adsorptions of CO on low coordination surface ruthenium atoms has been described.[195] However, the multiple CO adsorption seems unlikely due to low metal dispersion. CO chemisorption is better suited than H_2 chemisorption in the case of significant adsorption of H_2 on the support. This is explained by Bergeret et al.[166, 195, 196] It can be seen that samples supported on CNT shows lower H_2 and CO uptake compared than samples on carbon. This could be due to the high surface area of carbon compared to CNT, which affect the distribution of Ru on the support.[154] However, a closer examination reveals that actually, the CNTs possess better Ru dispersion ability than carbon. Even though the surface area of CNTs (281 m^2/g) is about half that of carbon (553 m^2/g), the Ru dispersion on CNT is 23% more than on carbon (CO chemisorption). This in agreement with literature reported by Fu et al.[197]

3.2.1.5 Transmission Electron Microscopy, TEM

TEM was performed to see the morphology and estimate the particle size of the catalysts. **Figure 3.2.4** shows the TEM images of 5 % Ru/C, the presence of discreet 2 nm Ru particles as well as big accumulation of Ru containing material around 10 nm in size are observed. A similar result was found by Iqbal et al. on their Ru/C prepared via impregnation for the hydrogenation of lactic acid. [198] As shown in **Figure 3.2.5**, the particle size distribution was quite broad ranging from 0.8 to 10 nm with mean particle size of 1.85± 0.73nm.

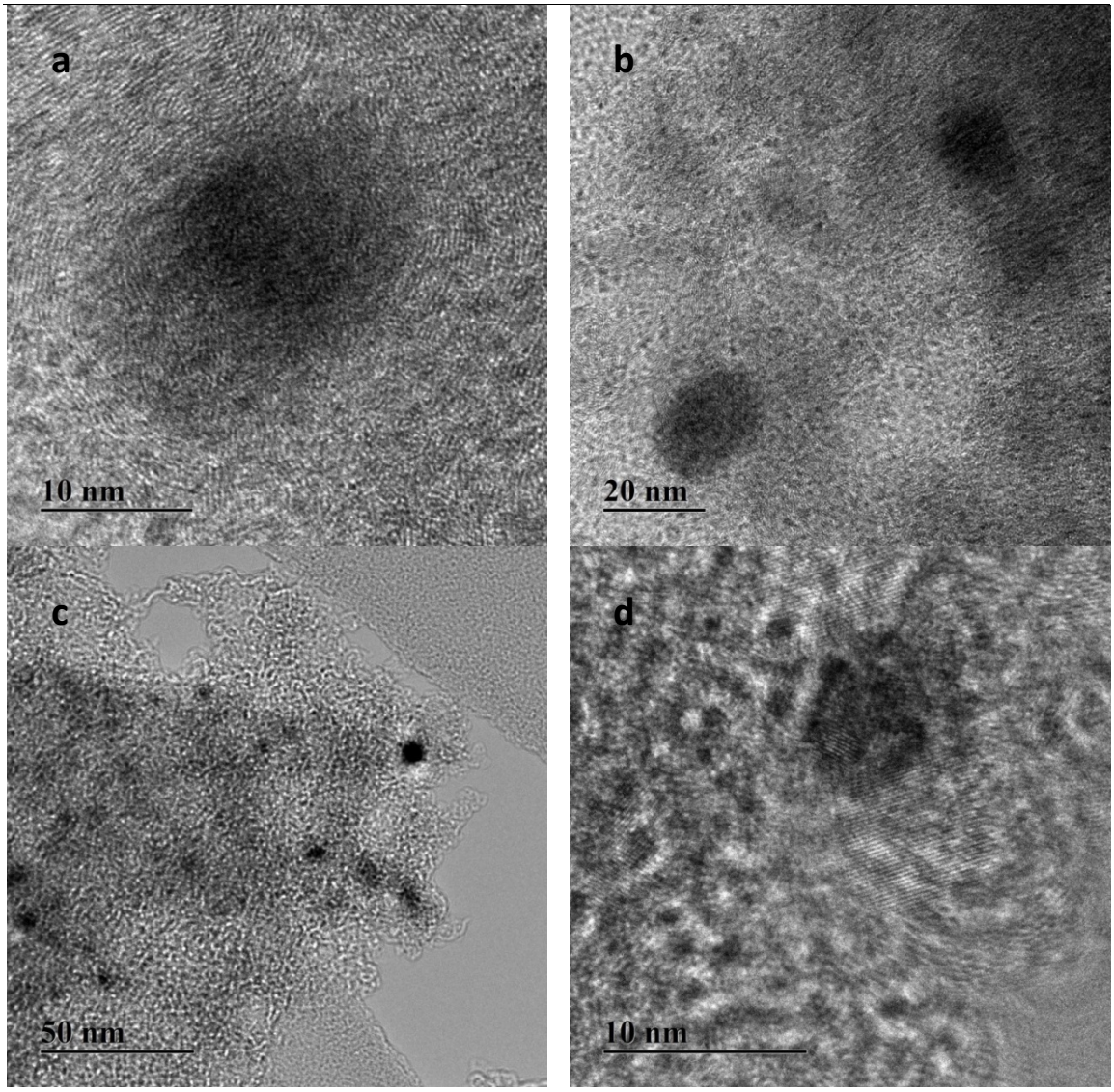

Figure 3.2.4 TEM images of reduced 5 % wt. Ru/C IW a) 10 nm b) 20 nm c) 50 nm and d) 10 nm

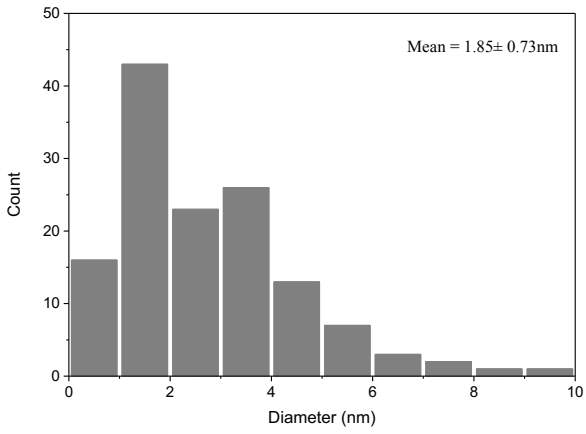

Figure 3.2.5 Particle size distribution of reduced 5 % wt. Ru/C IW based on TEM and ca. 200 particles.

Figure 3.2.6 result shows the TEM images of Ru/CNT, it can be seen that Ru is well distributed on CNT with average particle size of 1.5±0.5 nm. This is in agreement with literature. [125] It is also clear that most of Ru particles are located outside the tubes. Compared to Ru/C, the particle size distribution of Ru/CNT is narrower, ranging from 0 to 5 nm as shown in **Figure 3.2.7.**

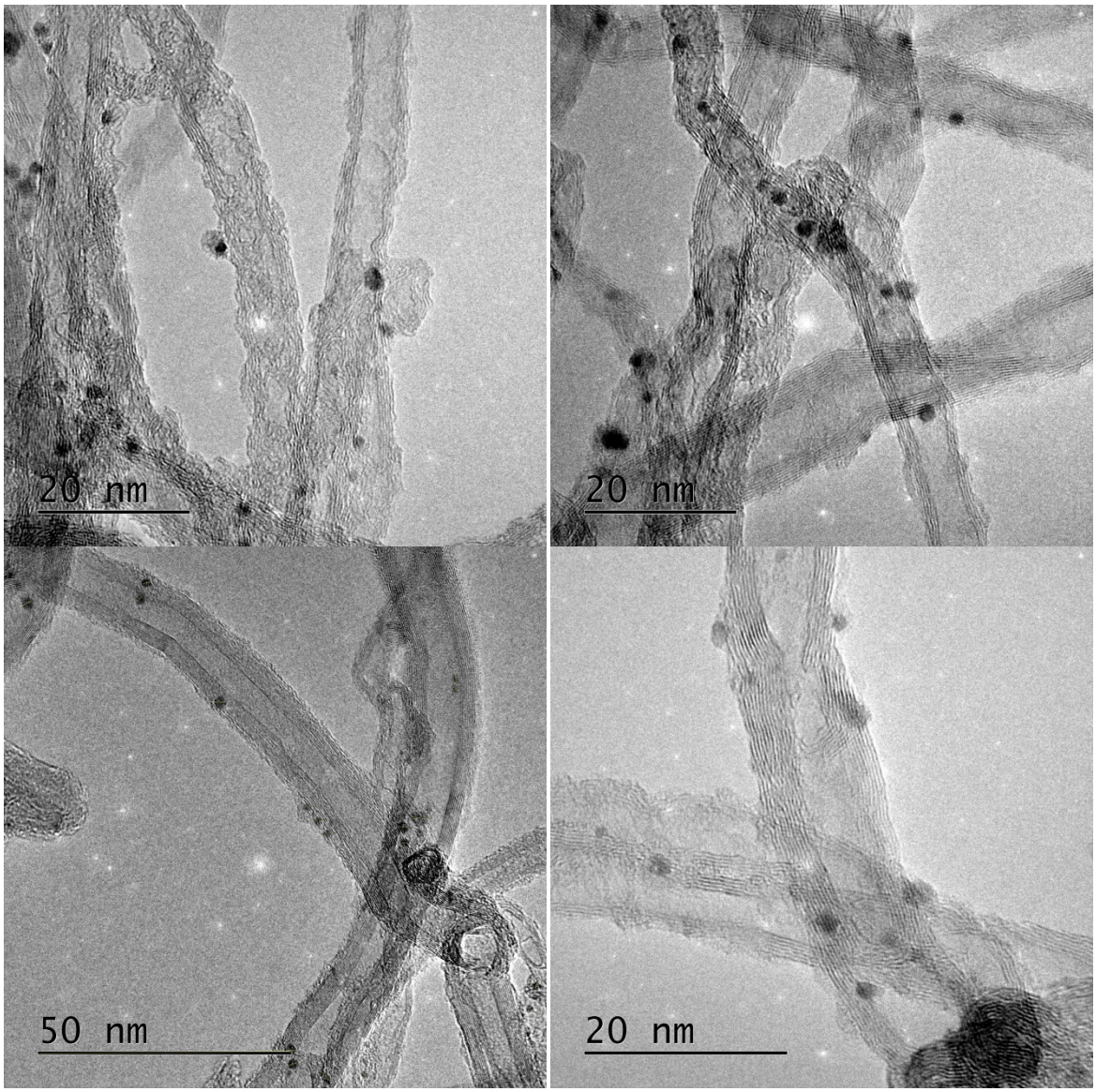

Figure 3.2.6 TEM images of reduced 5 % wt. Ru/CNT IW based on TEM and ca. 200 particles.

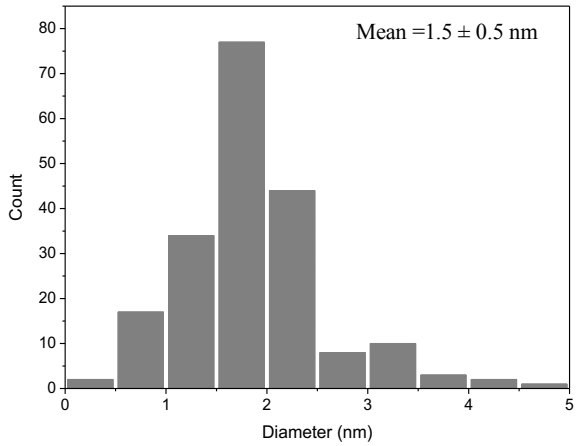

Figure 3.2.7 Particle size distribution of reduced 5 % wt. Ru/CNT IW based on TEM and ca. 200 particles.

3.2.1.6 X-ray Photoelectron Spectroscopy, XPS

The XPS measurement is performed to investigate the surface chemical composition of Ru catalysts. XPS analysis of the Ru/C catalyst system is well known to be difficult due to the overlapping of the C (1s) and Ru (3d) core levels and the asymmetric nature of Ru core level line shape. However, the chemical state information still could be estimated from the observation of Ru(3p) core levels.[198] **Figure 3.2.8** shows the XPS spectrum of Ru/C; fitting of Ru 3p Ru/C IW catalyst. The de-convolution of the XPS peaks reveals most of Ru is in metallic state Ru^0 and RuO_2. The binding energy at 462 eV and 464.2 eV correspond to Ru^0 and RuO_2 respectively. This is in agreement with other reports of ruthenium supported on carbon.[184, 198] It was suggested that the presence of RuO_2 resulted from the surface oxidation of Ru^0 nanoparticles since there was no presence of RuO_2 in the XRD analysis.[199]However recent work by Jungho et al. reported that RuO_2 plays an important role in catalyzing the hydrogenation of HMF into DHMF while both Ru and RuO_2 act in synergy for the production of DMF.[84]

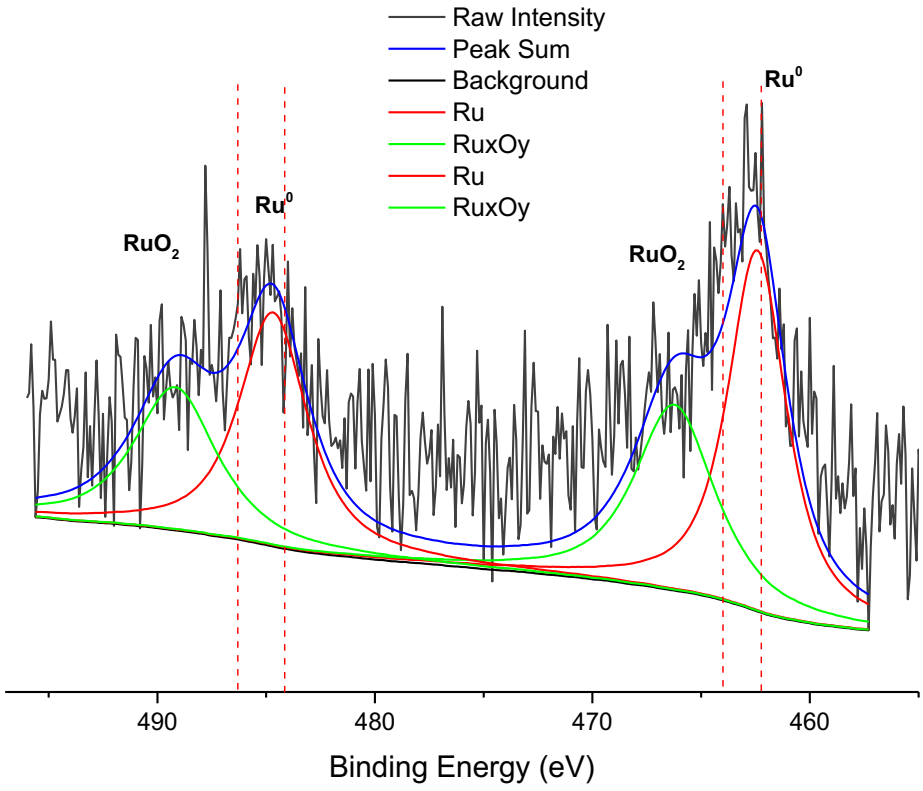

Figure 3.2.8 XPS of 5 % wt. Ru/C; fitting of Ru 3p.

The XPS analysis of the Ru/CNT catalyst revealed the same information. Ru (3p) was used to obtain the chemical state information of Ru/CNT catalysts due to the same reasons as Ru/C. **Figure 3.2.9** shows the de-convoluting peaks of Ru3p of Ru/CNT catalyst. It can be seen that most of Ru are in metallic state Ru^0 and RuO_2. The binding energy was shifted to higher energy levels. The binding energy at 465 eV and 467.2 eV corresponds to Ru^0 and RuO_2 respectively. It was reported that the binding energy is higher than that of metallic Ru in elementary substances (Ru^0) indicating that Ru is electron deficient due to the electronegativity difference between Ru and C or O. This would also mean that there is electron transfer from Ru to CNT through a strong metal-support interaction (SMSI).[120]

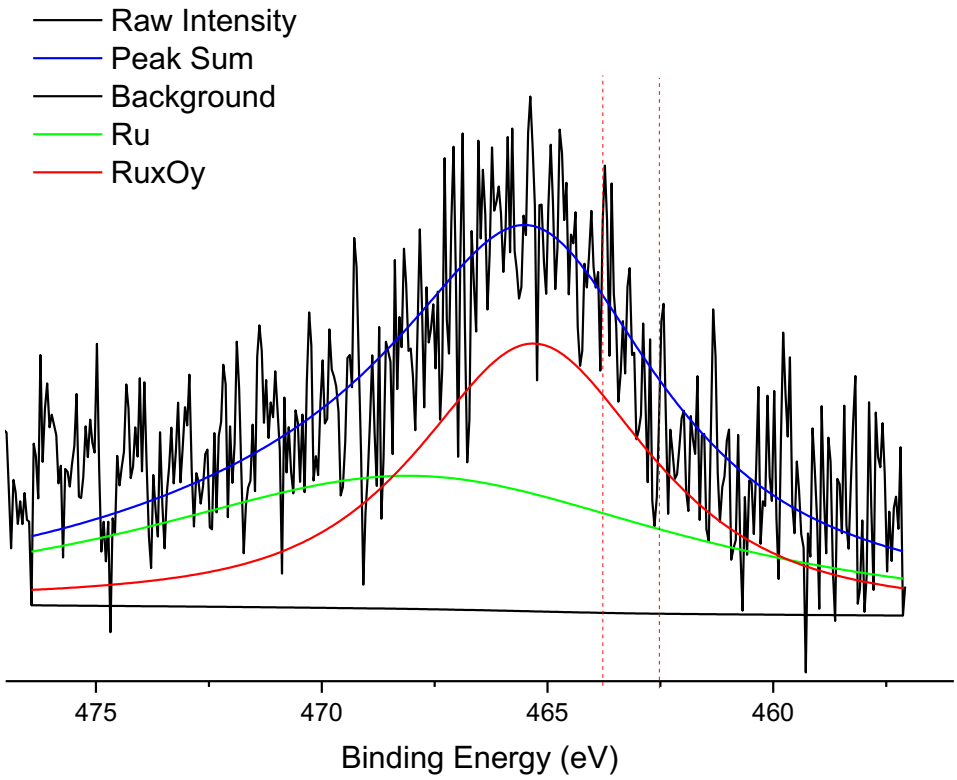

Figure 3.2.9 XPS of 5 % wt. Ru/CNT; fitting of Ru 3p.

3.2.2 Hydrogenation of HMF into DMF

The study of hydrogenation of HMF into DMF under several reactions conditions such as H_2 pressure, reaction temperatures, ruthenium loading and the effect of support used were performed.

3.2.2.1 Effect of H_2 Pressure

The influence of H_2 pressure on HMF hydrogenation was studied with commercial 5 % wt. % Ru/C from Sigma by varying the pressure in the range of 10, 20, 30 and 40 bar. Results of these experiments are given in **Figure 3.2.10-Figure 3.2.11**.

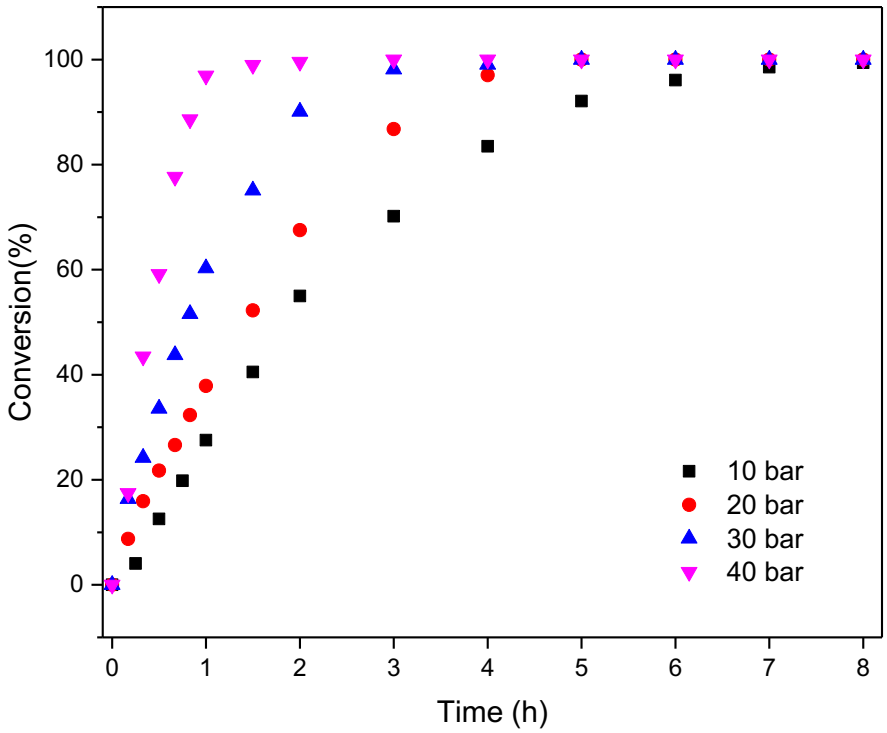

Figure 3.2.10 Conversion of HMF at a various H_2 pressure in time online reaction over 5 % Ru/C sigma. Reaction conditions: HMF, 40 mM; catalyst, 60 mg; solvent, Dioxane; temperature, 150 °C; stirring, 1100 rpm.

As presented in **Figure 3.2.10**, HMF conversion increases with the increase of H_2 pressure. At low pressure around 10 bar, it takes 8 hours to reach 100 % HMF conversion with only 36 % of DMF yield. This means that the hydrogenation of HMF into DMF is incomplete at lower H_2 pressure hence with the high yield of DHMF. The same results were observed in previous work. [31, 75, 82] As the H_2 pressure increases to 20, 30 and 40 bar, HMF conversion reached 100 % in 5, 4 and 2 hours respectively. This could be attributed to the fact that the increase of H_2 pressure enhanced the solubility of H_2 in the solvent and improved the hydrogenation of HMF.[31]

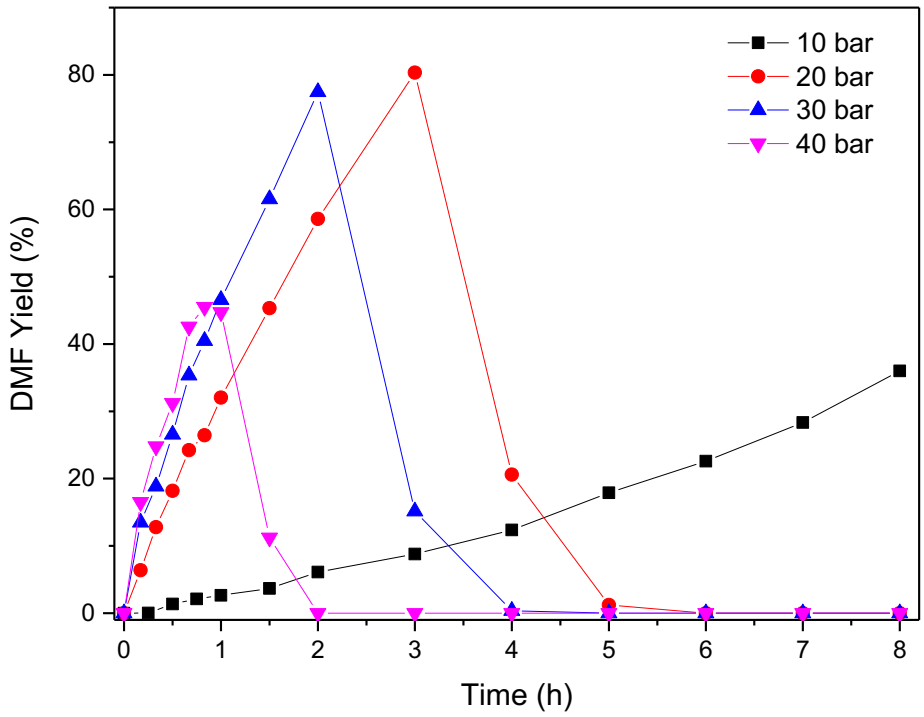

Figure 3.2.11 DMF yield at a various H_2 pressure in time online reaction over 5 % Ru/C sigma. Reaction conditions: HMF, 40 mM; catalyst, 60 mg; solvent, Dioxane; temperature, 150 °C; stirring, 1100 rpm.

Nevertheless, increasing H_2 pressure up to 40 bar did not improve DMF yield as shown in **Figure 3.2.11**. This is due to the high rate of consecutive hydrogenation of DMF ring occurred as the reaction time is prolonged. The consecutive hydrogenation reaction leads to the formation of ring hydrogenation product, DMTHF. The same phenomena were also been observed in previous work regarding on the effect of H_2 pressure.[31, 75, 78, 82] On decreasing H_2 pressure to 30 and 20 bar, DMF yield reached maximum 77 % and 80 % in 2 and 3 hours respectively. As the reaction time was prolonged, DMF yield drops as ring hydrogenation product, DMTHF, and ring opening product, 2-hexanol started to form as shown in **Figure 3.2.13** and **Figure 3.2.14**. Therefore, 20 bar of H_2 pressured was preferred for the optimum reaction pressure although it has slightly longer reaction time compared to 30 bar but with better DMF yield.

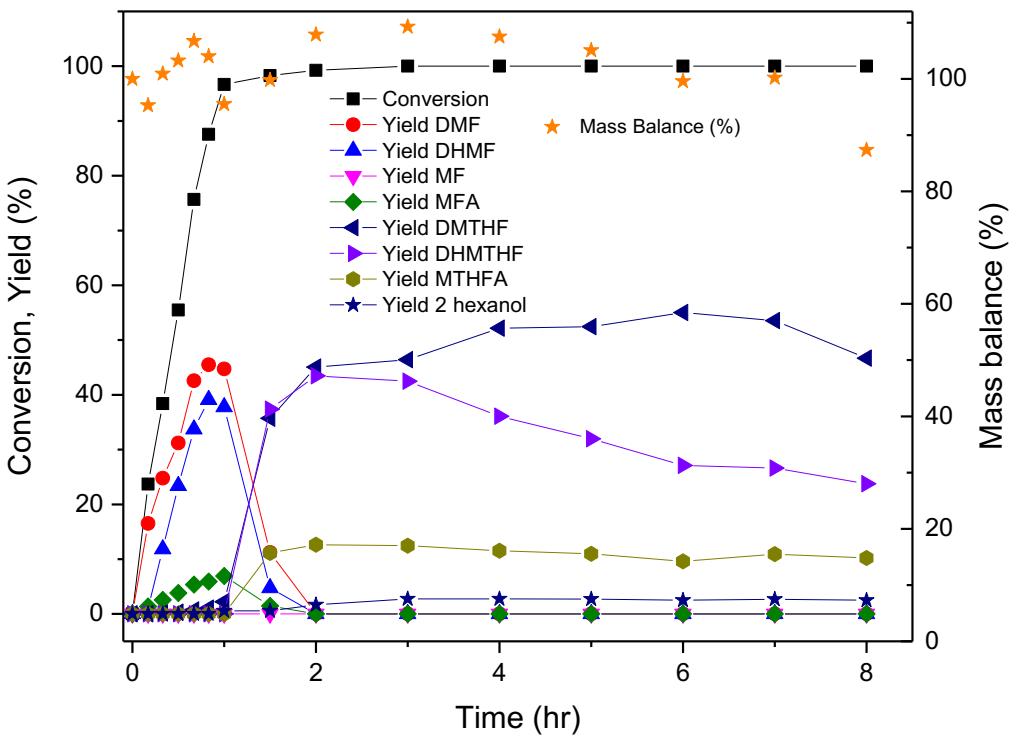

Figure 3.2.12 Time online reaction of HMF hydrogenation with 5 % Ru/C sigma at 40 bar H_2. Reaction conditions: HMF, 40 mM; catalyst, 60 mg; solvent, Dioxane; temperature, 150 °C; stirring, 1100 rpm.

Figure 3.2.12 depicted the product distribution at 40 bar of H_2. It can be seen that high pressure leads to faster conversion of HMF and formation of by-products consisting of ring hydrogenation of DHMF, MFA, and DMF as well as ring opening product, 2-hexanol. Total HMF conversion was achieved in close to 2 hr with a maximum 46 % DMF yield. Ring hydrogenation of DHMF resulted in the formation of DHMTHF which also could be hydrogenolysed to MTHFA which is a ring hydrogenation product of MFA. MTHFA then can be further hydrogenated to DMTHF which a product of ring hydrogenation of DMF. Therefore, it is not surprising to see a high yield of DMTHF since it can be formed from not only DMF but intermediates of DHMF and MFA as well (**Scheme 3**).

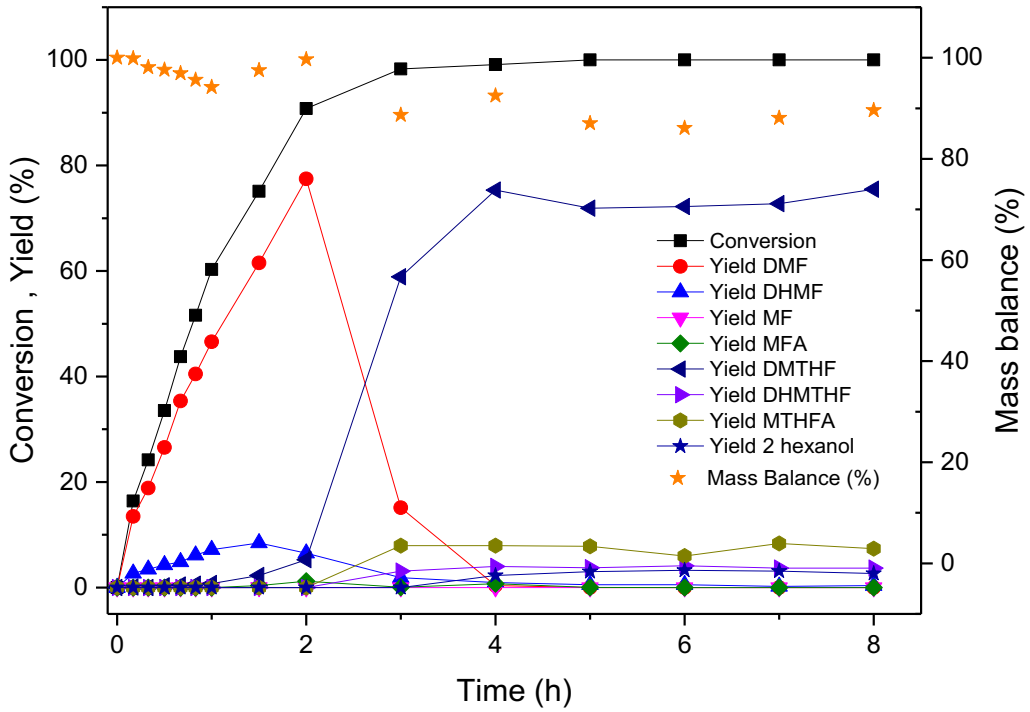

Figure 3.2.13 Time online reaction of HMF hydrogenation with 5 % Ru/C sigma at 30 bar H_2. Reaction conditions: HMF, 40 mM; catalyst, 60 mg; solvent, Dioxane; temperature, 150 °C; stirring, 1100 rpm.

Product distribution from the reaction at 30 bar H_2 is shown in **Figure 3.2.13.** It can be seen that HMF conversion is slower than 40 bar of H_2. The total conversion was achieved at 3 hours with a maximum 77 % DMF yield. There were less ring hydrogenation products from DHMF and MFA compared to 40 bar of H_2. This could be due to less selectivity of DHMF. There was about 10 % of MTHFA and 5 % of DHMTHF after 8 hours of reaction. The major product after 8 hours of reaction was DMTHF. This can be explained by the decreasing of DMF yield at 2 hours of reaction time.

At 20 bar of H_2, as shown in **Figure 3.2.14**, the product distribution is almost similar to 30 bar of H_2. However, HMF conversion was slower and the total conversion reached at 5 hours of reaction. Nevertheless, the selectivity to DMF was good with the highest yield of DMF (80 %) compared to other H_2 pressure. Because of that, there was also less intermediate products from ring hydrogenation of DHMF and MFA. The main by-product observed was DMTHF and 2-hexanol. Both are coming from ring

hydrogenation of DMF and ring opening of DMF and DMTHF. This can be explained why the yield of DMF decreased after 3 hours of reaction time.

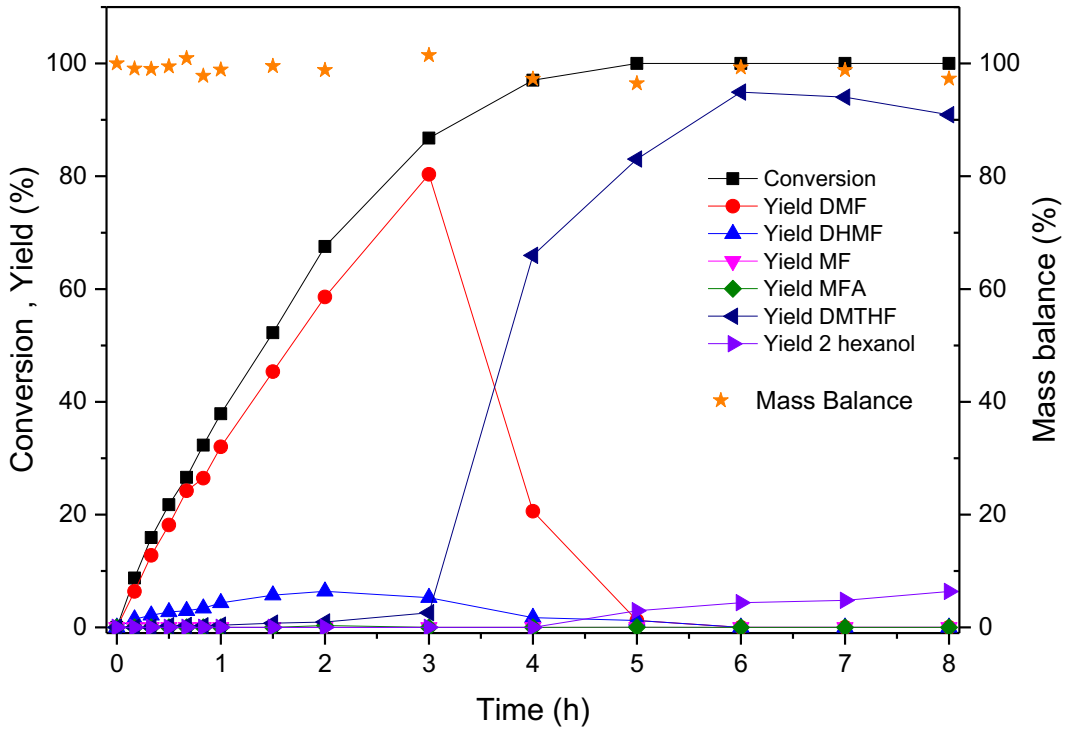

Figure 3.2.14 Time online reaction of HMF hydrogenation with 5 % Ru/C sigma at 20 bar H_2. Reaction conditions: HMF, 40 mM; catalyst, 60 mg; solvent, Dioxane; temperature, 150 °C; stirring, 1100 rpm.

The product distribution of HMF hydrogenation at low H_2 pressure is displayed in **Figure 3.2.15**. It can be noticed that the reaction was slower than the other H_2 pressures. Total HMF conversion was achieved in 8 hours. The reaction was more selective to DHMF as there was less H_2 available to speed up the conversion. It can be seen that DMF yield was continuously increased to 35 % after 8 hours followed by MFA with only 10 %. One can see that DMF yield started to increase as DHMF yield decreased. Longer reaction time is needed in order to obtain a high yield of DMF.

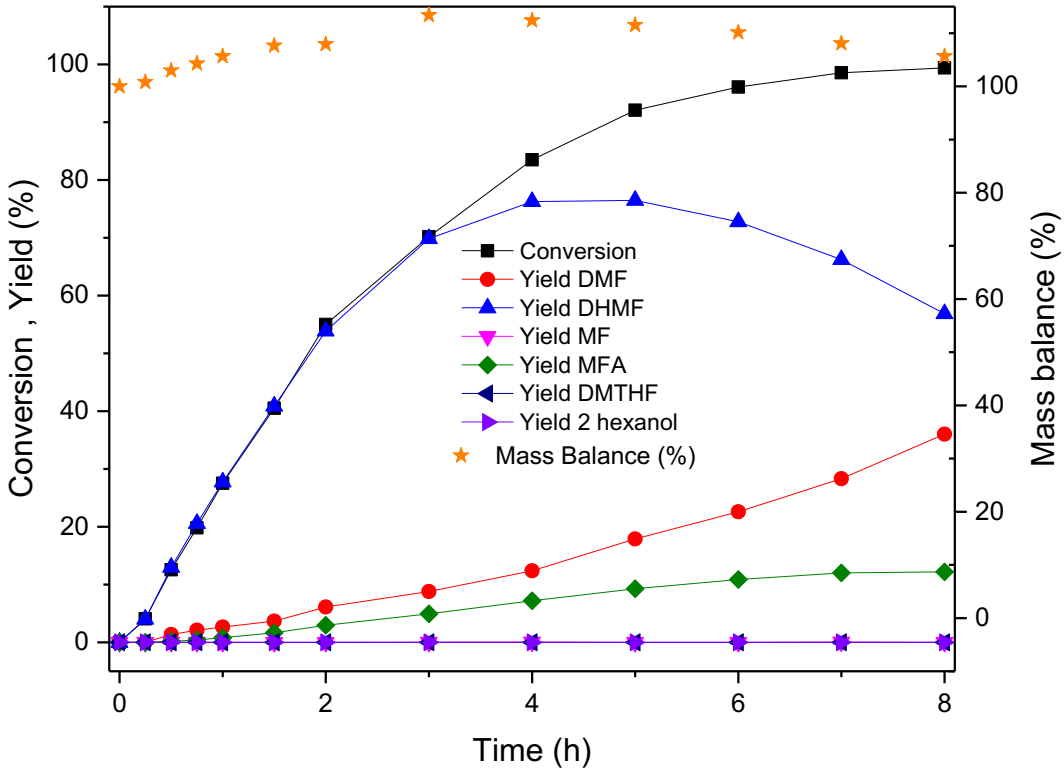

Figure 3.2.15 Time online reaction of HMF hydrogenation with 5 % Ru/C sigma at 10 bar H_2. Reaction conditions: HMF, 40 mM; catalyst, 60 mg; solvent, Dioxane; temperature, 150 °C; stirring, 1100 rpm.

3.2.2.2 Effect of Reaction Temperature

Hydrogenation of HMF to DMF was further optimized by changing the reaction temperature on 5 % Ru/C sigma catalyst in the range of 130 °C to 200 °C. As illustrated in **Figure 3.2.16**, the rate of HMF conversion increased as the temperature was increased from 130 to 170 °C. As can be observed, the increase of temperature does not seem to have important influences on the conversion above 170 °C. These results seem in agreement with the thermodynamic since hydrogenation reactions are exothermic and therefore it should not expect an increase in results.[147] Total HMF conversion reached at the shorter time as the temperature increased, from 8 hours to 2 hours. As the reaction rate increases with the increase of temperature, it leads to deep hydrogenation products as well as furan aromatic ring hydrogenation products such as DMTHF and 2 hexanol in agreement with the literature. [75, 82] The activation energy calculated for HMF hydrogenation over Ru/C at various temperature was 66.7 $kJmol^{-1}$.

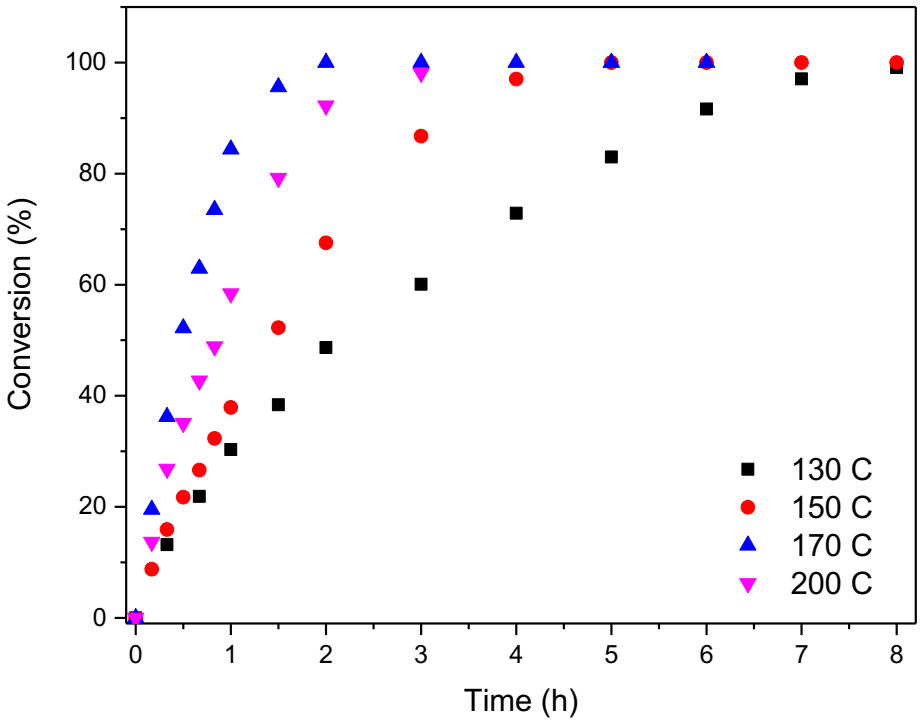

Figure 3.2.16 Conversion of HMF at various reaction temperatures in time online reaction over 5 % Ru/C sigma. Reaction conditions: HMF, 40 mM; catalyst, 60 mg; solvent, Dioxane; pressure, 20 bar; stirring, 1100 rpm.

Figure 3.2.17 shows that DMF yield increases to maximum of 80.3 % from 68.8 % upon increasing the temperature from 130 °C to 150 °C. At low temperature, the reaction rate was slow even though the DMF yield was continuously increased over time. However, above 170 °C to 200 °C, DMF yield started to decrease after several hours due to the high rate of ring hydrogenation. This finding is in agreement with the literature.[31, 75] Hu et al. performed hydrogenation reaction with Ru/C in the range of temperature of 160 to 220 °C at 20 bar H_2 in THF. It was found that lower reaction temperature resulted in low DMF yield (48 %) and high reaction temperature lead to the formation of by-products. Nagpure et al. found that 220 °C was the optimum reaction condition over Ru/ Mg–Al HT catalyst. However, DMF yield was only 58 % after 4 hours before it decreased due to the formation of ring hydrogenation product namely DMTHF.[75] This clearly implies that the ring hydrogenation is predominant at higher reaction temperatures, leading to the formation of DMTHF as the main product.

150 °C was found to be the optimum temperature in this work as it has the highest DMF yield (80 %) around 3 h reaction time.

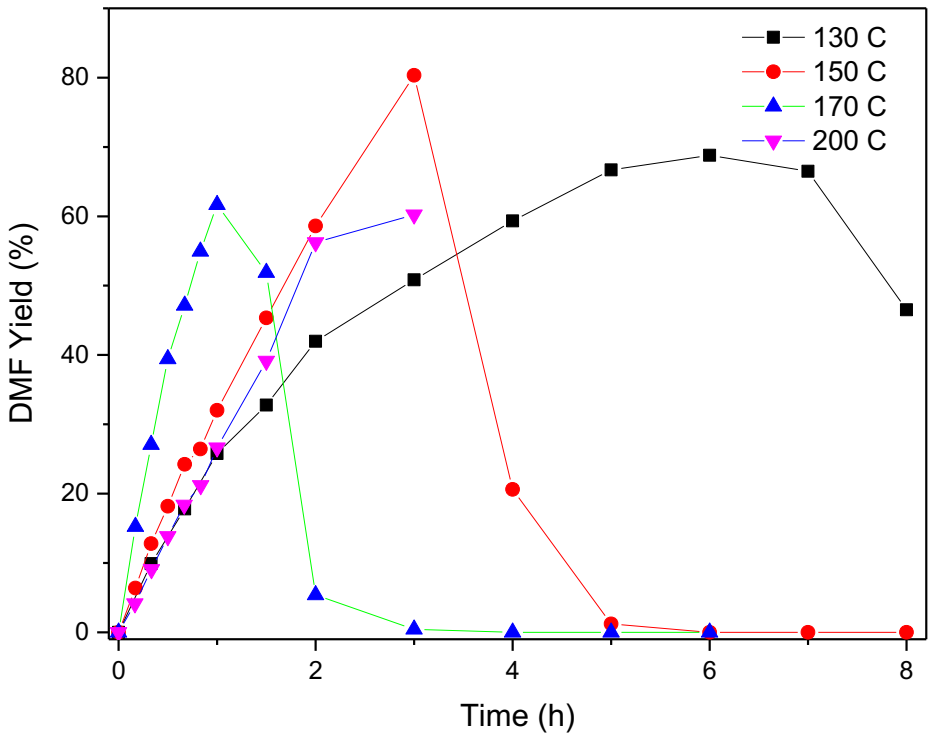

Figure 3.2.17 DMF yield at various reaction temperatures in time online reaction over 5 % Ru/C sigma. Reaction conditions: HMF, 40 mM; catalyst, 60 mg; solvent, Dioxane; pressure, 20 bar; stirring, 1100 rpm.

Figure 3.2.18 shows the reaction profile and product distribution of HMF hydrogenation at 130 °C. It can be seen that the reaction is selective towards DMF; however, the reaction was slow compared to other temperature. Total HMF conversion reached at 8 hours of reaction time. Maximum DMF yield reached at 68 % in 6 hours. After 6 hours DMF yield decreased due to the formation of ring hydrogenation and ring opening products, DMTHF and 2-hexanol.

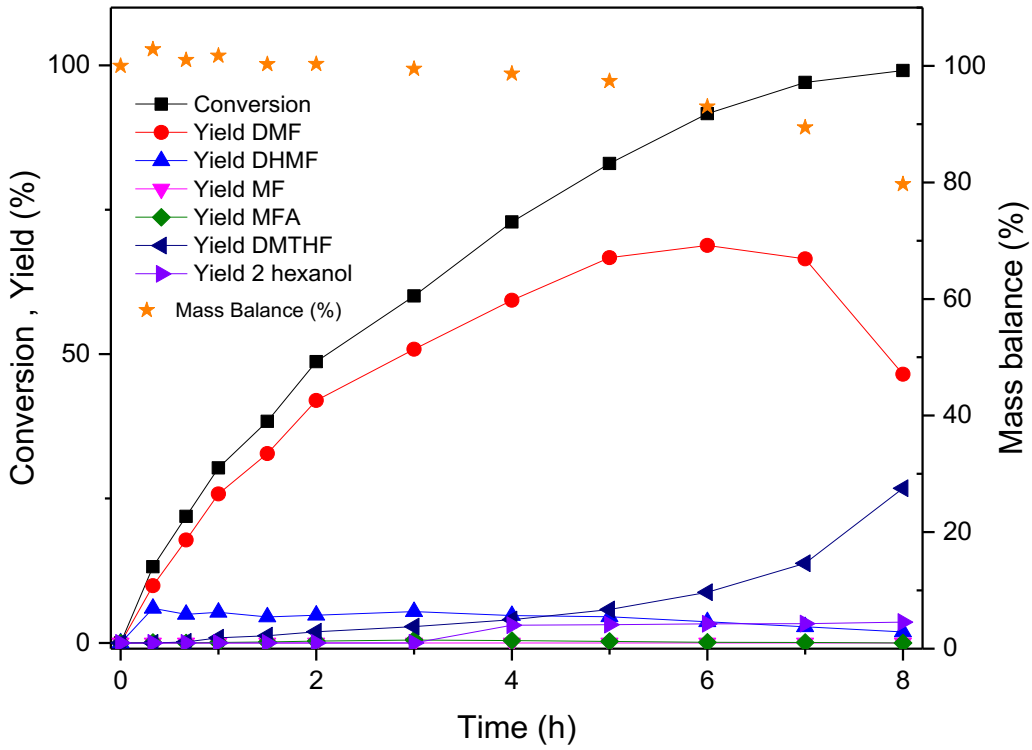

Figure 3.2.18 Time online reaction of HMF hydrogenation with 5 % Ru/C sigma at 130 °C. Reaction conditions: HMF, 40 mM; catalyst, 60 mg; solvent, Dioxane; pressure, 20 bar; stirring, 1100 rpm.

At 150 °C, as shown in **Figure 3.2.19**, the product distribution is almost similar to 130 °C. However, the reaction was much faster and HMF total conversion reached at 5 hours of reaction. The selectivity to DMF was good with the highest yield of DMF in 3 hours compared to other temperature. The main by-products observed were DMTHF and 2-hexanol. Both were coming from ring hydrogenation of DMF and ring opening of DMF and DMTHF. This can be explained why the yield of DMF decreased after 3 hours of reaction time.

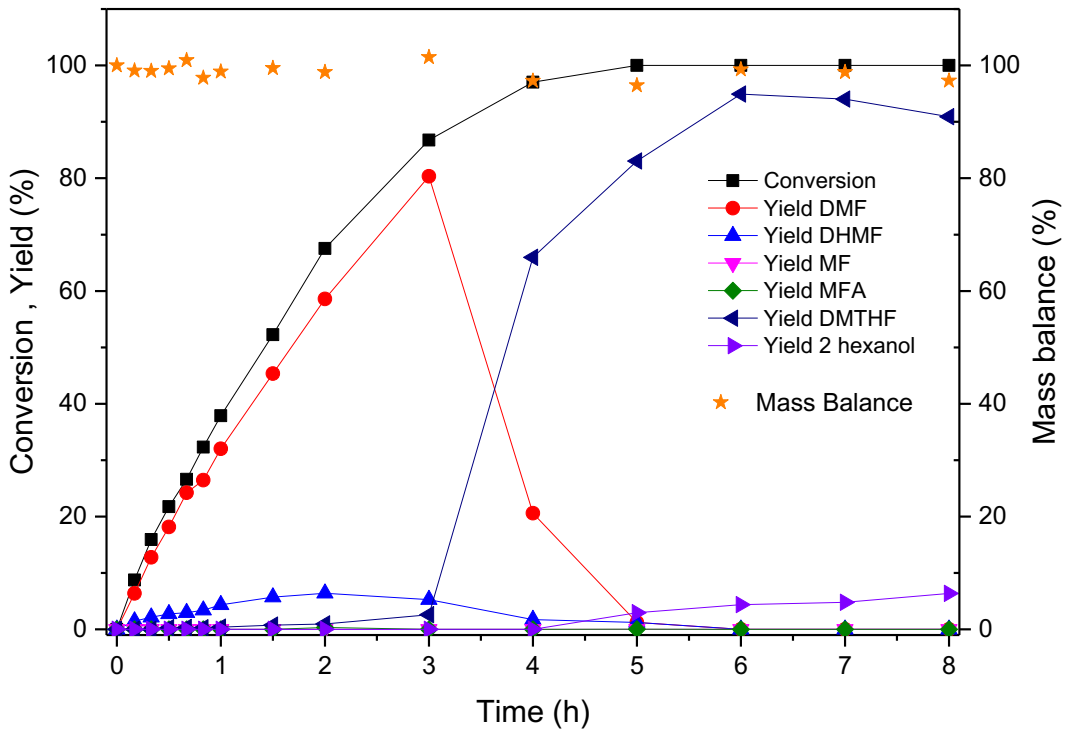

Figure 3.2.19 Time online reaction of HMF hydrogenation with 5 % Ru/C sigma at 150 °C. Reaction conditions: HMF, 40 mM; catalyst, 60 mg; solvent, Dioxane; pressure, 20 bar; stirring, 1100 rpm.

Figure 3.2.20 shows the product distribution of HMF hydrogenation at 170 °C. It can be seen that the reaction was much faster than 150 °C with total HMF conversion in 2 hours; however, DMF yield did not reach as high as a reaction at 150 °C due to the formation of ring hydrogenation and ring opening products, DMTHF and 2-hexanol. Both are quite stable with 60 % and 30 % of yield after 6 hours. **Figure 3.2.21** shows the product distribution of HMF hydrogenation at 200 °C. The reaction was much faster than 150 °C, DMF yield did not reach as high as a reaction at 150 °C due to the formation of ring hydrogenation and opening products namely MTHFA, DMTHF, and 2-hexanol. This was also observed by Kumalaputri et al.[73]

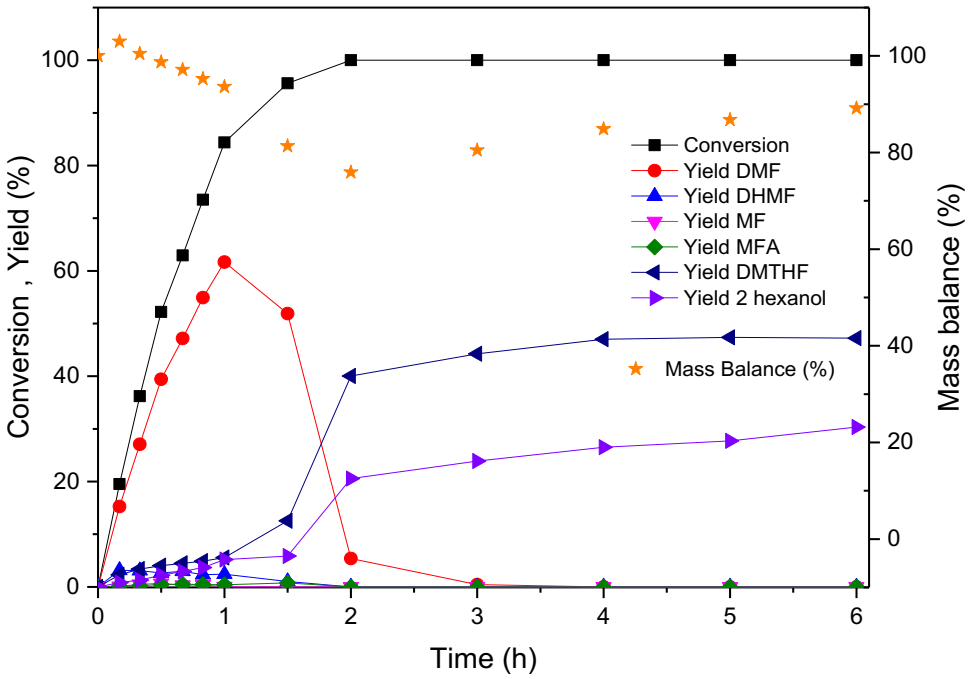

Figure 3.2.20 Time online reaction of HMF hydrogenation with 5 % Ru/C sigma at 170 °C. Reaction conditions: HMF, 40 mM; catalyst, 60 mg; solvent, Dioxane; H_2 pressure, 20 bar; stirring, 1100 rpm.

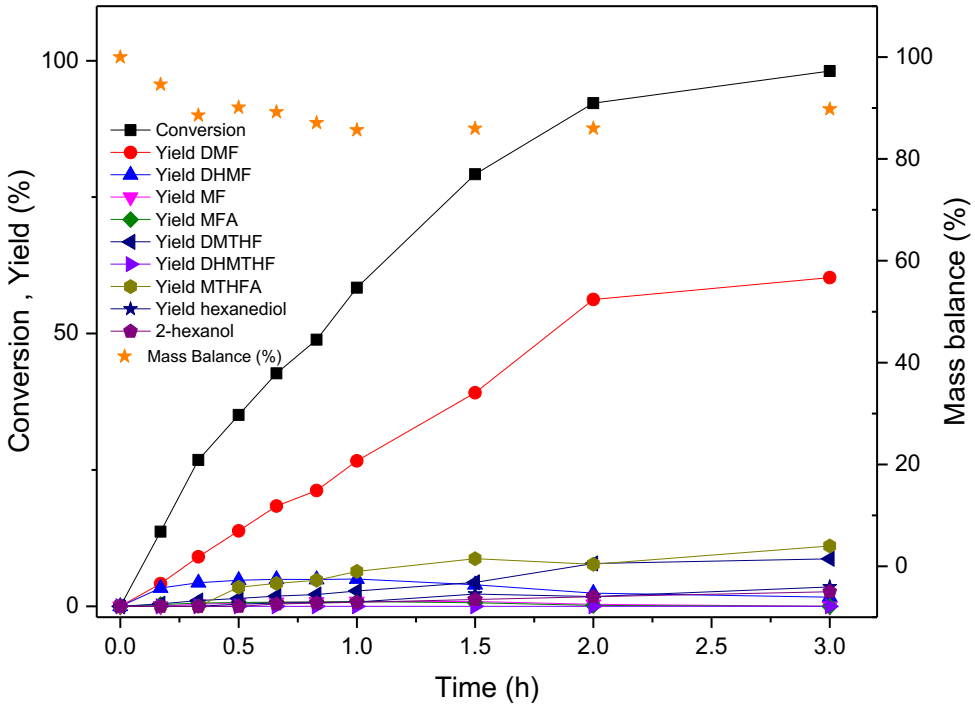

Figure 3.2.21 Time online reaction of HMF hydrogenation with 5 % Ru/C sigma at 200 °C. Reaction conditions: HMF, 40 mM; catalyst, 60 mg; solvent, Dioxane; pressure, 20 bar; stirring, 1100 rpm.

3.2.2.3 Effect of Ruthenium loading

To determine the optimum amount of Ru loading in the catalyst, Ru catalysts supported on carbon with loadings of 1.5 wt. %, 3 wt. % and 5 wt. % were prepared via incipient wetness impregnation and tested. As shown in **Figure 3.2.22** and **Figure 3.2.23** there were significant improvements in term of HMF conversion and DMF yield when Ru loading was increased from 1.5 wt. % to 5 wt. %. Commercial 5 % wt. Ru/C from Sigma showed superior reactivity in both of HMF conversion and DMF yield. 5 % Ru/C achieved 45 % HMF conversions after 6 hours followed by 3 % Ru/C and 1.5 % Ru/C with 38 % and 30 % respectively. It is suggested that by increasing Ru loading, it providing a more active site for the reaction to take place and thus promoted the hydrogenation of HMF as well as the formation of DMF. However excessive Ru loading would accelerate the occurrence of ring hydrogenation, ring opening products and most importantly increase the production cost of DMF. The same finding was observed by previous literature on hydrogenation of HMF to DMF with Ru catalyst supported on carbon. [31]

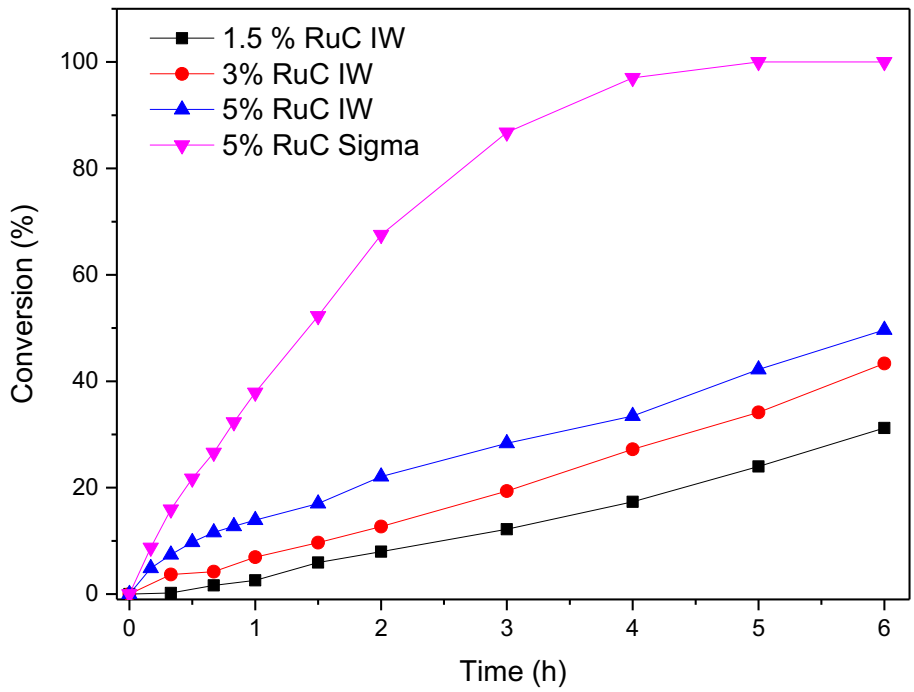

Figure 3.2.22 Conversion of HMF at various Ru loading in time online reaction over 5 % Ru/C. Reaction conditions: HMF, 40 mM; catalyst, 60 mg; solvent, Dioxane; temperature,150 °C; pressure, 20 bar; stirring, 1100 rpm.

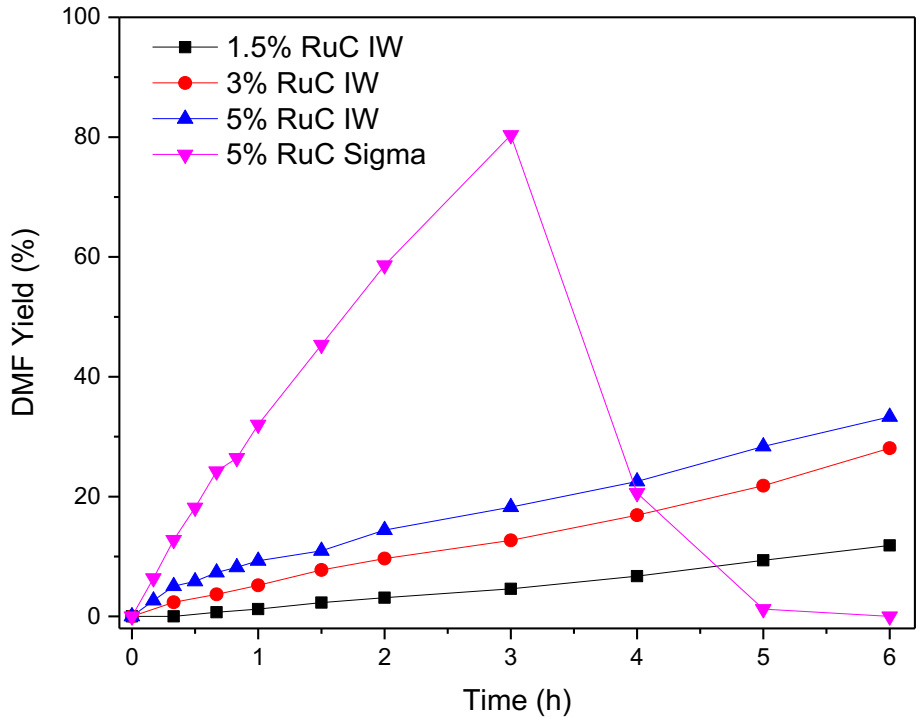

Figure 3.2.23 DMF yield at various Ru loading in time online reaction over 5 % Ru/C. Reaction conditions: HMF, 40 mM; catalyst, 60 mg; solvent, Dioxane; temperature, 150 °C; pressure, 20 bar; stirring, 1100 rpm.

Table 3.2.3 shows the amount of CO uptake and dispersion of Ru catalysts supported on C with different loading of Ru obtained from Co chemisorption. It can be seen that with the increasing of Ru loading from 1.5 % to 5 %, the amount of CO uptakes and metal dispersion were also increased. This could explain on the high conversion of HMF as the Ru loading was increased.

Table 3.2.3 CO uptake and metal dispersion of Ru catalysts with different loading of Ru based on CO chemisorption.

Entry	Catalyst	CO uptake (µmol/g)	D (%)
1	5% Ru/C sigma	122	24
2	5% Ru/C IW	66	13
3	3% Ru/C IW	33	11
4	1.5 % Ru/C IW	16	10

At iso-conversion, it was observed that there is a trend with DMF and DHMF yield as shown in **Figure 3.2.24**. As Ru loading increased from 1.5 % to 5 % DMF yield is increasing while DHMF is decreasing. This could be related to the active site available and the metal dispersion as shown in **Table 3.2.3**. Furthermore, the particle size of Ru might play an important role in resulting such trends. It was reported that smaller Ru crystallite size suppresses the ring hydrogenation thus leading to better DMF yield. [75]

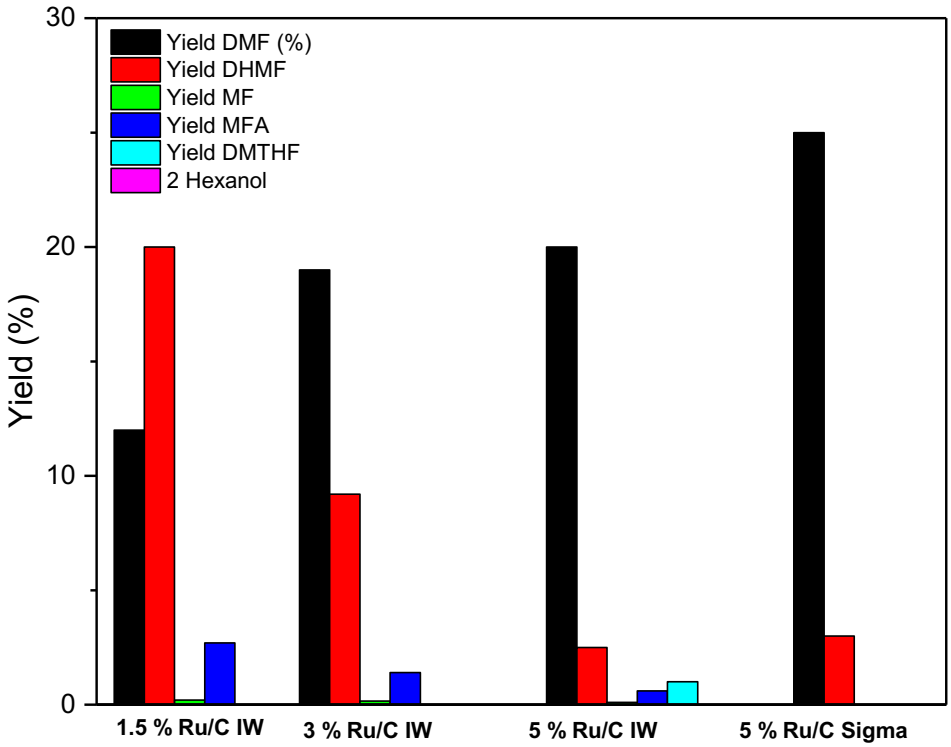

Figure 3.2.24 DMF yield at iso conversion of 30 % with the various loading of Ru/C and 5 % Ru/C-sigma. Reaction conditions: HMF, 40 mM; catalyst, 60 mg; solvent, Dioxane; temperature,150 °C; pressure, 20 bar; stirring, 1100 rpm. (Reaction time at 30% iso-conversion of 1.5 % Ru/C: 6 hr, 3 % Ru/C: 4.5 hr, 5 % Ru/C: 3 hr and 5% Ru/C sigma: 0.75 hr).

3.2.2.4 Effect of the support

Based upon prior literature, it is expected that the support plays an important role as it can maximise the active surface area of metal catalysts by dispersing them on its surface.[88] Thus it would affect the reactivity as well as product selectivity. Previous work carried out in our research group revealed that CNTs as supports for hydrogenating reactions can offer enhanced catalytic activities of supported molybdenum carbides and, we decided to evaluate whether the same was true for Ru in the hydrogenation of HMF.[200] Based on the optimum conditions from the preliminary test of 5 % Ru/C sigma, 5 wt. % Ru/CNT was synthesised via incipient impregnation method.

Table 3.2.4 BET surface area measurements and pore volume of carbon Norit and CNT.

Support	Surface area (m^2/g)	Pore Volume (cc/g)
Carbon Norit	553	0.75
CNT	281	1.73

As shown in **Table 3.2.4** BET surface area measurements and pore volume of carbon Norit and CNT, CNT has lower surface area compared to AC. However, due to its high pore volume, it can offer advantages regarding less mass transfer limitation compared to activated carbon as discussed in chapter 1. Furthermore, the electronic effect gives good reactivity when it is used as a support [120, 201, 202]. A blank reaction with only CNT shows that there is no significant reactivity with 8 % conversion after 6 hours. This could be due to the fact that there could trace present of Fe during CNT synthesis. However, the catalytic test of Fe catalyst in chapter 4 showed a poor activity. Chemisorption results show that Ru/CNT has lower dispersion than Ru/C (

Table 3.2.2). This could be due to the low surface area of CNT compared to AC as discussed in previous work. [154] However, TEM result shows that Ru is well distributed on CNT with a smaller average particle size of 1.5±0.5 nm compared to 5 % Ru/C IW. The smaller particles size of Ru supported on CNT could be also responsible for the high reactivity and TOF apart from the effect of CNT alone. On the contrary earlier, also that

smaller nanoparticle seemed to slow down the conversion of the intermediate to DMF (**Figure 3.2.23**).

Table 3.2.5 HMF conversion, DMF yield and TOF of blank reaction, carbon, CNT, and Ru catalysts supported on carbon and CNT.

entry	catalyst	Reaction time (h)	HMF conversion (%)	DMF yield (%)	DHMF yield (%)	TOF (h^{-1})[a]	TOF (h^{-1})[b]
1	none	2	0	0	0	-	-
2	carbon	2	4	0	0	-	-
3	CNT	6	8	0.8	7	-	-
4	5 % Ru/C	3	87	80.3	5	101	20
5	5% Ru/CNT	1	96	83.5	16	492	915

Reaction conditions: HMF, 40 mM; catalyst, 60 mg; solvent, Dioxane; pressure, 20 bar; stirring, 1100 rpm. [a] TOF of maximum DMF yield based on CO chemisorption. [b] TOF at 30 % iso conversion. Experimental errors (conversion and yield = ± 0.07%, TOF = ± 0.05).

Table 3.2.5 shows the result of blank reaction as a comparison to reaction with the catalyst. In the absence of a catalyst (entry 1), there was no conversion of HMF which implies that dioxane just acted as a solvent and do not play an active role in HMF conversion into DMF. On the other hand, the reaction with carbon (entry 2) and CNT (entry 3) showed 4 and 8 % conversion respectively. This suggested that some acid sites on the carbon and CNT in some extent contribute to side reactions such as etherification as reported in previous literature [64]. Though, it is still insignificant compared to the reaction with Ru (entry 4) for complete HMF hydrogenation into DMF as shown in the table **Table 3.2.5**. A blank test without sample withdrawal showed that the effect of volume of the reaction is negligible as a comparison to the time online reaction. With Ru/CNT (entry 5), HMF conversion and DMF yield were higher in a shorter time as compared to Ru/C. The TOF shows that Ru/CNT is 4 times better than Ru/C with TOF of 492 h^{-1}. This shows that CNT did play an active role in accelerating the conversion as well as selectivity towards DMF apart from the effect of smaller particles size of Ru catalyst supported on CNT. TOF at initial rate shows that Ru/CNT has higher TOF of 915 h^{-1} compared to Ru/C with only 20 h^{-1}. This implies that the particle size of Ru plays some role on the reactivity of HMF hydrogenation to some extent.

To explain the enhancement of activity due to the CNTs is complex due to morphological differences as well as electronic and metal-support interaction effects. A positive effect on activity could be attributed to an electronic effect of CNT derived from the curvature shape of CNT. This could consequently enhance the electron density of the metal thus improving the adsorption of C=O bonds resulting in higher reactivity. [120]

It is proposed that the unique properties of the CNT in H_2 adsorption/ spillover and electron transport may bring about positive effects in these catalytic reactions. Those active H-adspecies could be readily transferred to Ru active sites via CNT-promoted hydrogen spillover and thus increase the rate of a series of surface hydrogenation reactions. H_2 temperature-programmed desorption (H_2-TPD) measurements for some typical supported Ru catalysts from previous work demonstrated that the H_2 desorption from the Ru/CNT occurred from lower temperatures than that of other catalyst's support, which implies that the adsorbed hydrogen species on the CNT surface may be more active at the reaction temperature. Moreover, higher concentrations of adsorbed hydrogen occurred over the catalysts with CNT and zeolites H-beta and HY as supports.[158]

Figure 3.2.25 displays the products distribution of HMF hydrogenation with 5 % Ru/CNT. It can be seen that the reaction is faster than Ru/C with total HMF conversion in 1.5 hours. DMF yield reached a maximum of 83.5 % in 1 hour before declining, due to the formation of by-products coming from ring hydrogenation and ring opening of furan ring. DMTHF is the main by-product with 59 % yield followed by 1, 2-hexanediol, DHMTHF and 2-hexanol.

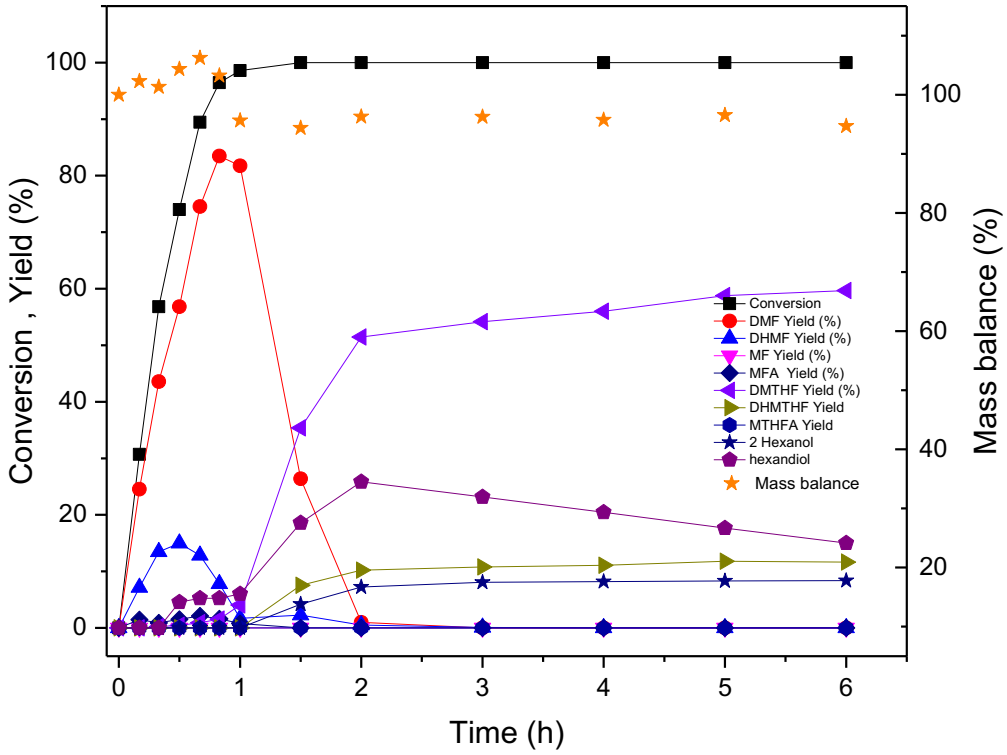

Figure 3.2.25 Time online reaction of HMF hydrogenation with 5 % Ru/CNT at 150 °C. Reaction conditions: HMF, 40 mM; catalyst, 60 mg; solvent, Dioxane; pressure, 20 bar; stirring, 1100 rpm.

3.2.2.5 Reaction pathways and intermediates

The reaction mechanism was studied by performing the hydrogenation reaction with different intermediate such as DHMF, MFA and DMF over 5 % Ru/CNT at 150 °C for 3 hr which was an ideal condition for DMF formation. Intermediates like DHMTHF and MTHFA were found to be predominant when DHMF were used as the starting material while DMF was converted mostly into DMTHF and 2-hexanol. No trace of hexanedione, HDN were present in all of the reactions as reported in the literature (**Scheme 3**).

Figure 3.2.26 shows the product distribution of DHMF hydrogenation. DHMF was converted into MFA, DMF and ring hydrogenation products of DHMF, MFA and DMF which are DHMTHF and MTHFA and DMTHF. Total DHMF conversion achieved in 1.5 hours with DHMTHF as the main product after 3 hours followed by MTHFA and DMTHF. A Low yield of DMF achieved when DHMF was employed as the starting substrate due to the formation of ring hydrogenation products.

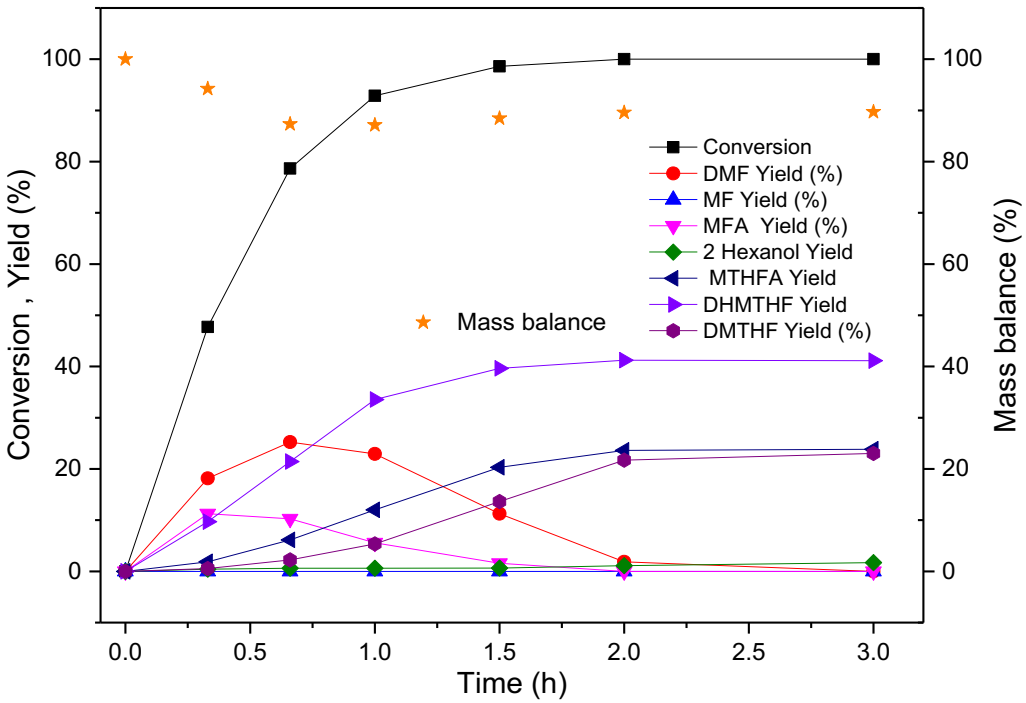

Figure 3.2.26 Product distribution of TOL reaction from DHMF as starting material. Reaction condition : temperature 150 °C , H_2 pressure 20 bar , catalyst ; 5 % Ru/CNT ,60 mg , time ; 6 hr , solvent ; Dioxane .

Figure 3.2.27 shows the product distribution of MFA hydrogenation. Compared to DHMF, MFA showed faster conversion which indicated that MFA was easily hydrogenolysed to DMF. This is in agreement with the literature when Ru or CNT was used.[75, 81] On the other hand, MFA showed poor reactivity over Cu catalysts although similar product distribution was observed as demonstrated by Kumalaputri et al.[73]Total conversion achieved at 0.75 hours with DMF, DMTHF and MTHFA as the main products. However, DMF yield decreased significantly after 0.5 hours as its being converted into DMTHF by ring hydrogenation.

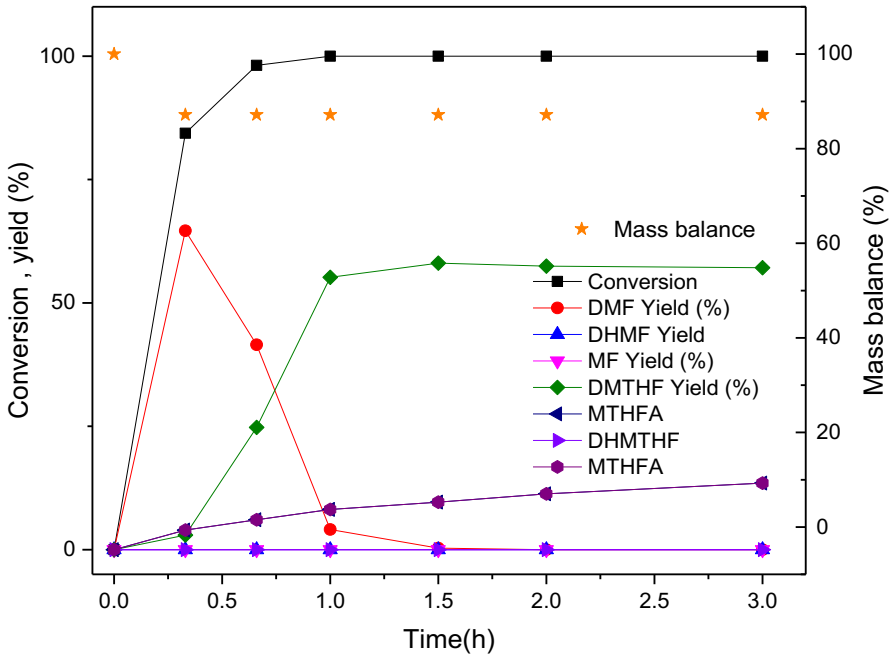

Figure 3.2.27 Product distribution of TOL reaction from MFA as starting material. Reaction condition : temperature 150 °C , H_2 pressure 20 bar , catalyst ; 5 % Ru/CNT ,60 mg , time ; 6 hr , solvent ; Dioxane .

Figure 3.2.28 shows the product distribution of DMF hydrogenation over Ru/CNT catalyst. DMF was totally converted into DMTHF and 2-hexanol after 0.75 hours. This confirms that DMF was active over Ru/CNT which leads to faster conversion and formation of ring hydrogenation and ring opening products namely DMTHF and 2-hexanol. The same observation was reported in the literature by Bottari et al.[83]

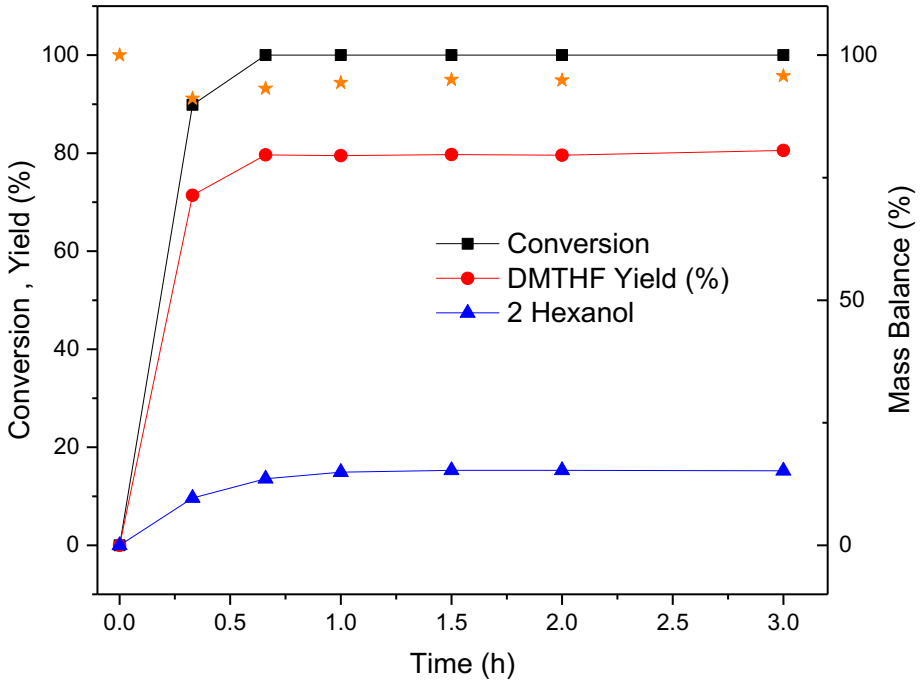

Figure 3.2.28 Product distribution of TOL reaction from DMF as starting material. Reaction condition : temperature 150 °C , H_2 pressure 20 bar , catalyst ; 5% Ru/CNT ,60 mg , time ; 6 hr , solvent ; Dioxane .

The possible reaction pathway for the conversion of HMF is illustrated in **Scheme 4**. DMF can be produced through pathway **1**. HMF was initially hydrogenated to DHMF and then further deoxygenated to form MFA and DMF. Notably, the furan ring of DHMF, MFA and DMF can be saturated to form ring hydrogenation products **(3)**. Subsequently at a prolonged reaction time, ring opening products **(4)**, 2-hexanol could be formed due to highly hydrogenation ability of Ru/CNT catalyst.

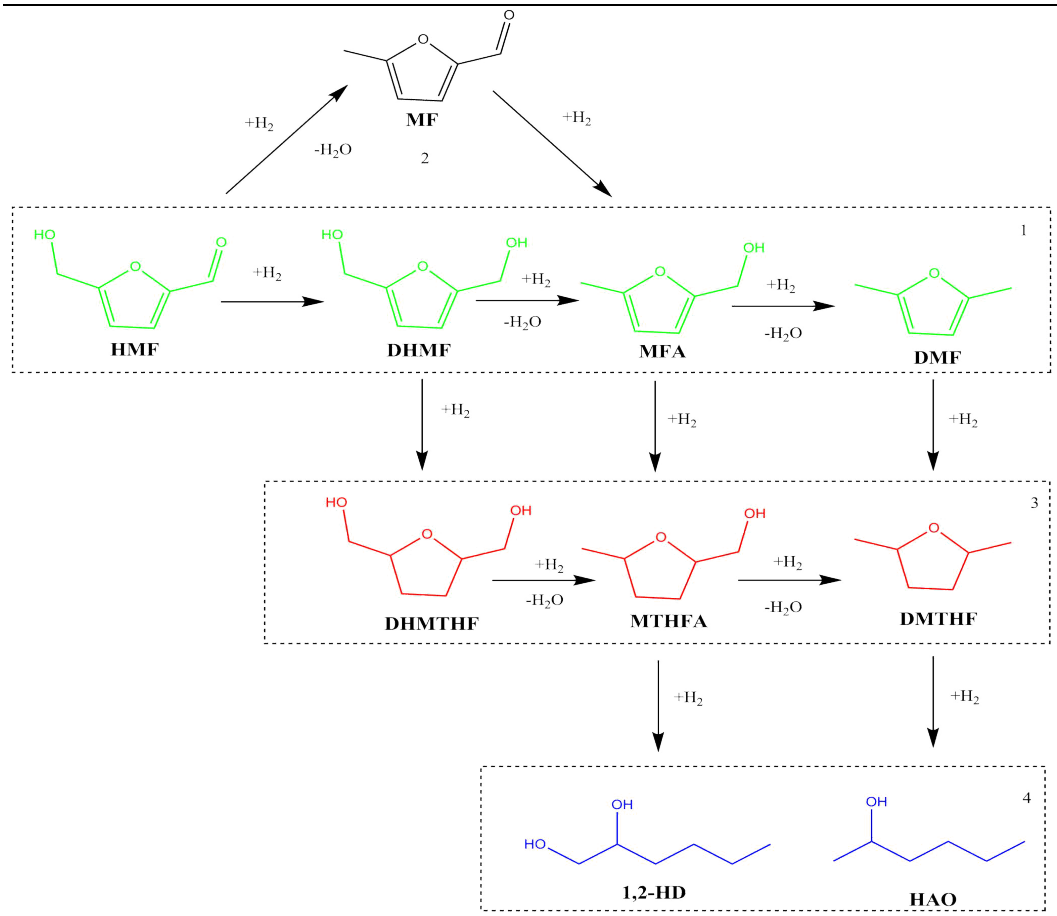

1 = Main reaction Pathways
2 = Alternative pathway through hydrogenation of hydroxyl group
3 = Ring hydrogenation products
4 = Ring opening products

Scheme 4 Possible reaction pathway in HMF hydrogenation over Ru/CNT.

3.2.2.6 Effect of Ru inside and outside of CNT

In order to further understand the effect of CNT as a support, an attempt to impregnate Ru inside and outside CNT was performed. It was proposed that the decoration of Ru outside CNTs turned electron rich compared with Ru confined inside CNTs due to the enhanced electron transfer from the concave interior surface to the convex exterior surface of CNTs. This confinement effect induced by the electronic effect has different influences on each substrate and following previous work on the confinement effect of CNT in benzene, p-chloronitrobenzene and cinamaldehyde hydrogenation, 5 % Ru/CNT inside and outside were synthesized. [120] As described in the literature, the key factor for the preparation of Ru inside CNT is that, after CNTs were well dispersed in acetone aided by ultrasound, extended stirring was necessary to

drive all the metal salts into the channels due to the concentration difference accompanied by the slow evaporation. For the preparation of Ru loaded outside CNTs, a key step is the protection of inner channels by inducing a medium as temporary blocker such as acetone during impregnation with a solution containing metal salts. Since CNTs were already well dispersed in acetone by ultrasound, once the metal slats solution were added, acetone was completely evaporated at its boiling point within 1 hour. Therefore, there was no enough time to drive the metal slats into the channels sufficiently. However, TEM images of reduced 5 % Ru/CNT (I) and 5 % Ru/CNT (O) show that Ru particles are located evenly inside and out. The results of HMF hydrogenation using 5 % Ru/CNT (I) and 5 % Ru/CNT (Out) are shown in **Figure 3.2.29**.

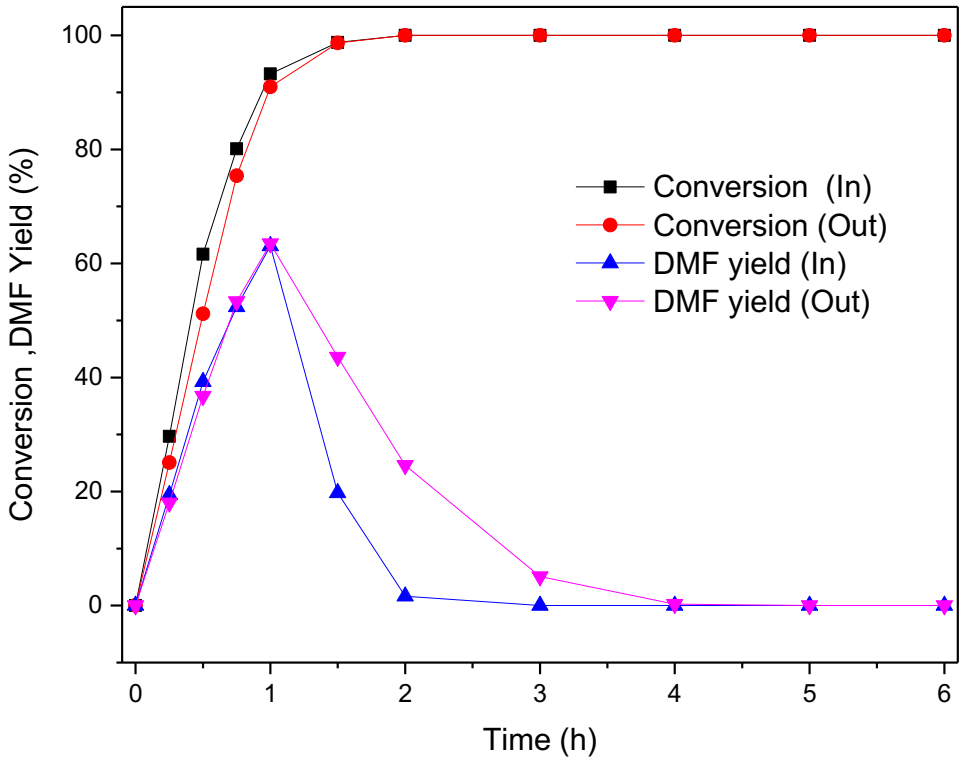

Figure 3.2.29 Conversion and DMF yield of 5 % Ru/CNT (In) and 5 % Ru/CNT (Out) at 150 °C. Reaction conditions: HMF, 40 mM; catalyst, 60 mg; solvent, Dioxane; pressure, 20 bar; stirring, 1100 rpm.

It can be seen that Ru/CNT (I) is slightly faster in converting HMF although the difference is negligible. However, compared to Ru/CNT IW, these two catalysts are less reactive. HMF conversion reached 100 % after 1.5 hr compared to Ru/CNT IW in just 1

hr. The DMF yield for both catalysts was really close after 1 hour with 63 %. This is 20 % less compared to Ru/CNT IW. The result from CO chemisorption in **Table 3.2.6** might explain this trend as Ru/CNT IW which has a mix of Ru inside and outside the tube has higher dispersion.

Table 3.2.6 CO uptakes and metal dispersion of Ru/CNT inside and outside based on CO chemisorption.

Catalyst	CO uptakes (µmol/g)	Metal Dispersion (%)
Ru/CNT inside	33.5	6.8
Ru/CNT outside	29.7	6.0
Ru/CNT IW	40.0	8.0

Wang et al.[120] reported that the electron rich Ru would be favourable for p-chloronitrobenzene hydrogenation but unfavourable for benzene hydrogenation. For cinnamaldehyde hydrogenation, the electron rich Ru would be favourable for the adsorption of C=O bond rather than C=C bond. It was proposed that the heat treatment could enhance the confinement effect induced by the electronic effect and it has different influences on the substrates.

However, in our work, it seems that the TEM images showed that Ru particles were located both on inside and out of CNT. This would result in less distinction of the electronic effect of Ru inside and out. Thus we suppose that this kind of confinement effect should be inexistent for our catalysts. This translated to the performance of the catalyst which showed the insignificant difference in the conversion and DMF yield.

3.3 Conclusions

Hydrogenation of HMF into DMF with Ru catalyst was investigated under several reaction conditions using commercial 5 wt. % Ru/C from Sigma in order to optimise the yield of desired product, DMF. 5% wt. Ru/C IW was successfully synthesised via incipient wetness impregnation method. XRD and TEM images revealed that the synthesised catalyst exhibited good dispersion with small particles size (1.85± 0.73nm). TPR study indicated that reduction at 400 °C under H_2 is sufficient to fully reduce the

catalyst into its metallic state. In addition, XPS analysis confirms that Ru present as Ru^0 which is responsible for the active site of the reaction.

It was revealed that the conversion is better with higher H_2 pressure, however, DMF yield is lower due to side reaction. The moderate H_2 pressure at 20 bar was found to be the best pressure condition without compromising DMF yield as maximum yield 80.3 % was reached in 3 hours.

The optimal reaction temperature was found to be at 150 °C as it gives the highest DMF yield compared to other temperatures. Higher temperature leads to consecutive side reactions while lower temperature resulted in partial hydrogenation product mostly DHMF.

It was also discovered that 5 wt. % Ru loading exhibited the best reactivity and DMF yield compared to lower Ru loadings. This is due to the fact that metal dispersion increased as Ru loading was increased as shown by CO chemisorption **(Table 3.2.3)**. However, the performance of 5 % Ru/C IW is still lower than 5 wt. % Ru/C from Sigma being it is the commercial catalyst for Ru/C.

After all the preliminary tests of finding the optimum condition for HMF hydrogenation into DMF, the effect of using CNT as the support was also been investigated. Remarkably it was a good outcome since the reactivity of the reaction and the yield of DMF was improved. The TOF of DMF production was increased from 101 h^{-1} to 492 h^{-1} with CNT as the support. It is proposed that the smaller particle size of Ru supported on CNT compared to carbon obtained from TEM analysis responsible for this enhancement apart from the effect of CNT alone. In addition, this could be attributed to the electronic effect of CNT derived from the curvature shape of CNT. This consequently enhanced the electron density of metal thus improving the adsorption of C=O bonds resulting in higher reactivity. [120] The effect of Ru decorated inside and out of CNT did not show any different improvement in the reactivity of the reaction compared to Ru/CNT IW. Moreover, the performance DMF yield was 20 % less than Ru/CNT IW.

Chapter 4 HMF hydrogenation with elements transition metals: Co and Ni supported on C and CNT

4.1 Introduction

Up to now, most of the catalysts being used in the transformation of HMF to DMF involved precious metals such as Ru, Pt, and Pd. [45] Thus an alternative catalytic system based on non-precious metals (Co, Ni, Cu, and Fe) is crucial from the economic point of view since they are cheaper (**Figure 4.1.1**).[70, 203] As discussed in chapter 1, transitional metals have partially occupied d-orbitals, the symmetry of which is suitable for the formation of chemical bonds with neutral molecules. These metal also have several stable oxidation states and can have different coordination number as results of the changes in the number of d-electrons.[204]

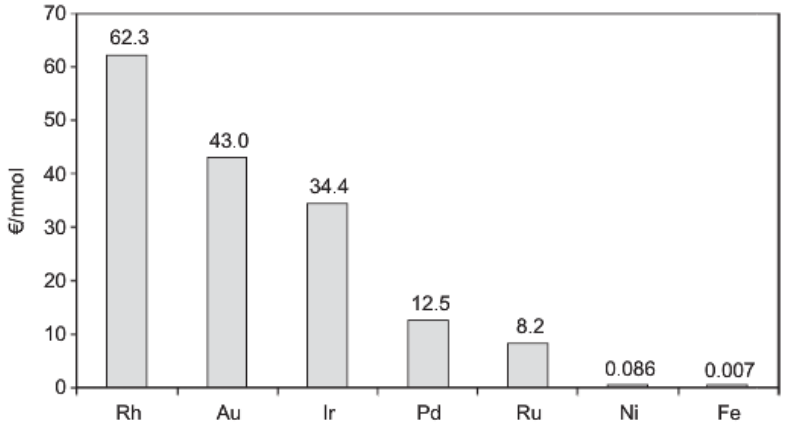

Figure 4.1.1 Relative prices for some transition metals (Sigma-Aldrich, 2012)[205]

Ni and Co are the typical active metals for hydrogenation process since both metals can hydrogenate both C=C and C=O bonds.[77, 133] Furthermore, a Cu-based catalyst has also been utilised for the hydrogenation of HMF. Recently, Iriondo et. al. demonstrated that Cu catalyst supported on ZrO_2 had the best selectivity towards DMF among other compared metals and supports such as Pt/HYAL and Ru/TiO2.[147] It was suggested that the neutral nature of the support and Cu influenced positively on the selectivity towards DMF by suppressing the C-C bond cleavage of tertiary carbon of the HMF thus avoiding the formation of furfural. Roman et al.[17] found that CuCrO4 produced 61 % yield for DMF and 29 % yield for MFA, the intermediate product at 220 °C in 1-butanol in a flow reactor system. However, this catalyst deactivated in the presence of chloride

species (introduced during the dehydration step of fructose and not completely removed during evaporation) which induced sintering of copper.[206] Kumalaputri et al.[73] demonstrated a combined yield of DMF and DMTHF as high as 81 % over Cu on doped porous metal oxides catalyst at 220 °C, 50 bar H_2.

Ni supported on Co_3O_4 has also shown good activity as an additive to Co_3O_4 in converting HMF into DMF with 76 % yield at 130 °C and 10 bar H_2 in 24 hr. It was suggested that Ni improved the hydrogenation ability and selectivity to DMF since both of the elements have good ability to break C-O bonds.[76] Ni supported on Al_2O_3 from Kong et al. shows that Ni is promising for HMF hydrogenation with a high yield of DMF, DMTHF, and DHMTHF.[77] The selectivity of products can be tuned by balancing the surface metallic Ni and acid sites of the support via calcination. 91 % yield of DMF was achieved in 4 hr at 180 °Cand 12 bar of H_2. Previous work by Kong et. al demonstrated the switchable synthesis of DMF and DHMTHF over Raney-Ni catalysts with a high yield.[207] Low reaction temperature (100 °C) along with high H_2 pressure (60 bar) favours the formation of DHMTHF by suppressing the C-O hydrogenolysis while high temperature (180 °C) favours DMF.

Catalysts based on Ni and Co were also used in the chemoselective hydrogenation of furfural. Furfural hydrogenation is pretty much similar to HMF hydrogenation apart from the lack of a methyl and a hydroxyl group.[141] Ni/SiO_2 was reported to have better reactivity than Rh/SiO_2 for hydrogenation of furfural and selectivity to furfuryl alcohol.[141] Cu/TiO_2 was reported to have a high yield of furfuryl alcohol (99 %) in 3 hr at 125 °C and 10 bar of H_2.[208]

The utilisation of new and cheap metals for hydrogenation of HMF to DMF should be explored more since this could be beneficial as an alternative for the precious metal. Not enough work has been dedicated toward HMF hydrogenation with non-precious metals and the study of the effect of the support could reduce the need for the very expensive metals and not so expensive ones could be used with a compromise in activity. However, the efficiency of non-noble metal should be improved as typically a high loading is

needed.[209] Apart from the transitional metal being used as a monometallic catalyst for hydrogenation, the combination of these metals with other transitional metal or noble metals is also getting attention.[45, 68, 83] However, this will be discussed in chapter 5.

In this chapter, the reactivity of cheap and effective transitional metal-based catalysts for the selective hydrogenation of HMF to DMF are discussed. The effect of CNT used was also studied.

4.2 Results and Discussion

In this chapter, characterization and catalytic activity of prepared catalysts from transitional metals namely, cobalt, nickel, copper and iron will be discussed and compared with the state of art. The effect of using CNT as compared to carbon on HMF hydrogenation will be discussed.

4.2.1 Characterization of Catalyst

The prepared catalysts via incipient wetness impregnation with 5 wt % metal loading (Ru/C, Ru/CNT. Ni/C, Ni/CNT, Co/C, Co/CNT, Cu/CNT, Fe/CNT) were characterised using characterization techniques such as X-ray diffraction (XRD), temperature programmed reduction (TPR), chemisorption, Transition electron microscopy (TEM) and Inductive Coupled Plasma- Optical Emission Spectroscopy, ICP-OES. The catalyst preparations are as described in experimental section (Chapter 2).

4.2.1.1 Inductive Coupled Plasma- Optical Emission Spectroscopy, ICP-OES

ICP-OES of prepared catalyst was performed to determine the actual metal loading of the catalysts. The results are shown in **Table 4.2.1**. It can be seen that all catalyst has close loading to its theoretical loading apart from Ru/C IW and Co/CNT. This could be due to experimental error while preparing this catalyst.

Table 4.2.1 ICP results of prepared Ru, Co and Ni catalysts

Entry	Catalysts	Theoretical loading (%)	ICP loading (%)
1	Ru/C IW	5	3.0
2	Ru/CNT	5	4.8
3	Co/C	5	4.8
4	Co/CNT	5	5.3
5	Ni/C	5	4.8
6	Ni/CNT	5	4.8

4.2.1.2 X-ray diffraction, XRD

Powder XRD was recorded for fresh and reduced catalysts to identify the presence of impregnated metal on the support. The XRD patterns of reduced catalysts supported on activated carbon are shown in **Figure 4.2.1**. The diffraction peaks at 20.7°, 26.6°, 45.6° and 59° can be indexed to carbon planes (220), (002) and (103) (JCPDS card 00-026-1080). For Ru/C, the diffraction peak could not be seen due to either small size of particles or good dispersion as reported in previous work. [184] For Ni/C catalyst, peaks at 44.5° and 51.8° can be indexed to Ni (111), (200) (JCPDS card 00-004-0850) while the peak at 44.2° belongs to the characteristic of Co phase (111) JCPDS card 00-015-0806). It can be seen that the peaks of Co and Ni are broader than Ru/C which means that they have bigger size particles or more amorphous than Ru.

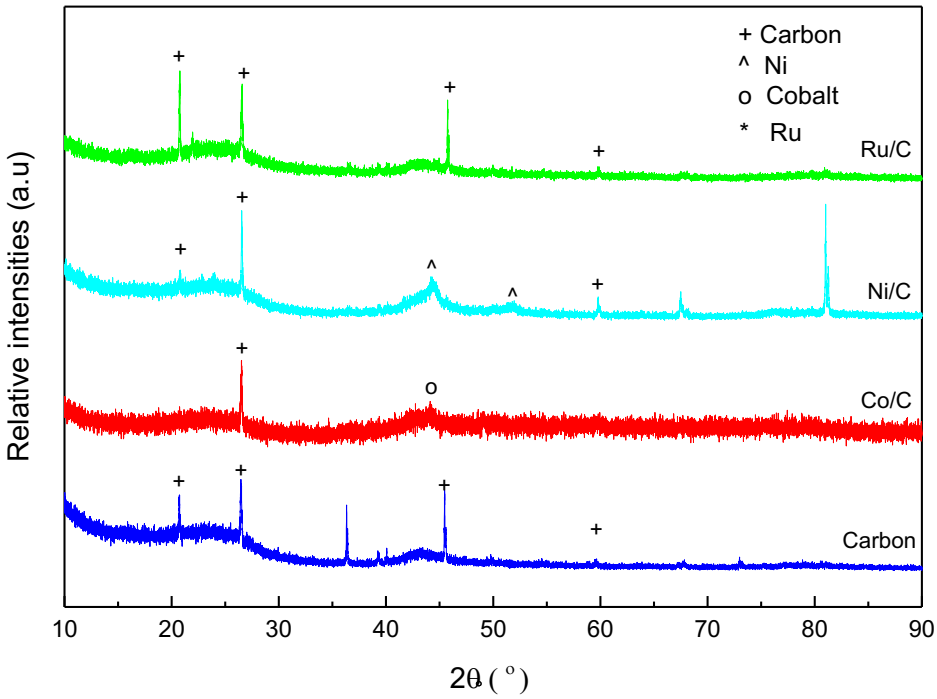

Figure 4.2.1 XRD patterns (Cu Kα radiation) for reduced carbon, 5 % Ru/C, 5 % Ni/C and 5 % Co/C.

Figure 3.2.2. shows the XRD patterns of reduced catalysts supported CNT. The diffraction peaks at 26.4° and 42.8° can be indexed to carbon (002) and (100) (JCPDS card no. 00-001-0640). For Ru/CNT the peak at 44° can be indexed to (101) plane of metallic Ru (JCPDS card no. 06-0663). There were no diffraction peaks for Co in the XRD pattern, which suggests that Co is either very small or there is too little of it. This also shows that the active component was loaded on support with high dispersion.[31, 151] Peak at 44.5° in Ni/CNT is due to the diffraction plane (111) of metallic Ni (JCPDS card no.00-004-0850) For Cu/CNT, peaks at 43.3 °, 50.4 ° and 74 ° can be indexed to (111), (200) and (220) planes of metallic Cu respectively (JCPDS card no. 00-004-0836). It can be seen that Cu peak, especially at 43.3 °, is really sharp compared to other metals, which means that Cu is either well crystalline or the particle size is bigger.[167] There was no diffraction peak of Fe present in the Fe/CNT XRD pattern which means that Fe is the either small size of particles or good dispersion.[81]

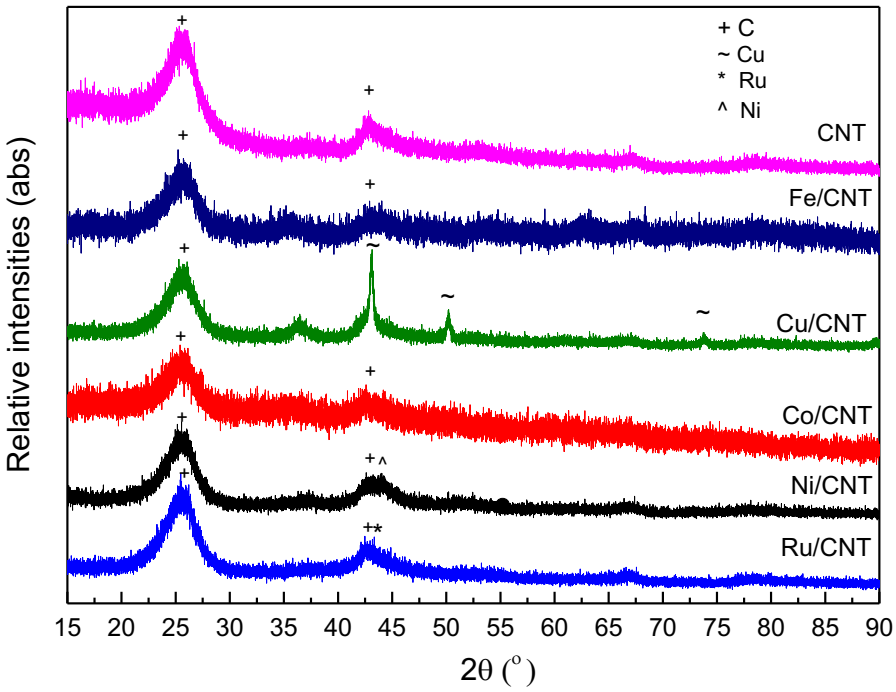

Figure 4.2.2 XRD patterns (Cu Kα radiation) for reduced carbon nanotube, 5 % Ru/CNT, 5 % Ni/CNT,5 % Co/CNT, 5 % Cu/CNT and 5 % Fe/CNT.

4.2.1.3 Temperature Programmed Reduction, TPR

Temperature programmed reduction (TPR) studies help to understand the activation of catalysts under H_2 atmosphere. **Figure 4.2.3** shows the TPR profiles for carbon supported metals catalysts. Ru/C catalyst exhibited two peaks at 100 °C and 200 °C respectively. The first peak could be due to the reduction of Ru precursor ($RuCl_3$) and later is the reduction of Ru^{3+} to Ru^{x+}.[210] It was reported that the broader peak in Ru around 500 °C to 700 °C can be attributed to carbon methanation of the support.[211]

TPR profile for Ni/C shows two main peaks, the first peak at 208 °C is due to decomposition of precursor nitrates and the second peak at 260 °C is due to the reduction of Ni^{2+} to Ni^0.[188, 212] The broad consumption peaks at high temperature (300 to 500 °C) may be ascribed to gasification of carbon atom on the support. Similarly, TPR profiles for Co/C shows two broad peaks. The first peak at ca. 162 °C is due to decomposition of Co precursor and the second peak around 300 was associated with

the reduction of Co^{2+} to Co^0.[188, 213] The broad peak between ca. 300 to 500 °C is again attributed to carbon methanation of the support as explained by the literature.[214]

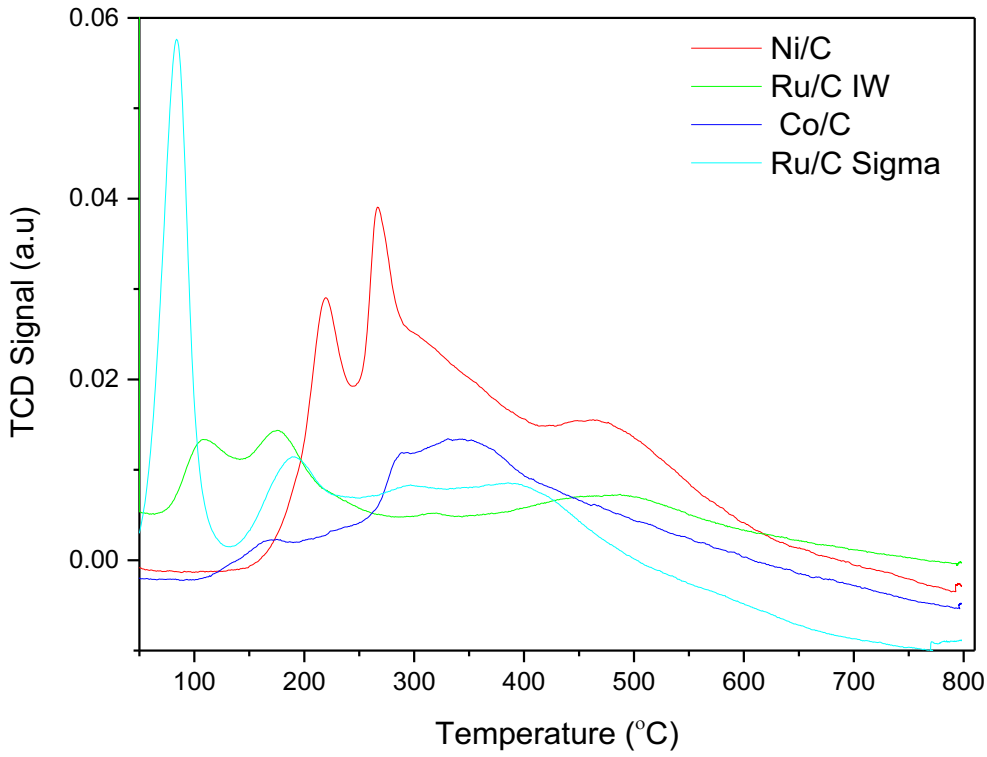

Figure 4.2.3 TPR profiles of as-synthesized 5 % wt. catalysts supported on C.

Figure 4.2.4 shows the TPR profiles of Ru, Co, Ni, Cu and Fe supported on CNT. Ru/CNT shows two main reduction peaks at ca. 110 °C and 160 °C. The first peak could be assigned to the decomposition of the ruthenium precursor ($RuCl_3$) and the later one due to Ru^{3+} to Ru^0.[188] The TPR profile for Ni/CNT shows two main peaks at 208 °C due to the decomposition of the precursor nitrates and at 240 °C due to the reduction of Ni^{2+} to Ni^0. The broad consumption peaks at high temperature (300 to 500 °C) may be ascribed to gasification of carbon atoms from the support.

Similarly, TPR profiles for Co/CNT do not show any significant differences. The peak at ca. 162 °C is due to decomposition of Co precursor and reduction of Co^{2+} to Co^0. The broad peak between ca. 300 to 500 °C again attributed to methanation of the support.[214] The reduction peaks for Ru, Ni, and Co seem to match with the literature as reported by Cerro et al. [188] It is also worth to mention that catalyst supported on

CNT have lower reduction temperatures than those supported on C. According to Tavasoli et al. who synthesised Co supported on CNT via an impregnation technique, the reduction temperature of cobalt oxide species shifted to lower temperature and enhanced the reducibility of the catalyst. The author suggested that by using CNT support interaction between cobalt surface species decreased greatly.[193] Cu/CNT show a sharp peak at 190 °C which is due to the of Cu precursor and Cu^{2+} to Cu^{0} [11] while Fe/CNT shows two peaks, at 192 °C and a broad peak at 200 to 400 °C.

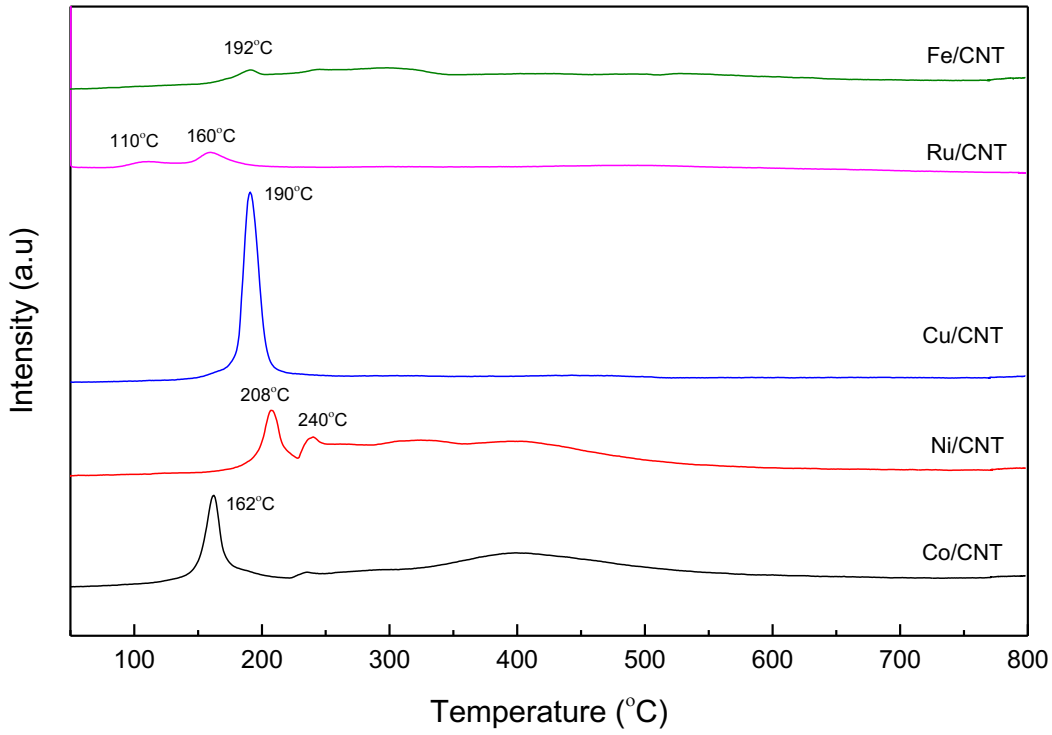

Figure 4.2.4 TPR profiles of as-synthesized 5 % wt. catalysts supported on CNT

4.2.1.4 Chemisorption

The quantification of active metal sites and the dispersion was investigated by CO chemisorption as shown in **Table 4.2.2**. Samples supported on CNT show lower CO uptake compared to the samples on carbon except for 5 % Co/C and 5 % Ni/C. The

dispersion increased as Co and Ni were supported on CNT. The same pattern was observed by Fu et al. who synthesised Co on AC and CNT. The author found that Co supported on CNT has lower H_2 uptake compared to Co on AC from chemisorption analysis.[197] It is also observed that given the high surface of carbon (553 m^2/g) compared to CNT (281 m^2/g), the dispersion of catalyst supported on CNT is actually better than on carbon. This may be due to the uniform and straight pore structure of CNT which allow better dispersion of the catalysts especially Co. This clearly shows that the combination of a high surface area and a well-defined mesoporous structure are favourable for a better dispersion.

Table 4.2.2 CO uptakes and metal dispersion, D based on CO chemisorption.

entry	Catalyst	CO chemisorption (µmol/g)	D[a] (%)
1	Ru/C sigma	21.0	4.80
2	Ru/C	66.0	13.00
3	Co/C	3.2	0.37
4	Ni/C	2.7	0.31
5	Ru/CNT	40.0	8.20
6	Co/CNT	5.1	0.60
7	Ni/CNT	12.2	1.43

[a] metal dispersion

4.2.1.5 Transmission Electron Microscopy, TEM

TEM was performed to see the morphology and also estimate the particle size of the catalysts. **Figure 4.2.5** shows the TEM images of 5 % Ni/C and 5 % Ni/CNT catalysts. Ni/C showed good distribution although there was an agglomeration of particles in some region (**Figure 4.2.5 a and b**). The average Ni particles size is 4.53± 2nm with a relatively narrow distribution ranging from 2 nm to 8 nm. Lattice measurement study did not found any Ni or NiO with an average of 1.86 Å. The reason behind this could be that Ni-C solid solution can be fluctuating solid state with the lattice parameters variable depending upon the degree of carbon incorporation as reported in the

literature.[215] **Figure 4.2.5 (c and d)** showed that Ni was decorated on the CNT with a good dispersion where most of Ni particles are located outside of the tubes. The average particle size of 5 % Ni/CNT is 4.5± 1nm nm which is close to Ni supported on carbon.

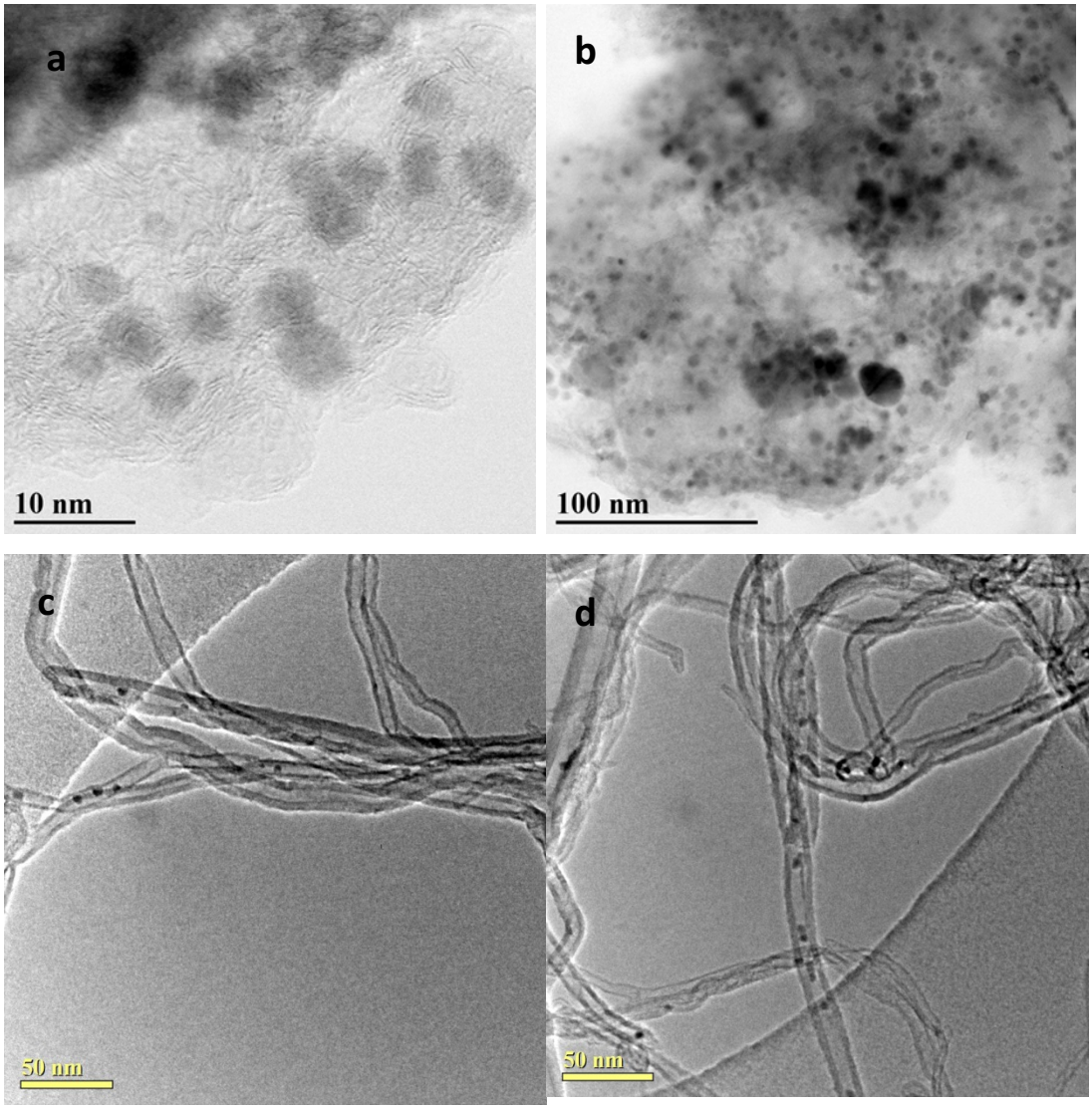

Figure 4.2.5 TEM images of reduced 5 % wt. Ni/C (a) (b) and reduced 5% wt. Ni/CNT (c) (d).

The size distributions were obtained by counting more than 200 particles and the particles size distribution of reduced Ni/C and Ni/CNT are shown in **Figure 4.2.6** (a and b). Both Ni catalysts have relatively narrow particles size distribution from 2-9 nm.

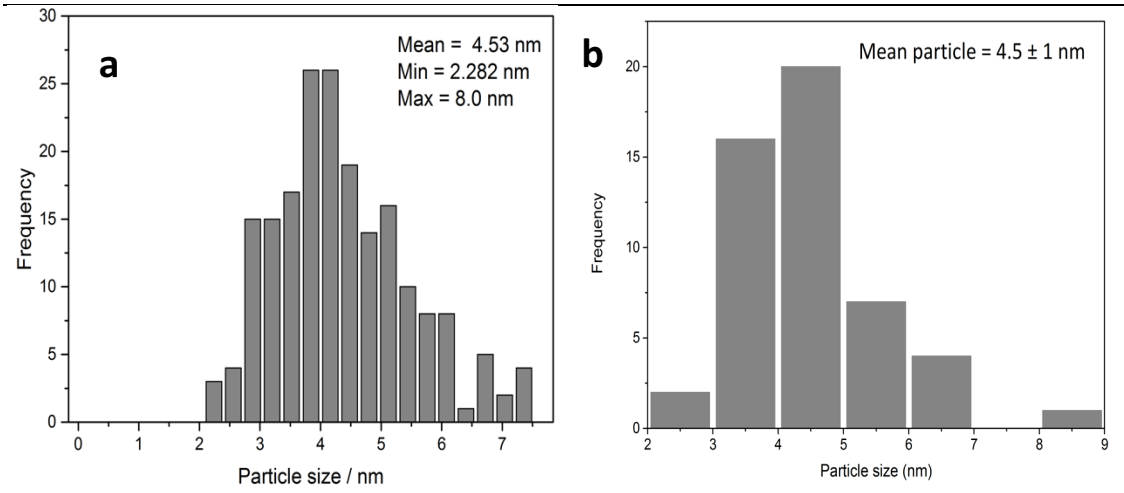

Figure 4.2.6 Particle size distribution of reduced a) 5 % wt. Ni/C and b) 5 % wt. Ni/CNT based on TEM and ca. 200 particles.

Figure 4.2.7 shows the TEM images and particle size distribution of reduced 5 wt % Co/C catalyst. Compared to 5 % Ni/C catalyst, Co has a smaller average particle size with 2.56 ± 1.7 nm. It can be seen that Co/C has a good dispersion although it appears that Co particles seem to agglomerates with a big cluster in some region. It can be seen that the particle size distribution is quite narrow with most of the particle in the range of 1-3 nm (**Figure 4.2.7 c**). The bigger particle size could be due to the agglomeration or cluster of Co.

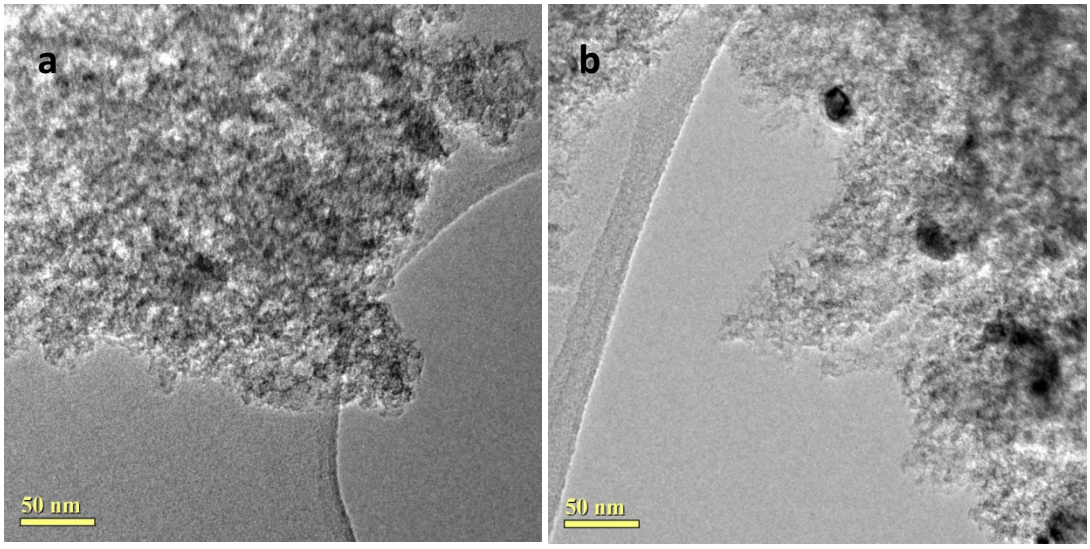

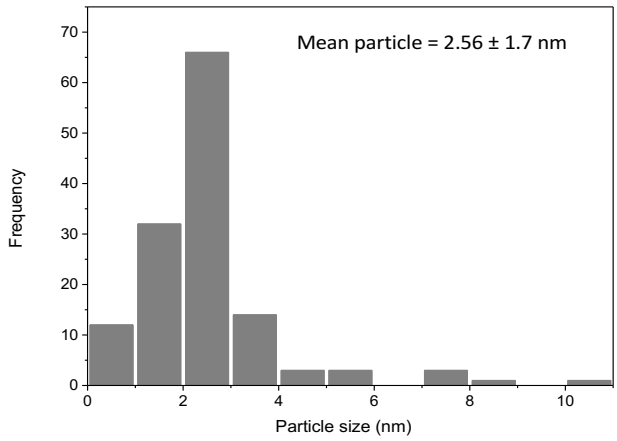

Figure 4.2.7 TEM images of-of reduced 5 % wt. Co/C (a)(b) and (c) particle size distribution based on TEM and ca. 200 particles.

4.2.2 Hydrogenation of HMF into DMF

The study of Hydrogenation of HMF to DMF using different transition metals was carried out under reaction conditions determined from the previous chapter.

4.2.2.1 Effect of Transitional metal for HMF hydrogenation

Hydrogenations of HMF to DMF have been performed with 5 % wt. metal loading catalysts Co/C, Ni/C, Cu/C and Fe/C. **Figure 4.2.8** shows the conversion of HMF for each catalyst. Surprisingly, Ru is not the most reactive in term of HMF conversion with only 50 % conversion after 6 hours, while Ni/C and Co/C have slightly better HMF conversion up to 70 % and 60 % after 6 hours. It has previously been reported that Ni and Co are good hydrogenation catalyst, however, they are not that good at hydrogenolysis. [70, 78, 80] Besides, the low HMF conversion of Ru/C IW could be due to the lower loading of Ru based on ICP-OES analysis compared to Ni/C and Co/C. (**Table 4.2.1**). Nevertheless, Ru/C exhibited the highest TOF (based on moles of metal) with 3.74 h^{-1} compared to Ni/C (0.78 h^{-1}) and Co/C (0.21h^{-1}).

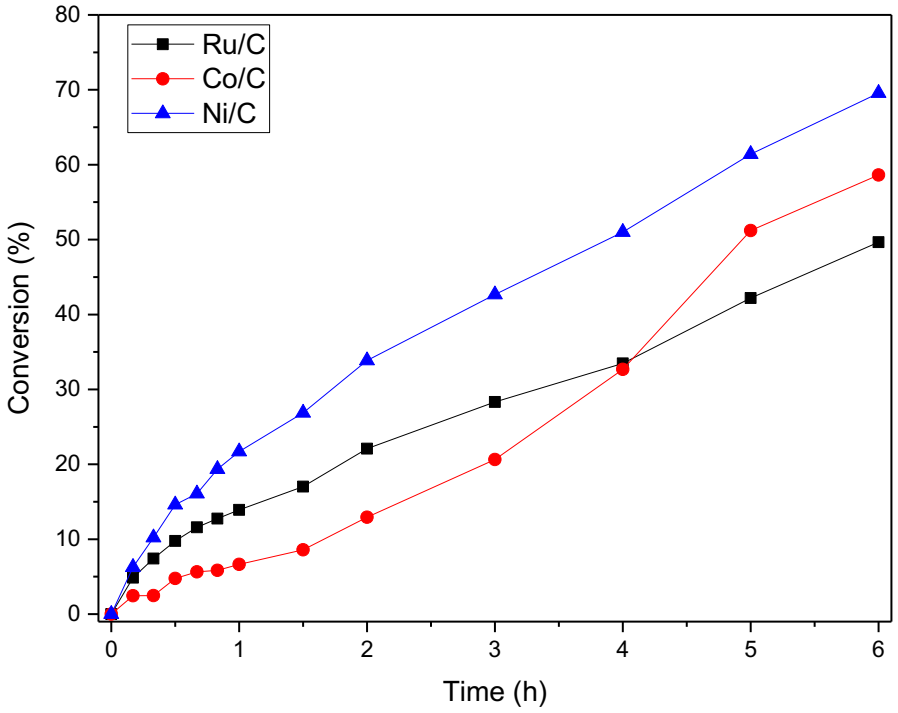

Figure 4.2.8 Conversion of HMF with the carbon supported catalyst of 5 % Ru/C, 5 % Co/C and 5 % Ni/C. Reaction conditions: HMF, 40 mM; catalyst, 60 mg; solvent, Dioxane; pressure, 20 bar H_2; stirring, 1100 rpm.

Nevertheless, as shown in **Figure 4.2.9** 5 % wt Ru/C showed the best DMF yield with 33 % followed by 5 % wt. Ni/C with 19 %. 5 % wt. Co/C showed low DMF yield with only 5% after 6 hours. This demonstrated that Ru is good at hydrogenolysis of HMF compared to Ni and Co.[17, 64, 216, 217] In addition, TEM analysis revealed that Ru exhibited smaller particle sizes compared to Co and Ni with 1.8 nm, 2.5 nm, and 4.53 nm respectively. Furthermore, CO chemisorption studies revealed that Ru has better dispersion than Ni and Co thus providing more active sites for the reaction to occur (**Table 4.2.2**).

The previous study on HMF hydrogenation with Co seems to agree with our finding where Co is relatively efficient in hydrogenating HMF however it is not good in converting HMF into DMF. Previous work by Chen et al. found that Co supported on activated carbon resulted in low selectivity toward DMF although total hydrogenation of HMF was achieved after 8 hours of reaction time. It was speculated that although Co/AC already reduced under hydrogen at 400 °C prior to the reaction, it is difficult to keep the reduced cobalt species from being oxidized. [78]

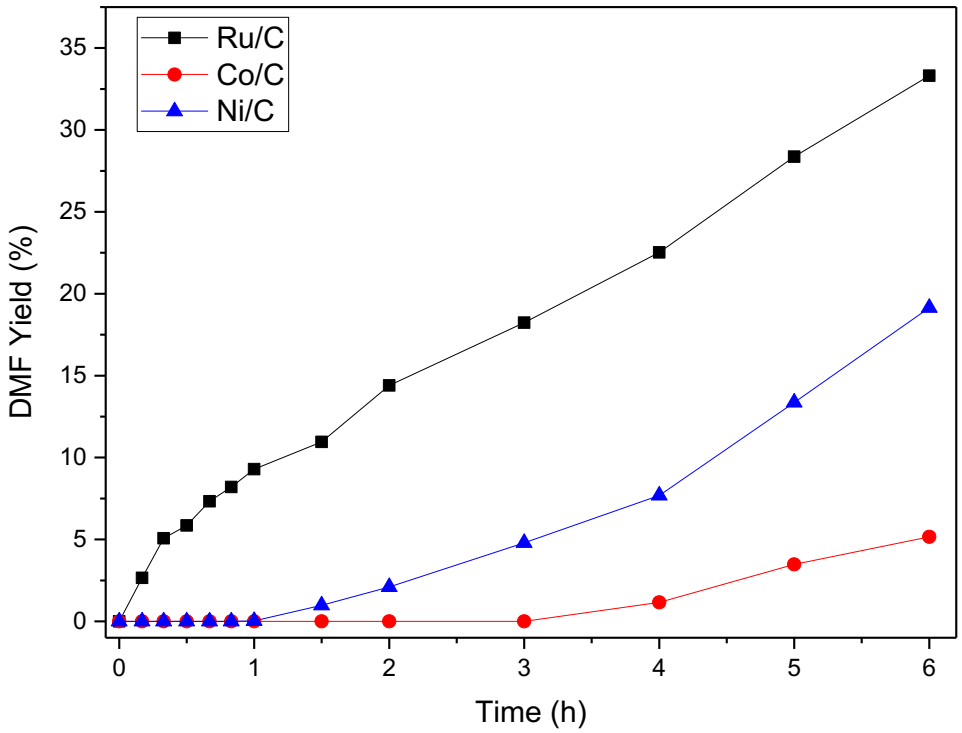

Figure 4.2.9 DMF yield with the various monometallic catalyst of 5 % Ru/C, 5 % Co/C and 5 % Ni/C at 150 °C. Reaction conditions: HMF, 40 mM; catalyst, 60 mg; solvent, Dioxane; pressure, 20 bar; stirring, 1100 rpm.

Figure 4.2.10 shows the product distribution of HMF hydrogenation with 5 % Co/C catalyst. It can be seen that DHMF is the main product with the highest yield, (47 %) followed by MFA (6 %) and DMF (5 %). This shows that Co is not as active as Ru as it may take longer reaction time to convert all intermediate products into DMF. Previous work by Chen et al. reported that total HMF conversion was achieved with Co/AC at higher reaction temperature, 180 °C, 50 bar H_2 and 8 hours of reaction time. However, DMF yield remains low.[78] This indicated that Co/C is good at hydrogenating HMF but not that good in hydrogenolysing the hydroxyl group to further converting DHMF to MFA and DMF compared to Ru.

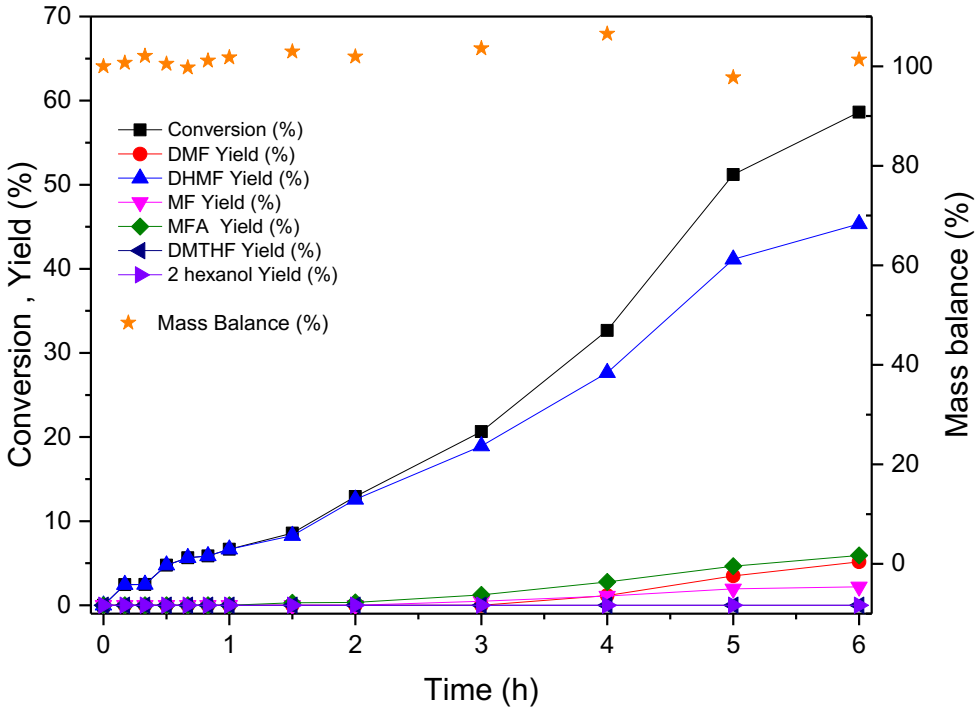

Figure 4.2.10 Time online reaction of HMF hydrogenation with 5 % Co/C at 150 °C. Reaction conditions: HMF, 40 mM; catalyst, 60 mg; solvent, Dioxane; pressure, 20 bar H_2; stirring, 1100 rpm.

Compared to 5 % wt. Co/C, 5 % wt. Ni/C demonstrated slightly faster reaction as shown in **Figure 4.2.11**. After 4 hours, DMF yield increased to 19 % while DHMF yield is 46 % followed by 7 % yield of MFA. It can be seen that DHMF yield started to reach a plateau with the increment of MFA and DMF in 5 hours of reaction time. Longer reaction time will further convert DHMF and MFA into DMF. The initial reaction rates of Ni (120 h^{-1}) is 4-5 times more active than Co (26 h^{-1}) at iso-conversion of 30 %.This demonstrated that Ni is better than Co in hydrogenolyse HMF to MFA and DMF. However, Ru is still better than Ni and Co in converting HMF to DMF. The previous study by Luo et al. showed that Ni supported on carbon exhibited relatively low selectivity for DMF along with Pt while Zn and Cu catalysts were not active.[80]

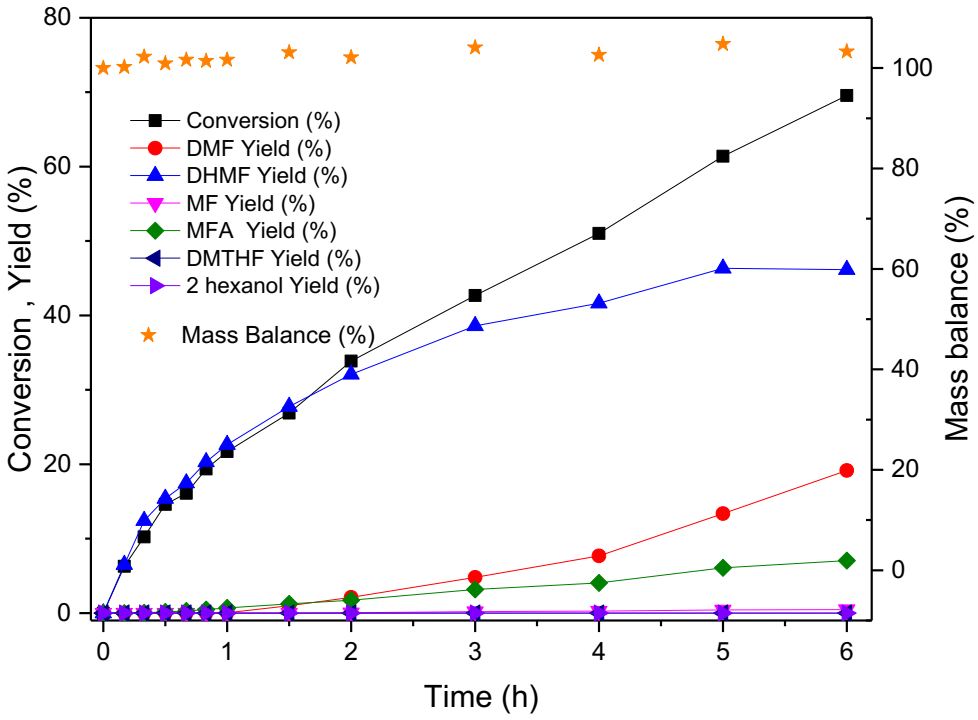

Figure 4.2.11 Time online reaction of HMF hydrogenation with 5 % Ni/C at 150 °C. Reaction conditions: HMF, 40 mM; catalyst, 60 mg; solvent, Dioxane; pressure, 20 bar H_2; stirring, 1100 rpm.

4.2.2.2 Effect of the support

As shown in the previous chapter (Chapter 3), CNT enhanced the reactivity of Ru catalyst when it was used as the support compared to carbon. Thus the effect of CNT on transitional metals, (Ni, Co, Cu, and Fe) have also been studied using the same metal loading (5 %) synthesised via incipient wetness impregnation. The result of the tests is shown in **Figure 4.2.12**.

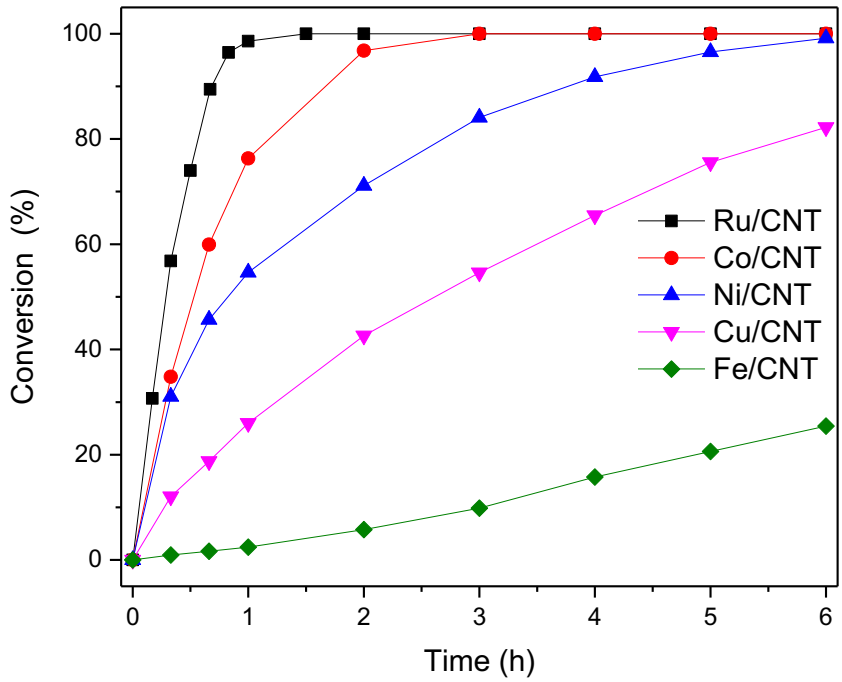

Figure 4.2.12 DMF yield with the various monometallic catalyst of 5 % Ru/C, 5 % Co/C and 5 % Ni/C at 150 °C. Reaction conditions: HMF, 40 mM; catalyst, 60 mg; solvent, Dioxane; pressure, 20 bar H_2; stirring, 1100 rpm.

Surprisingly, the same effects as Ru were observed with Co and Ni as depict in **Figure 4.2.13**. Both of HMF conversion and DMF yield were significantly improved compared to catalysts supported on carbon. This could be attributed to the electronic effect of CNT derived from the curvature shape of CNT. This consequently enhanced the electron density of metal thus improving the adsorption of C=O bonds resulting in higher reactivity. [120] However, Ru still being the most active one with 100 % HMF conversion in 1.5 hours followed by Co, Ni, Cu, and iron. This could be due to a smaller particle size of Ru compared to Ni and Co as confirmed by TEM. Both Co and Ni reached 100 % HMF conversion in 3 and 6 hours respectively while Cu and Fe just reached 80 % and 25 % after 6 hours of reaction time. This is still a lot better than when carbon was used as the support, so it confirms the activity of Fe for this reaction.

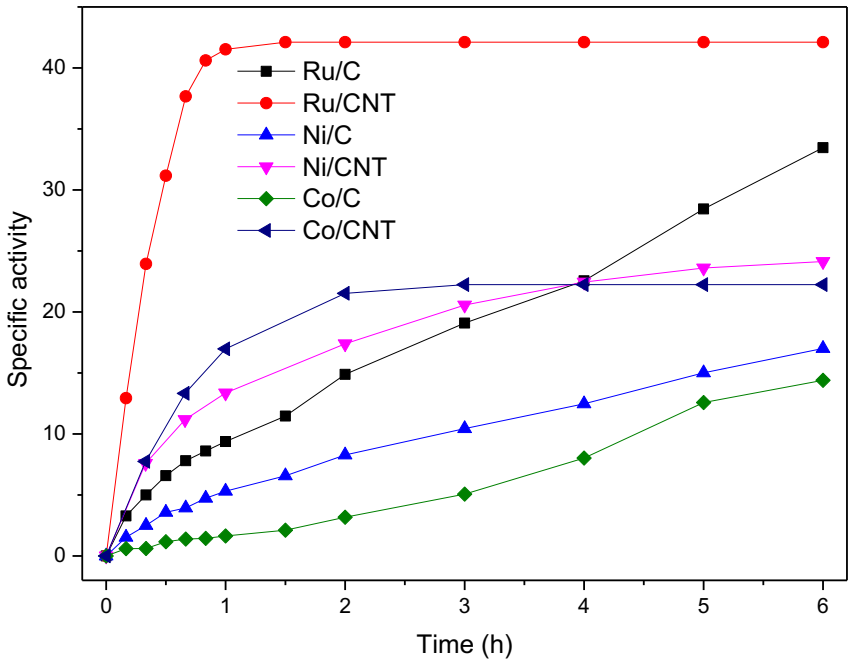

Figure 4.2.13 The effect of support on the specific activity of HMF hydrogenation over Ru, NI and Co supported on carbon and CNT at 150 °C Reaction conditions: HMF, 40 mM; catalyst, 60 mg; solvent, Dioxane; pressure, 20 bar H_2; stirring, 1100 rpm.

The same trends were observed with DMF yield as shown in **Figure 4.2.14**. The highest DMF yield obtained with Ru/CNT in 1 hour of reaction time before it started to decrease as the formation of ring hydrogenation and ring opening products. However, for Co and Ni, there were steady increments of DMF yield. In the beginning, Ni has better DMF yield than Co, but after 3 hours Co surpasses Ni with maximum DMF yield of 82 % after 6 hours followed by Ni, Cu, and Fe with DMF yield of 60 %, 10 %, and 5.9 % respectively.

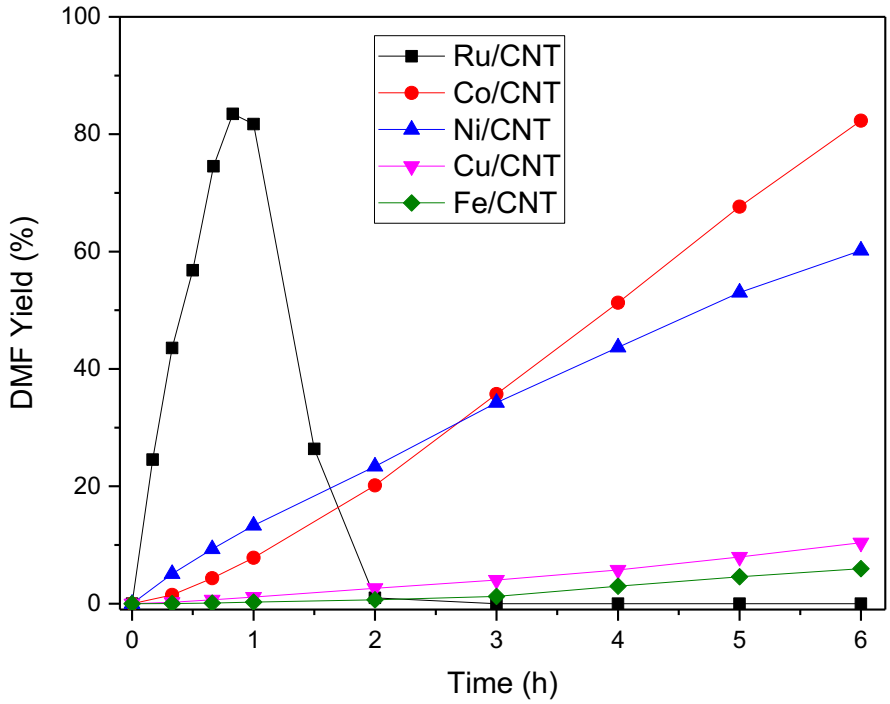

Figure 4.2.14 DMF yield with the various monometallic catalyst of 5 % Ru/C, 5 % Co/C and 5 % Ni/C at 150 °C. Reaction conditions: HMF, 40 mM; catalyst, 60 mg; solvent, Dioxane; pressure, 20 bar H_2; stirring, 1100 rpm.

Product distribution from the time online, TOL reaction with 5 % Co/CNT is shown in **Figure 4.2.15**. It can be seen that HMF was totally converted in 3 hours and DMF is steadily formed as HMF is converted into DHMF and MFA. However, in the beginning, it can be seen that DHMF yield is high up to 63 % before it sharply decreased around 2 hours followed by decreasing of MFA yield at 3 hours. This led to a high yield of DMF with 82 % yield after 6 hours of reaction. There was no ring hydrogenation as well as ring opening products were formed, which is desirable for high yield of DMF.

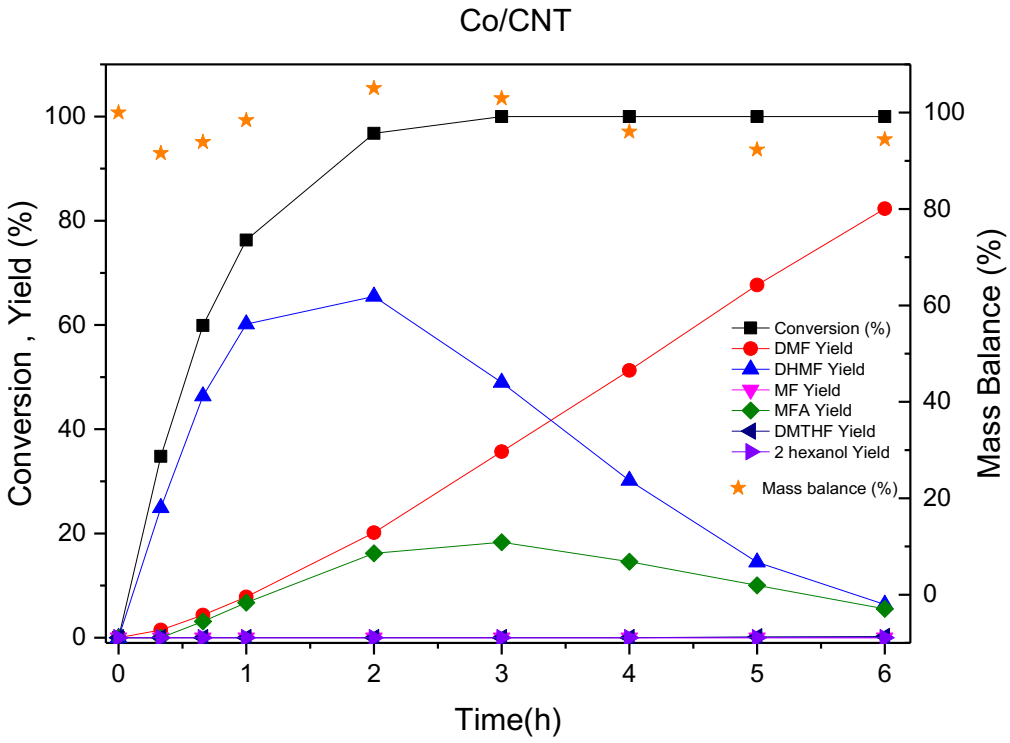

Figure 4.2.15 Time online reaction of HMF hydrogenation with 5 % Co/CNT at 150 °C. Reaction conditions: HMF, 40 mM; catalyst, 60 mg; solvent, Dioxane; H_2 pressure ; 20 bar; stirring, 1100 rpm.

The performance of 5 % Ni/CNT is similar to Co/CNT as shown in **Figure 4.2.16**. It can be seen that HMF is fully converted in 6 hours with 60 % yield of DMF, 18 % of DHMF and 7 % of MFA. DHMF and MFA appear to be more difficult to convert to DMF as compared to 5 % Co/CNT. Longer reaction times would result in higher DMF yield as more DHMF and MFA will be converted into DMF. Similar work on HMF hydrogenation with Ni/CNT shows a similar result, although the reaction conditions were harsh and the metal loading was higher (10 wt %) compared to ours.[81] The reaction was performed at 200 °C in n-butanol, 30 bar H_2 for 3 hours and product selectivity obtained are 46 % DMF, 13 % DHMF, 10 % MFA, 7.9 % DMTHF and 22 % mainly contained a mixture of ethers, decarbonylation product, ring opening product and humin.

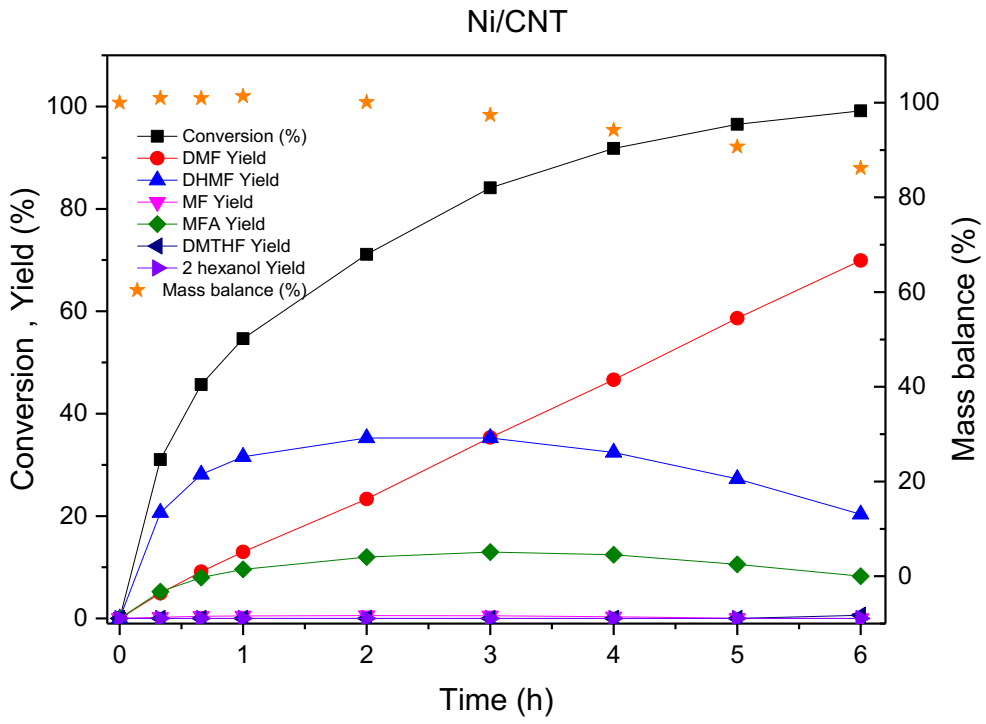

Figure 4.2.16 Time online reaction of HMF hydrogenation with 5 % Ni/CNT at 150 °C. Reaction conditions: HMF, 40 mM; catalyst, 60 mg; solvent, Dioxane; H_2 pressure ; 20 bar ; stirring, 1100 rpm.

5 % wt. loading of Cu/CNT and Fe/CNT are the least reactive catalysts compared to 5 % wt. loading of Ru/CNT, Co/CNT, and Ni/CNT. Nevertheless, they are still showing some DMF conversion, which is better than Cu and Fe supported on C based on the previous trend. **Figure 4.2.17** shows the product distribution from the TOL reaction of 5 % wt. Cu/CNT. After 6 hours of reaction time, 80 % of HMF was converted, DHMF being the main product with 65 % yield followed by DMF with 10 % yield and finally MFA with 5 % yield. Longer reaction time would result in higher DMF yield as more DHMF and MFA will be converted into DMF, highlighting that the most sustainable and abundant of the transition metals is also able to catalyse this reaction.

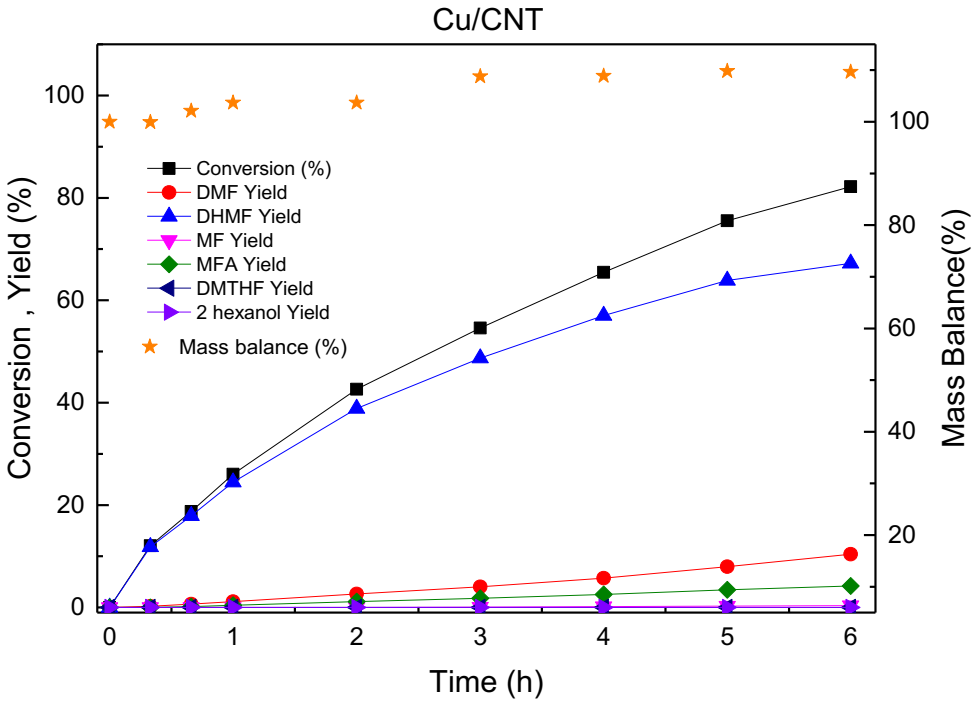

Figure 4.2.17 Time online reaction of HMF hydrogenation with 5 % Cu/CNT at 150 °C. Reaction conditions: HMF, 40 mM; catalyst, 60 mg; solvent, Dioxane; H_2 pressure ; 20 bar ; stirring, 1100 rpm.

Figure 4.2.18 shows the product distribution from the TOL reaction with 5 % wt. Fe/CNT. It can be seen that, after 6 hours, only 22 % of HMF were converted with DHMF being the main product with 18 % yield. This followed by DMF and MFA with a yield of 5 and 2 % respectively. Similar work on HMF hydrogenation with Fe/CNT by Yu et al. showed relatively similar result if not better, although the reaction conditions were harsh compared to ours.[81] The reaction was performed at 200 °C in n-butanol, 30 bar H_2 for 3 hours and the HMF conversion was only 3.2 %. The product selectivity obtained are as follow with DHMF being the main product with 31 % of selectivity and the remaining of 69 % mainly contained a mixture of ethers, decarbonylation product, ring opening product and humin.

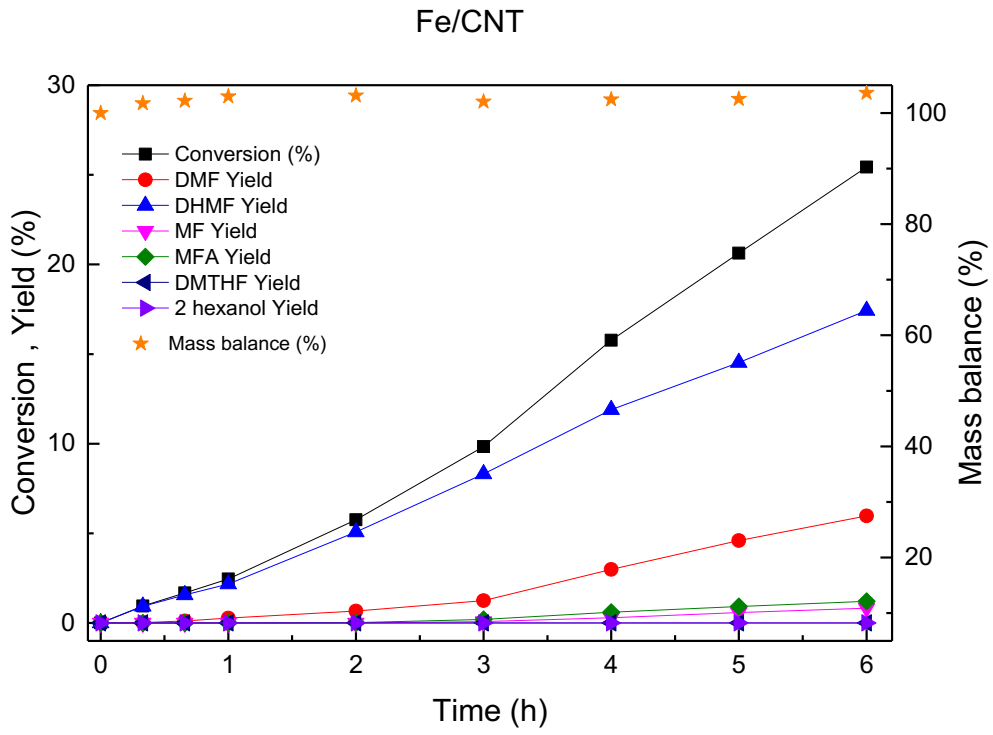

Figure 4.2.18 Time online reaction of HMF hydrogenation with 5 % Fe/CNT at 150 °C. Reaction conditions: HMF, 40 mM; catalyst, 60 mg; solvent, Dioxane; H_2 pressure ; 20 bar ; stirring, 1100 rpm.

Table 4.2.3 summarises the catalytic activity of Co, Ni, Cu and Fe catalysts supported on C and CNT as well as TOF (specific DMF yield at maximum), particle size based on TEM and dispersion from CO chemisorption. It was observed that the HMF conversion and DMF yield are independent on the particle size and most likely structural sensitive. The complex hydrogenolysis reaction appears to need larger or specific aggregates of atoms as their active centres. The TOF comparison with the particles size shows a variation which is a characteristic to the structure sensitive based in the theory of active centre by H.S. Taylor.[218] This is in agreement with the finding from Nakagawa et al.[148] and Ohyama et al. [107] For example, although Co/C has lower particle size than Ni/C, Ni demonstrated higher HMF conversion and DMF yield as well as the TOF. However, for the effect of CNT as the support, a clear improvement in the conversion of HMF can be seen. The faster conversion, in this case, leads to a higher yield of DMF as the intermediates product such as DMHF and MFA are converted to

DMF. One can speculate that some other factors such as metal dispersion, the surface structure of a catalyst and peculiar metal electronic effect of each metal would also contribute to this trend.[92] There are two ways in which the surface structure of catalyst can influence the stability of reaction intermediates and the activation energy of an elementary surface chemical reaction. One effect is entirely electronic and the other effect is purely geometrical as discussed in chapter 1.

Table 4.2.3 HMF conversion, DMF yield, TOF and particle size of catalysts supported on carbon and CNT.

catalyst	HMF conversion (%)	DMF yield (%)	TOF (h^{-1})[a]	TOF (h^{-1})[b]	Particle size (nm)[c]	Dispersion, %
Co/C	59	5.28	66	0.2	2.56 ±1.7	0.37
Ni/C	70	19.00	286	0.9	4.53 ±2	0.31
Co/CNT	100	82.30	648	3.1	N/A	0.60
Ni /CNT	100	60.18	197	2.5	4.50 ±1	1.43
Cu/CNT	82	11.63	N/A	N/A	N/A	N/A
Fe/CNT	25	6.82	N/A	N/A	N/A	N/A

Reaction conditions: 30 ml 40 mM HMF; catalyst, 60 mg; solvent, Dioxane; pressure, 20 bar; stirring, 1100 rpm. Reaction time 6 hrs. [a] TOF of maximum DMF yield based on CO chemisorption [b] TOF based on mole of metal .[c] particle size based on TEM. Experimental errors (conversion and yield = ± 0.07 %, TOF [a] = ± 0.05).

The lower yield of DMF is normally the consequence of partial hydrogenation of HMF resulting in DHMF which is the DMF intermediate and not the result of unwanted side reactions. This can be observed in the case of Co/C, Ni/C, Cu/CNT and Fe/CNT. A high yield of DMF is contributed to the hydrogenolysis of the intermediate compounds like DHMF and MFA to DMF which are strongly dependent on the employed metal. In the case of metal supported on Fe_2O_3, Pd was more active in further hydrogenolysis to DMF than Cu and Ni due to the strong metal-support interaction which favours the C-O cleavage reactions.[71]

4.3 Conclusions

As a continuation from the previous chapter, hydrogenation of HMF to DMF with transitional metals namely Co, Ni, Cu and Fe catalyst supported on carbon was investigated under optimum reaction conditions as determined in Chapter 3. The effect of CNT as a support was also investigated. Incipient wetness impregnation techniques were employed in the catalysts preparation.

It was discovered that among transitional metals catalyst supported on carbon, Ni shows a good reactivity in converting HMF with 70 % conversion after 6 hours followed by Co/C with 60 % conversion. It was better than 5% Ru/C which has 50 % HMF conversion, however, the high conversion did not translate into a high yield of DMF as both Ni/C and Co/C produced higher DHMF as opposed to DMF. This could mean that Ni and Co are not as good as Ru in hydrogenolyse the hydroxyl group in order to get to DMF. The reason behind this could be attributed to the particles sizes as determined by TEM and the metal dispersion from CO chemisorption analysis which affect the product selectivity by influencing the adsorption behaviour of the substrate.

The same trends as for Ru were observed when CNT was used as the support for Co, Ni, Cu and Fe. All catalysts displayed a significant improvement in HMF conversion as well as DMF yield. This could be attributed to the electronic effect of CNT which enhanced the electron density of metal thus improving the adsorption of C=O bond resulting in slightly higher reactivity. As opposed to Co/C, Co/CNT shows the best reactivity in HMF conversion and DMF yield compared to Ni/CNT. These were followed by Cu/CNT and Fe/CNT. The overall reactivity of the metals could be ranked as followed; Co>Ni >Cu>Fe.

Chapter 5 HMF hydrogenation over Ru-Co and Ru-Ni bimetallic catalyst

5.1 Introduction

Bimetallic nanoparticle have received a lot of attention in catalytic studies, for example selective oxidation of alcohol,[149] glycerol,[219] glucose,[220] and HMF [221], Fischer-Tropsch for the synthesis of hydrocarbon C_5 and above [150] or hydrogenation reactions of aromatic [151, 222] and biomass derived substrate . This is due to the positive synergistic effect that can be found between two metals and the ability to tune the selectivity of the catalyst.

The synergistic effects typically found are normally derived by the alloying of the metals. The changes in the catalytic properties can be associated with changes in the electronic properties of the active components in the alloy, in addition to the influence of geometrical effects or with a combination of these effects.[223] For instance in benzene hydrogenation, Yoon et al. [153] have synthesized bimetallic Pd-Rh/CNT via a microemulsion method that exhibited higher TOFs when compared to the monometallic catalysts. The enhanced activity was attributed to the alloying effect between these two catalysts. Another example was shown by Zhu et al., Ru-Ni/C (0.024 wt % Ru, 1 wt % Ni) showed the highest TOF for hydrogenation of benzene compared to monometallic Ni/C and Ru/C. [151] It was also speculated that the additional metals can improve the size and the morphology of active particles as well as the catalysts selectivity.[154]

Besides improving the reactivity of the reaction, the bimetallic system also can help in reducing the dependence on noble metal by incorporating transition metal such as Ni and Co. Not only they are cheaper but in certain molar ratios, they could result in better reactivity than the noble metals itself. [156]

As for HMF hydrogenation, Dumesic et al.[17] developed a carbon-supported copper-ruthenium (CuRu/C) catalyst as an alternative catalyst from the previously used CuCro4 catalyst that showed a moderate yield of DMF. They found that bimetallic catalyst CuRu/C showed better performance in the hydrogenolysis reaction compared yielding 76-79 % DMF. Following their work DMF received a lot of attention. Huang et al.[70] exploited nickel based catalysts with another Lewis acid site that possess deoxygenation ability in order to improve DMF selectivity. 96 % yield of DMF was achieved over nickel tungsten carbide catalyst on active carbon (Ni-W_2C/AC) at 180 °C

and 40 bar of H_2. Nevertheless, a high loading of tungsten carbide was used. Recently Chen et al. demonstrated that carbon coated Cu-Co bimetallic nanoparticles showed an excellent performance in selective hydrogenolysis of HMF to DMF with 99.4 % yield of DMF at 180 °C, 50 bar H_2 in 8 hrs. [78] XPS analysis revealed that the coexistence of cobalt oxide species was responsible for the synergistic effect between cobalt species and copper. Luo et al. reported that (10 wt. %) Pt-Ni alloyed nanocrystals supported on carbon with ratio 3:1 exhibited high yield of DMF compared to other compositions and respective monometallic catalysts. [80] It was suggested the optimal composition of Pt-Ni attributed to the high yield of DMF. High yield of the mixture of both DMF and DMTHF was also obtained when Cu-Zn nanoalloyed was used in HMF hydrogenation as demonstrated by Giovanni et al.[83] The author proposed that the synergistic effect between active Cu^0 sites with Lewis acidic ZnO sites was responsible for the high reactivity.[157] Ni-Fe/CNT (10 % wt.) also displayed high selectivity towards DMF and DHMF depending on the temperature. This was attributed to the formation of Ni-Fe alloy species that were beneficial for the C-O bond cleavage. [81]

In this chapter, the effect of Ru-Co and Ru-Ni supported on C with different molar ratios were investigated and the best metal compositions of these two metals were then supported on CNT to study the effect of support used.

5.2 Results and Discussion

Results of characterization of the prepared bimetallic catalysts as well as the hydrogenation tests will be discussed in this subchapter.

5.2.1 Characterization of catalysts

The prepared bimetallic catalysts were characterised using X-ray diffraction (XRD), temperature programmed reduction (TPR), chemisorption, transmission electron microscopy (TEM) and Inductive Coupled Plasma- Optical Emission Spectroscopy, ICP-OES.

5.2.1.1 Inductive Coupled Plasma- Optical Emission Spectroscopy, ICP-OES

Inductive Coupled Plasma- Optical Emission Spectroscopy, ICP-OES was performed on the samples to determine the real metal loading of prepared catalysts. The results are

shown in **Table 5.2.1**. We realised that the actual loading is lower than theoretically expected loading as used in the synthesis. We attempted a synthesis to produce catalysts with 5 wt % loading in all cases, but the loading of Ru is much lower. It is possible that that Ru was not fully digested and the solution used to impregnate the catalysts was consistently diluted for all the synthesis; whereas Co and Ni loading was quite close to the theoretical loading. In this chapter, we will use the experimental loadings and metal ratios obtained by ICP.

Table 5.2.1 ICP-OES results of prepared bimetallic catalysts.

Entry	Catalyst Label[a]	Theoretical ratio Ru:M	ICP loading (%)			
			Total	Ru	Co	Ni
1	3.6 % RuCo/C 1:1	2:1	3.6	1.8	1.8	0
2	3.4 % RuCo/C 1:3	1:1	3.4	0.8	2.6	0
3	3.5 % RuCo/C 1:5	1:2	3.5	0.6	2.9	0
4	3.4 % RuNi/C 1:1	2:1	3.4	1.8	0	1.6
5	3.2 % RuNi/C 1:3	1:1	3.2	0.7	0	2.4
6	3.6 % RuNi/C 1:8	1:2	3.6	0.4	0	3.2
7	4.2 % RuCo/CNT 1:20	1:2	4.2	0.2	4	0
8	3.4 % RuNi/CNT 1:3	1:1	3.4	0.8	0	2.6

[a]Catalysts are labelled using the total metal content as a wt % and Ru:M as measured by ICP.

5.2.1.2 X-ray diffraction, XRD

Figure 5.2.1 and **Figure 5.2.2** show the XRD patterns of synthesised bimetallic RuCo/C and RuNi/C catalysts. As revealed, diffraction peaks at 20.8°, 26.6°, 46°, 50.3° and 59° can be indexed to carbon which is matched with JCPDS no 00-022-1069. As for reduced bimetallic catalysts, as the molar ratio of Ru increased there could be seen the presence of sharp Ru diffraction peak at 44.3° and RuO_2 peaks at 54.3° matched with JCPDS no 00-006-0663. On the other hand, as the molar ratio of Co increased, there

could be seen the presence of CoO peak at 38.5° matched with JCPDS no 01-080-1532 in all RuCo/C catalysts. As for RuCo/C 1:1 there is an ambiguous peak at 43.6° with a d-spacing value of 2.07 Å which is lower than d-spacing of Ru (2.14 Å). This could be the result of Co being incorporated into Ru face-centred cubic, FCC structure which resulted in the shift of Ru peak at 42.15° to a higher angle during alloying with a concomitant lattice contraction.[68] This is in agreement with previous literature by Park et al. who demonstrated the alloying of Pt/Ru/Ni.[224] This could explain the difference of this catalyst in reactivity compared to the monometallic catalyst. Apart from that, the absence of Co and Ru peaks could be due to small particle size and good distribution of these metals on carbon. [184]

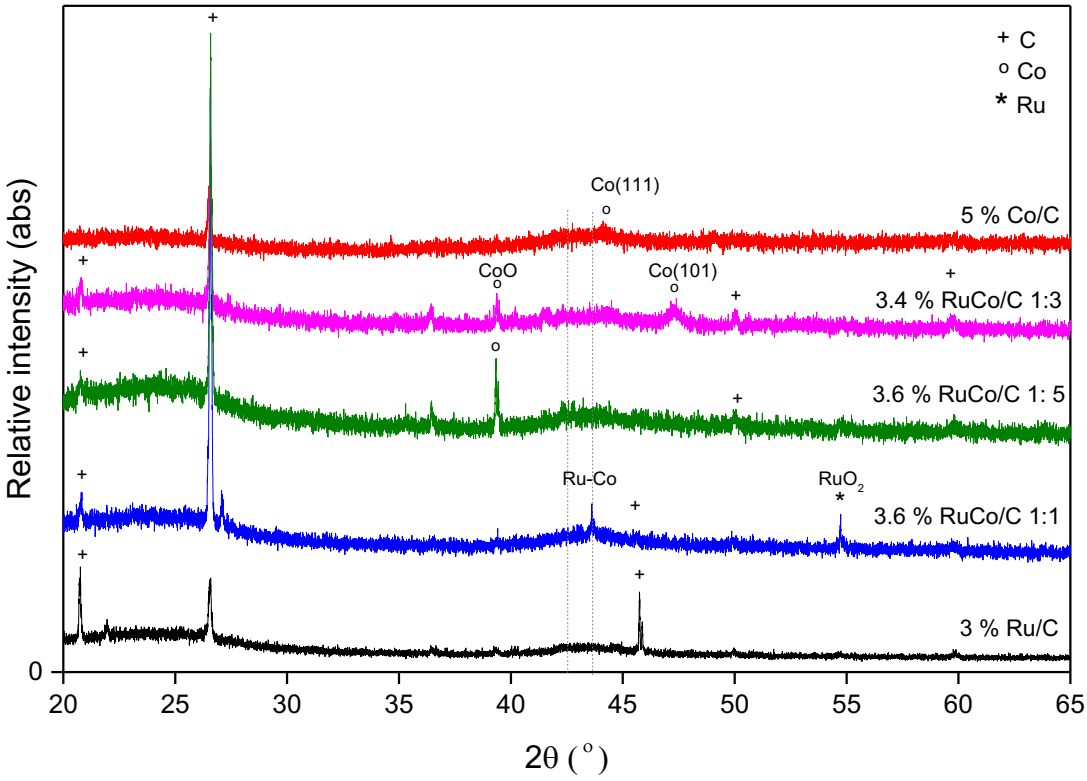

Figure 5.2.1 XRD patterns (Cu Kα radiation) for reduced 5 % Ru/C, 3.5 % RuCo/C 1:5, 3.4 % RuCo/C 1:8, 3.6 % RuCo/C 1:1 and 5 % Co/C.

As for Ru-Ni bimetallic catalysts, diffraction peaks at 20.8°, 26.6°, 36.4°, 50.3° and 60° can be indexed to carbon which is matched with JCPDS no 00-022-1069. The diffraction peak of Ni can be seen at 39.1° (matched with JCPDS no 00-045-1027) for most of Ni bimetallic catalysts. It can be seen that there was a shift of diffraction to a higher angle

which indicated the formation of the alloy as previously reported in the literature.[224, 225] Diffraction peak of Ru can be seen at 42.4° (JCPDS no 00-066-0663) on both RuNi/C 1:1 and RuNi/C 1:8. This could mean that Ru is not well distributed or bigger in size on carbon at these molar ratios.

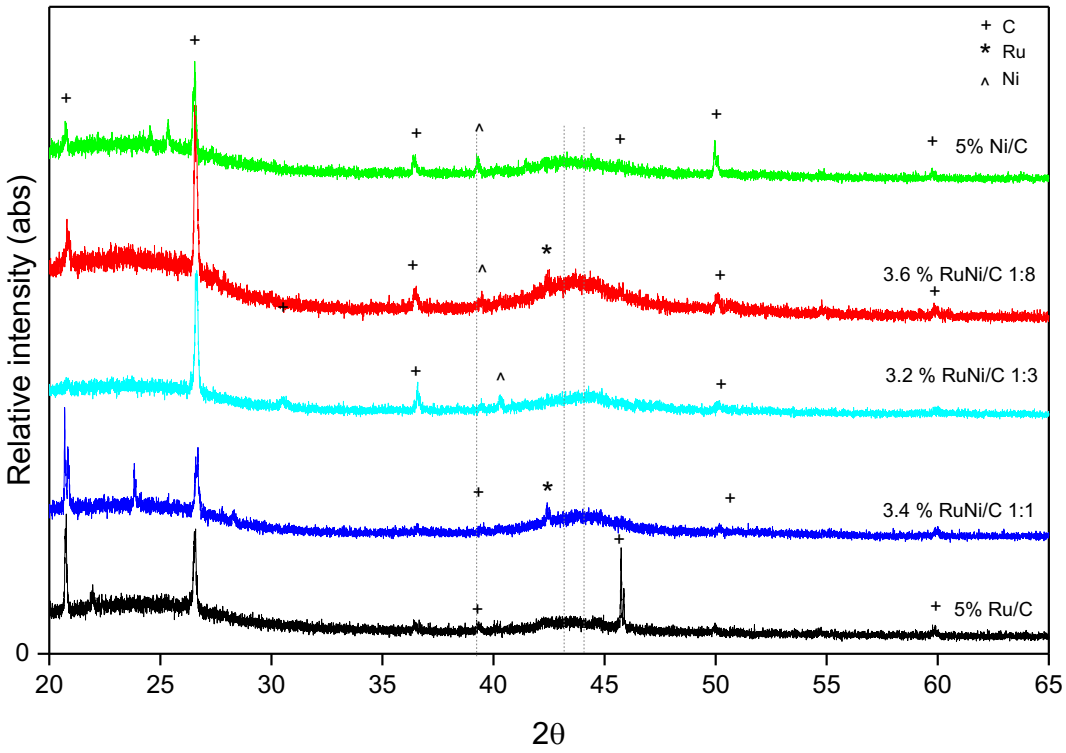

Figure 5.2.2 XRD patterns (Cu Kα radiation) for reduced 5 % Ru/C, 3.6 % RuNi/C 1:8, 3.2 % RuNi/C 1:3 , 3.4 % RuNi/C 1:1 and 5 % Co/C.

The XRD patterns of Ru, Co and Ni mono and bimetallic samples supported on CNT are shown in **Figure 5.2.3**. The diffraction peaks at 26.4° and 42.8° can be indexed to carbon (002) and (100) (JCPDS 00-00600663). Despite the reasonable overall metal loadings of 5-3.4wt%, there were no diffraction peaks due to the metals or their oxides, which suggest that Ru, Ni, and Co are either too small to be detected or in an amorphous phase. This also suggests that the active metals were loaded on the support with high dispersion.[31, 151]

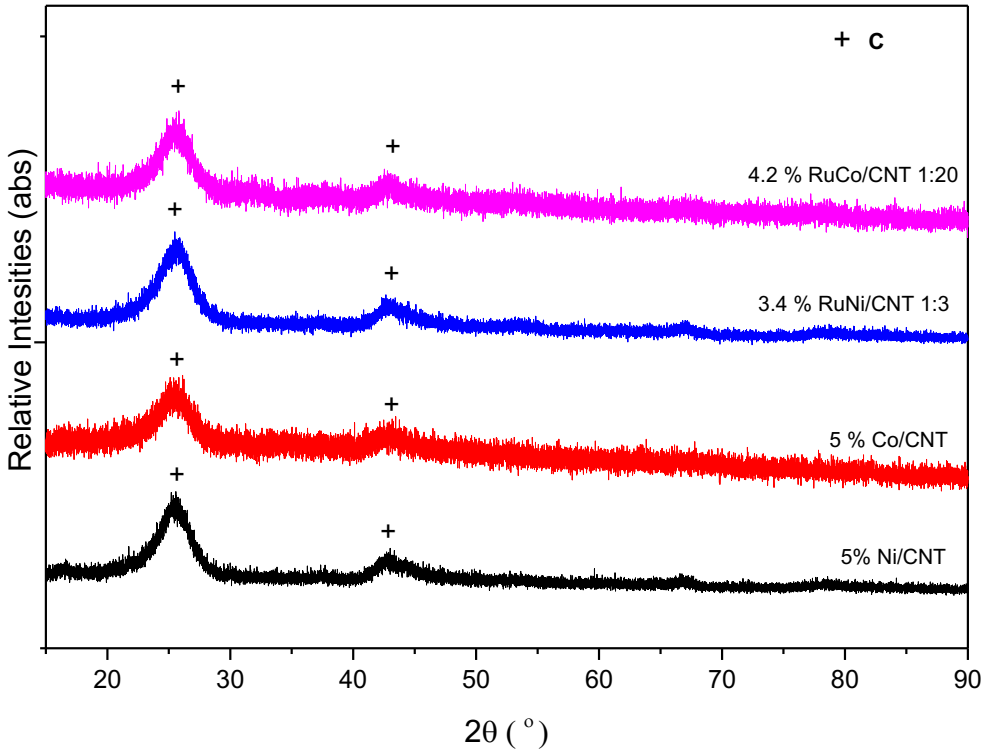

Figure 5.2.3 XRD patterns (Cu Kα radiation) for reduced CNT, 5 % Ru/CNT, 4.2 % RuCo/CNT 1:20, 3.4 % RuNi/CNT 1:3, 5 % Ni/CNT and 5 % Co/CNT.

5.2.1.3 Temperature Programmed Reduction, TPR

Temperature programmed reduction (TPR) studies helped to understand the activation of the catalysts in the H_2 atmosphere as well as reducibility of metal catalyst supported on carbon. The TPR profiles of the monometallic and bimetallic catalysts of RuCo/C are shown in **Figure 5.2.4**. Ru/C catalyst exhibited two peaks at 150 °C and 300 °C, respectively. This could be reduction peak of $RuCl_3$ precursor and later the Ru^{3+} to Ru^{x+}.[210] It was reported that the broader peak in Ru around 500 to 700 °C can be attributed to the methanation of the carbon support.[211] As for Co/C, the reduction temperature of the precursor was reported around 320 °C and a broad peak between 400 and 800 °C was associated with Co species. [213] The additions of Ru to Co decreased the reduction temperature of Co that normally occurs at a high temperature of around400/up to 800 °C. [213] It is probably due to the spill-over effect of H_2,

where due to the lower reduction temperature of Ru than Co, Ru, in turn, enhances the reduction temperature of Co as discussed in the literature.[226]

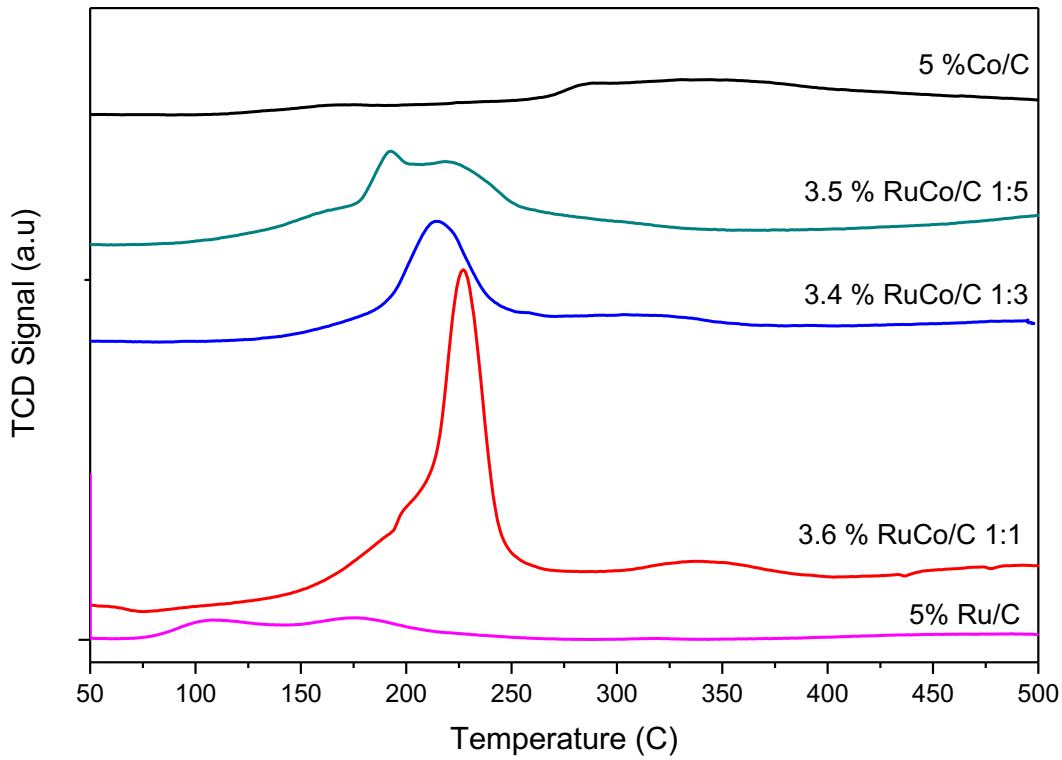

Figure 5.2.4 TPR profiles of as-prepared 5 wt. % RuCo bimetallic catalysts supported on C (H_2, 60cc min^{-1}, 10°min^{-1}).

Figure 5.2.5 shows the reduction profile of RuNi bimetallic catalysts with its monometallic catalysts of Ru and Ni. It can be seen that there were two peaks at 208 °C and 240 °C. The peaks can be assigned to reduction Ni^{2+} to Ni^0 and Ni precursor (Ni $(NO_3)_2$). [212] It can be seen that the position of the maximum H_2 consumption peak for bimetallic materials shifted to lower reduction temperature as Ru content was increased. Moreover, the addition of Ru to Ni, the metals mixture presented essentially peaks of intermediate between those corresponding monometallic samples. This would suggest the formation of an alloy between two metals.

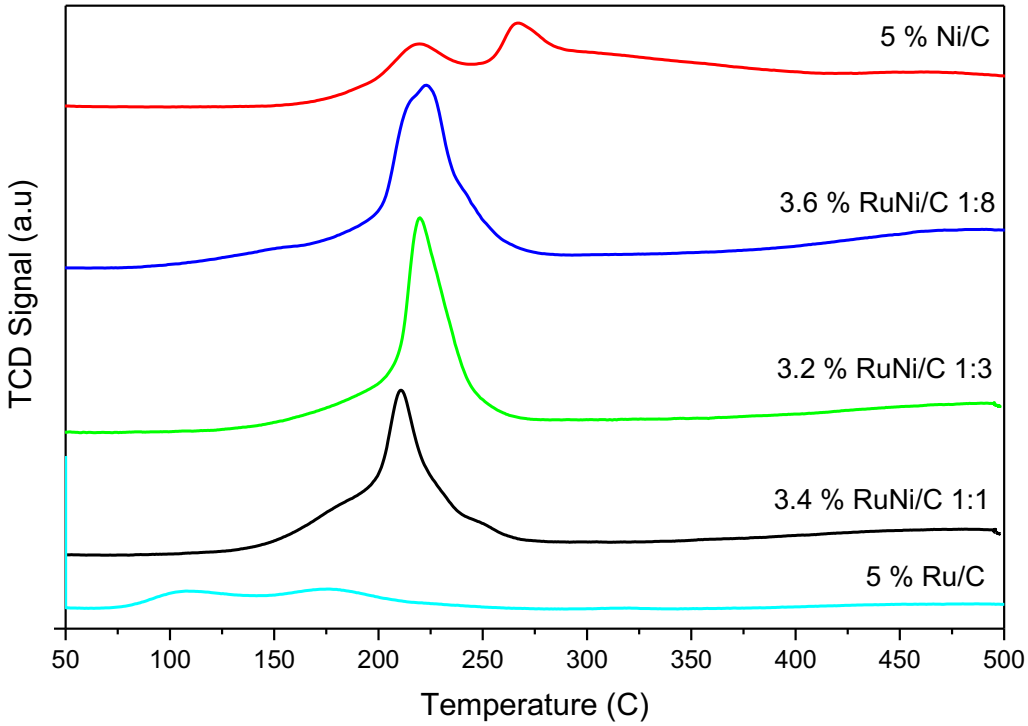

Figure 5.2.5 TPR profiles of as-prepared 5 % wt. RuNi bimetallic catalysts supported on C.

Figure 5.2.6 shows the TPR profiles of Ru, Co and Ni mono and bimetallic samples supported on CNT. Ru/CNT shows two main reduction peaks at ca. 110 °C and 160 °C. The first peak could be assigned to the reduction of ruthenium precursor ($RuCl_3$) and later one due to Ru^{3+} to Ru^0. [188] TPR profile for Ni/CNT consists of two main peaks at 208 °C due to decomposition of precursor nitrates and 240 °C due to the reduction of Ni^{2+} to Ni^0. The broad consumption peaks at high temperature (300 to 500 °C) may be ascribed to gasification of the carbon support. Similarly, TPR profiles for Co/CNT do not show any significant difference. The peak at ca. 162 °C is due to the decomposition of the Co precursor (Co nitrate) and reduction of Co^{2+} to Co^0. The broad peak between ca. 300 to 500 °C is again attributed to the methanation of the support. As for bimetallic 3.4 % RuNi/CNT 1:3 and 4.2 % RuCo/CNT 1:20 only one peak shows at 244 °C and 228 °C, respectively. This is expected since the amount of Ru present in this catalyst is now very small. Nevertheless, comparison with the monometallic analogues indicates a marked decrease of the reduction temperature, so suggesting some alloying effect. [227] Effect of metal alloying could be further proved with XPS and HRTEM.[228]

From TPR profile it was assured that by performing reduction under H_2 at 400 °C it would be sufficient to reduce the catalyst to its metal state.

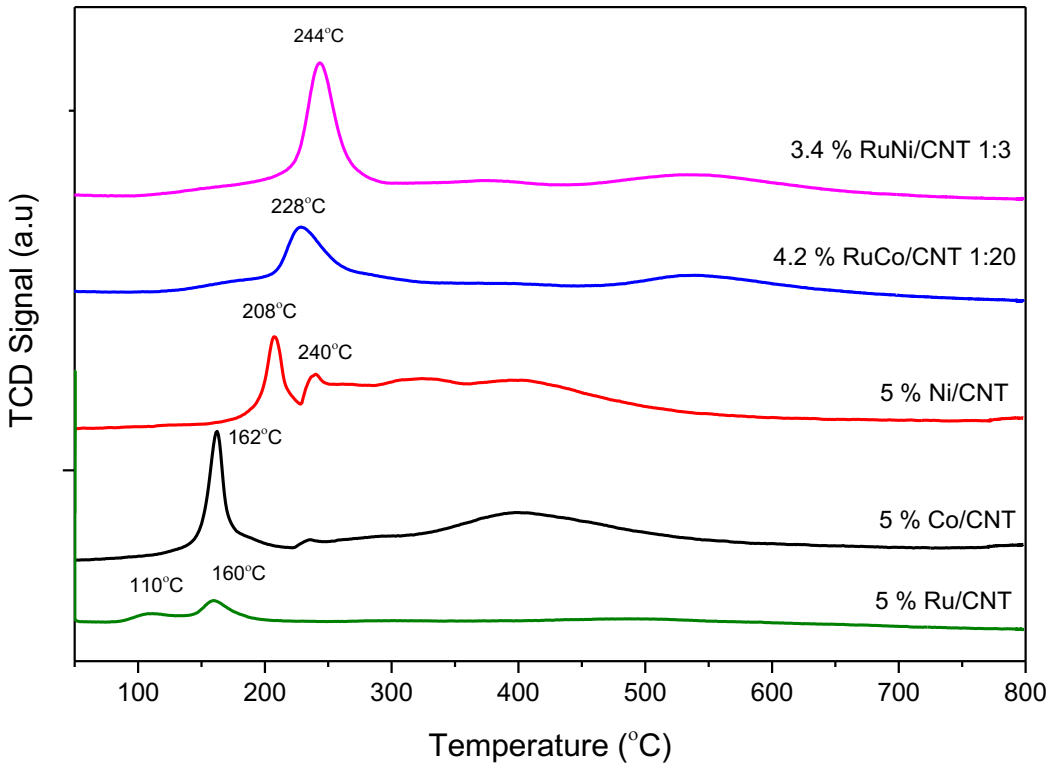

Figure 5.2.6 TPR profiles of as-prepared 5 % wt. monometallic and bimetallic catalysts of Ru, Ni, and Co supported on CNT.

5.2.1.4 Chemisorption

The quantification of active metal sites and the dispersion was investigated by CO chemisorption as shown in Table 5.2.2. It can be seen that samples supported on CNT show lower CO uptake compared than samples on carbon. This could be due to high surface area of carbon compared to CNT, which affect the distribution of Ru on the support. [14] It can be seen that 3.5 % RuCo/C 1:5 has the highest CO uptakes and dispersion among other ratios of RuCo catalysts while for RuNi catalysts it was 3.4 % RuNi/C 1:1. As for bimetallic RuCo and RuNi supported on CNT, both exhibited low dispersion compared to carbon supported catalysts of similar composition. However, 4.2 % RuCo/CNT 1:20 has higher dispersion than 3.4 % RuNi/CNT 1:3. The variance in the value of CO uptakes and dispersion can be related to the amount of metal loading as well as the molar ratios.

Table 5.2.2 CO uptakes and dispersion of Ru-Co and Ru-Ni bimetallic catalysts.

Entry	Catalysts	CO uptakes (µmol/g)	D, (%)
1	3.6 % RuCo/C 1:1	13.6	2.8
2	3.4 % RuCo/C 1:3	10	1.7
3	3.5 % RuCo/C 1:5	36.2	5.0
4	3.4 % RuNi/C 1:1	14	2.3
5	3.2 % RuNi/C 1:3	10.3	1.5
6	3.6 % RuNi/C 1:8	7.11	1.22
7	4.2 % RuCo/CNT 1:20	4.22	0.60
8	3.4 % RuNi/CNT 1:3	4.98	0.19

5.2.1.5 Transmission Electron Microscopy, TEM

TEM was performed to examine the morphology and also estimate the particle size of the prepared bimetallic catalysts. The particle sizes of reduced bimetallic catalysts are tabulated in **Table 5.2.3**. It can be seen that bimetallic RuNi/C possess smaller size than the monometallic Ni. RuNi/C with a molar ratio of 2:1 has the smallest size with 1.67 nm while 1:1 and 1:2 are 3.28 nm and 3.34 nm, respectively. However, for bimetallic RuCo the particle size is bigger.

Table 5.2.3 Particles size of bimetallic catalysts from TEM.

Entry	Catalysts	Particle Size (nm)
1	5% Ru/C	2.60
2	5% Ru/CNT	1.50
3	5% Ni/C	4.53
4	5% Co/C	2.50
5	3.2 % RuNi/C 1:3	3.28
6	3.4 % RuNi/C 1:1	1.67
7	3.6 % RuNi/C 1:8	3.34
8	3.5 % RuCo/C 1:5	4.40
9	3.4 % RuCo/C 1:3	8.36

10	3.6 % RuCo/C 1:1	N/A
11	3.4 % RuNi/CNT 1:3	2.90
12	4.2 % RuCo/CNT 1:20	2.30

Figure 5.2.7 showed the TEM images of bimetallic 3.5 % RuCo/C 1:5 catalyst. The TEM images indicate that there is a presence of big particles around 7 nm which suggested the presence of CoO apart from Ru and Co particles. These results are in agreement with the XPS data that showed the presence of CoO in 3.5 % RuCo/C 1:5 (Figure 5.2.17). The average particle size was found to be 4.4 nm with a broad particle size distribution ranging from 0.77 nm to 22 nm as shown in **Figure 5.2.8**.

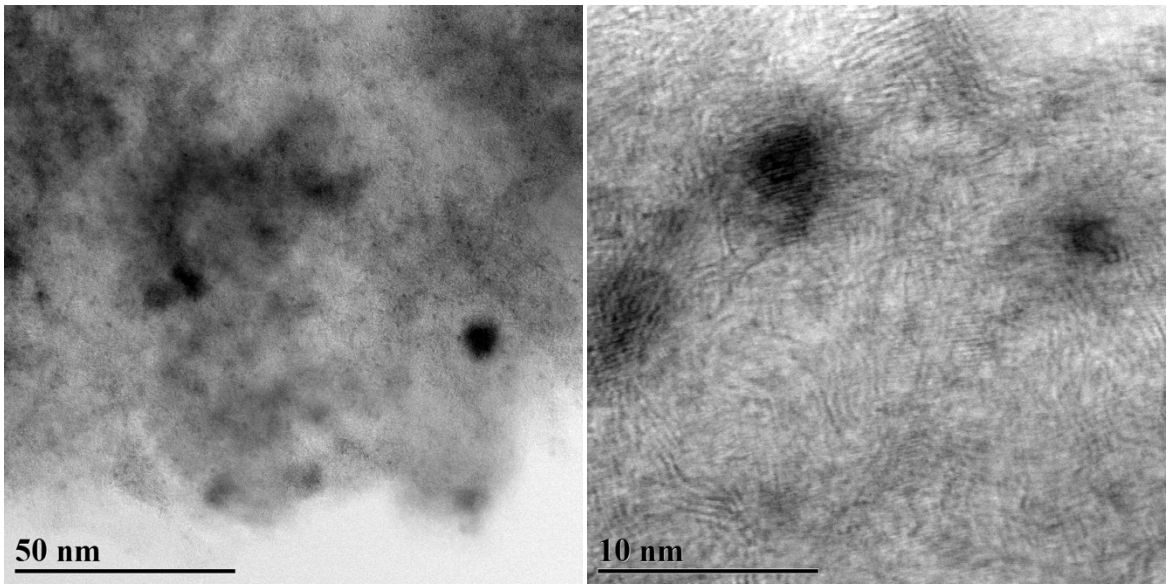

Figure 5.2.7 TEM images of reduced bimetallic 3.5 % RuCo/C 1:5 catalyst.

Based on TEM result it showed that the smaller particles are almost exclusively Ru and the larger particles of 5-10 nm are primarily Co with small amounts of ruthenium. The energy-dispersive spectroscopy (EDS) elemental mapping revealed that the particle contains Ru, Co and also the oxide.

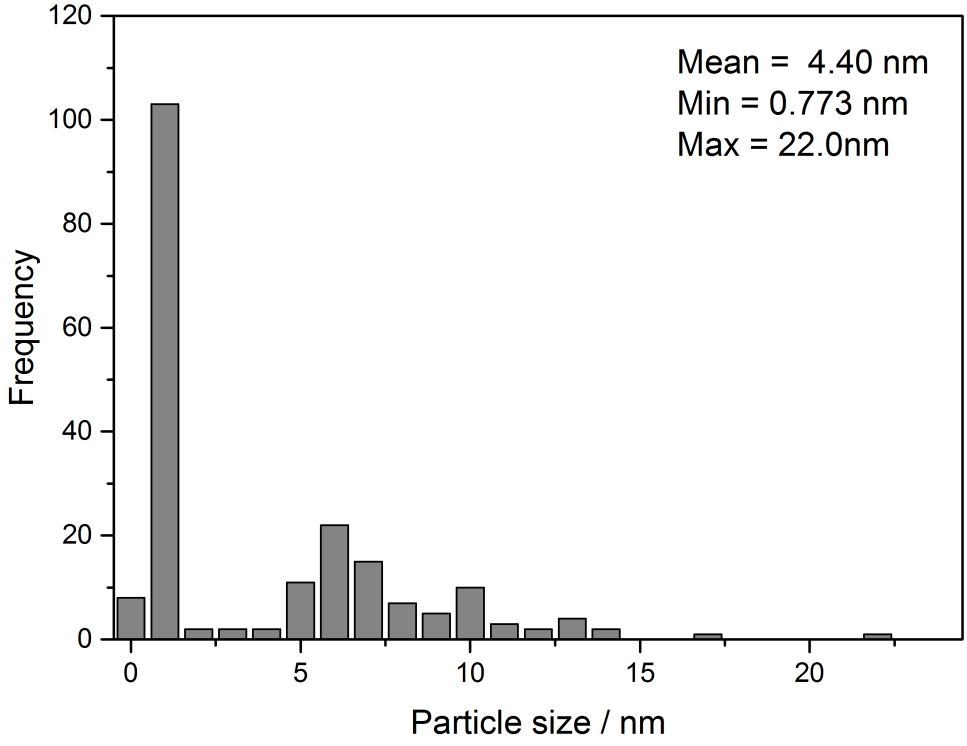

Figure 5.2.8 Particle size distribution of reduced bimetallic 3.5 % RuCo/C 1:5 catalyst based on TEM and ca. 200 particles.

Figure 5.2.9 shows the TEM images of bimetallic 3.2 % RuNi/C 1:3catalyst. It can be seen that the particles are well distributed with a mix of Ru and Ni with average particle size of 3.28 nm. The larger particles are due to the NiO as proved by lattice measurement from HRTEM matched with NiO (111) with a distance of 0.242 nm.

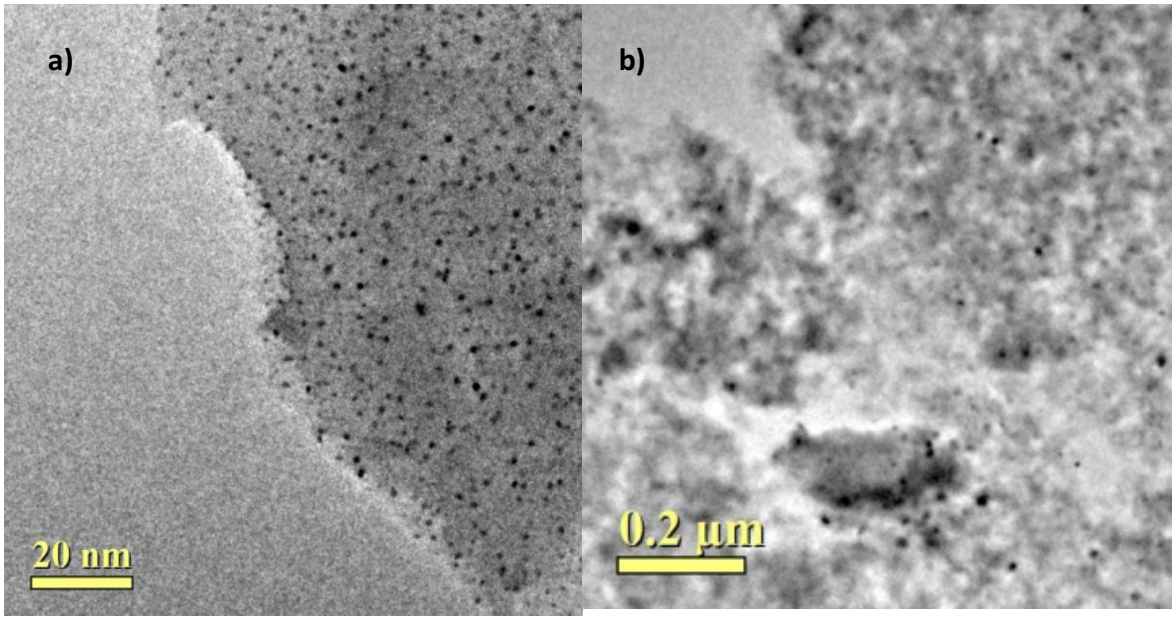

Figure 5.2.9 TEM images of reduced bimetallic 3.2 % RuNi/C 1:3 catalyst at various resolutions (a) 20 nm and (b) 0.2 µm.

Figure 5.2.10 showed the particle size distribution of reduced bimetallic 3.2 % RuNi/C 1:3 based on TEM. It can be seen that the particle size distribution is broadly ranging from 0.8 to 40 nm. The larger ranges of particles could be due to the present of NiO.

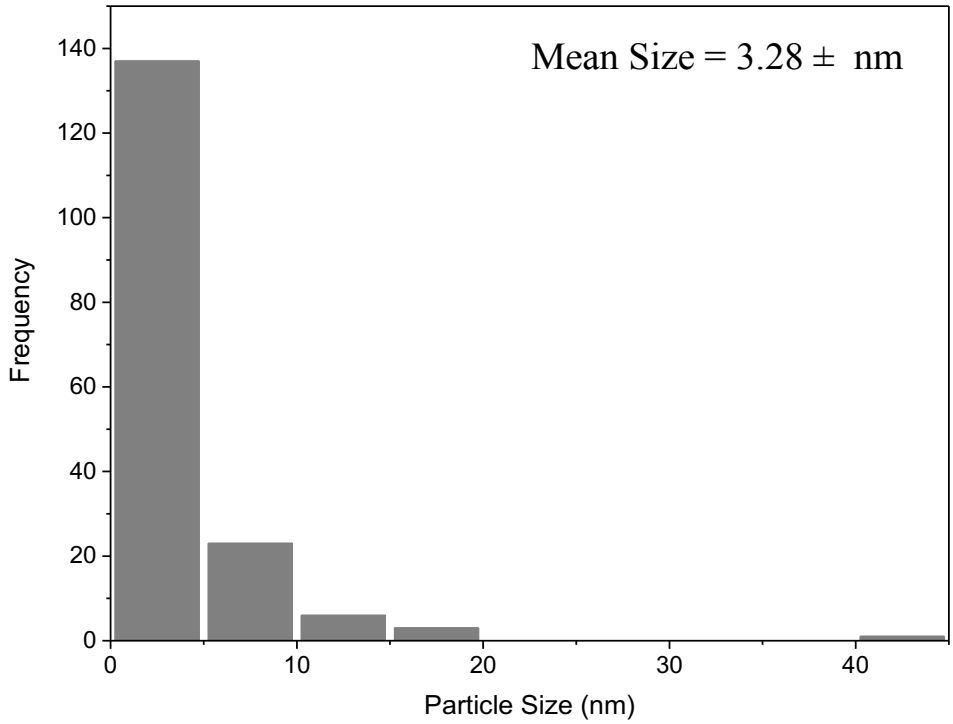

Figure 5.2.10 Particle size distribution of reduced bimetallic 3.2 % RuNi/C 1:3 catalyst based on TEM and ca. 200 particles.

The TEM images of bimetallic 4.2 % RuCo/CNT 1:20 indicated that Ru and Co are well distributed outside the CNT with average particle size of 2.3 nm which is smaller than the average particle size of 3.5 % RuCo/C 1:5 as shown in **Figure 5.2.11**. An agglomeration or cluster of Ru-Co can be noticed present in some region which might explain the broad particle distribution.

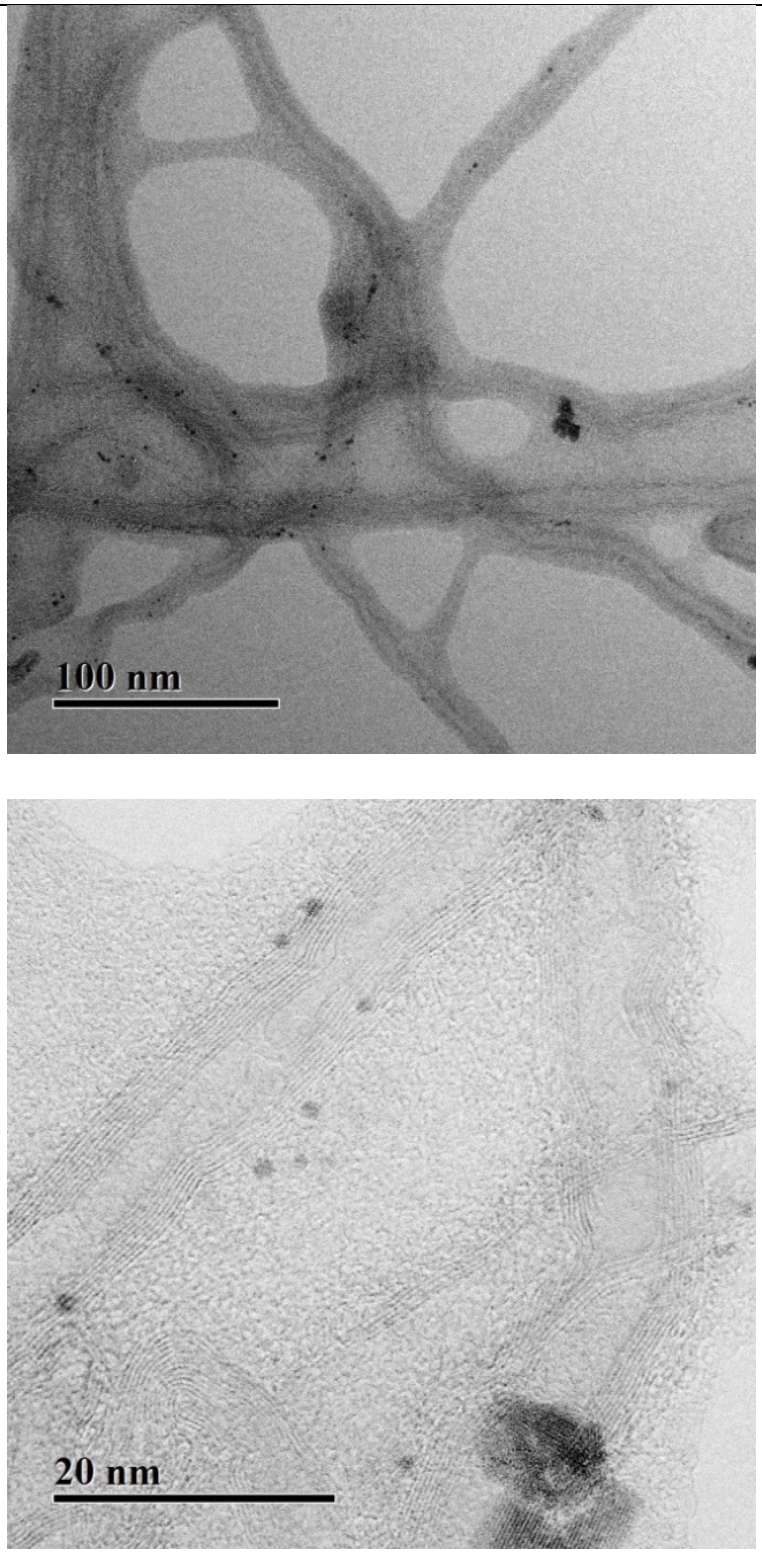

Figure 5.2.11 TEM images of reduced 5 % bimetallic 4.2 % RuCo/CNT 1:20 catalyst.

4.2 % RuCo/CNT 1:20 shows a broad particle size distribution ranging from 0.5 to 12 nm in size as shown in

Figure 5.2.12. However the particle size distribution of 4.2 % RuCo/CNT 1:20 is still narrower compared to 3.5 % RuCo/C 1:5 which range from 0.7 to 20 nm in size.

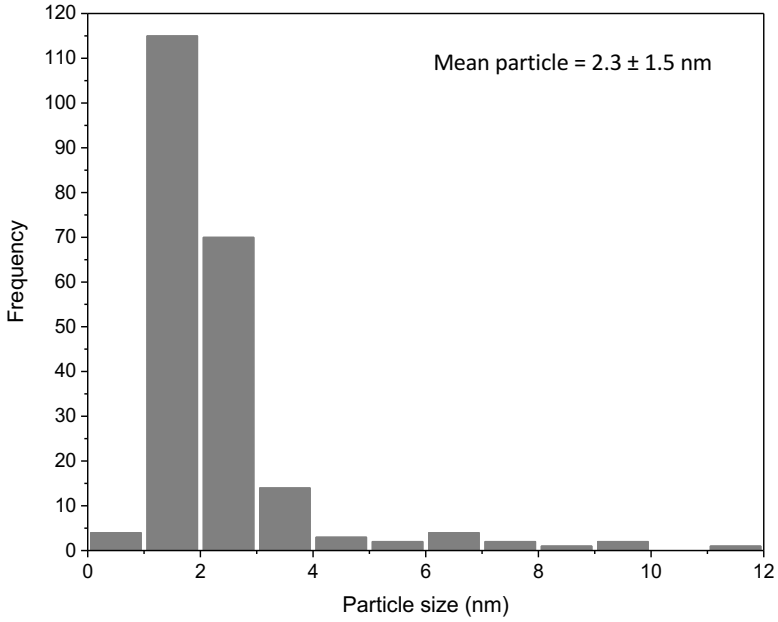

Figure 5.2.12 Particle size distribution of bimetallic 4.2 % RuCo/CNT 1:20 catalyst based on TEM and ca. 200 particles.

Contrary to 4.2 % RuCo/CNT 1:20, 3.4 % RuNi/CNT 1:3 exhibited better dispersions of Ru and Ni located mostly outside the tubes as shown in **Figure 5.2.13**. The average particle size is about 2.3 nm which is lower than 3.2 % RuNi/C 1:3. The particle size distribution of 3.4 % RuNi/CNT 1:3 is narrower than 3.2 % RuNi/C 1:3 which most of the particle size are ranging between 1 to 6 nm as shown in **Figure 5.2.14**.

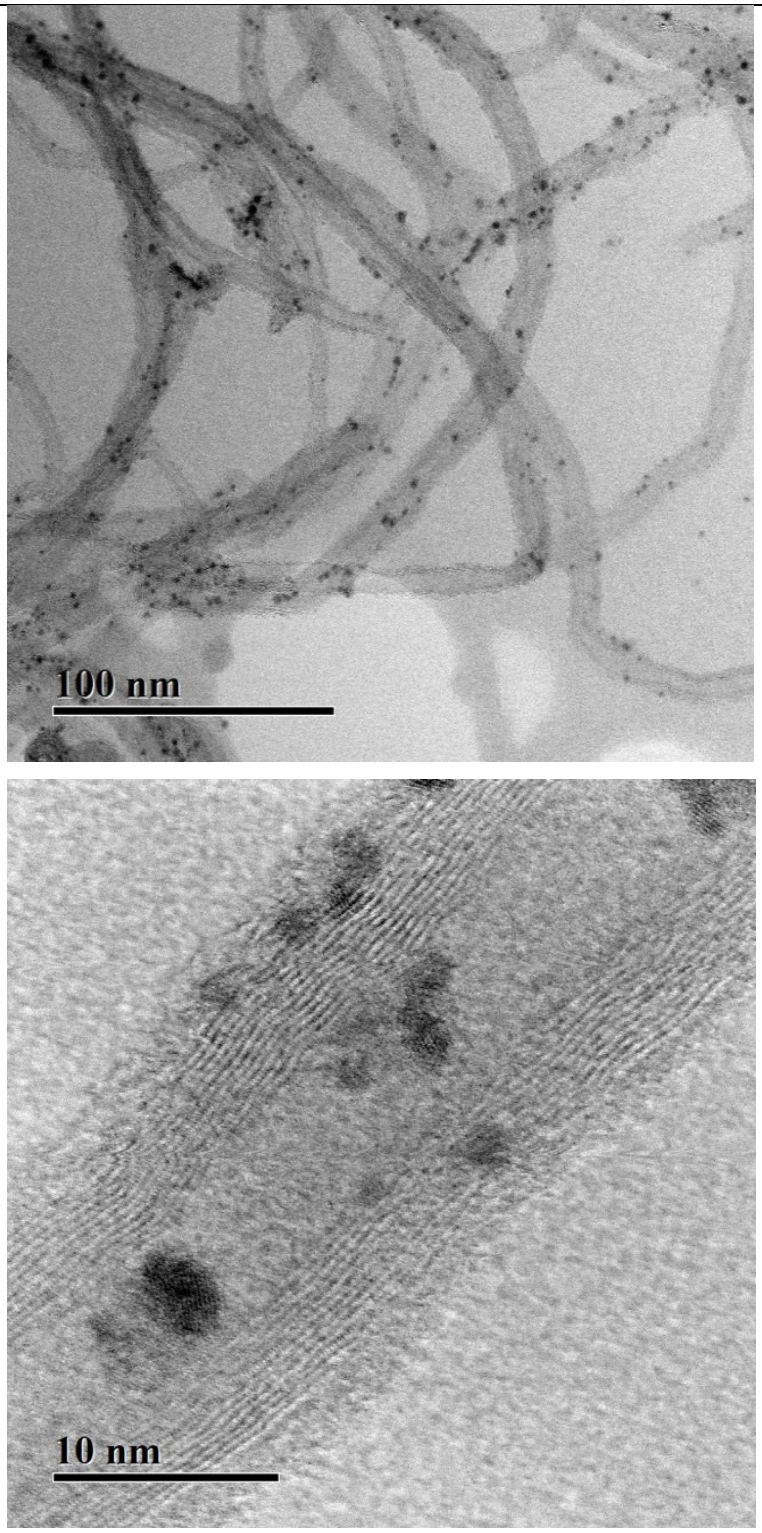

Figure 5.2.13 TEM images of reduced 5 % bimetallic 3.4 % RuNi/CNT 1:3 catalyst.

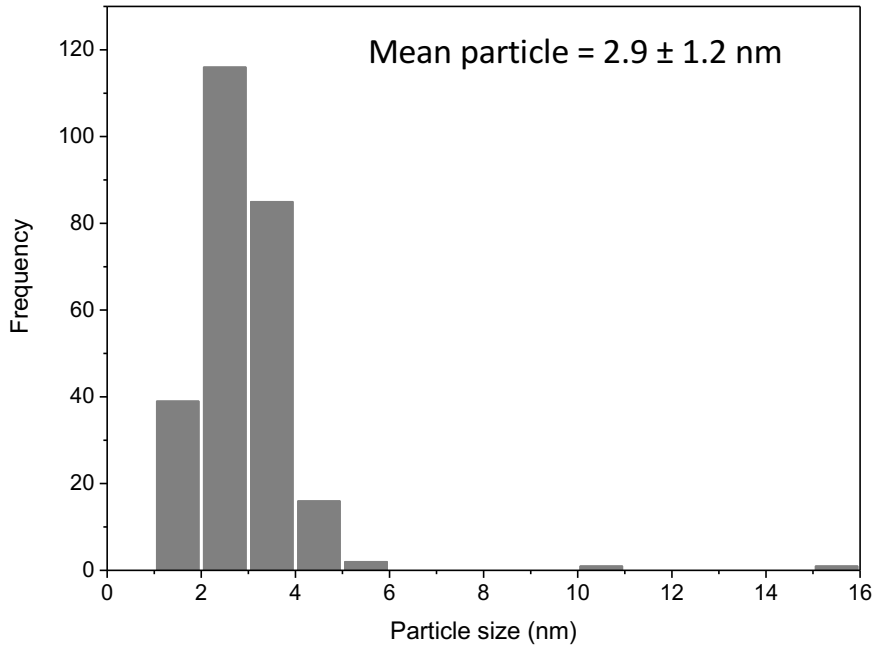

Figure 5.2.14 Particle size distribution of bimetallic 3.4 % RuNi/CNT 1:3 catalyst based on TEM and ca. 200 particles.

5.2.1.6 X-ray Photoelectron Spectroscopy, XPS

The XPS measurement was performed to investigate the surface chemical composition of bimetallic catalysts. The XPS spectra reveal the presence of Ru, Co, Ni, O and C. **Figure 5.2.15** shows the XPS survey spectrum of 3.5 % RuCo/C 1:5 catalyst. It can be observed that the peak at 284 eV belongs to Ru 3d which is overlapping with C 1s peak and the peak at 780 eV belongs to Co 2p. [78]

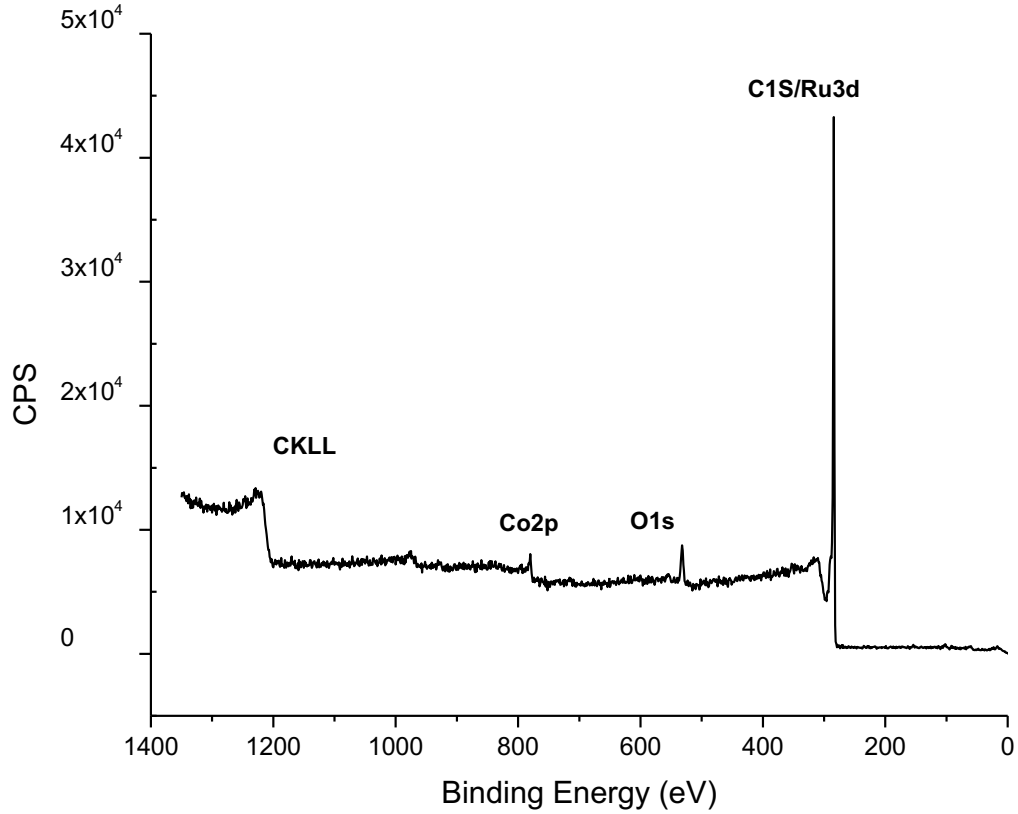

Figure 5.2.15 XPS survey spectrum of 3.5 % RuCo/C 1:5 catalyst.

Figure 5.2.16 shows the XPS spectra of Co 2p of bimetallic Ru-Co catalysts. It can be seen that Co 2p peaks show complex patterns which agreed with the finding reported by Chen et al.[78] All RuCo catalysts show similar XPS peaks of Co 2p apart from 3.5 % RuCo/C 1:5 showing the peaks of cobalt oxide species at 780 eV and 797 eV. The binding energy of 776.9 eV indicated the Co in the metallic state [78] However, peculiarly there was no peak of Co and Cobalt oxide presence in 3.4 % RuCo/C 1:1 and 3.6 % RuCo/C 1:3. It can be speculated that this is due to the low sensitivity of XPS equipment which requires substantial metal loading or there was no presence of Co on the surface of the catalysts.

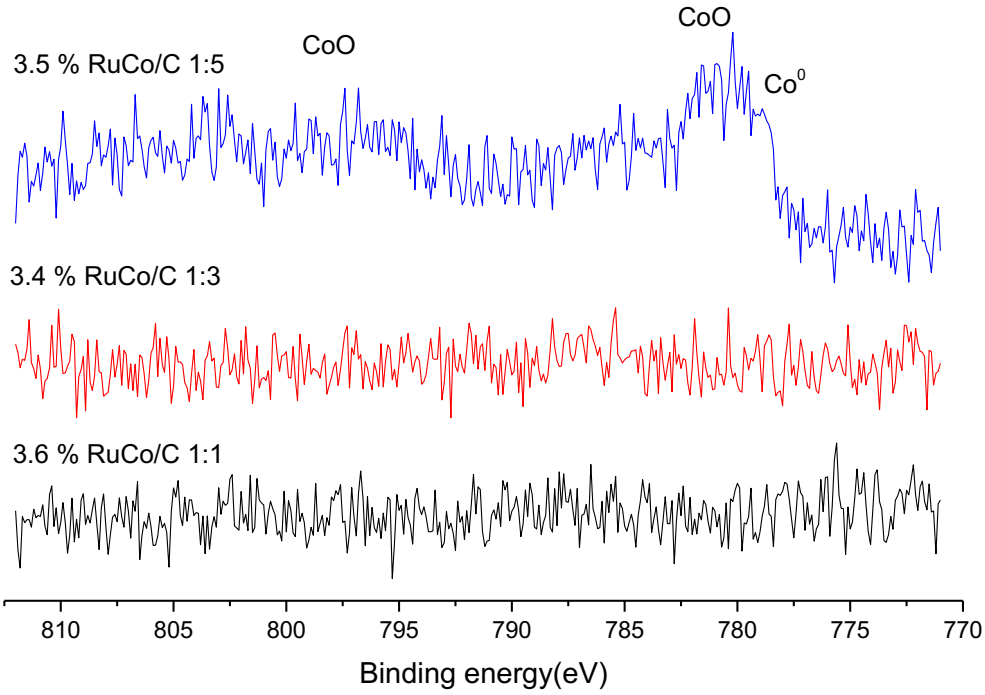

Figure 5.2.16 XPS spectra Co 2p of bimetallic RuCo/C catalysts.

Figure 5.2.17 shows the fitting of Co 2p of bimetallic of 3.5 % RuCo/C 1:5 and **Table 5.2.4** presents the binding energy and the composition of each ruthenium and cobalt species present in of 3.5 % RuCo/C 1:5 based on an analysis using the CASA software The peaks of cobalt oxide species can be observed at 780 eV and 797 eV, whereas Co in the metallic state is shown at 777.6 eV in agreement with findings in the literature.[78] The fitting from Casa XPS software suggests that most of the Co is present as CoO (59 %), while Co in the metallic state was 40.6 %. On the other hand, Ru 3p fitting showed that most of Ru were in a metallic state with 60 % and RuO_2 only 40 %.

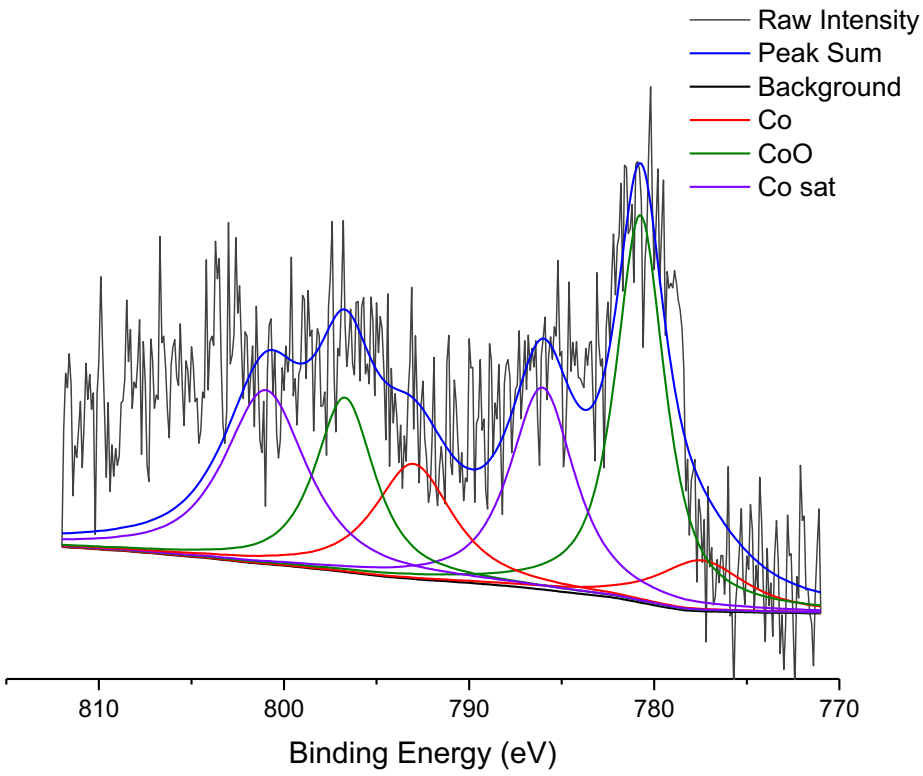

Figure 5.2.17 XPS spectra Co 2p for of 3.5 % RuCo/C 1:5 catalyst.

Table 5.2.4 XPS analysis for the binding energy and percentages of Ru and Co species for of 3.5% RuCo/C 1:5.

Catalyst		**Ru 3p (3/2)**		**Co 2p**		
		Ru	RuO_2	Co	CoO	Co sat
3.5 % RuCo/C 1:5	BE (eV)	461.9	465.8	777.6	780.7	785.9
	AR (%)	59.98	40.03	40.6	59.39	-
Reference [78]	BE (eV)	462	464.2	777.5	781.6	785.2, 801

Figure 5.2.18 shows the XPS survey spectrum of 3.4 % RuNi/C 1:3 catalyst. It reveals the presence of ruthenium, nickel, carbon and oxygen. Ru 3d which is overlapping with C1s is at the binding energy value of 284 eV.[224] Ni 2p can be seen at binding energy value of 870 eV.

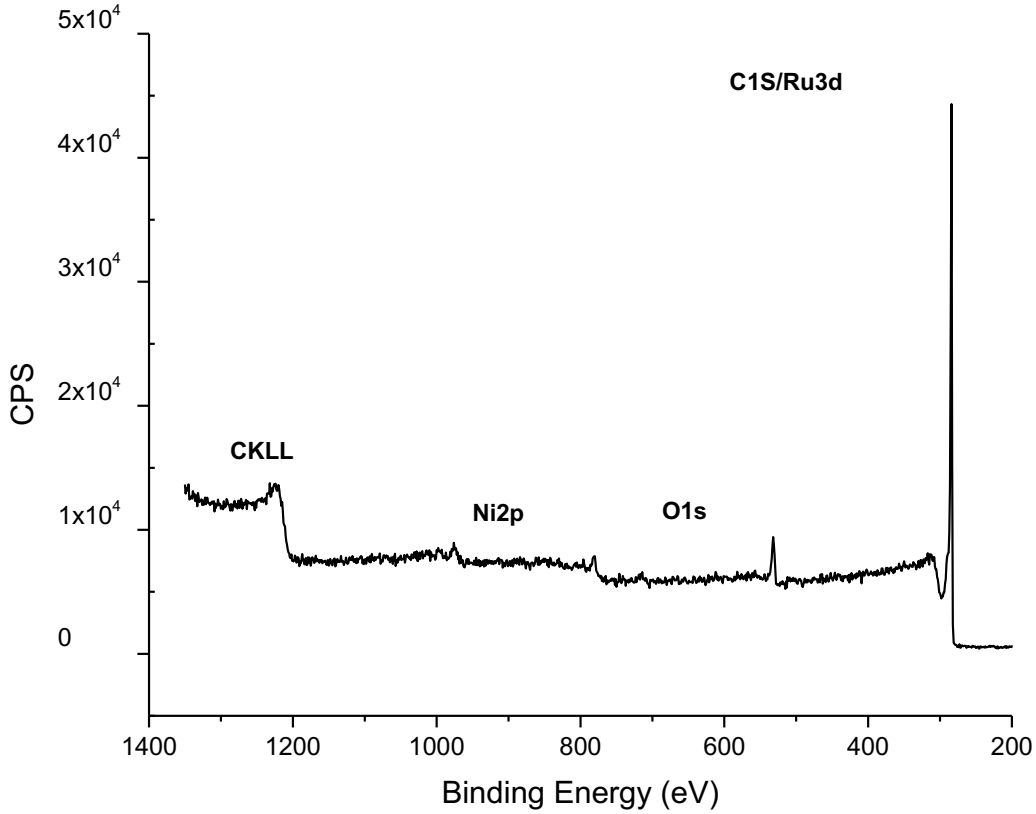

Figure 5.2.18 XPS survey spectrum of 3.4 % RuNi/C 1:3 catalyst.

Figure 5.2.19 shows the XPS spectra of Ni 2p of bimetallic Ru-Ni catalysts. In general, Ni 2p spectrum shows a complex structure with intense satellite signals adjacent to the main peaks due to multielectron excitation.[224] XPS data show that an increase of Ni content in the catalyst leads to increase of nickel oxide. The peaks at 854 and 856 eV belong to NiO. Other nickel oxide peaks from Ni $2p_{3/2}$ can be found at 855.4 eV and 857.1 eV which corresponds to Ni $(OH)_2$ and NiOOH respectively. Ni $2p_{1/2}$ peaks which appeared at binding energies of 870, 871.2, 872.9 and 874.4 eV correspond to Ni(0), NiO, $Ni(OH)_2$ and NiOOH species, respectively. The same findings were reported by Zhu et al.[184] However, there was no significant peak of Ni 2p that corresponds to nickel in the metallic state which usually shows at 852.7 and 869.9 eV apart from 3.6 % RuNi/C 1:8.[203] This could be due to high loading of Ni compared to other metal ratios.

The XPS fitting for Ni 2p of bimetallic 3.4 % RuNi/C 1:3 is shown in **Figure 5.2.20** and **Table 5.2.5** present the binding energy and the composition of each ruthenium and cobalt species present in 3.4 % RuNi/C 1:3 based on CASA analysis.

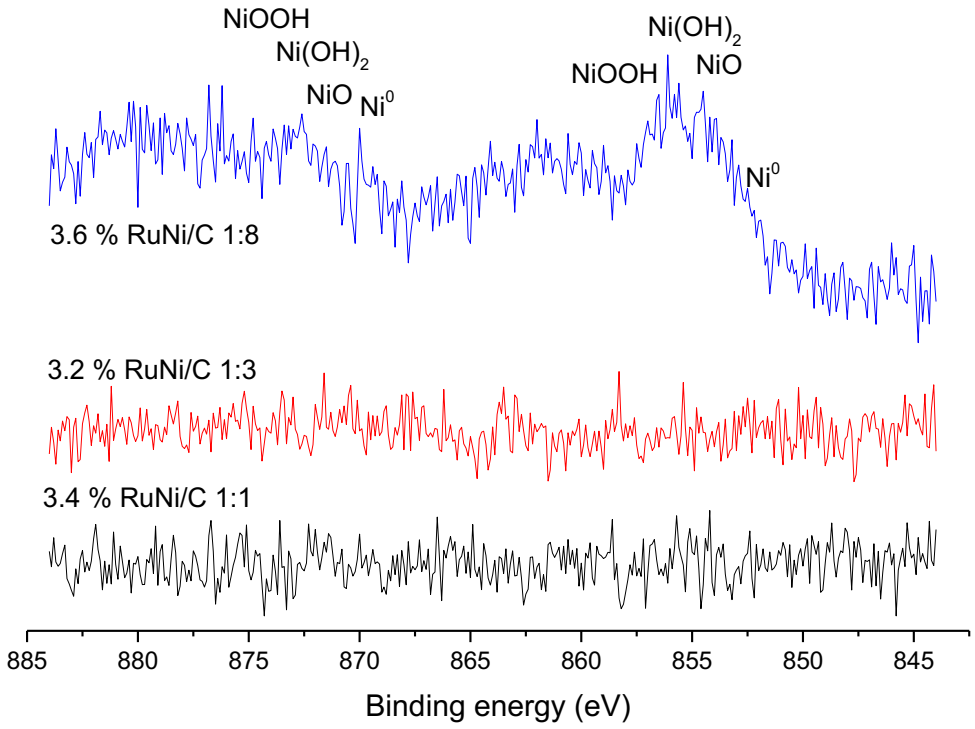

Figure 5.2.19 XPS spectra Ni 2p of bimetallic RuNi/C catalysts.

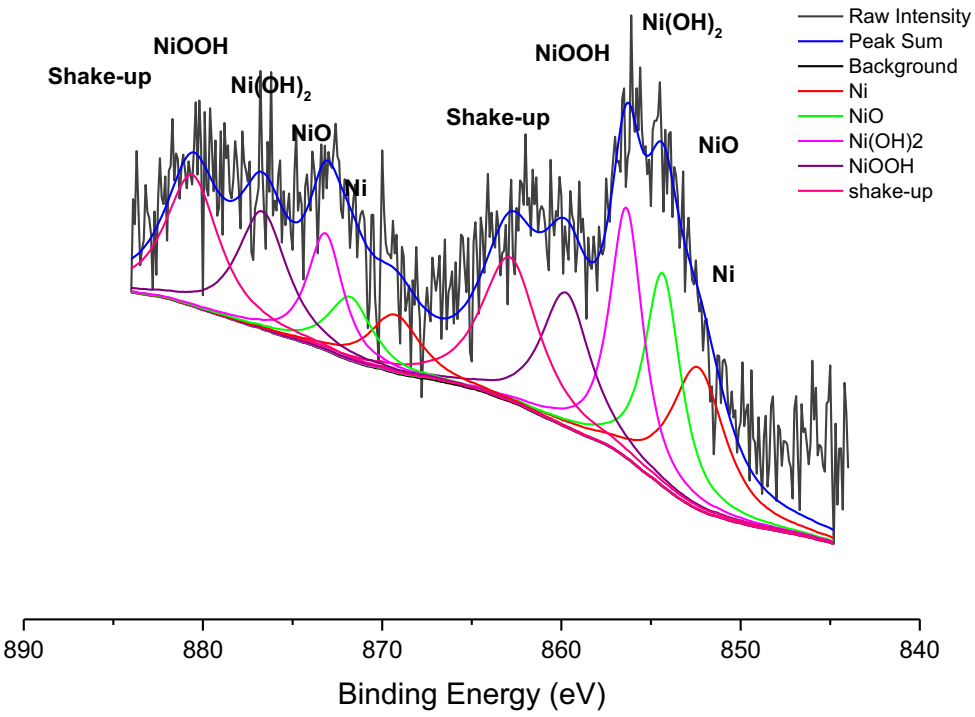

Figure 5.2.20 XPS spectra Ni 2p for 3.4 % RuNi/C 1:3 catalyst.

Table 5.2.5 XPS analysis for the binding energy and percentages of Ru and Ni species for RuNi/C 1:1

Catalyst		Ru 3p (3/2)		Ni 2p			
		Ru	RuO_2	Ni	NiO	$Ni(OH)_2$	NiOOH
3.4 % RuNi/C 1:3	BE (eV)	462	464.2	852.4	854.4	856.4	859
	AR (%)	38.44	61.54	27	43.43	9.71	19.85
Reference [184]	BE (eV)	462	464.2	852.7	853.9	855.4	857.1

5.2.2 Hydrogenation of HMF into DMF

The effect of a bimetallic catalyst consisting of RuCo and RuNi supported on carbon and CNT in HMF hydrogenation were tested. It is important to note that the objective of this study is to reduce the content of Ru in the catalyst composition and so produce cheaper and more sustainable catalysts for this demanding reaction. As a consequence, the catalysts will be benchmarked against the widely used and well-understood 5 wt % Ru/C catalysts, even when all our bimetallic catalysts will contain only a small fraction of that amount of precious metal.

5.2.2.1 Effect of addition of Co to Ru on Carbon

The effect of bimetallic catalyst supported on carbon composed of Ru and Co in 1:1, 1:5 and 1:8 molar ratios with the metal loading of 3.5 wt. % has been explored.

Figure **5.2.21** and Figure 5.2.22 summarised the HMF conversion and DMF yield of bimetallic RuCo/C with different ratios compared to monometallic of Ru/C and Co/C. It can be seen that all bimetallic catalysts show an improvement in the rate of HMF conversion especially in the initial reaction rate (first hour of reaction time). It was better than both Ru/C and Co/C. However only 5 % Ru/C and 3.5 % RuCo 1:5 reach 100 % conversion after 5 hours followed by 3.6 % RuCo/C 1:1, 3.4 % RuCo/C 1:3 and 5 % Co/C. It seems like the combination of Ru with Co confers the catalytic system with higher intrinsic activity as TOFs calculated after 15 min reaction confirms. However, the

reaction rate decreases for all the bimetallic catalysts after 20-30 minutes on-line, which could potentially be due to changes in the metal structure or oxidation state or maybe carbon deposition. Nevertheless, the enhancement in the initial rate of reaction and its subsequent deactivation is exclusive of the bimetallic nanoparticles. Note that conversion rates achieved with Ru are linear for 2 h until conversion values > 65 %. The 5 % Co/C catalyst, on the other hand, does not show evidence of deactivation and maintains the same reaction rates for about 6 hours, further highlighting that there is a synergistic effect between Ru and Co at initial reaction times which is slowly being lost with time online for the three bimetallic systems. It is also notable that the optimum metal loading corresponds to a 3.5 % weight metal loading, comprising of a 1:5 Ru:Co ratio.

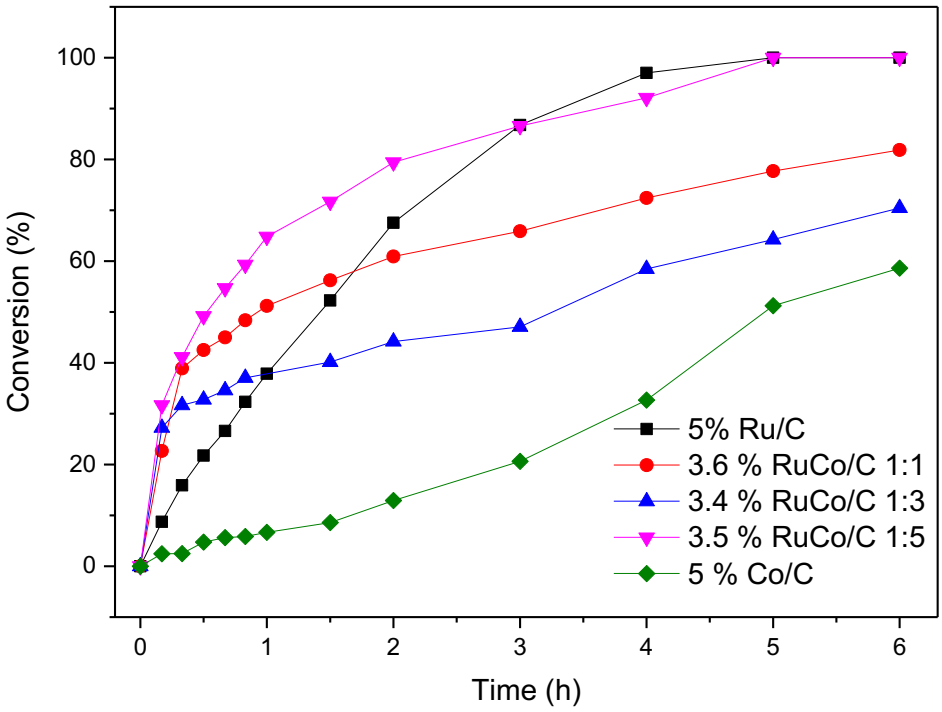

Figure 5.2.21 Conversion of HMF with the monometallic catalyst of 5 % Ru/C, 5 % Co/C and bimetallic RuCo catalysts. Reaction conditions: HMF, 40 mM; catalyst, 60 mg; solvent, Dioxane; pressure, 20 bar H_2; temperature 150 °C, stirring, 1100 rpm

As illustrated in **Scheme 5** the conversion of HMF to DMF involves several intermediates products (DHMF, MFA) and DMF yield could vary not only due to the parallel reactions but also due to the consecutive reactions that lead to the formation of ring hydrogenation product, DMTHF and ring opening product, 2-hexanol.

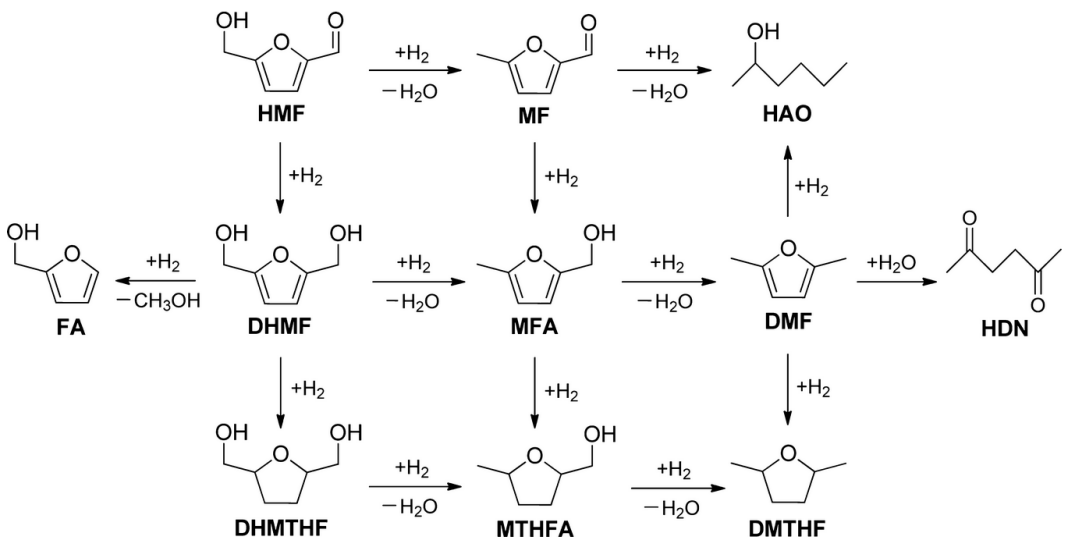

Scheme 5 Reaction pathways of HMF hydrogenation.

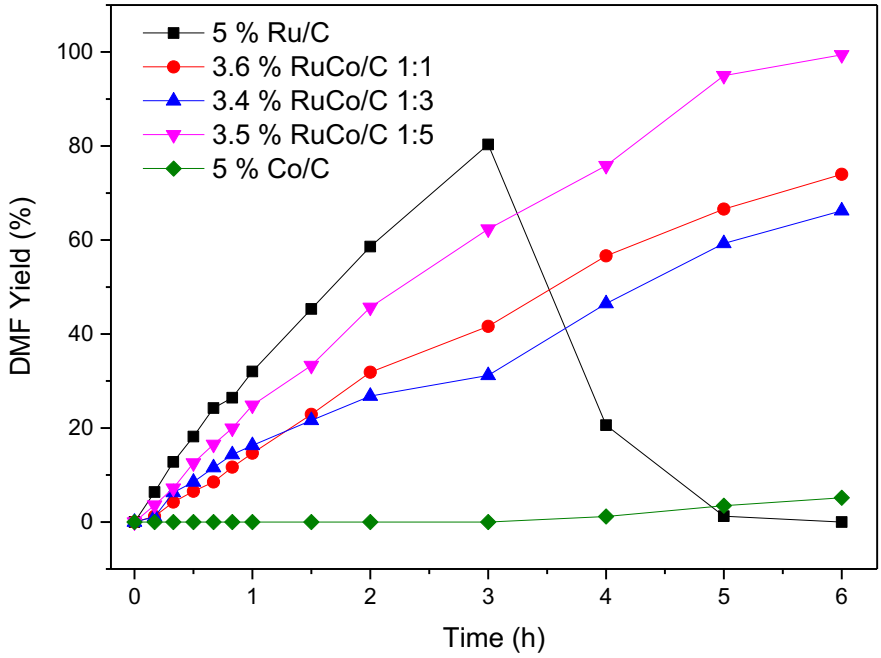

Figure 5.2.22 DMF yield with the monometallic catalyst of 5 % Ru/C, 5 % Co/C and bimetallic RuCo catalysts. Reaction conditions: HMF, 40 mM; catalyst, 60 mg; solvent, Dioxane; pressure, 20 bar H_2; temperature 150 °C stirring, 1100 rpm.

A quick inspection of the yield and conversion graphs reveals some important information that deserves attention. For the bimetallic catalysts and Co/C, the DMF yields obtained seem to follow a similar relative trend to the conversions with time on

line. However, despite the superior TOFs and initial conversion values that the bimetallic catalysts demonstrated against Ru/C, it is later that produces better yields of DMF for the first 3 h of hours of reaction. This is a clear reflection of the complex multistep reaction and how the activation of HMF might require a different set of active sites than the subsequent hydrogenolysis reaction and, this highlights the need to develop catalysts with optimum activities for both steps.

However, it also seems that for the Ru catalyst there is maximum yield that can be obtained due to consecutive reactions. Monometallic Ru/C achieved 80 % yield in 3 hours before it started to decrease due to the formation of ring hydrogenation and ring opening products, namely DMTHF and 2- hexanol (**Scheme 5**). On the other hand, monometallic Co/C showed a poor yield of DMF with only 5 % after 6 hours. All bimetallic RuCo/C exhibited good yield of DMF and the trend is similar for the HMF conversion of each molar ratio. This really shows that synergistic effect between these two metals was present. It has been previously reported that the higher yields of DMF result from the fact that DMF is unreactive over bimetallic catalysts hence less formation of ring hydrogenation and ring opening products.[229] The lack of covalent bonding between the furan ring with Co_3O_2 oxide protects the ring from further side reactions and explains the low reactivity of DMF. 3.5 % RuCo/C 1:5 showed the highest DMF yield of 99% in 6 hours. This surpassed the performance of 5% Ru/C although the reaction is slower. This means that this composition of Ru and Co improved the selectivity of DMF and suppressed the formation of ring hydrogenation and ring opening products.

This phenomenon can be explained by a recent study by Luo et al. [80, 229], Chen et al.[78] This agreed with XRD diffraction pattern of 3.5 % RuCo/C 1:5 which showed the presence of CoO peak around 40°. The main reason for the superior performance of 3.5 % RuCo/C 1:5 is that the alloy formed a monolayer of oxide on the surface, which interacted weakly with furan ring to prevent the hydrogenation of the ring and ring opening products from DMF. At the same time, these acted as active sites to perform the hydrogenolysis process. In contrast to bimetallic RuCo/C, DMF ring might interact strongly with Ru, promoting the ring hydrogenation and ring opening products thus lowering the yield of DMF after 3 hours as shown in **Figure 5.2.23**. The proposed successive hydrogenolysis mechanism of DHMF on Pt-Co alloy is depicted in **Figure**

5.2.23. DHMF undergoes C-O bond cleavage on a honeycomb edge site consisting of two Co atoms forming loosely bound radical and an OH group. Next, an H_2 atom transfers from the OH to the radical, yielding MFA and a chemisorbed oxygen atom. The second hydroxymethyl group undergoes similar C-O scission forming DMF as the final product.

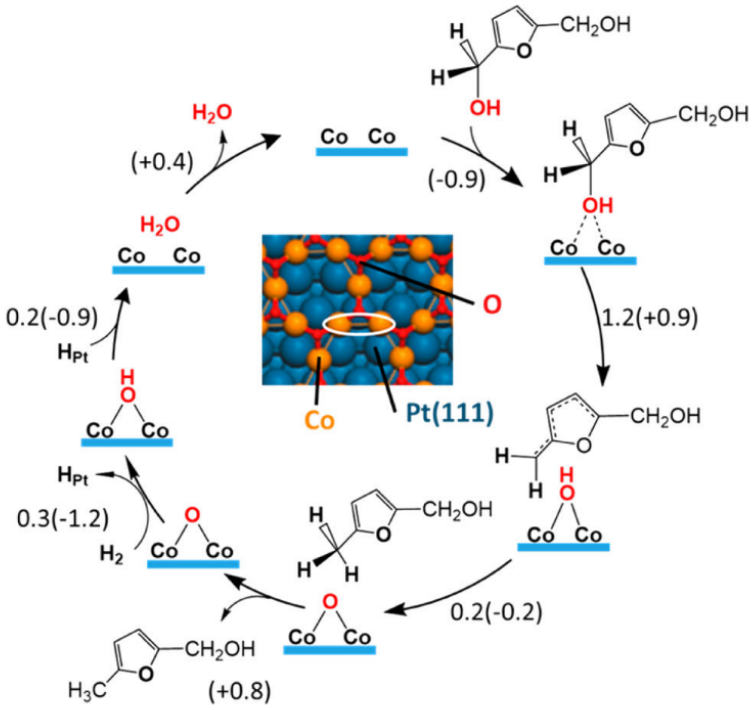

Figure 5.2.23 Reaction mechanism of DHMF hydrodeoxygenation to MFA on the Co_3O_2/Pt(111) surface based on DFT calculation.[229]

5.2.2.2 Effect of addition of Ni to Ru on Carbon

Bimetallic catalysts supported on carbon with a total metal loading of 3.5 wt % and comprising of Ru and Ni in 1:1, 1:3 and 1:8 molar ratios have been explored. HMF conversion among monometallic and bimetallic catalysts is displayed in **Figure 5.2.24**. It can be seen that 3.2 % RuNi/C 1:3 shows excellent reactivity and better than other catalysts. HMF was fully converted in 3 hours of reaction time, faster than Ru/C which reached 100 % conversion in 5 hours. 3.4 % RuNi/C 1:1 and 1:8 showed superior conversion for the first 30 minutes, but after that time lower conversions than Ru/C are observed but better than monometallic Ni/C. This demonstrated that bimetallic

RuNi/C, especially RuNi/C 1:3 has a synergistic effect which enhanced the hydrogenation of HMF.

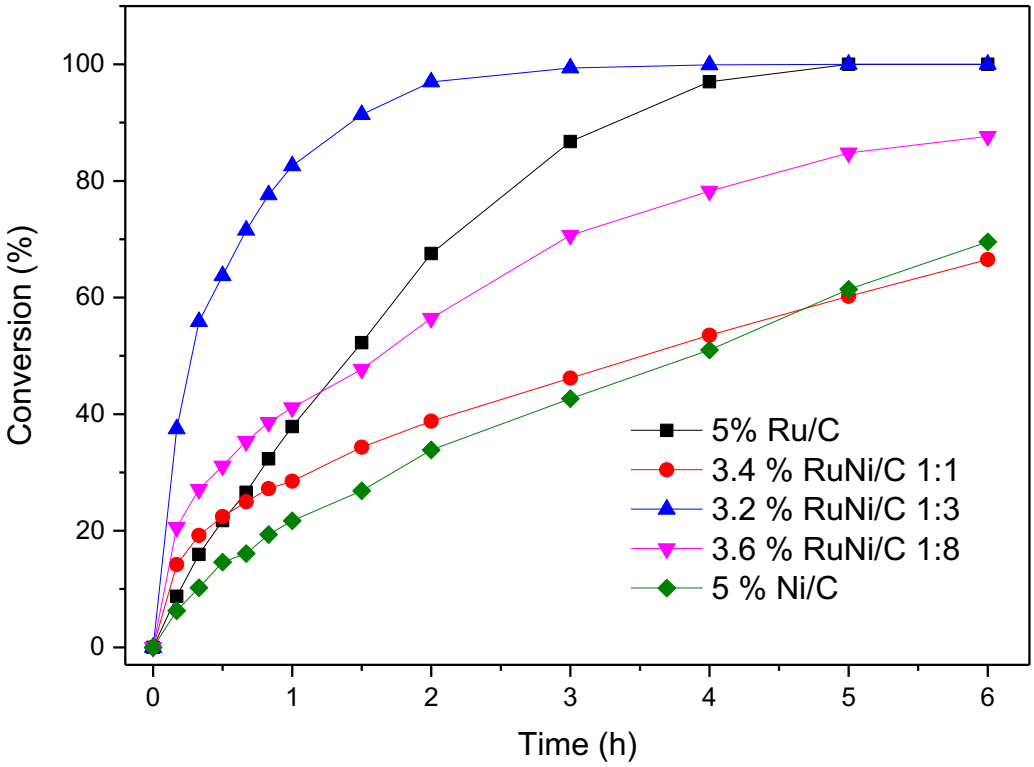

Figure 5.2.24 Conversion of HMF with the monometallic catalyst of 5 % Ru/C, 5 % Ni/C and bimetallic RuNi catalysts. Reaction conditions: HMF, 40 mM; catalyst, 60 mg; solvent, Dioxane; pressure, 20 bar H_2; temperature 150 °C stirring, 1100 rpm.

Figure 5.2.25 shows a comparison of DMF yields with the monometallic catalyst of 5 % Ru/C, 5 % Ni/C and bimetallic RuNi/C catalysts. DMF yields for all the bimetallic RuNi/C catalysts are better than monometallic of Ni/C which demonstrated the synergistic effect of Ru and Ni. Nevertheless, in terms of the rate of DMF formation, 5 % Ru/C shows a maximum yield of 83 % in 3 hours since Ru is better at hydrogenolysis of HMF to DMF compared to Ni as discussed in chapter 4, before decreasing due to the formation of ring hydrogenation (DMTHF) and ring opening products (2- hexanol). This could be due to the strong interaction of Ru active site on furan ring. [229] Bimetallic RuNi/C 1:3 showed the highest DMF yield after 6 hours with 92 %. This is therefore indicated that Ru-Ni/C bimetallic catalysts are more selective and stable than their

monometallic counterparts and that there is an optimum Ru: Ni ratio. The high selectivity of DMF in bimetallic RuNi especially with 1:1 ratio can be attributed to the suppression of the formation of ring hydrogenation products due to unreactive DMF with the bimetallic catalyst system as explained in the previous subchapter with Ru-Co. However, since Ni is more easily reduced than Co, the effect of Ni on the bonding of the furan on RuNi alloys is likely due to the oxophilicity of Ni, similar to what was reported for the effect of alloying of Ni-Fe and Ni-Pt alloy catalysts.[80, 230] The effect of oxophilic metal was discussed in chapter 1.

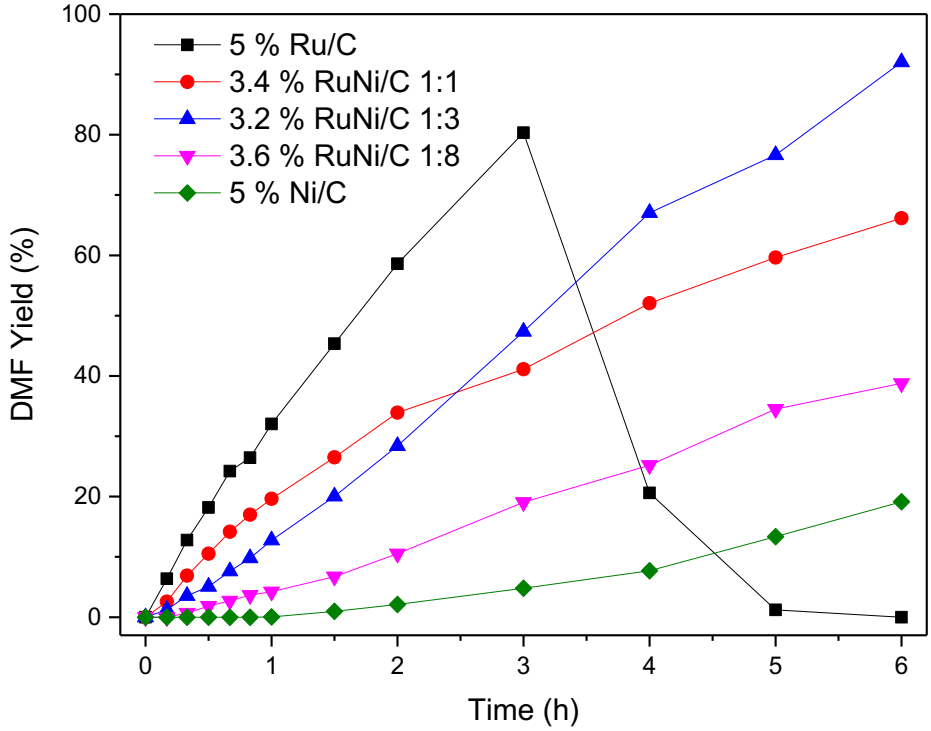

Figure 5.2.25 DMF yield with the monometallic catalyst of 5 % Ru/C, 5 % Ni/C and bimetallic RuNi catalysts. Reaction conditions: HMF, 40 mM; catalyst, 60 mg; solvent, Dioxane; pressure, 20 bar H_2; temperature 150 °C stirring, 1100 rpm.

Nevertheless, looking at the yield comparison it is possible that slightly higher metal loadings and a higher Ru:Ni would have produced enhanced yields per unit of time while retaining the higher selectivity induced by the alloy formation.

5.2.2.3 Effect of addition of Co to Ru on CNT

Finally, we want to exploit our findings in earlier chapters whereby much higher activities can be obtained with CNTs as supports. **Figure 5.2.26** shows a comparison of the conversion rates obtained with both monometallic catalysts and also with 3.5 % RuCo/C 1:5. 4.2 % RuCo/CNT 1:20 showed superior activity by fully converting HMF in less than 1 hour. This is much better than monometallic Ru/CNT, Co/CNT and our most active bimetallic catalyst (3.5 % RuCo/C 1:5 supported on C). The synergistic effect between Ru and Co still presence although CNT enhanced the reactivity of the catalysts as compared to carbon supported catalysts. This level of activity for 4.2 % RuCo/CNT 1:20 is surprising and very exciting, particularly considering that it contains 25 times less Ru than the 5% Ru/CNT.

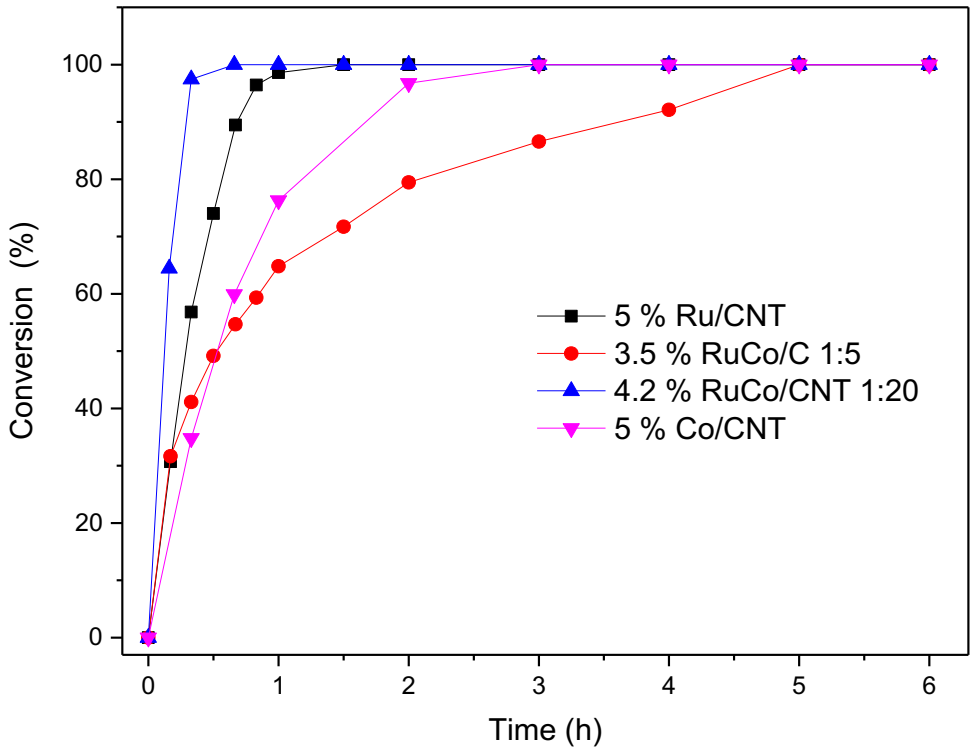

Figure 5.2.26 Conversion of HMF with the monometallic catalyst of 5 % Ru/CNT, 5 % Co/CNT and bimetallic RuCo/CNT catalysts. Reaction conditions: HMF, 40 mM; catalyst, 60 mg; solvent, Dioxane; pressure, 20 bar H_2; temperature 150 °C stirring, 1100 rpm.

The effect of CNT on bimetallic RuCo 1:20 on the DMF yield is displayed in **Figure 5.2.27**. It can be seen that CNT increased the speed of DMF conversion from

HMF to maximum before the yield decreased due to the formation of ring hydrogenation and ring opening products. However, Ru/CNT is slightly better in DMF yield with 83 % in 1 hour compared to RuCo/CNT 1:20 with 78 % in 2 hours. The product distribution of HMF hydrogenation over RuCo/CNT1:20 are shown in **Appendix 21**. However, for monometallic Co/CNT and carbon support catalysts, due to the slower activity of DMF, the reaction is more selective towards DMF. TOF calculation based on maximum DMF yield revealed that 4.2 % RuCo/CNT 1:20 has the highest TOF with 2153 h^{-1}.

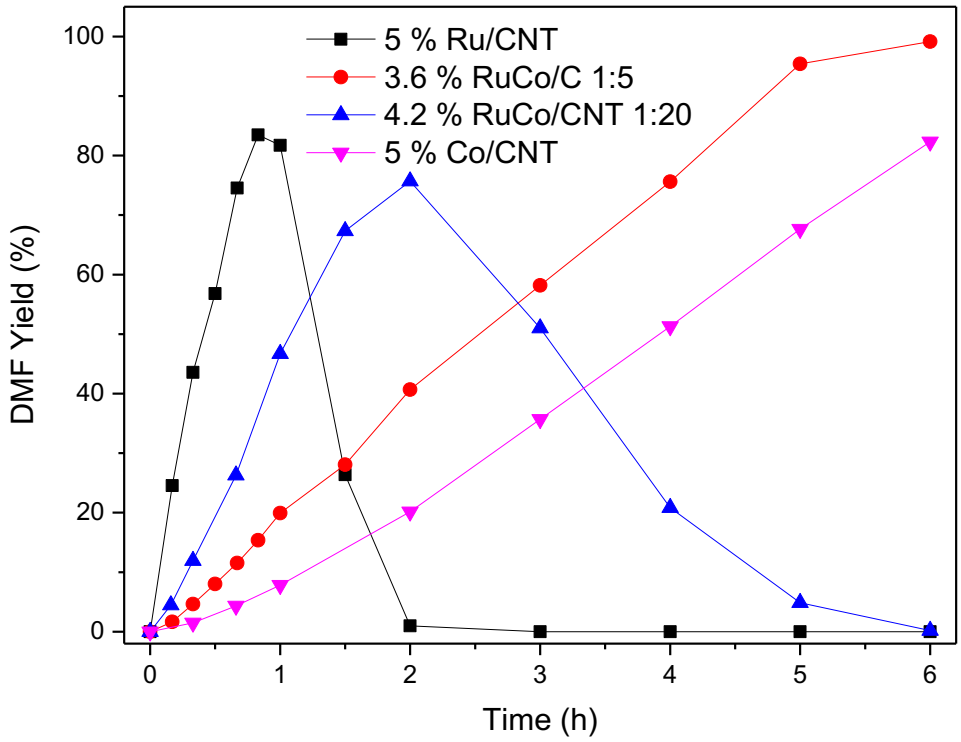

Figure 5.2.27 DMF yield with the monometallic catalyst of 5 % Ru/CNT, 5 % Co/CNT and bimetallic catalysts of RuCo (RuCo/C 1:5 and RuCo/CNT 1:20). Reaction conditions: HMF, 40 mM; catalyst, 60 mg; solvent, Dioxane; pressure, 20 bar H_2; temperature 150 °C stirring, 1100 rpm.

5.2.2.4 Effect of addition of Ni to Ru on CNT

The effect of CNT as support on the best bimetallic RuNi/C molar ratio was explored and the result is showed in **Figure 5.2.28**. 3.4 % RuNi/CNT 1:3 exhibited the best

reactivity in HMF conversion. HMF was fully converted in 1 hour, which is slightly better than 5 % Ru/CNT followed by 3.2 % RuNi/C 1:3 and 5 % Ni/CNT. This suggested that the enhancement of the reactivity of RuNi bimetallic is due to the synergistic effect of these metals apart from the effect of CNT as a support. It can be seen that bimetallic RuNi/C 1:3 had better reactivity than monometallic Ni/CNT which demonstrated the effectiveness of a synergistic effect between Ru and Ni. Nevertheless, it is shown that CNT improved the reactivity of the catalyst compared to the carbon supported catalyst as 3.4 % RuNi/CNT 1:3 has higher reactivity than 3.2 % RuNi/C 1:3.

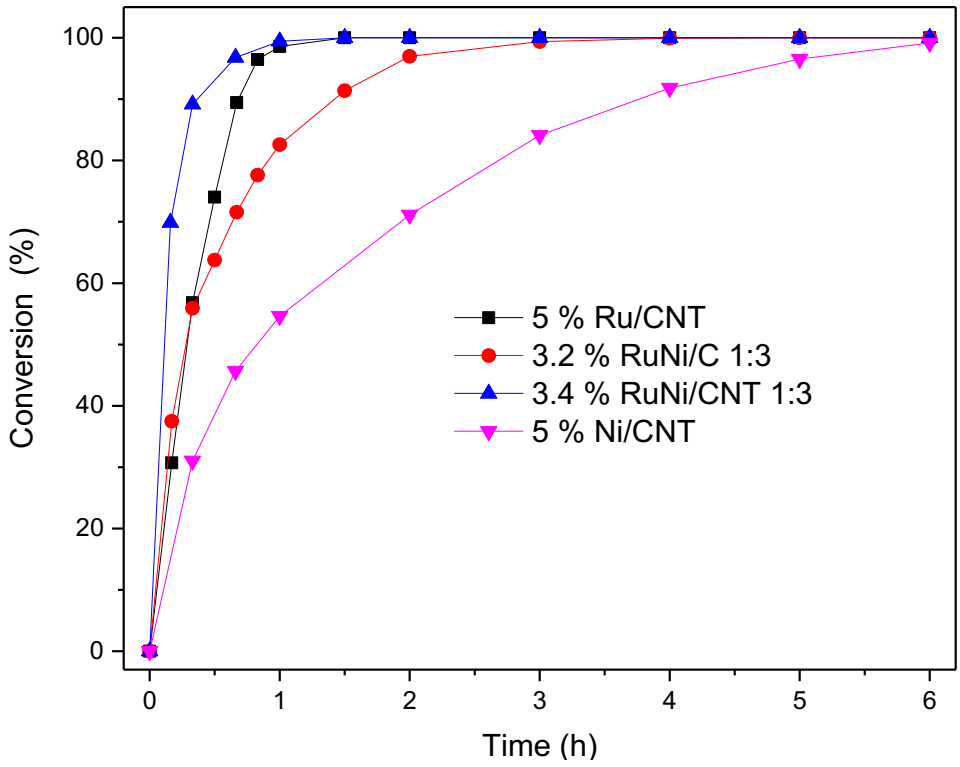

Figure 5.2.28 Conversion of HMF with the monometallic catalyst of 5 % wt. Ru/CNT, 5 % wt. Ni/CNT and bimetallic catalysts of RuNi (RuNi/C 1:3 and RuCo/CNT 1:3).Reaction conditions: HMF, 40 mM; catalyst, 60 mg; solvent, Dioxane; pressure, 20 bar H_2; temperature 150 °C stirring, 1100 rpm.

5 % Ru/CNT is the fastest catalyst in converting HMF into DMF with a maximum yield in 1 hour as shown in **Figure 5.2.29**. 3.4 % RuNi/CNT 1:3 is better than 5 % Ru/CNT in term of DMF yield (88 %) but longer reaction time needed to achieve high yield.

However, after 2 hours, DMF yield decreased due to the formation of ring hydrogenation, DMTHF and ring opening product, 2-hexanol as shown in **Appendix 22**. 3.4 % RuNi/CNT 1:3 was also demonstrated good conversion and DMF yield compared to monometallic of Ni/CNT. This again demonstrated the synergistic effect between Ru and Ni despite the type of support used. Surprisingly, 3.2 % RuNi/C 1:3 displayed the best selectivity toward DMF with the highest DMF yield 98 % after 6 hours. This suggested that the slower reactivity allowing the further formation of DMF without being converted into ring hydrogenation and ring opening products. TOF calculation based on maximum DMF yield revealed that 3.4 % RuNi/CNT 1:3 has the highest TOF value with 2082 h^{-1}.

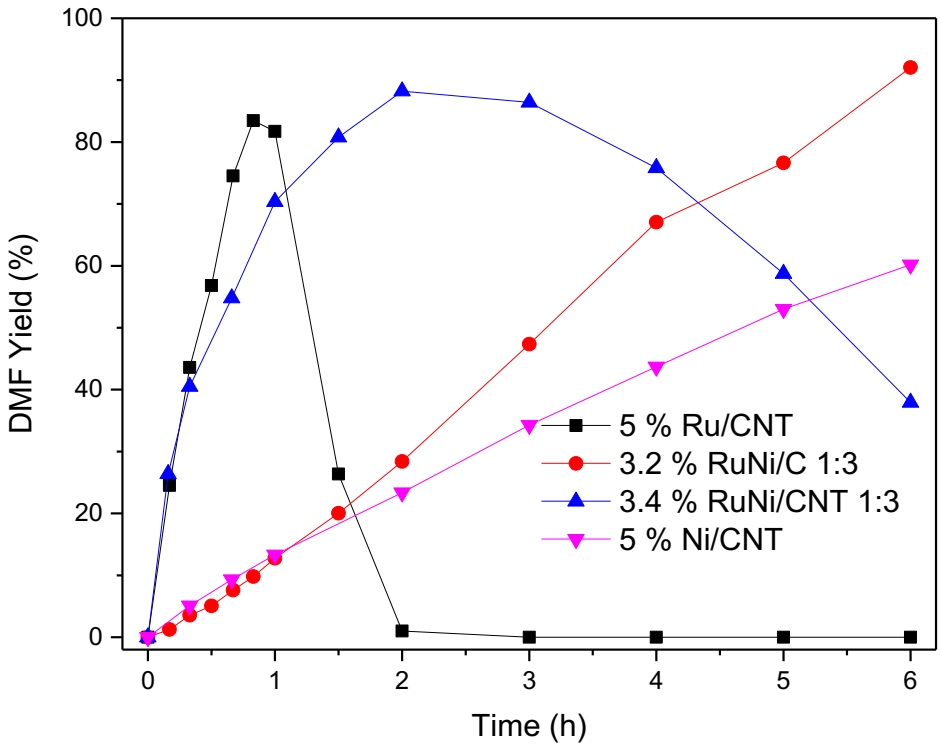

Figure 5.2.29 Conversion of HMF with the monometallic catalyst of 5 % Ru/CNT, 5 % Ni/CNT and bimetallic RuNi/CNT catalysts. Reaction conditions: HMF, 40 mM; catalyst, 60 mg; solvent, Dioxane; pressure, 20 bar H_2; stirring, 1100 rpm.

Table 5.2.6 summarised the catalytic activities (HMF conversion and DMF yield) with the characterization results of the bimetallic catalysts supported on carbon and CNT. Although we do not have sufficient experimental data to evaluate the particle size effect, it was observed that the HMF conversion and DMF yield do not correlate with

the particle size, although the most active catalysts displayed particle sizes between 2-3 nm which could indicate that the reaction is structure sensitive. The comparison of TOF with the particle size showed a variation.[218] It is most likely that hydrogenolysis reaction appears to need larger or specific aggregates of atoms as their active centres. For example, although RuNi/C 1:1 have the lowest particle size among RuNi catalysts, however, it showed the lowest HMF conversion and low DMF yield. Particles size between 2-4 nm seems to favour the HMF conversion and DMF yield. CNT as the support exhibited a clear improvement in the conversion of HMF can be seen based on the TOF (specific DMF yield at maximum) as the shorter time needed to obtain total conversion, however, DMF decreased as the reaction progress due to the formation of ring hydrogenation and ring opening products.

Table 5.2.6 HMF conversion, DMF yield, TOF and particle size of bimetallic catalysts supported on carbon and CNT.

catalyst	HMF conversion (%)	DMF yield (%)	TOF (h^{-1})[b]	Particle size (nm)[c]	TOF[d] ($^{h-1}$)
3.6 % RuCo/C 1:1	82	75	220	-	15
3.4 % RuCo/C 1:3	70	65	260	8.36	27
3.5 % RuCo/C 1:5	100	99	105	4.40	56
3.4 % RuNi/C 1:1	67	65	186	1.67	12
3.2 % RuNi/C 1:3	100	92	381	3.28	47
3.6 % RuNi/C 1:8	88	40	225	3.34	35
4.2 % RuCo/CNT 1:20[a]	100	76	2153	2.3	383
3.4 % RuNi/CNT 1:3[a]	100	88	2082	2.9	111

Reaction conditions: 30 ml 40 mM HMF; catalyst, 60 mg; solvent, Dioxane; pressure, 20 bar; stirring, 1100 rpm. Reaction time 6 hrs, [a] reaction time 2 hours, [b] TOF of maximum DMF yield based on CO chemisorption .[c] particle size based on TEM. [d] TOF of specific DMF yield based on mole of Ru. Experimental errors (conversion and yield = ± 0.07 %, TOF a = ± 0.05).

Figure 5.2.30 shows the TOL plot of specific yields of DMF based on Ru in the catalysts. This demonstrates that we are able to reduce the content of Ru in a catalyst an order of magnitude without losing much DMF yield. 3.5 % RuCo/C 1:5 (0.6 % Ru) and 3.2 % RuNi 1:3 (0.7 % Ru)have better specific DMF yield as compared to 5% Ru/C and 5 %

Ru/CNT. 4.2 % RuCo/CNT 1:2 with only 0.2 % loading of Ru showed the highest specific DMF yield. This finding is a positive outcome in order to reduce the dependent on the expensive noble metal without compromising the activity and the yield of desired product, in our case DMF.

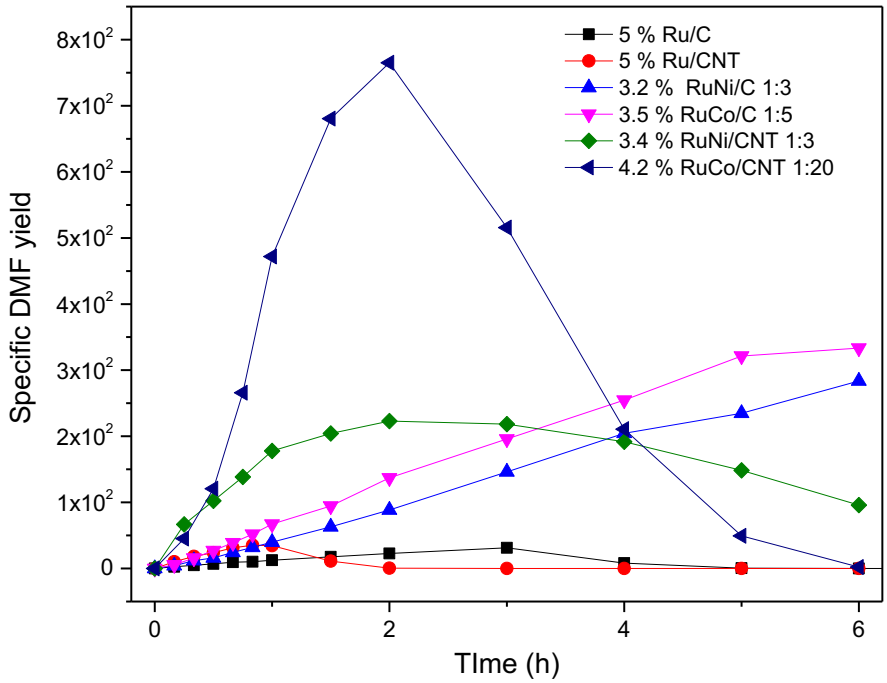

Figure 5.2.30 Specific DMF yield of the monometallic catalyst of 5 % Ru/C, 5 % Ru/CNT and bimetallic catalysts of RuNi (RuNi/C 1:3 and RuCo/CNT 1:3) and RuCo (RuCo/C 1:5 and RuCo/CNT 1:20). HMF, 40 mM; catalyst, 60 mg; solvent, Dioxane; pressure, 20 bar H_2; stirring, 1100 rpm. Specific DMF yield is calculated as moles of DMF produced over moles of Ru in the catalysts.

Overall bimetallic catalysts demonstrated superior HMF conversion as well as DMF yield. The specific yield was increased by 14 times over 3.5 % RuCo/C 1:5 and 12 times over 3.2 % RuNi/C 1:3 as compared to monometallic Ru/C. This clearly indicates that using Ru monometallic is not the most effective use of Ru, but that it must be combined to reduce the price while enhancing the yield of the target product.

5.3 Conclusions

In conclusion, a bimetallic catalyst consisting of Ru-Co and Ru-Ni displayed some improvement in catalytic activity of HMF conversion as well as DMF yield. It was shown that addition of Co and Ni to Ru in specific molar ratio demonstrated the synergistic effect of these catalysts as they showed better reactivity than the monometallic catalysts counterparts. The alloys formation was confirmed by XRD by the shift in the diffraction peaks due to the incorporation of Co and Ni to Ru structure.

As for Ru-Co/C catalysts, the molar ratio of 1:5 showed an excellent activity in HMF conversion as a high yield of DMF of 98 % after 6 hours was obtained. This could be due to the presence of CoO monolayer on the surface of the catalyst as confirmed by XPS analysis, which prevents the furan ring to be adsorbed in the planar position thus preventing the ring hydrogenation and ring opening products from forming. This phenomenon was also reported by previous literature that used PtCo bimetallic catalysts for HMF hydrogenation.

The effect of the addition of Ni to Ru also resulted in a positive result. Bimetallic RuNi/C 1:3 demonstrated the best activity and DMF yield compared to its monometallic counterpart as well as the other molar ratios of RuNi catalysts. Total HMF conversion was achieved in 3 hours with 98 % of DMF yield after 6 hours. This could be attributed to the synergistic effect normally derived upon the alloying of metals. The changes in the catalytic properties are associated with the changes in the electronic properties of the active component in the alloy.

The same promoting effect as in chapter 3 and 4 was observed when CNT was used as the support for bimetallic catalysts. The activities of supported catalysts with CNT were enhanced for both of RuNi/CNT and RuCo/CNT. Both catalysts achieved total HMF conversion in less than 1 hour better than Ru/CNT. However, in the case of DMF yield, bimetallic shows slower conversion than Ru/CNT. Nevertheless, RuNi/CNT 1:3 demonstrated higher yield than Ru/CNT and RuCo/CNT 1:20 with 90 % yield of DMF in 2 hours. This level of activity for RuCo/CNT 1:20 is surprising and very exciting, particularly considering that it contains 25 times less Ru than the 5% Ru/CNT.

Overall, the bimetallic system of RuCo and RuNi with specific molar ratios showed an improvement in reactivity compared to their monometallic counterparts, considering the lower loading of each metal compared to their monometallic counterparts. This proved the synergistic effect of this system. The only difference when different supports were used was that CNT improved the reaction rates however this is also lead to the formation of ring hydrogenation and ring opening products. Carbon has lower reaction rate however it gives better DMF yield after 6 hours. High yield of DMF was obtained even at low Ru content in a bimetallic catalyst without losing much DMF yield. 3.5 % RuCo/C 1:5 (0.6 % Ru) and 3.2 % RuNi 1:3 (0.7 % Ru)have better specific DMF yield as compared to 5% Ru/C and 5 % Ru/CNT. 4.2 % RuCo/CNT 1:2 with only 0.2 % loading of Ru showed the highest specific DMF yield. This finding is a positive outcome in order to reduce the dependence on the expensive noble metal without compromising the activity and the yield of desired product, in our case DMF. The specific yield was increased by 14 times over 3.5 % RuCo/C 1:5 and 12 times over 3.2 % RuNi/C 1:3 as compared to monometallic Ru/C. This clearly indicates that using Ru monometallic is not the most effective use of Ru, but that it must be combined to reduce the price while enhancing the yield of target product (DMF).

Chapter 6 A facile one-step microwave assisted carbonisation technique for the synthesis of Ru/C for HMF hydrogenation

5.1 Introduction

The utilisation of carbon material for heterogeneous catalysis has been explored by many scientists since it is one of the most abundant elements available. Most of the carbon materials like carbon black, activated carbon, carbon nanotubes and graphene have been widely used as a support to provide a surface area for the active metal for specific reactions[109-111, 231]. Although some of them are really good in facilitating the catalytic activity, they can be expensive, for instance, CNT and graphene. The exploitation of biomass as the source of carbon coupled with a suitable synthesis technique could provide more alternative for carbonaceous material with cost effective and environmentally friendly steps.[232]

Hydrothermal carbonisation, HTC is a process to increase the carbon content of biomass via dehydration reaction in aqueous solution under mild conditions. The use of hydrothermal synthesis between 180 and 220 °C allowed one to obtain various types of carbonaceous structures, namely powders, microspheres[233], spheroidal [234], nanofibers [235] or sponge-like mesoporous carbon that has many applications. [162] Up to now, several studies [236-239] have proved that different type of biomass could be used to obtain carbon under hydrothermal conditions, yet there is still a lack of clear comparison on the characterization of this material been made.

In the 20th century, the interest in synthetic coalification has brought the discovery of low-temperature hydrothermal synthesis of carbon spheres derived from sugar such as glucose. [240-242] Wang et al. found that hard carbon with a perfect spherical morphology was formed when glucose was hydrothermally treated at 190 °C for 5 hours before carbonised at a high temperature of about 1000 °C. It was also found that the particle size can be controlled by regulating the sugar concentration as well as the dwell time.[240] A study of hydrothermal carbons from various sources of biomass has been demonstrated by Titirici et al.[162] It was found that all sugars in their hexose form, degraded into HMF which finally condensed into a carbon-like material having the same morphological similarities and the same chemical and structural composition. **Figure 5.1.1** illustrated the structural model of carbon particle formed from hydrothermal carbonisation based on solid state NMR studies.

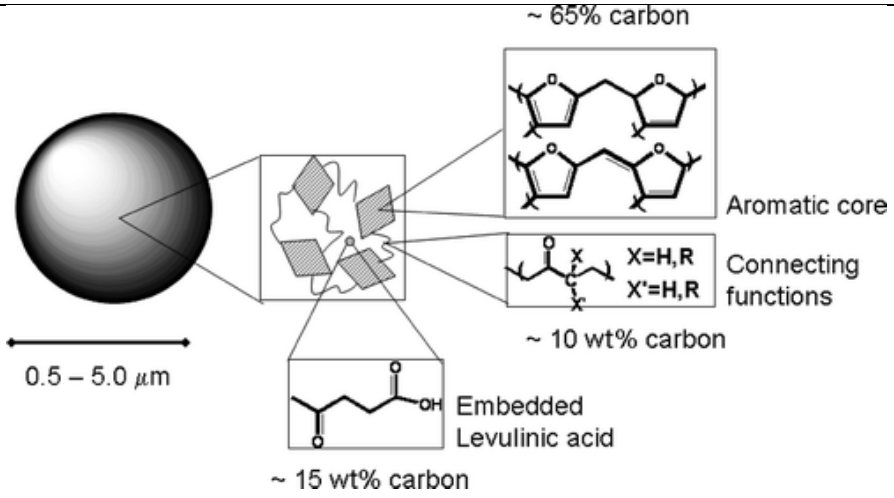

Figure 5.1.1 Structural model of carbon particle formed from hydrothermal carbonisation.[242]

The conventional synthesis of hydrothermal carbon using autoclave generally requires long reaction times. On the other hand, microwave heating has attracted a lot of interest in material synthesis due to its rapid heating, reduced synthesis time, energy savings and environmental friendliness.[163] A review on microwave synthesis of carbon materials has been discussed by Menendez et al. [243] Jung et al. have demonstrated the hydrothermal carbonisation of glucose using microwave-assisted heating at 210 °C for 15 min. Depending on the concentration of glucose solution, the average diameter of the formed particles varied from 201 to 650 nm.[161]

Performing the HTC in the presence of metal cation has shown to accelerate the HTC of starch, shortening the reaction times several hours, resulting in the synthesis of various metal-carbon nano-architectures.[244] Yu et al. have synthesised metal/carbon nanocables by one-pot hydrothermal carbonisation co-reduction process using starch and noble metal salts as starting materials.[245] The synthesis was done at 160 °C in an autoclave for 12 hours. It was reported that HTC reaction of glucose with metal salts produced a variety of metal/metal oxide/HTC as a result of reductive properties of glucose. [246]

In this chapter, we want to combine the two aforementioned approaches in the one-pot synthesis of HTC supported metal catalysts containing mainly Ru using the microwave. The resulting metal supported HTC catalysts were then tested for HMF hydrogenation to firstly compare with the conventional impregnation techniques and evaluate whether much of the metal in the synthesis would be available to catalyse the reaction. The effect of catalyst preparation was also investigated where Ru was

supported on carbonised HTC via incipient wetness impregnation as opposed to the one-pot synthesis via microwave.

5.2 Results and Discussion

Characterization and catalytic activity of prepared HTC and Ru/HTC in HMF hydrogenation will be discussed in this chapter.

5.2.1 Characterization

Characterization of prepared HTC and Ru/HTC using characterization techniques such as XRD, ICP-OES, elemental analysis, TGA, SEM, and chemisorption will be discussed in this subchapter.

5.2.1.1 Optimisation of HTC synthesis conditions

In order to optimise the synthesis of HTC to be used as the support several parameters such as temperature; time, the effect of stirring as well as the effect of using conventional autoclave and microwave were varied during the synthesis. **Table 5.2.1** summarised the yield and carbon content of synthesised HTC.

The synthesis of HTC via autoclave (entry 1) was used at the benchmark to compare with the microwave assisted HTC synthesis. As expected, HTC synthesis via microwave required half the time of autoclave method to obtain the same yield of carbon (entry 3). As shown in Table 6.2.1, the synthesis temperature in the range of 180-210 °C did not show any significant difference in terms of HTC yield as well as carbon content, although higher temperature favours higher content of carbon. This is because these ranges of synthesis temperature were found to be the optimum temperature based on the previous work.[160] At lower temperature such as 130-160 °C carbon content tends to be low. As for HTC yield, the theoretical value that is achievable when glucose is used as starting material is 60 %. This value can be explained by the mechanism of HTC where, from each molecule of glucose that reacts to form HTC carbon, four water molecules (40 % of the starting mass) are eliminated. [248] These represent an unavoidable yield loss which must be taken into account.

Table 5.2.1 Summary of HTC yield and a carbon content from various synthesis conditions.

Entry	HTC	Synthesis Conditions			HTC yield (%)[a]	Carbon (%)[b]	Particle Size (nm)
		Glucose Concentration (M)	(°C)	time (h)			
1	HTC 1[c]	0.6	180	24	38	65	-
2	HTC 2	0.6	180	6	40	59	-
3	HTC 3	0.6	180	12	43	65	581±70
4	HTC 4	0.6	200	6	41.	67	517±49
5	HTC 5[c]	0.6	180	48	39	66	-
6	HTC 6[d]	0.6	200	6	40	64	534±58
7	HTC 7	0.6	200	5	36	65	-
8	HTC 8	0.6	200	4	38	66	539±66
9	HTC 9	0.6	200	3	38	66	490±60
10	HTC 10	0.6	200	6	35	64	-
11	HTC 11[d]	0.6	200	1	-	-	447±53
12	HTC 12[d]	0.6	200	0.5	-	-	-
13	HTC 13	0.5	210	0.25	-	-	-
14	HTC 14	1	210	0.25	-	-	426±48
15	CNT	-	-	-	-	82	-
16	Norit SX Plus	-	-	-	-	87	-
17	HTC_{550}	-	-	-	-	87	-

[a]Yield based on the initial weight of glucose. [b] based on the C-H-N-S elemental analysis. [c] synthesis using autoclave and conventional heating [d] with stirring

It can be seen that for HTC synthesis via microwave, it takes a shorter amount of synthesis time compared to the autoclave for the same yield or carbon content (HTC 1 and 3). This showed that microwave synthesis could replace the conventional autoclave for HTC synthesis reducing synthesis times at least four times.

Following the previous results of synthesised HTC, reaction conditions of 6 hours at 200 °C were chosen as it gives better thermal stability up to 550 °C with only 45 % weight loss compared to other sample prepared in the microwave reactor as shown by TGA plots in **Figure 6.2.1**. Furthermore, from SEM results, it was shown to have more uniform particle size compared to other conditions.

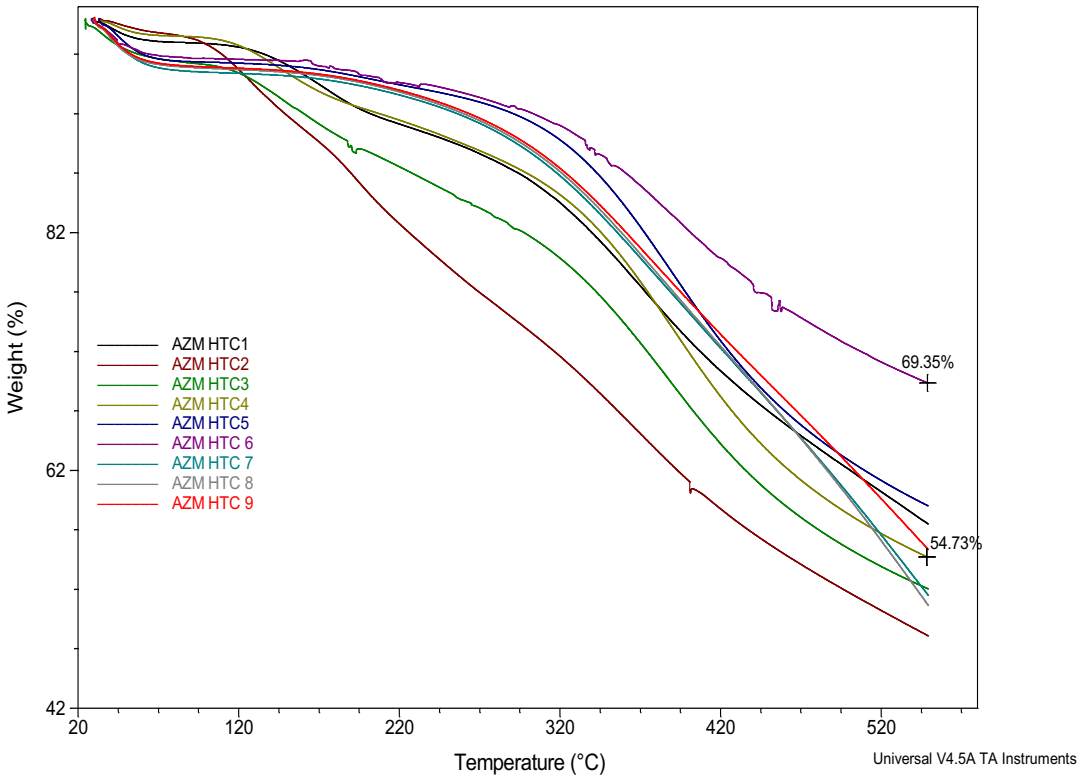

Figure 6.2.1 TGA plots of synthesised HTC from glucose at various conditions. TGA conditions: N_2 flow, heating rate 10 °/min. HTC 6 showed 69.35 % weight remaining at 550 °C while HTC 4 with only 54.73 % weight remaining.

In order to improve the HTC as a support for the catalyst, several tests were done to improve the surface area by varying the time of synthesis (3, 4 and 5 hours) and the effect of stirring. It was found that with stirring, HTC produced was more thermally stable as showed in TGA analysis (**Figure 6.2.1**) with almost 70 % weight remaining at 550 °C. HTC without stirring only had 55 % weight remaining at 550 °C. It was speculated that stirring increase the rate of polymerization thus improved the thermal stability.[247] As for the effect of synthesis time, shorter time did not show significant differences in terms of particle size (**Figure 6.2.6**). **Table 6.2.2** shows the HTC supported catalyst synthesised at different synthesis conditions.

Table 6.2.2 HTC supported catalyst with different synthesis conditions.

Entry	Catalysts	Synthesis Conditions		
		Temperature (C)	Time (hr)	Glucose Concentration (M)
1	Ru/HTC	200	6	0.6
2	Ni/HTC	200	6	0.6
3	Co/HTC	200	6	0.6
4	Ru/HTC1	200	1	0.6
5	Ru/HTC2	210	0.25	1.0

Ru on HTC with were synthesised using the one-step microwave technique. In a typical process, for Ru/HTC, 2.5 g of glucose and a specific amount of metal salts were dissolved in deionized water (23 ml). The solution was sealed in 35 ml glass vessel and heated to 200 °C for 6 hours using the microwave. The product was collected by filtration, washed with deionized water and alcohol before dried in vacuum oven at 60 °C. For the rest of catalyst supported on HTC1 and HTC2, the steps were the same apart from varying the concentration of glucose, time and synthesis temperature.

5.2.1.2 Inductive Coupled Plasma- Optical Emission Spectroscopy, ICP-OES

ICP of prepared catalyst was done to determine the actual metal loading of the catalysts. The results are shown in **Table 6.2.3**. It can be seen that one-pot method has more metal leaching compared to incipient wetness impregnation. For Ru/HTC catalysts the amount of metal leaching is correlated with the synthesis time. Lower loading obtained as the synthesis time shorten to 0.25 hours. It is also speculated that the lower loading could be due the poor digestion prior to ICP as seen in Chapter 5. This could affect the performance of the catalyst since the active site depends on the catalyst loading if the dispersion is good.

Table 6.2.3 ICP-OES result of prepared catalysts supported on HTC.

Entry	Catalysts	Theoretical loading (%)	ICP loading (%)
1	Ru/HTC	5	3.16
2	Ru/HTC IW	5	4.00
3	Ru/HTC 1	5	2.00
4	Ru/HTC 2	5	0.40
5	Ni/HTC	5	0.60
6	Co/HTC	5	0.20

6.2.1.3 X-Ray Diffraction, XRD

The synthesised HTC were analysed with XRD and **Figure 6.2.2** shows the XRD patterns of synthesised HTC. It can be seen that the diffraction peaks at 2θ = 16° and 42.9° can be assigned to carbon and graphite which were matched with JCPDS no. 01-074-2330. The large noisy bump in a wide range of 2 θ instead of high intensity peaks observed for ordered crystalline material indicates that HTC is mostly amorphous. A similar finding was observed by Titirici et al. [244] and Zheng et al.[234]

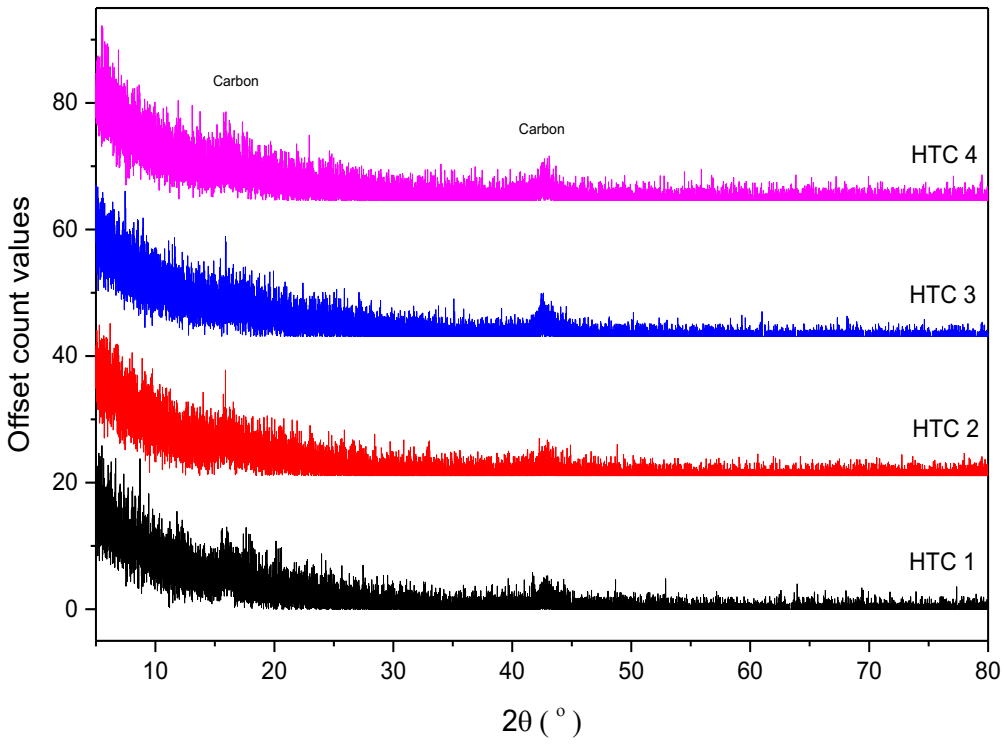

Figure 6.2.2 XRD patterns of synthesised HTC.

Figure 6.2.3 shows the XRD patterns of synthesised catalysts supported on HTC. It can be seen that the synthesised catalyst on HTC was mostly in an amorphous form based on the broad peak of the diffraction patterns. It can be seen that the diffraction peak at 2θ = 42.9° which can be assigned to carbon (JCPDS no. 01-074-2330) was less intense compared to as-synthesised HTC. However, the carbon peak at 18° was broader which corresponding to the structure of carbon with hexagonal phase (JCPDS no. 75-1621). The broadening of these peaks suggests the possible presence of an amorphous carbon phase.[234] The absence of diffraction patterns of Ru and Ni could be due to the low loading of metal as revealed by ICP-OES analysis as well as possibly small particle size.

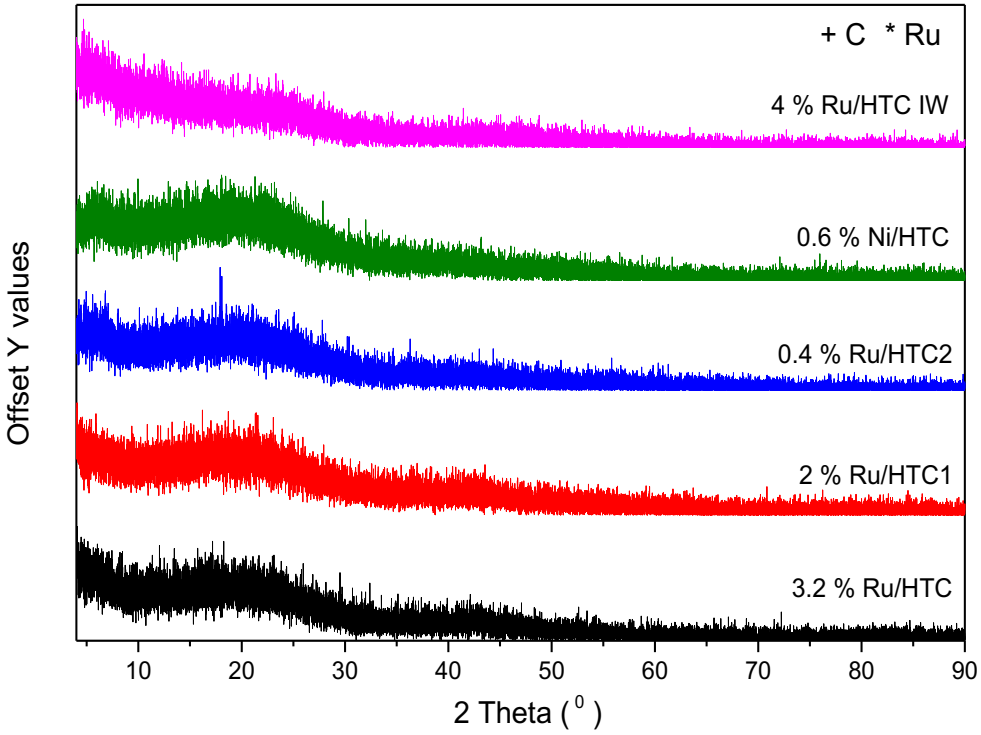

Figure 6.2.3 XRD patterns of synthesised catalysts supported on HTC.

6.2.1.4 Temperature Programmed Reduction (TPR)

Temperature programmed reduction (TPR) was performed on the synthesised HTC and Ru supported HTC to understand the activation of catalysts as well as reduction profiles of catalysts under H_2 atmosphere. **Figure 6.2.4** shows TPR plots of 5 % wt. Ru/HTC compared to HTC blank, Ru/C. It can be seen that the H_2 uptakes for Ru/HTC are lower

compared to Ru/C both IW and Sigma. It could suggest that most of the Ru is already reduced. This is in the agreement with literature that glucose has a reductive property which could reduce the metal into it metallic state.[246] The negative peak observed (3.2 % Ru/ HTC) around 140 °C could be due to the technical issue when the H_2 flow stopped while the experiment was conducted. It was also proposed that the aldehyde groups of the carbohydrate were responsible for the in-situ reduction of the metal salts resulting in carbon materials loaded with metallic nanoparticles.[232] However, it can be noticed that the huge peak at 400 to 800 °C indicated that the gasification/decomposition of carbon. It was more pronounced in the case of HTC when compared to carbon.

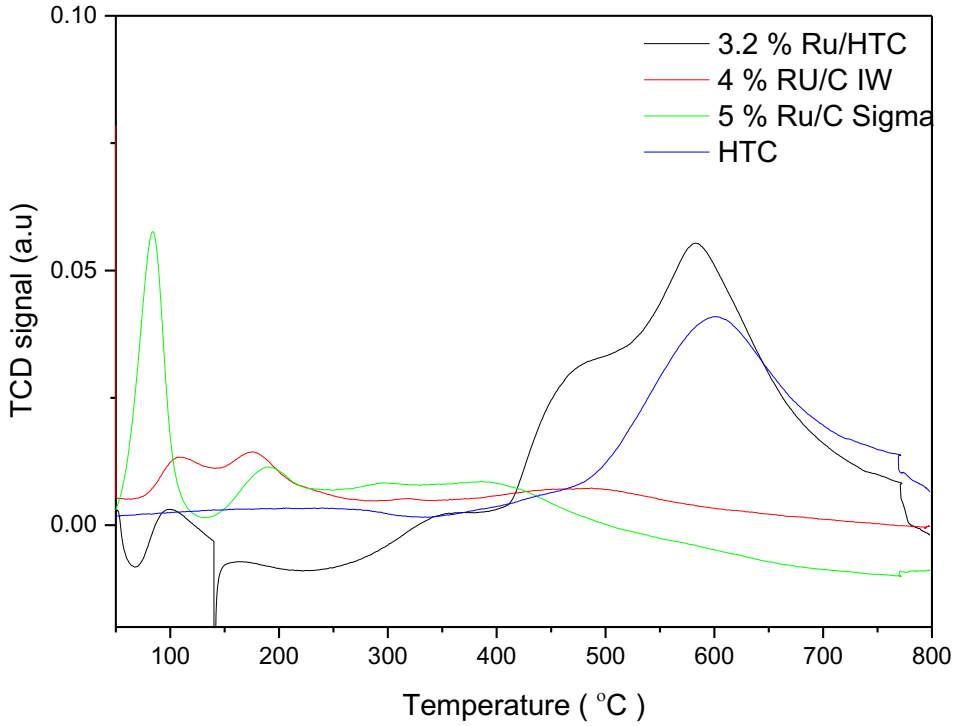

Figure 6.2.4 TPR profiles of synthesized HTC, 3.2 % Ru/HTC, 4 % Ru/C IW and 5 % Ru/C sigma.

6.2.1.5 CO Chemisorption

The quantification of active metal sites and the dispersion was investigated by CO chemisorption as shown in

Table 6.2.4. It can be seen that 2 % Ru/HTC1 has the highest CO uptakes while 0.4 % Ru/HTC 2 has the lowest. However, 0.4 % Ru/HTC 2 shows the highest dispersion with 2.50 %. This could be related to the Ru loadings in each catalyst as determined by ICP-OES (**Table 6.2.3**).

Table 6.2.4 CO uptakes and dispersion of catalyst supported on HTC from chemisorption.

Entry	Catalysts	CO uptakes (µmol/g)	Dispersion, D (%)
1	3.2 % Ru/HTC	1.51	0.50
2	4 % Ru/HTC IW	1.38	0.35
3	2 % Ru/HTC 1	1.70	0.90
4	0.4 % Ru/HTC 2	0.98	2.50

*2 % Ru/HTC1 were synthesized with the same condition as HTC 11 and 0.4% Ru/HTC 2 was synthesized with the same condition as HTC 14 (Table 6.21)

6.2.1.6 Scanning Electron Microscopy, SEM

The morphology and particle sizes of synthesised HTC were examined by SEM. The particles size distribution was determined based on ca. 200 particles counting.

6.2.1.6.1 Effect of Stirring

Figure 6.2.5 shows the SEM images of the carbonaceous structure of hydrothermal carbon synthesised via microwave at 200 °C for 6 hours with and without stirring, HTC4 and HTC 6 respectively. The structures of both HTC showed an interconnected spherical shape with mean particle sizes of 517±49 nm and 534±58 nm. It can be seen that stirring did not affect much on the morphology of synthesised HTC as many literatures did not perform synthesis with the stirring effect. However, it was learned that stirring effect enhanced the thermal stability of synthesised HTC as revealed from TGA analysis as previously discussed subchapter 6.2.1.1.

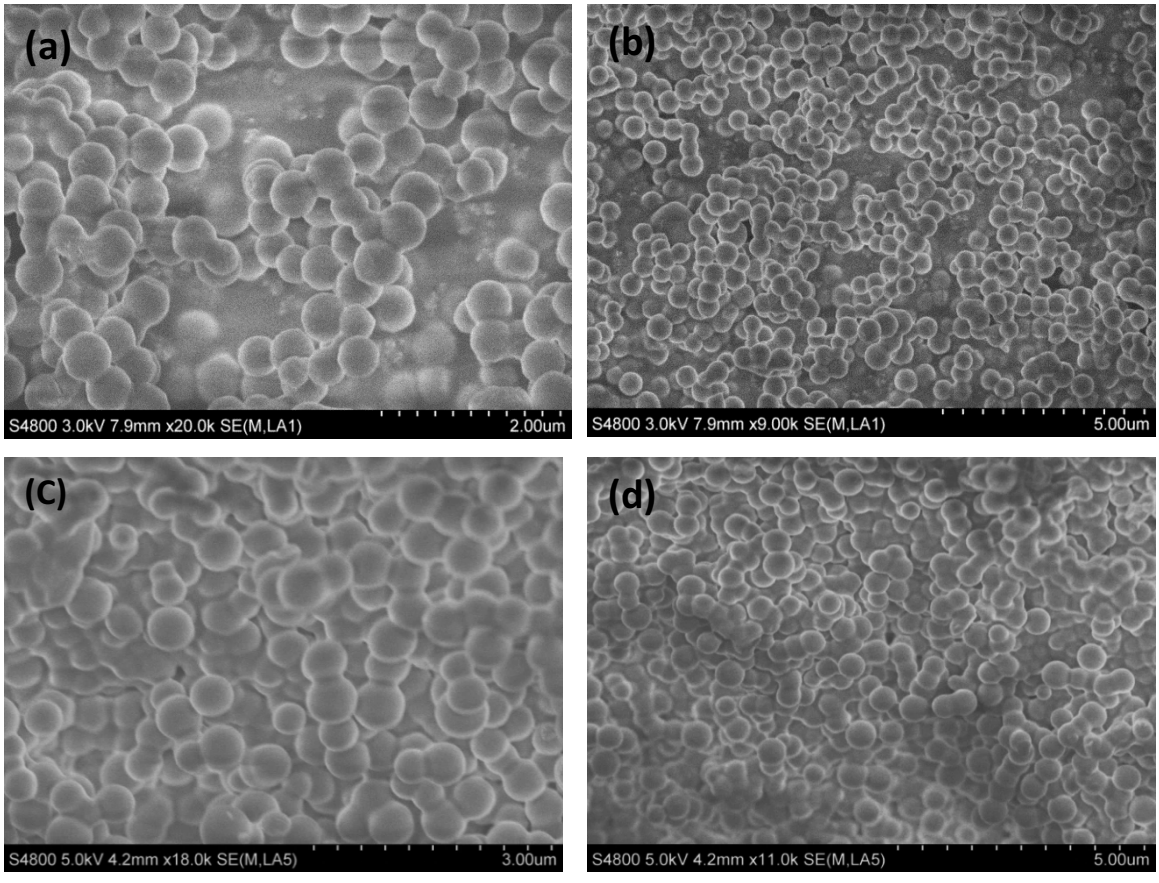

Figure 6.2.5 SEM images of HTC4 (a), (b) and HTC 6 (c), (d).

Figure 6.2.6 shows the particle size distributions of HTC 4 and HTC 6. Both HTCs have narrow particles size distribution ranging from 0.3 to 0.7 um. However, HTC without stirring has more uniform particle size distribution and slightly smaller mean size.

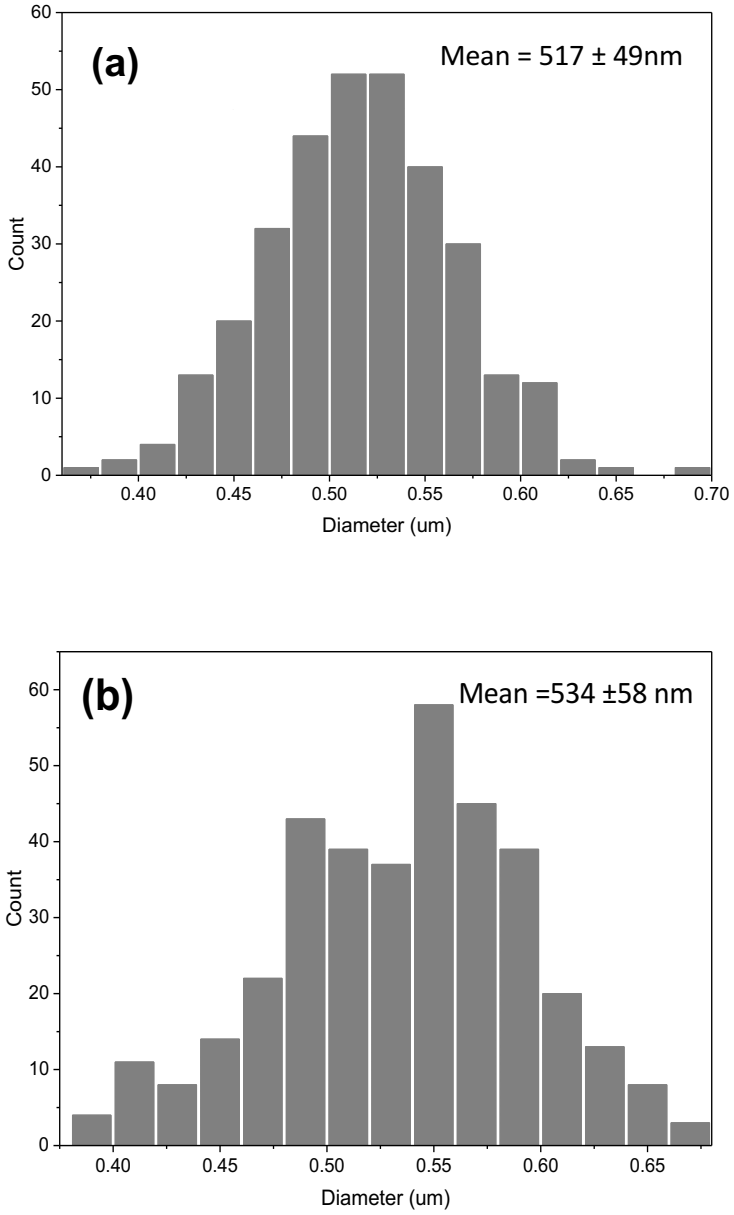

Figure 6.2.6 Particle size distribution of HTC4 (a) and HTC 6 (b) based on SEM and ca. 200 particles.

6.2.1.6.2 Effect of synthesis time

Figure 6.2.7 shows the SEM images of HTC 9 (a), (b) and HTC 11 (c), (d) which was synthesised in 3 and 1 hour. It can be seen that the particle is less uniform with a shorter amount of time. However, the mean particle size decreased from 490 to 447 nm as the synthesis time was decreased from 3 to 1 hours. The same findings were reported in the literature regarding the effect of synthesis time.[240, 241]

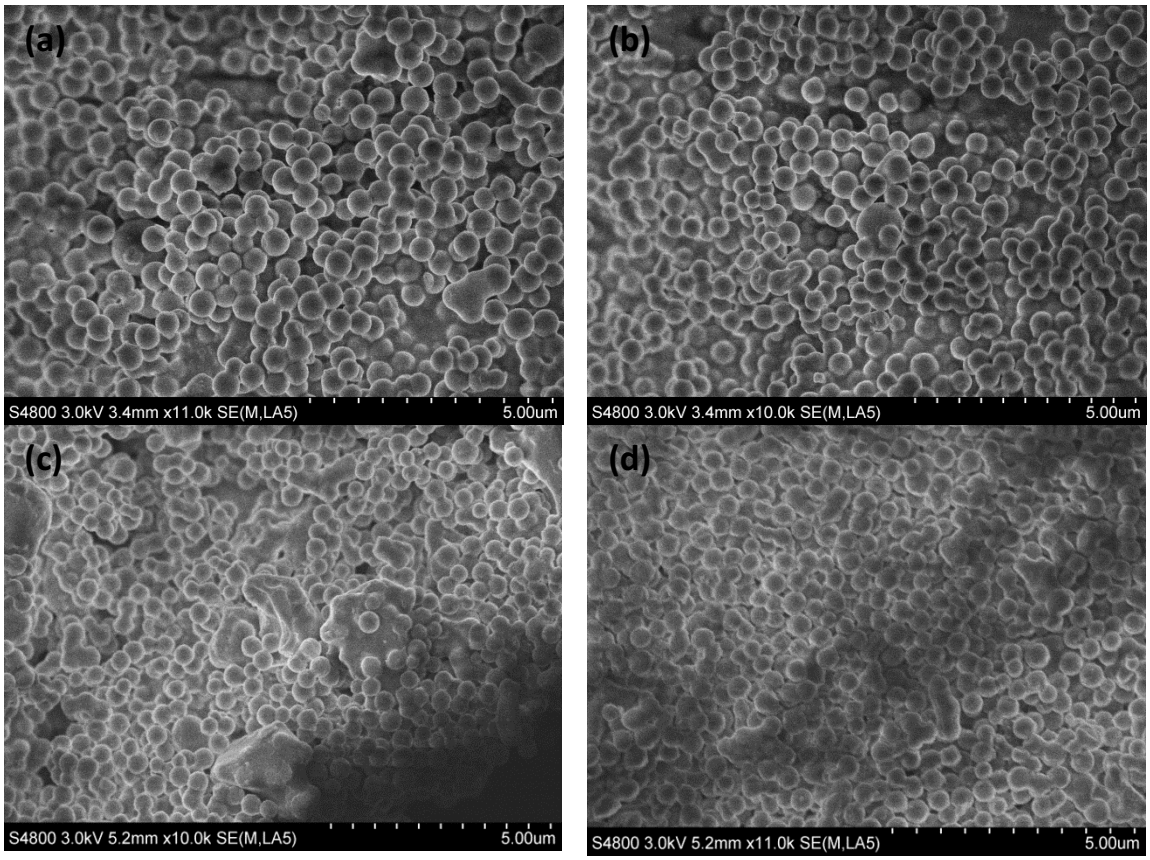

Figure 6.2.7 SEM images of HTC9 (a), (b) and HTC 11 (c), (d)

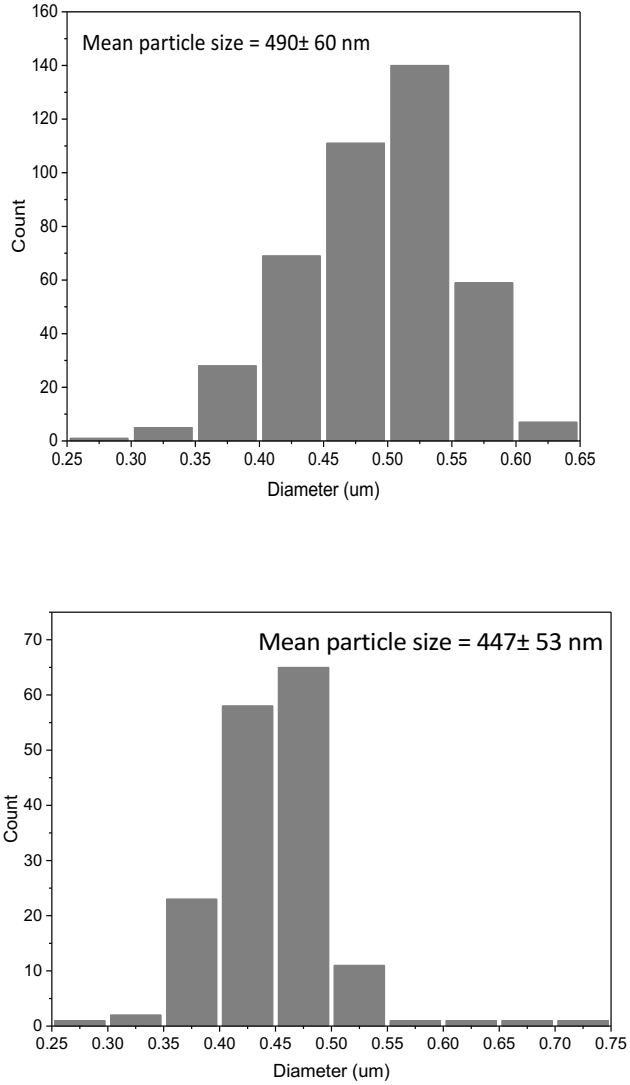

Figure 6.2.8 Particle size distribution of HTC9 (a) and HTC 11 (b) based on SEM and ca. 200 particles.

In order to further optimise the surface area of HTC, different concentration of glucose, temperature and time were varied as tabulated in **Table 5.2.1**. HTC 13 and HTC 14 were reproduced from previous work on HTC which resulted in smaller particle sizes. [161] **Figure 6.2.9** shows the SEM images and the particle size distribution of HTC 14. SEM images showed that HTC 14 has a uniform particle size and the histogram analysis revealed that the average particle size was 426±48 nm, which was smaller than other HTCs synthesised at different conditions. This trend is in agreement with Jung et al.[161]

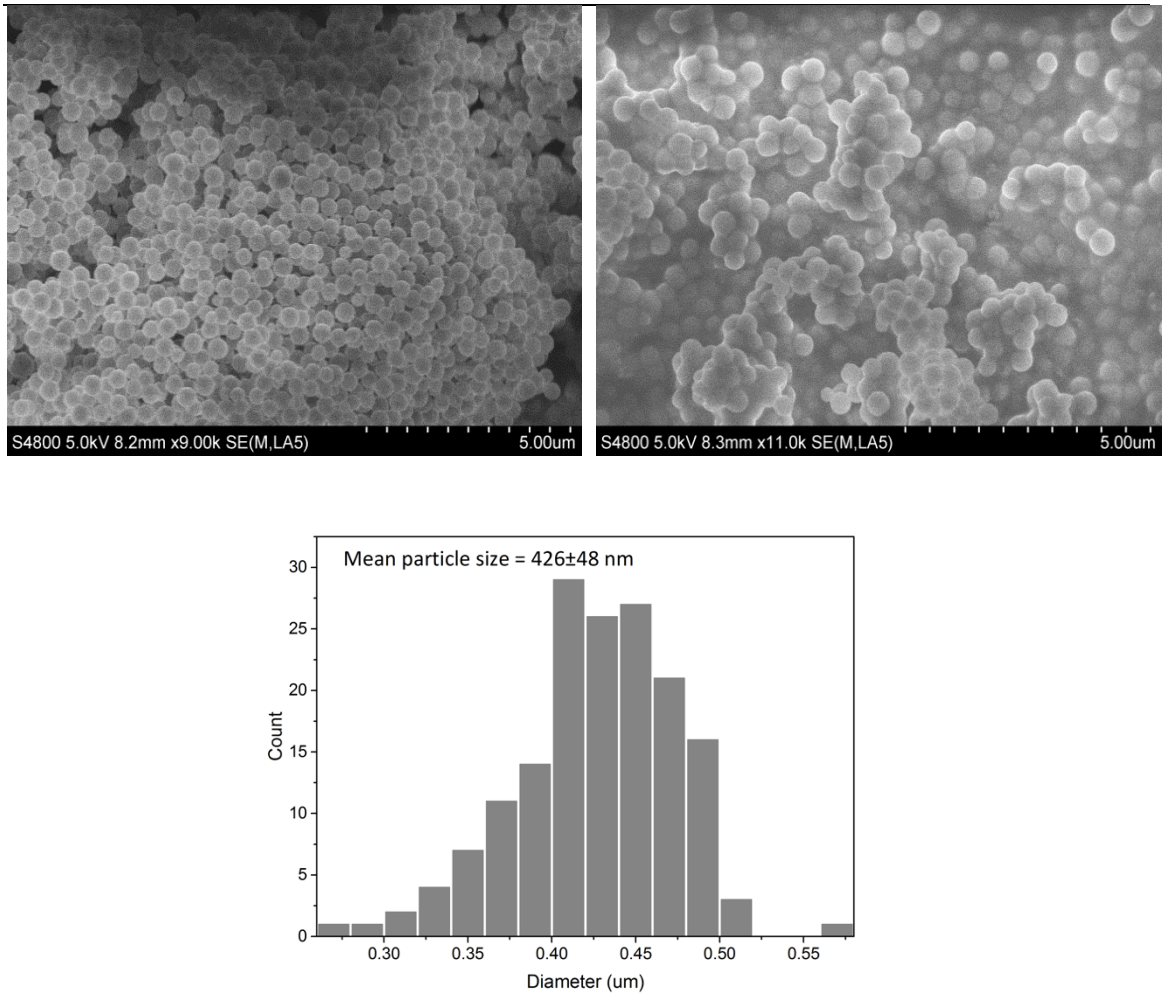

Figure 6.2.9 SEM images and particle size distribution based on SEM and ca. 200 particles of HTC 14

6.2.2 Hydrogenation of HMF to DMF

The effect of HTC as the support was investigated by performing HMF hydrogenation. Hydrogenation of HMF to DMF was performed using 3.2 % wt. Ru/HTC synthesised in the microwave reactor with different synthesis condition as shown in **Table 6.2.5**.Reaction conditions: temperature 150 °C, H_2 pressure 20 bar, catalyst; 60 mg, time; 6 hr, solvent; Dioxane.

Table 6.2.5 Ru supported on HTC with different synthesis conditions.

Entry	Catalysts	Synthesis Conditions		
		Temperature (C)	Time (hr)	Glucose Concentration (M)
1	3.2 % Ru/HTC	200	6	0.6
2	2.0 % Ru/HTC1	200	1	0.6
3	0.4% Ru/HTC2	210	0.25	1.0

Figure 6.2.10 showed the TOL plot of HMF hydrogenation with 3.2 % Ru/HTC catalyst for 6 hr. It can be seen that 43 % of HMF was converted to DHMF with 100 % selectivity (43 % yield). This suggested that 3.2 % Ru/HTC is not very good at hydrogenolysing DHMF intermediate to DMF which is the key point in DMF production. Longer reaction time possibly needed in order to convert DHMF to DMF.

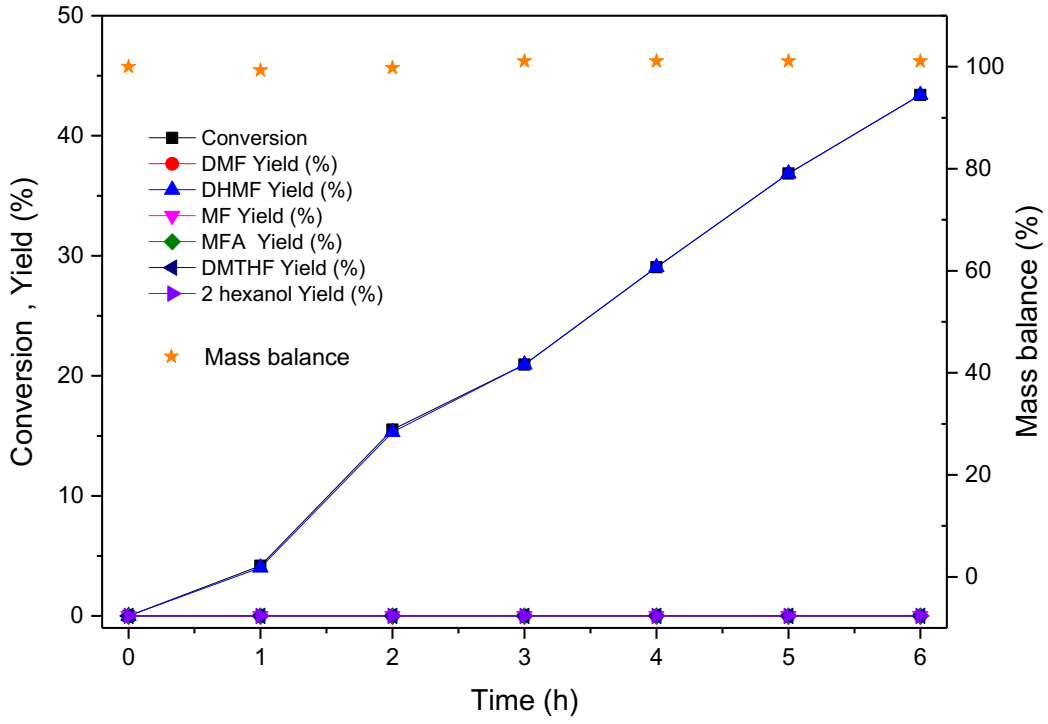

Figure 6.2.10 TOL reaction of HMF hydrogenation with 3.2 % Ru/HTC. Reaction condition: 30 ml of HMF (40 mM), temperature 150 °C, H_2 pressure 20 bar, catalyst; 60 mg, time; 6 hr, solvent; Dioxane.

When a reaction with reduced 3.2 % Ru/HTC was performed as shown in **Figure 6.2.11**, the conversion was slightly lower with only 35 % conversion and DHMF being the main product. Moreover, there was still no DMF being converted from DHMF. This catalyst seemed to have partially hydrogenated HMF to DHMF. This suggested that reduction under H_2 did not improve the reactivity as Ru was already reduced by glucose during the synthesis as confirmed by TPR analysis.

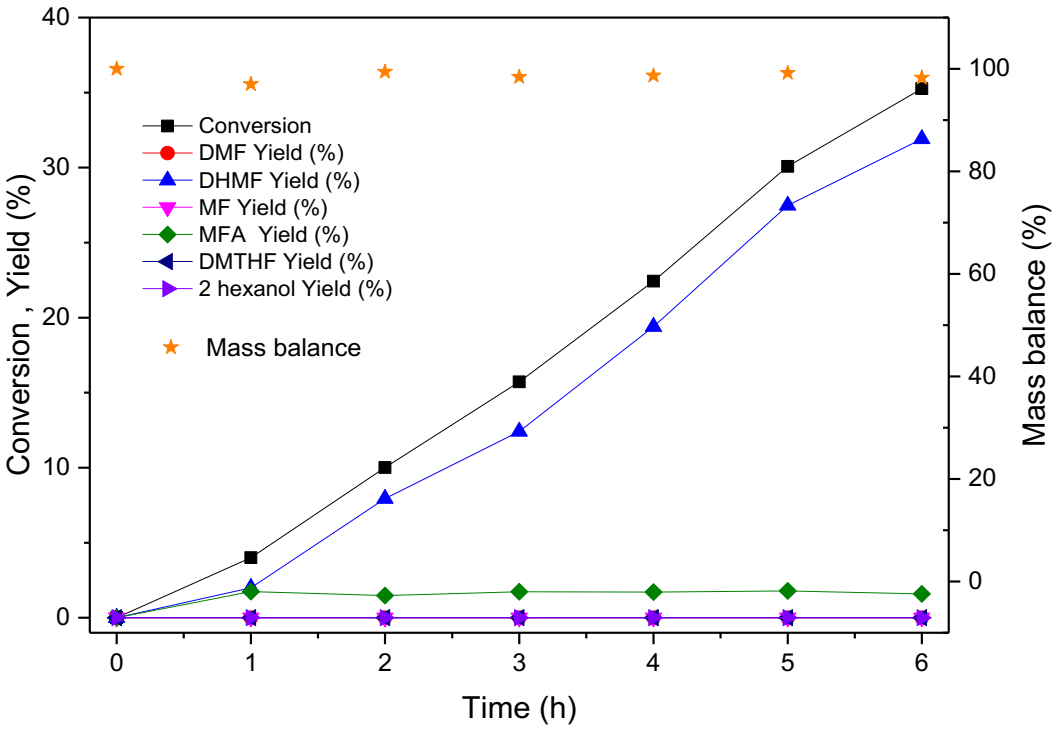

Figure 6.2.11 TOL reaction of HMF hydrogenation with 3.2 % Ru/HTC RED. Reaction conditions: 30 ml of HMF (40 mM), temperature 150 °C, H_2 pressure 20 bar, catalyst; 60 mg, time; 6 hr, solvent; Dioxane.

Figure 6.2.12 shows the TOL plot of the reaction profile of 2 % Ru/HTC1 after 6 hr. It can be seen that HMF conversion was increased to 73 % after 6 hours compared to 2 % Ru/HTC1 Ru/HTC reaction (43 %). This could be due to the smaller particle size of the support which gives more surface area as well as the dispersion as shown in **Table 6.2.4**. However, the selectivity towards DHMF still remained the same.

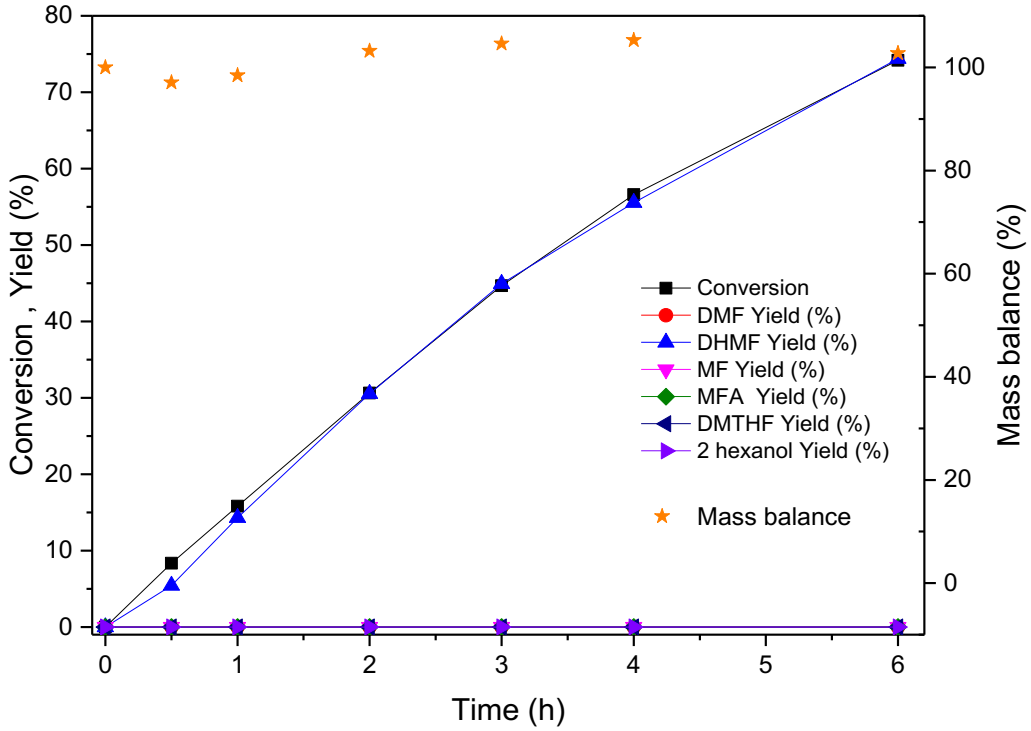

Figure 6.2.12 TOL profile of HMF hydrogenation with 2.0 % Ru/HTC1. Reaction condition: 30 ml of HMF (40 mM), temperature 150 °C, H_2 pressure 20 bar, catalyst; 60 mg, time; 6 hr, solvent; Dioxane.

In order to further investigate the effect of synthesis conditions, 0.4 % Ru/HTC 2 was synthesised with more concentrated glucose (1 M) and shorter synthesis time (15 min) as well as higher synthesis temperature (210 °C). The TOL reaction profile is shown in

Figure 6.2.13. It can be seen that HMF conversion was 49 % after 6 hours with DHMF being the most product produced with 40 % yield followed by MFA with 4 % yield.

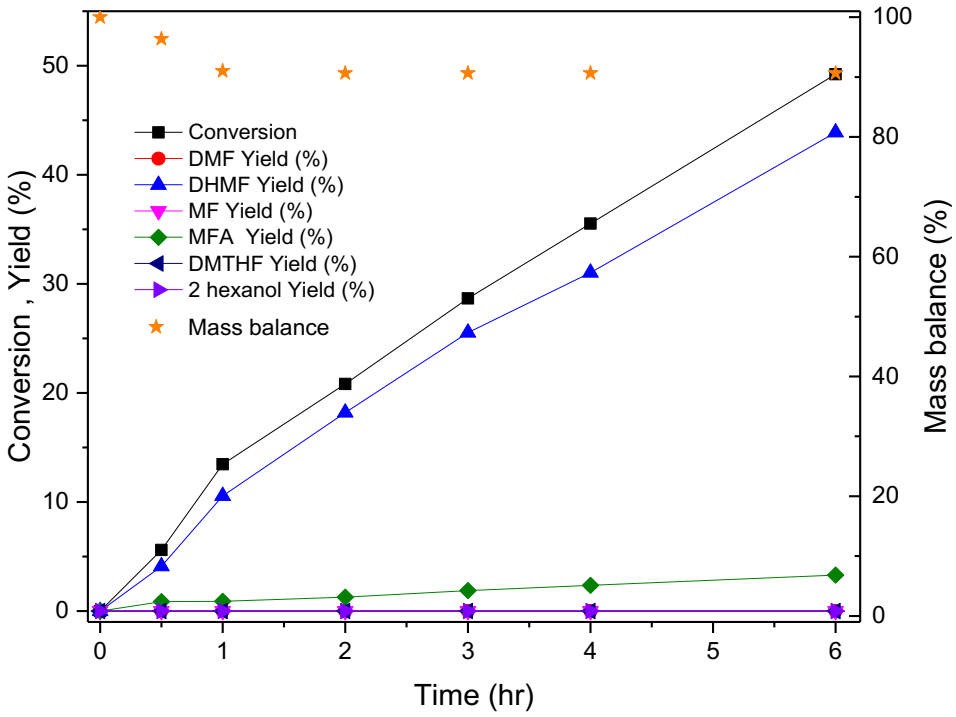

Figure 6.2.13 TOL profile of HMF hydrogenation with 0.4 % Ru/HTC 2. Reaction conditions: 30 ml of HMF (40 mM), temperature 150 °C, H_2 pressure 20 bar, catalyst; 60 mg, time; 6 hr, solvent; Dioxane.

As for the HMF conversion, 2 % Ru/HTC1 has the highest conversion after 6 hours of reaction with 73 %, followed by 0.4 % Ru/HTC 2 and 3.2 % Ru/HTC with 49 % and 43 %, respectively. The reason could be that shorter synthesis times produced a smaller particle size of HTC, thus high surface area. This is in the agreement of metal dispersion result obtained from CO chemisorption. However, for the reaction with 0.2 % Co/HTC and 0.6 % Ni/HTC, there was an insignificant conversion of HMF with less than 10 % after 6 hours.

6.2.2.1 Effect of catalyst preparation

4 % Ru/HTC IW was synthesised via incipient wetness impregnation as a comparison to the one step microwave-assisted technique. The procedures are as described in chapter 2 in which Ru metal salt was impregnated on carbonised HTC (HTC_{550}) via incipient wetness impregnation and reduced under H_2 before the catalytic test. The result of HMF hydrogenation with 4 % Ru/HTC IW are shown in **Figure 6.2.14**

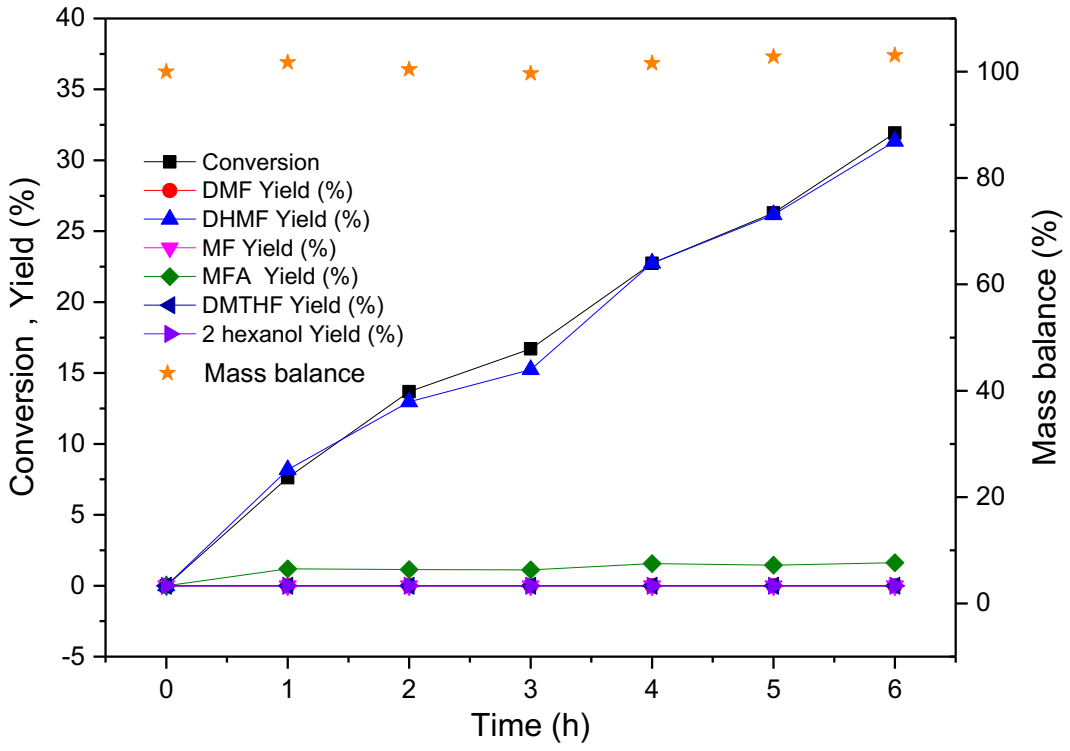

Figure 6.2.14 TOL profile of HMF hydrogenation with 4 % wt. Ru/HTC IW. Reaction condition: temperature 150 °C, H_2 pressure 20 bar, catalyst; 60 mg, time; 6 hr, solvent; Dioxane.

Figure 6.2.14 shows the TOL profile of HMF hydrogenation with 4 % Ru/HTC IW after 6 hr. It can be seen that 32 % of HMF was converted to DHMF and MFA with a selectivity of 97 % and 3 %, respectively. This is a bit lower than 3.2 % Ru/HTC synthesised with microwave reactor. This trends can be attributed to the dispersion of 4 % Ru/HTC IW which is lower than 3.2 % Ru/HTC as shown in **Table 6.2.4**.

In terms of synthesis method, it can be established that incipient wetness has more metal compared to one step microwave synthesis. Indeed, based on TOF, catalysts synthesised with microwave have better TOF and specific activity (conversion corrected by mole of metal) as shown in **Figure 6.2.15** and **Table 6.2.6** (entry 6 and 7). 0.4 % Ru/HTC2 has the highest TOF at a maximum yield of DHMF with 2378 h^{-1} (entry 7), 3 times higher than 4 % Ru/HTC IW. TOF based on metal loading shows that even 0.4 % Ru/HTC2 has the least Ru loading among Ru/HTC catalysts, it exhibited high catalytic activity with 26h^{-1} (9 times higher than 4 % Ru/HTC IW) as shown in **Table 6.2.6** (entry 7). This improvement of TOF can be related to the dispersion of each

catalyst as shown in **Table 6.2.4**. So that we can conclude that the one step procedure is at least as effective as the two step synthesis whereby the metal is impregnated into the pre-formed carbon.

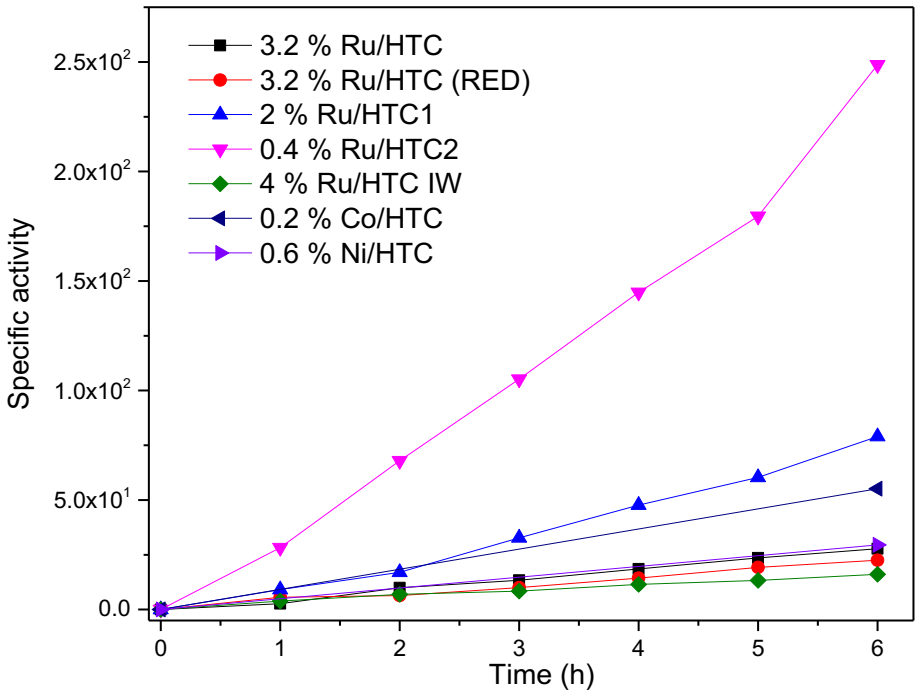

Figure 6.2.15 Specific activity of 3.2 % Ru/HTC, 3.2 % Ru/HTC RED,2 % Ru/HTC1, 0.4 % Ru/HTC1, 4 % Ru/HTC IW, 0.2 % Co/HTC and 0.6 % Ni/HTC. Reaction conditions; HMF, 40 mM; catalyst, 60 mg; solvent, Dioxane; pressure, 20 bar H_2; stirring, 1100 rpm. Specific DMF yield is calculated as moles of DMF produced over moles of Ru in the catalysts. Specific activity was calculated based on mole HMF converted over mole of metal in the catalysts.

0.4 % Ru/HTC demonstrated superior specific activity compared to the rest of catalysts supported on HTC as shown in Figure 6.2.15. This indicates that the one-step synthesis of Ru/HTC as listed in Table 6.2.5 (entry 3) was the best condition for the active catalyst. This is due to the shorter synthesis time (0.25 h), high synthesis temperature(210 °C) and higher glucose concentration (1 M) favour the formation of small nanospheres as described in the literature.[161, 234] Unfortunately, at the time of submitting this thesis we did still not have the TEM to further inform about particle size distribution and heterogeneity of the catalyst sample.

Table 6.2.6 Summary of conversion, yield, ICP metal loading and TOF of HMF hydrogenation with supported HTC catalysts.

Entry	Catalyst	Conversion (%)	DHMF Yield (%)	Specific activity [d] (h^{-1})	TOF [e] (h^{-1})	TOF [f] (h^{-1})
1	3.2 % Ru/HTC [a]	43	43	4.6	1151	5
2	3.2 % Ru/HTC RED [b]	35	35	3.8	-	
3	4 % Ru/HTC IW [c]	32	32	2.7	869	3
4	0.2 % Co/HTC [a]	5	0	9.2	-	-
5	0.6 % Ni/HTC [a]	9	0	4.9	-	-
6	2 % Ru/HTC1 [a]	73	73	13.2	2124	10
7	0.4 % Ru/HTC2 [a]	49	44	41.5	2378	26

[a] Catalysts synthesised via in-situ microwave techniques. [b] reduced under H_2 at 400 °C for 4 hr [c] Catalysts synthesised incipient wetness impregnation, IW. [d] Specific activity based on mole of HMF converted over mole of metal over time [e]TOF at 30 % iso-conversion, based on the number of active sites from CO Chemisorption. [f] TOF based on metal loading at 6 hr of reaction time. Experimental errors (conversion and yield = ± 0.07 %, TOF a = ± 0.05).

6.3 Conclusions

As a conclusion, we were able to synthesise HTC nano-spheres from glucose with good thermal stability up to 550 °C using the microwave-assisted technique. The particle size of nanospheres can be tuned by varying the glucose concentration, synthesis temperature, synthesis time as well as stirring.

It was found that with stirring, HTC produced is more thermally stable as shown in TGA analysis (**Figure 6.2.1**) with almost 70 % weight remaining at 550 °C. HTC without stirring only has 55 % weight remaining at 550 °C. As for the effect of synthesis time, shorter time leads to smaller particle size. The particle size was decreased from 534 nm to 447 nm when the synthesis time was reduced from 6 hours to 1 hour (**Figure 6.2.6** and **Table 5.2.1**).

In term of synthesis method, it can be concluded that catalysts prepared by facile one-step microwave assisted carbonisation technique demonstrated better catalytic activity as compared to a catalyst prepared via incipient wetness. Based on TOF, catalysts synthesised with microwave have better TOF values being 0.4 % Ru/HTC2 has the highest TOF with 26 h^{-1} almost 9 times higher than 4 % Ru/HTC IW.

One step microwave assisted synthesis of carbon supported Ru is a promising technique to simultaneously synthesise a catalyst as well as HTC in a shorter amount of time compared to the conventional hydrothermal and incipient wetness impregnation method. This technique also allows the metal to be reduced at the same time during catalysts synthesis. However, further optimisation is needed to produce an optimum catalyst with less metal leaching. In addition, the effect of metal precursors, as well as the effect of acidic synthesis conditions should be explored in order to develop a good catalyst.

Chapter 7 Conclusions & Outlook

7.1 Conclusions

This research work was aimed at the study of the HMF to DMF reaction, aiming to discover more active and selective catalysts than the prior art and, with an specific focus on producing more sustainable and cheaper catalysts via the use of non-precious metals or enhancing catalytic activity with the use of CNTs as support, which has demonstrated to always enhance reaction rates and therefore reduce reaction times by many fold. The cost of producing CNTs for catalysis is still prohibitive, however, we expect that production methods might make them affordable in the future and/or this research work at least inform in future support design for this highly important reaction and catalytic systems.

Initially, the hydrogenation of HMF to DMF was investigated under several reaction conditions using commercial 5 wt. % Ru/C from Sigma in order to optimise the yield of the desired product, DMF. The optimum reaction conditions were found to be at 150 °C and 20 bar of H_2, although this is just indicative and other catalysts might be optimised under different conditions Ru/C IW was successfully synthesised via incipient wetness and 5 % wt. loading of Ru was found to be the optimum Ru loading. XRD and TEM images revealed that the synthesised catalyst exhibited good dispersion with small particles size (1.5-1.8 nm). TPR study indicated that reduction at 400 °C under H_2 is sufficient to fully reduce the catalyst into its metallic state. In addition, XPS analysis confirms the presence as Ru^0 which is the responsible for the active site of the reaction. The effect of using CNT as the support increased TOFs calculated at optimum DMF production to increase from 101 h^{-1} to 492 h^{-1}. It is proposed that the smaller particle size of Ru supported on CNT compared to carbon obtained from TEM analysis could be partially responsible for this enhancement, however, it can also be attributed to the electronic effect of CNT derived from the curvature shape of CNT. This consequently enhanced the electron density of metal thus improving the adsorption of C=O bonds resulting in higher reactivity. [120] The effect of Ru decorated inside and out of CNT did not show any different improvement in the reactivity of the reaction compared to Ru/CNT IW, however, these results still need further work to ensure the location of the ruthenium nanoparticles

In Chapter 4, the hydrogenation of HMF to DMF with transitional metals namely Co, Ni, Cu and Fe catalyst supported on carbon was investigated It was discovered that among transitional metals catalyst supported on carbon, Ni shows a good reactivity in converting HMF with 70 % conversion after 6 hours followed by Co/C with 60 % conversion. It was better than 5 % Ru/C which has only 50 % HMF conversion; however, the high conversion did not translate into a high yield of DMF as both Ni/C and Co/C produced higher DHMF as opposed to DMF. This means that Ni and Co are not as good as Ru in hydrogenolyse the hydroxyl group in order to get to DMF.[31, 78] In addition to considering electronic effects and chemisorption properties of each metal, differences in particle size distribution could also affect the activity. Remarkably, when CNT was used as the support for Co, Ni, Cu and Fe all catalysts displayed a very significant improvement in HMF conversion as well as DMF yields. This work exemplifies the importance of the support material in determining the activity of supported metal nanoparticles for catalysis and how sometimes the study of the support can be the route to non-precious metals catalysts displaying the same performance as precious and non-sustainable ones. This enhancement could be attributed to the electronic effect of CNT, which enhanced the electron density of metal thus improving the adsorption of the C=O bond resulting in higher reactivity. Co/CNT shows the best reactivity in HMF conversion and DMF yield compared to Ni/CNT. These were followed by Cu/CNT and Fe/CNT. The overall reactivity of the metals could be ranked as followed; Co>Ni>Cu>Fe. It is also important to note that the reported yields for the less active catalysts could be increased by simply increasing the catalytic loading in the reaction tests, therefore presenting a cheaper alternative to the precious metals.

However, we envisaged that it could still be beneficial for the process to add small amounts of Ru in order to form bimetallic catalysts that would minimise the use of precious metals to a more sustainable level. We found that real synergistic effects occur when alloying the precious and non-precious metal component so that superior activities were found per unit of metal when bimetallic catalysts were used. In chapter 5, a bimetallic catalyst consisting of Ru-Co and Ru-Ni displayed remarkable superior catalytic activity fast in HMF conversion as well as DMF yield. It was shown that addition of Co and Ni to Ru in specific molar ratio demonstrated the synergistic effect

of these catalysts as they showed better reactivity than the monometallic catalysts counterparts. The alloys formation was confirmed by XRD by the shift in the diffraction peaks due to the incorporation of Co and Ni to Ru structure. As for Ru-Co/C catalysts, the molar ratio of 1:5 showed an excellent activity in HMF conversion as a high yield of DMF of 98 % after 6 hours was obtained. This could be due to the presence of CoO monolayer on the surface of the catalyst as confirmed by XPS analysis, which prevents the furan ring to be adsorbed in the planar position thus preventing the ring hydrogenation and ring opening products from forming. The effect of the addition of Ni to Ru also resulted in a positive result. Bimetallic RuNi/C 1:3 demonstrated the best activity and DMF yield compared to its monometallic counterpart as well as the other molar ratios of RuNi catalysts. Total HMF conversion was achieved in 3 hours with 98 % of DMF yield after 6 hours. This could be attributed to the synergistic effect normally derived upon the alloying of metals. The changes in the catalytic properties are associated with the changes in the electronic properties of the active component in the alloy.

The same promoting effect as in chapter 3 and 4 was observed when CNT was used as the support for bimetallic catalysts. The activities of supported catalysts with CNT were enhanced for both of RuNi/CNT and RuCo/CNT. Both catalysts achieved total HMF conversion in less than 1 hour, better than Ru/CNT. However, in the case of DMF yield, bimetallic shows slower conversion than Ru/CNT. Nevertheless, RuNi/CNT 1:3 demonstrated higher yield than Ru/CNT and RuCo/CNT 1:20 with 90 % yield of DMF in 2 hours. Longer reaction time led to the formation of ring hydrogenation and ring opening products, such as DMTHF and 2-hexanol. Overall, the bimetallic system of 3.5 % RuCo 1:5 and 3.2 RuNi 1:3 with specific molar ratios showed an improvement in reactivity compared to their monometallic counterparts, considering the lower loading of each metal compared to their monometallic counterparts. This proved the synergistic effect of this system. The only difference when different supports were used was that CNT improved the reaction rates however this is also lead to the formation of ring hydrogenation and ring opening products. Carbon has lower reaction rate however it gives better DMF yield after 6 hours. High yield of DMF was obtained even at low Ru content in a bimetallic catalyst without losing much DMF yield. 3.5 % RuCo/C 1:5 (0.6 % Ru) and 3.2 % RuNi 1:3 (0.7 % Ru)have better specific DMF yield as

compared to 5% Ru/C and 5 % Ru/CNT. 4.2 % RuCo/CNT 1:2 with only 0.2 % loading of Ru showed the highest specific DMF yield. This finding is a positive outcome in order to reduce the dependence on the expensive noble metal without compromising the activity and the yield of desired product, in our case DMF.

In chapter 6, we were able to synthesise HTC nanospheres with good thermal stability up to 550 °C using the microwave-assisted technique from glucose. The particle size of nanospheres can be tuned by varying the glucose concentration, synthesis temperature, synthesis time as well as stirring. It was found that with stirring, HTC produced is more thermally stable as shown in TGA analysis with almost 70 % weight remaining at 550 °C. HTC without stirring only has 55 % weight remaining at 550 °C. As for the effect of synthesis time, shorter time leads to smaller particle size. The particle size was decreased from 534 nm to 447 nm when the synthesis time was reduced from 6 hours to 1 hour. However, based on TOF, catalysts synthesised with microwave have better TOF. Ru/HTC2 has the highest TOF with 26 h^{-1} almost 7 times higher than Ru/HTC IW. In-situ microwave synthesis is a promising technique to simultaneously synthesise a catalyst as well as HTC in a shorter amount of time compared to the conventional hydrothermal method. However, further optimisation is needed to produce an optimum catalyst. Therefore, the effect of metal precursors, as well as the effect of acidic synthesis conditions should be explored in order to get a good catalyst.

7.2 Outlook

Selective hydrogenation of HMF to DMF has been extensively explored by many researchers, and some of them were able to achieve high conversion as well as high yield of DMF under certain reaction conditions. However, the main challenge is to reduce the operational cost by employing cost-effective catalysts as an alternative to the expensive noble metals. Future studies could focus on more variety of inexpensive metals combinations as an alloy and sustainable support without compromising the high yield of DMF. For example, the combination of non-noble metals such as Ni, Co, Cu and Fe would be interesting since Ni and Co are capable of converting HMF to DMF although specific metal ratio and loading are crucial in resulting a better catalyst. The catalysts stability and leaching tests should also be performed in order to study the catalyst deactivation. The catalyst after reaction needs to be studied and look for

carbon deposits and changes in oxidation state and sintering. Up to know most of the kinetic studies are focusing on furfural and less study about HMF.The kinetic study would be helpful to learn the adsorption behaviour of HMF and its intermediates which would provide some insights into the principles of selectivity control than can guide catalyst selection. As for hydrothermal carbonisation supported catalyst, further optimisation is needed to produce an optimum catalyst. Therefore, the effect of metal precursors, as well as the effect of acidic synthesis conditions should be explored in order to get a good catalyst with less metal leaching.

References:

1. Chen, W.-Y., T. Suzuki, and M. Lackner, *Handbook of Climate Change Mitigation and Adaptation*. 2016: Springer.
2. Balat, M., *An overview of biofuels and policies in the European Union.* Energy Sources, Part B, 2007. **2**(2): p. 167-181.
3. Gallezot, P., *Conversion of biomass to selected chemical products.* Chem Soc Rev, 2012. **41**(4): p. 1538-58.
4. Chheda, J.N., G.W. Huber, and J.A. Dumesic, *Liquid-phase catalytic processing of biomass-derived oxygenated hydrocarbons to fuels and chemicals.* Angewandte Chemie International Edition, 2007. **46**(38): p. 7164-7183.
5. Hill, C.A., *Wood modification: chemical, thermal and other processes*. Vol. 5. 2007: John Wiley & Sons.
6. Alonso, D.M., S.G. Wettstein, and J.A. Dumesic, *Bimetallic catalysts for upgrading of biomass to fuels and chemicals.* Chemical Society Reviews, 2012. **41**(24): p. 8075-8098.
7. Chakar, F.S. and A.J. Ragauskas, *Review of current and future softwood kraft lignin process chemistry.* Industrial Crops and Products, 2004. **20**(2): p. 131-141.
8. Zakzeski, J., et al., *The Catalytic Valorization of Lignin for the Production of Renewable Chemicals.* Chemical Reviews, 2010. **110**(6): p. 3552-3599.
9. Wyman, C.E., et al., *Hydrolysis of cellulose and hemicellulose.* Polysaccharides: structural diversity and functional versatility, 2005. **1**: p. 1023-1062.
10. Lewkowski, J., *Synthesis, chemistry and applications of 5-hydroxymethyl-furfural and its derivatives.* 2001.
11. Besson, M., P. Gallezot, and C. Pinel, *Conversion of Biomass into Chemicals over Metal Catalysts.* Chemical Reviews, 2013. **114**(3): p. 1827-1870.
12. Bozell, J.J. and G.R. Petersen, *Technology development for the production of biobased products from biorefinery carbohydrates-the US Department of Energy's "Top 10" revisited.* Green Chemistry, 2010. **12**(4): p. 539-554.
13. Bozell, J.J., *An evolution from pretreatment to fractionation will enable successful development of the integrated biorefinery.* BioResources, 2010. **5**(3): p. 1326-1327.
14. Bozell, J.J. and G.R. Petersen, *Technology development for the production of biobased products from biorefinery carbohydrates—the US Department of Energy's "top 10" revisited.* Green Chemistry, 2010. **12**(4): p. 539-554.
15. Zeitsch, K.J., *The chemistry and technology of furfural and its many by-products*. Vol. 13. 2000: Elsevier.
16. Wettstein, S.G., et al., *A roadmap for conversion of lignocellulosic biomass to chemicals and fuels.* Current Opinion in Chemical Engineering, 2012. **1**(3): p. 218-224.
17. Roman-Leshkov, Y., et al. *Production of dimethylfuran for liquid fuels from biomass-derived carbohydrates*. Nature 2007 Jun 21 [cited 447 7147]; 982-5]. Available from: http://www.ncbi.nlm.nih.gov/pubmed/17581580http://www.nature.com/nature/journal/v447/n7147/pdf/nature05923.pdf.
18. da Costa Sousa, L., et al., *'Cradle-to-grave'assessment of existing lignocellulose pretreatment technologies.* Current opinion in biotechnology, 2009. **20**(3): p. 339-347.
19. Mosier, N., et al., *Features of promising technologies for pretreatment of lignocellulosic biomass.* Bioresource technology, 2005. **96**(6): p. 673-686.
20. Bals, B., et al., *Evaluation of ammonia fibre expansion (AFEX) pretreatment for enzymatic hydrolysis of switchgrass harvested in different seasons and locations.* Biotechnology for biofuels, 2010. **3**(1): p. 1.

21. Tao, L., et al., *Process and technoeconomic analysis of leading pretreatment technologies for lignocellulosic ethanol production using switchgrass.* Bioresource technology, 2011. **102**(24): p. 11105-11114.
22. Zhao, X., K. Cheng, and D. Liu, *Organosolv pretreatment of lignocellulosic biomass for enzymatic hydrolysis.* Applied microbiology and biotechnology, 2009. **82**(5): p. 815.
23. Agbor, V.B., et al., *Biomass pretreatment: fundamentals toward application.* Biotechnology advances, 2011. **29**(6): p. 675-685.
24. Brandt, A., et al., *Ionic liquid pretreatment of lignocellulosic biomass with ionic liquid–water mixtures.* Green Chemistry, 2011. **13**(9): p. 2489-2499.
25. Lau, M.W., C. Gunawan, and B.E. Dale, *The impacts of pretreatment on the fermentability of pretreated lignocellulosic biomass: a comparative evaluation between ammonia fiber expansion and dilute acid pretreatment.* Biotechnology for biofuels, 2009. **2**(1): p. 1.
26. Kamm, B., P.R. Gruber, and M. Kamm, *Biorefineries–industrial processes and products*. 2006: Wiley Online Library.
27. Corma, A., S. Iborra, and A. Velty, *Chemical Routes for the Transformation of Biomass into Chemicals.* Chemical Reviews, 2007. **107**(6): p. 2411-2502.
28. van Putten, R.-J., et al., *Hydroxymethylfurfural, A Versatile Platform Chemical Made from Renewable Resources.* Chemical Reviews, 2013. **113**(3): p. 1499-1597.
29. Rosatella, A.A., et al., *5-Hydroxymethylfurfural (HMF) as a building block platform: Biological properties, synthesis and synthetic applications.* Green Chemistry, 2011. **13**(4): p. 754-793.
30. Tong, X.L., Y. Ma, and Y.D. Li, *Biomass into chemicals: Conversion of sugars to furan derivatives by catalytic processes.* Applied Catalysis a-General, 2010. **385**(1-2): p. 1-13.
31. Hu, L., et al., *Selective Transformation of 5-Hydroxymethylfurfural into the Liquid Fuel 2,5-Dimethylfuran over Carbon-Supported Ruthenium.* Industrial & Engineering Chemistry Research, 2014. **53**(8): p. 3056-3064.
32. Moreau, C., M.N. Belgacem, and A. Gandini, *Recent Catalytic Advances in the Chemistry of Substituted Furans from Carbohydrates and in the Ensuing Polymers.* Topics in Catalysis, 2004. **27**(1): p. 11-30.
33. Gandini, A. and M.N. Belgacem, *Furans in polymer chemistry.* Progress in Polymer Science, 1997. **22**(6): p. 1203-1379.
34. Timko, J.M. and D.J. Cram, *Furanyl unit in host compounds.* Journal of the American Chemical Society, 1974. **96**(22): p. 7159-7160.
35. Shaw, P.E., J.H. Tatum, and R.E. Berry, *Acid-catalyzed degradation of d-fructose.* Carbohydrate Research, 1967. **5**(3): p. 266-273.
36. Zhao, H., et al., *Metal chlorides in ionic liquid solvents convert sugars to 5-hydroxymethylfurfural.* Science, 2007. **316**(5831): p. 1597-1600.
37. Antal, M.J., W.S.L. Mok, and G.N. Richards, *Mechanism of formation of 5-(hydroxymethyl)-2-furaldehyde from d-fructose and sucrose.* Carbohydrate Research, 1990. **199**(1): p. 91-109.
38. Van Dam, H., A. Kieboom, and H. Van Bekkum, *The conversion of fructose and glucose in acidic media: formation of hydroxymethylfurfural.* Starch-Stärke, 1986. **38**(3): p. 95-101.
39. Kuster, B., *5-Hydroxymethylfurfural (HMF). A review focussing on its manufacture.* Starch-Stärke, 1990. **42**(8): p. 314-321.
40. Cottier, L. and G. Descotes, *5-(Hydroxymethyl) furfural Syntheses and Chemical Transformations.* ChemInform, 1994. **25**(36).
41. Hahn-Hägerdal, B., et al., *Bio-ethanol – the fuel of tomorrow from the residues of today.* Trends in Biotechnology, 2006. **24**(12): p. 549-556.
42. Balat, M. and H. Balat, *Recent trends in global production and utilization of bio-ethanol fuel.* Applied Energy, 2009. **86**(11): p. 2273-2282.

43. Dodić, S.N., et al., *Potential contribution of bioethanol fuel to the transport sector of Vojvodina.* Renewable and Sustainable Energy Reviews, 2009. **13**(8): p. 2197-2200.
44. Dumesic, J.A., Y. Rom, and J.N. Chheda, *Catalytic process for producing furan derivatives in a biphasic reactor*. 2009, Google patents ,US 7572925 B2.
45. Saha, B. and M.M. Abu-Omar, *Current Technologies, Economics, and Perspectives for 2,5-Dimethylfuran Production from Biomass-Derived Intermediates.* ChemSusChem, 2015. **8**(7): p. 1133-42.
46. Xu, N., J. Gong, and Z. Huang, *Review on the production methods and fundamental combustion characteristics of furan derivatives.* Renewable and Sustainable Energy Reviews, 2016. **54**: p. 1189-1211.
47. Zhong, S., et al., *Combustion and Emissions of 2,5-Dimethylfuran in a Direct-Injection Spark-Ignition Engine.* Energy & Fuels, 2010. **24**(5): p. 2891-2899.
48. Binder, J.B. and R.T. Raines, *Simple Chemical Transformation of Lignocellulosic Biomass into Furans for Fuels and Chemicals.* Journal of the American Chemical Society, 2009. **131**(5): p. 1979-1985.
49. Tong, X., Y. Ma, and Y. Li, *Biomass into chemicals: Conversion of sugars to furan derivatives by catalytic processes.* Applied Catalysis A: General, 2010. **385**(1–2): p. 1-13.
50. Williams, C.L., et al., *Cycloaddition of biomass-derived furans for catalytic production of renewable p-xylene.* Acs Catalysis, 2012. **2**(6): p. 935-939.
51. Wang, D., et al., *Selective production of aromatics from alkylfurans over solid acid catalysts.* ChemCatChem, 2013. **5**(7): p. 2044-2050.
52. Chang, C.-C., et al., *Ultra-selective cycloaddition of dimethylfuran for renewable p-xylene with H-BEA.* Green Chemistry, 2014. **16**(2): p. 585-588.
53. Rinaldi, R. and F. Schüth, *Acid hydrolysis of cellulose as the entry point into biorefinery schemes.* ChemSusChem, 2009. **2**(12): p. 1096-1107.
54. Lei, H., S. Yong, and L. Lu, *Pathways and mechanisms of liquid fuel 2, 5-dimethylfuran from biomass.* Progress in Chemistry, 2011. **23**(10): p. 2079-2084.
55. Dutta, S. and M. Mascal, *Novel Pathways to 2,5-Dimethylfuran via Biomass-Derived 5-(Chloromethyl)furfural.* ChemSusChem, 2014. **7**(11): p. 3028-3030.
56. Mascal, M. and E.B. Nikitin, *Dramatic Advancements in the Saccharide to 5-(Chloromethyl) furfural Conversion Reaction.* ChemSusChem, 2009. **2**(9): p. 859-861.
57. Verevkin, S.P., et al., *Biomass-Derived Platform Chemicals: Thermodynamic Studies on the Conversion of 5-Hydroxymethylfurfural into Bulk Intermediates.* Industrial & Engineering Chemistry Research, 2009. **48**(22): p. 10087-10093.
58. De, S., S. Dutta, and B. Saha, *One-pot conversions of lignocellulosic and algal biomass into liquid fuels.* ChemSusChem, 2012. **5**(9): p. 1826-1833.
59. Hu, L., L. Lin, and S. Liu, *Chemoselective Hydrogenation of Biomass-Derived 5-Hydroxymethylfurfural into the Liquid Biofuel 2,5-Dimethylfuran.* Industrial & Engineering Chemistry Research, 2014. **53**(24): p. 9969-9978.
60. Zhang, J., L. Lin, and S. Liu, *Efficient Production of Furan Derivatives from a Sugar Mixture by Catalytic Process.* Energy & Fuels, 2012. **26**(7): p. 4560-4567.
61. Chidambaram, M. and A.T. Bell, *A two-step approach for the catalytic conversion of glucose to 2,5-dimethylfuran in ionic liquids.* Green Chemistry, 2010. **12**(7): p. 1253-1262.
62. Thananatthanachon, T. and T.B. Rauchfuss, *Efficient Production of the Liquid Fuel 2,5-Dimethylfuran from Fructose Using Formic Acid as a Reagent.* Angewandte Chemie International Edition, 2010. **49**(37): p. 6616-6618.
63. Hansen, T.S., et al., *One-pot reduction of 5-hydroxymethylfurfural via hydrogen transfer from supercritical methanol.* Green Chemistry, 2012. **14**(9): p. 2457-2461.
64. Jae, J., et al., *Production of Dimethylfuran from Hydroxymethylfurfural through Catalytic Transfer Hydrogenation with Ruthenium Supported on Carbon.* ChemSusChem, 2013. **6**(7): p. 1158-1162.

65. Chatterjee, M., T. Ishizaka, and H. Kawanami, *Hydrogenation of 5-hydroxymethylfurfural in supercritical carbon dioxide-water: a tunable approach to dimethylfuran selectivity.* Green Chemistry, 2014. **16**(3): p. 1543-1551.
66. N. Lucas, et al., *Novel catalysts for valorization of biomass to value-added chemicals and fuels.* Journal of Chemical Science 2014. **126**(2): p. 403-413.
67. Zu, Y., et al., *Efficient production of the liquid fuel 2,5-dimethylfuran from 5-hydroxymethylfurfural over Ru/Co3O4 catalyst.* Applied Catalysis B: Environmental, 2014. **146**(0): p. 244-248.
68. Wang, G.H., et al., *Platinum-cobalt bimetallic nanoparticles in hollow carbon nanospheres for hydrogenolysis of 5-hydroxymethylfurfural.* Nat Mater, 2014. **13**(3): p. 293-300.
69. Shun, N., I. Naoya, and E. Kohki, *Selective hydrogenation of biomass-derived 5-hydroxymethylfurfural (HMF) to 2,5-dimethylfuran (DMF) under atmospheric hydrogen pressure over carbon supported PdAu bimetallic catalyst.* Catalysis Today, 2014.
70. Huang, Y.-B.B., et al., *Nickel-tungsten carbide catalysts for the production of 2,5-dimethylfuran from biomass-derived molecules.* ChemSusChem, 2014. **7**(4): p. 1068-1072.
71. Scholz, D., C. Aellig, and I. Hermans, *Catalytic Transfer Hydrogenation/Hydrogenolysis for Reductive Upgrading of Furfural and 5-(Hydroxymethyl)furfural.* ChemSusChem, 2014. **7**(1): p. 268-275.
72. Mitra, J., X. Zhou, and T. Rauchfuss, *Pd/C-catalyzed reactions of HMF: decarbonylation, hydrogenation, and hydrogenolysis.* Green Chemistry, 2014. **17**(1): p. 307-313.
73. Kumalaputri, A.J., et al., *Tunable and Selective Conversion of 5-HMF to 2,5-Furandimethanol and 2,5-Dimethylfuran over Copper-Doped Porous Metal Oxides.* ChemSusChem, 2014. **7**(8): p. 2266-2275.
74. Saha, B., C.M. Bohn, and M.M. Abu-Omar, *Zinc-Assisted Hydrodeoxygenation of Biomass-Derived 5-Hydroxymethylfurfural to 2,5-Dimethylfuran.* ChemSusChem, 2014. **7**(11): p. 3095-3101.
75. Nagpure, A.S., et al., *Renewable fuels from biomass-derived compounds: Ru-containing hydrotalcites as catalysts for conversion of HMF to 2,5-dimethylfuran.* Catalysis Science & Technology, 2015. **5**(3): p. 1463-1472.
76. Yang, P., et al., *Catalytic production of 2,5-dimethylfuran from 5-hydroxymethylfurfural over Ni/Co3O4 catalyst.* Catalysis Communications, 2015. **66**(0): p. 55-59.
77. Kong, X., et al., *Rational design of Ni-based catalysts derived from hydrotalcite for selective hydrogenation of 5-hydroxymethylfurfural.* Green Chemistry, 2015. **17**(4): p. 2504-2514.
78. Chen, B., et al., *Carbon-coated Cu-Co bimetallic nanoparticles as selective and recyclable catalysts for production of biofuel 2,5-dimethylfuran.* Applied Catalysis B: Environmental, 2017. **200**: p. 192-199.
79. Shi, J., et al., *Production of 2,5-dimethylfuran from 5-hydroxymethylfurfural over reduced graphene oxides supported Pt catalyst under mild conditions.* Fuel, 2016. **163**: p. 74-79.
80. Luo, J., et al., *Base metal-Pt alloys: A general route to high selectivity and stability in the production of biofuels from HMF.* Applied Catalysis B: Environmental, 2016. **199**: p. 439-446.
81. Yu, L., et al., *Robust and Recyclable Nonprecious Bimetallic Nanoparticles on Carbon Nanotubes for the Hydrogenation and Hydrogenolysis of 5-Hydroxymethylfurfural.* ChemCatChem, 2015. **7**(11): p. 1701-1707.
82. Nagpure, A.S., N. Lucas, and S.V. Chilukuri, *Efficient Preparation of Liquid Fuel 2,5-Dimethylfuran from Biomass-Derived 5-Hydroxymethylfurfural over Ru–NaY Catalyst.* ACS Sustainable Chemistry & Engineering, 2015. **3**(11): p. 2909-2916.

83. Bottari, G., et al., *Copper–Zinc Alloy Nanopowder: A Robust Precious-Metal-Free Catalyst for the Conversion of 5-Hydroxymethylfurfural.* ChemSusChem, 2015. **8**(8): p. 1323-1327.
84. Jungho, J., et al., *The Role of Ru and RuO2in the Catalytic Transfer Hydrogenation of 5-Hydroxymethylfurfural for the Production of 2,5-Dimethylfuran.* ChemCatChem, 2014. **6**(3): p. 848-856.
85. March, J., *Reactions, mechanisms, and structure.* Advanced Organic Chemistry, 1985. **3**: p. 173-176.
86. Fogler, H.S., *Elements of chemical reaction engineering*. 1992: Prentice-Hall.
87. Nørskov, J.K., et al., *Heterogeneous Catalysis and a Sustainable Future*, in *Fundamental Concepts in Heterogeneous Catalysis*. 2014, John Wiley & Sons, Inc. p. 1-5.
88. Deutschmann, O., et al., *Heterogeneous Catalysis and Solid Catalysts, 1. Fundamentals*, in *Ullmann's Encyclopedia of Industrial Chemistry*. 2000, Wiley-VCH Verlag GmbH & Co. KGaA.
89. Dittmeyer, R. and G. Emig, *Simultaneous heat and mass transfer and chemical reaction.* Handbook of heterogeneous catalysis, 2008.
90. Joshi, S.S. and V.V. Ranade, *8.3 Heterogeneous Catalysts*, in *Industrial Catalytic Processes for Fine and Specialty Chemicals*. Elsevier.
91. Nørskov, J.K., et al., *The Electronic Factor in Heterogeneous Catalysis*, in *Fundamental Concepts in Heterogeneous Catalysis*. 2014, John Wiley & Sons, Inc. p. 114-137.
92. Nørskov, J.K., et al., *Catalyst Structure*, in *Fundamental Concepts in Heterogeneous Catalysis*. 2014, John Wiley & Sons, Inc. p. 138-149.
93. Sinfelt, J.H., *Bimetallic catalysts: discoveries, concepts, and applications*. Vol. 7. 1983: Wiley-Interscience.
94. Arnold, H., et al., *Handbook of Heterogeneous Catalysis.* Wiley-VCH, 1997. **3**: p. 2165.
95. Liu, J., et al., *Bimetallic ruthenium-copper nanoparticles embedded in mesoporous carbon as an effective hydrogenation catalyst.* Nanoscale, 2013. **5**(22): p. 11044-11050.
96. Ferrando, R., J. Jellinek, and R.L. Johnston, *Nanoalloys: From Theory to Applications of Alloy Clusters and Nanoparticles.* Chemical Reviews, 2008. **108**(3): p. 845-910.
97. Ghosh Chaudhuri, R. and S. Paria, *Core/Shell Nanoparticles: Classes, Properties, Synthesis Mechanisms, Characterization, and Applications.* Chemical Reviews, 2012. **112**(4): p. 2373-2433.
98. Alayoglu, S. and B. Eichhorn, *Rh–Pt Bimetallic Catalysts: Synthesis, Characterization, and Catalysis of Core–Shell, Alloy, and Monometallic Nanoparticles.* Journal of the American Chemical Society, 2008. **130**(51): p. 17479-17486.
99. Alayoglu, S., et al., *Structural and Architectural Evaluation of Bimetallic Nanoparticles: A Case Study of Pt–Ru Core–Shell and Alloy Nanoparticles.* ACS Nano, 2009. **3**(10): p. 3127-3137.
100. Zhang, H., et al., *Nanocrystals Composed of Alternating Shells of Pd and Pt Can Be Obtained by Sequentially Adding Different Precursors.* Journal of the American Chemical Society, 2011. **133**(27): p. 10422-10425.
101. Wang, L. and Y. Yamauchi, *Strategic Synthesis of Trimetallic Au@Pd@Pt Core–Shell Nanoparticles from Poly(vinylpyrrolidone)-Based Aqueous Solution toward Highly Active Electrocatalysts.* Chemistry of Materials, 2011. **23**(9): p. 2457-2465.
102. Kolasinski, K.W., *Surface science: foundations of catalysis and nanoscience*. 2012: John Wiley & Sons.
103. Spendelow, J., P. Babu, and A. Wieckowski, *Electrocatalytic oxidation of carbon monoxide and methanol on platinum surfaces decorated with ruthenium.* Current Opinion in Solid State and Materials Science, 2005. **9**(1): p. 37-48.
104. *Carbon materials for catalysis*, ed. P. Serp and J.L.s. Figueiredo. 2009, Hoboken, N.J.: John Wiley & Sons.

105. Alamillo, R., et al., *The selective hydrogenation of biomass-derived 5-hydroxymethylfurfural using heterogeneous catalysts.* Green Chemistry, 2012. **14**(5): p. 1413-1419.
106. Cai, H., et al., *Biomass into chemicals: One-pot production of furan-based diols from carbohydrates via tandem reactions.* Catalysis Today, 2014. **234**(0): p. 59-65.
107. Ohyama, J., et al., *Selective hydrogenation of 2-hydroxymethyl-5-furfural to 2,5-bis(hydroxymethyl)furan over gold sub-nano clusters.* RSC Advances, 2013. **3**(4): p. 1033-1036.
108. Schlögl, R., et al., *Preparation of Solid Catalysts: Sections 2.1.9 – 2.2.1.6*, in *Handbook of Heterogeneous Catalysis*. 2008, Wiley-VCH Verlag GmbH. p. 138-264.
109. Pham-Huu, C. and M.-J. Ledoux, *Carbon nanomaterials with controlled macroscopic shapes as new catalytic materials.* Topics in Catalysis, 2006. **40**(1): p. 49-63.
110. Serp, P., M. Corrias, and P. Kalck, *Carbon nanotubes and nanofibers in catalysis.* Applied Catalysis A: General, 2003. **253**(2): p. 337-358.
111. Rodríguez-Reinoso, F., *The role of carbon materials in heterogeneous catalysis.* Carbon, 1998. **36**(3): p. 159-175.
112. Auer, E., et al., *Carbons as supports for industrial precious metal catalysts.* Applied Catalysis A: General, 1998. **173**(2): p. 259-271.
113. Furimsky, E., *Carbons and carbon-supported catalysts in hydroprocessing*. 2008: Royal Society of Chemistry.
114. Ebbesen, T. and A. P M, *Large-scale synthesis of carbon.* Nature, 1992. **358**: p. 16.
115. Bhushan, B., *Handbook springer of nanotechnology*. 2007, Springer, Berlin.
116. Balasubramanian, K. and M. Burghard, *Chemically Functionalized Carbon Nanotubes.* Small, 2005. **1**(2): p. 180-192.
117. Lee, K., et al., *Progress in the synthesis of carbon nanotube-and nanofiber-supported Pt electrocatalysts for PEM fuel cell catalysis.* Journal of Applied Electrochemistry, 2006. **36**(5): p. 507-522.
118. Li, Y., G.-H. Lai, and R.-X. Zhou, *Carbon nanotubes supported Pt–Ni catalysts and their properties for the liquid phase hydrogenation of cinnamaldehyde to hydrocinnamaldehyde.* Applied surface science, 2007. **253**(11): p. 4978-4984.
119. Bligaard, T., *Linear energy relations and the computational design of selective hydrogenation/dehydrogenation catalysts.* Angewandte Chemie International Edition, 2009. **48**(52): p. 9782-9784.
120. Wang, Y., et al., *Ruthenium nanoparticles loaded on multiwalled carbon nanotubes for liquid-phase hydrogenation of fine chemicals: An exploration of confinement effect.* Journal of Catalysis, 2015. **329**: p. 95-106.
121. Yang, S.H., et al., *Interaction of a transition metal atom with intrinsic defects in single-walled carbon nanotubes.* The Journal of Physical Chemistry B, 2006. **110**(28): p. 13941-13946.
122. Charlier, J.C., *Defects in Carbon Nanotubes.* Accounts of Chemical Research, 2002. **35**(12): p. 1063-1069.
123. Yamabe, T., K. Fukui, and K. Tanaka, *The science and technology of carbon nanotubes*. 1999: Elsevier.
124. Maiti, A. and A. Ricca, *Metal–nanotube interactions – binding energies and wetting properties.* Chemical Physics Letters, 2004. **395**(1–3): p. 7-11.
125. Machado, B.F., et al., *Understanding the surface chemistry of carbon nanotubes: Toward a rational design of Ru nanocatalysts.* Journal of Catalysis, 2014. **309**: p. 185-198.
126. Ouyang, M., J.-L. Huang, and C.M. Lieber, *Fundamental electronic properties and applications of single-walled carbon nanotubes.* Accounts of Chemical Research, 2002. **35**(12): p. 1018-1025.

127. Nunzi, F., et al., *The coordination chemistry of carbon nanotubes: a density functional study through a cluster model approach.* The Journal of Physical Chemistry B, 2002. **106**(41): p. 10622-10633.
128. Blase, X., et al., *Hybridization effects and metallicity in small radius carbon nanotubes.* Physical Review Letters, 1994. **72**(12): p. 1878-1881.
129. Haddon, R., *Electronic structure, conductivity and superconductivity of alkali metal doped (C60).* Accounts of chemical research, 1992. **25**(3): p. 127-133.
130. Loiseau, A., et al., *Understanding carbon nanotubes.* Lecture notes in physics, 2006. **677**: p. 555.
131. Menon, M., A.N. Andriotis, and G.E. Froudakis, *Curvature dependence of the metal catalyst atom interaction with carbon nanotubes walls.* Chemical Physics Letters, 2000. **320**(5–6): p. 425-434.
132. Duca, D., F. Ferrante, and G. La Manna, *Theoretical Study of Palladium Cluster Structures on Carbonaceous Supports.* The Journal of Physical Chemistry C, 2007. **111**(14): p. 5402-5408.
133. Nakagawa, Y., M. Tamura, and K. Tomishige, *Catalytic Reduction of Biomass-Derived Furanic Compounds with Hydrogen.* Acs Catalysis, 2013. **3**(12): p. 2655-2668.
134. Chatterjee, M., T. Ishizaka, and H. Kawanami, *Selective hydrogenation of 5-hydroxymethylfurfural to 2,5-bis-(hydroxymethyl)furan using Pt/MCM-41 in an aqueous medium: a simple approach.* Green Chemistry, 2014. **16**(11): p. 4734-4739.
135. Sheldon, R.A., I.W.C.E. Arends, and U. Hanefeld, *Introduction: Green Chemistry and Catalysis*, in *Green Chemistry and Catalysis*. 2007, Wiley-VCH Verlag GmbH & Co. KGaA. p. 1-47.
136. Medlin, J.W., *Understanding and controlling reactivity of unsaturated oxygenates and polyols on metal catalysts.* ACS Catalysis, 2011. **1**(10): p. 1284-1297.
137. Delbecq, F. and P. Sautet, *A density functional study of adsorption structures of unsaturated aldehydes on Pt (111): A key factor for hydrogenation selectivity.* Journal of Catalysis, 2002. **211**(2): p. 398-406.
138. NI, Z.-M., et al., *Adsorption and Decarbonylation Reaction of Furfural on Pt (111) Surface.* Acta Physico-Chimica Sinica, 2013. **29**(9): p. 1916-1922.
139. Haubrich, J., et al., *Adsorption and vibrations of α, β-unsaturated aldehydes on pure Pt and Pt− Sn alloy (111) surfaces I. prenal.* The Journal of Physical Chemistry C, 2008. **112**(10): p. 3701-3718.
140. Nakagawa, Y., et al., *Total Hydrogenation of Furfural and 5-Hydroxymethylfurfural over Supported Pd–Ir Alloy Catalyst.* ACS Catalysis, 2014. **4**(8): p. 2718-2726.
141. Vetere, V., et al., *Transition metal-based bimetallic catalysts for the chemoselective hydrogenation of furfuraldehyde.* Journal of the Brazilian Chemical Society, 2010. **21**: p. 914-920.
142. Aramendıa, M., et al., *Selective liquid-phase hydrogenation of citral over supported palladium.* Journal of Catalysis, 1997. **172**(1): p. 46-54.
143. Vicente, A., et al., *The relationship between the structural properties of bimetallic Pd–Sn/SiO 2 catalysts and their performance for selective citral hydrogenation.* Journal of catalysis, 2011. **283**(2): p. 133-142.
144. Mueller, W.M., J.P. Blackledge, and G.G. Libowitz, *Metal hydrides*. 2013: Elsevier.
145. Tamura, M., et al., *Rapid synthesis of unsaturated alcohols under mild conditions by highly selective hydrogenation.* Chemical Communications, 2013. **49**(63): p. 7034-7036.
146. Fouilloux, P., *The nature of raney nickel, its adsorbed hydrogen and its catalytic activity for hydrogenation reactions (review).* Applied Catalysis, 1983. **8**(1): p. 1-42.
147. Iriondo, A., et al., *2,5-DMF production through hydrogenation of real and synthetic 5-HMF over transition metal catalysts supported on carriers with different nature.* Catalysis Today, 2016.

148. Nakagawa, Y., et al., *Total Hydrogenation of Furfural over a Silica-Supported Nickel Catalyst Prepared by the Reduction of a Nickel Nitrate Precursor.* ChemCatChem, 2012. **4**(11): p. 1791-1797.
149. Sugano, Y., et al., *Supported Au–Cu Bimetallic Alloy Nanoparticles: An Aerobic Oxidation Catalyst with Regenerable Activity by Visible-Light Irradiation.* Angewandte Chemie International Edition, 2013. **52**(20): p. 5295-5299.
150. Iglesia, E., et al., *Bimetallic Synergy in Cobalt Ruthenium Fischer-Tropsch Synthesis Catalysts.* Journal of Catalysis, 1993. **143**(2): p. 345-368.
151. Zhu, L., et al., *An efficient and stable Ru-Ni/C nano-bimetallic catalyst with a comparatively low Ru loading for benzene hydrogenation under mild reaction conditions.* RSC Advances, 2013. **3**(3): p. 713-719.
152. Ruban, A., H.L. Skriver, and J.K. Nørskov, *Surface segregation energies in transition-metal alloys.* Physical Review B, 1999. **59**(24): p. 15990.
153. Yoon, B., H.-B. Pan, and C.M. Wai, *Relative Catalytic Activities of Carbon Nanotube-Supported Metallic Nanoparticles for Room-Temperature Hydrogenation of Benzene.* The Journal of Physical Chemistry C, 2009. **113**(4): p. 1520-1525.
154. Oosthuizen, R.S. and V.O. Nyamori, *Carbon Nanotubes as Supports for Palladium and Bimetallic Catalysts for Use in Hydrogenation Reactions.* Platinum Metals Review, 2011. **55**(3): p. 154-169.
155. Li, H., H. Li, and J.-F. Deng, *Glucose hydrogenation over Ni–B/SiO2 amorphous alloy catalyst and the promoting effect of metal dopants.* Catalysis Today, 2002. **74**(1–2): p. 53-63.
156. Jordão, M.H., V. Simões, and D. Cardoso, *Zeolite supported Pt-Ni catalysts in n-hexane isomerization.* Applied Catalysis A: General, 2007. **319**: p. 1-6.
157. Sun, J., et al., *Fabrication of active Cu-Zn nanoalloys on H-ZSM5 zeolite for enhanced dimethyl ether synthesis via syngas.* Journal of Materials Chemistry A, 2014. **2**(23): p. 8637-8643.
158. Kang, J., et al., *Ruthenium Nanoparticles Supported on Carbon Nanotubes as Efficient Catalysts for Selective Conversion of Synthesis Gas to Diesel Fuel.* Angewandte Chemie International Edition, 2009. **48**(14): p. 2565-2568.
159. Wang, C., et al., *Tailored cutting of carbon nanotubes and controlled dispersion of metal nanoparticles inside their channels.* Journal of Materials Chemistry, 2008. **18**(47): p. 5782-5786.
160. Falco, C., N. Baccile, and M.-M. Titirici, *Morphological and structural differences between glucose, cellulose and lignocellulosic biomass derived hydrothermal carbons.* Green Chemistry, 2011. **13**(11): p. 3273-3281.
161. Jung, A., et al., *Synthesis of high carbon content microspheres using 2-step microwave carbonization, and the influence of nitrogen doping on catalytic activity.* Carbon, 2013. **60**: p. 307-316.
162. Titirici, M.-M., M. Antonietti, and N. Baccile, *Hydrothermal carbon from biomass: a comparison of the local structure from poly- to monosaccharides and pentoses/hexoses.* Green Chemistry, 2008. **10**(11): p. 1204-1212.
163. Thostenson, E.T. and T.W. Chou, *Microwave processing: fundamentals and applications.* Composites Part A: Applied Science and Manufacturing, 1999. **30**(9): p. 1055-1071.
164. Haque, K.E., *Microwave energy for mineral treatment processes - A brief review.* International Journal of Mineral Processing, 1999. **57**(1): p. 1-24.
165. Jarvis, K.E., A.L. Gray, and R.S. Houk, *Handbook of inductively coupled plasma mass spectrometry*. 1991: Chapman and Hall.
166. Bergeret, G. and P. Gallezot, *Particle Size and Dispersion Measurements*, in *Handbook of Heterogeneous Catalysis*. 2008, Wiley-VCH Verlag GmbH & Co. KGaA.

167. Fultz, B. and J. Howe, *Diffraction and the X-Ray Powder Diffractometer*, in *Transmission Electron Microscopy and Diffractometry of Materials*. 2013, Springer Berlin Heidelberg: Berlin, Heidelberg. p. 1-57.
168. Niemantsverdriet, J.W., *Temperature-Programmed Techniques*, in *Spectroscopy in Catalysis*. 2007, Wiley-VCH Verlag GmbH & Co. KGaA. p. 11-38.
169. Hall, W.K., et al., *Characterization of Solid Catalysts: Sections 3.2.3 – 3.2.4*, in *Handbook of Heterogeneous Catalysis*. 2008, Wiley-VCH Verlag GmbH. p. 689-770.
170. Niemantsverdriet, J.W., *Appendix: Metal Surfaces and Chemisorption*, in *Spectroscopy in Catalysis*. 2007, Wiley-VCH Verlag GmbH & Co. KGaA. p. 297-320.
171. Webb, P.A., *Introduction to chemical adsorption analytical techniques and their applications to catalysis.* Micromeritics Instrument Corp. Technical Publications, 2003.
172. Jr, J.G.G., S. Kim, and W.D. Rhodes, *Turnover frequencies in metal catalysis: Meanings, functionalities and relationships*, in *Catalysis: Volume 17*, J.J. Spivey and G.W. Roberts, Editors. 2004, The Royal Society of Chemistry. p. 320-348.
173. Niemantsverdriet, J.W., *Microscopy and Imaging*, in *Spectroscopy in Catalysis*. 2007, Wiley-VCH Verlag GmbH & Co. KGaA. p. 179-216.
174. Niemantsverdriet, J.W., *Photoemission and Auger Spectroscopy*, in *Spectroscopy in Catalysis*. 2007, Wiley-VCH Verlag GmbH & Co. KGaA. p. 39-83.
175. Thompson, M., *amc technical briefs CHNS Elemental Analyser.* Analytical Methods Committee, 2008.
176. Le Page, J.F., et al., *Characterization of Solid Catalysts: Sections 3.1.4 – 3.2.2*, in *Handbook of Heterogeneous Catalysis*. 2008, Wiley-VCH Verlag GmbH. p. 582-689.
177. Chorkendorff, I. and J.W. Niemantsverdriet, *Concepts of Modern Catalysis and Kinetics*. 2003: Wiley.
178. Elena Stashenko , J.R.M., *Gas Chromatograhphy - Mass spectrocmetry, Advances in Gas Chromatography*. 2014.
179. Sawardeker, J.S., J.H. Sloneker, and A. Jeanes, *Quantitative determination of monosaccharides as their alditol acetates by gas liquid chromatography.* Analytical Chemistry, 1965. **37**(12): p. 1602-1604.
180. Sørensen, R.Z., et al., *Promoted Ru on high-surface area graphite for efficient miniaturized production of hydrogen from ammonia.* Catalysis Letters, 2006. **112**(1): p. 77-81.
181. Rojas, S., et al., *Preparation of carbon supported Pt and PtRu nanoparticles from microemulsion: Electrocatalysts for fuel cell applications.* Applied Catalysis A: General, 2005. **285**(1–2): p. 24-35.
182. Wakita, H., T. Takeguchi, and W. Ueda, *Enhancement of selectivity for preferential CO oxidation over SO2-pretreated Ru/Al2O3 catalyst by the presence of sulfur compounds.* Journal of Molecular Catalysis A-Chemical, 2007. **268**(1-2): p. 139-147.
183. Zhao, J., et al., *One-step green synthesis of a ruthenium/graphene composite as a highly efficient catalyst.* RSC Advances, 2015. **5**(10): p. 7679-7686.
184. Zhu, L., et al., *Effect of ruthenium nickel bimetallic composition on the catalytic performance for benzene hydrogenation to cyclohexane.* Applied Catalysis A: General, 2015. **499**: p. 124-132.
185. Su, F., et al., *Thermally Reduced Ruthenium Nanoparticles as a Highly Active Heterogeneous Catalyst for Hydrogenation of Monoaromatics.* Journal of the American Chemical Society, 2007. **129**(46): p. 14213-14223.
186. Wei, Z., et al., *One-pot production of 2,5-dimethylfuran from fructose over Ru/C and a Lewis-Bronsted acid mixture in N,N-dimethylformamide.* Catalysis Science & Technology, 2016.
187. Guerrero-Ruiz, A., P. Badenes, and I. Rodríguez-Ramos, *Study of some factors affecting the Ru and Pt dispersions over high surface area graphite-supported catalysts.* Applied Catalysis A: General, 1998. **173**(2): p. 313-321.

188. Cerro-Alarcón, M., A. Guerrero-Ruíz, and I. Rodríguez-Ramos, *Stereoselective hydrogenation of Paracetamol to trans-4-acetamidocyclohexanol on carbon-supported Ru M (M = Co, Ni) bimetallic catalysts.* Catalysis Today, 2004. **93–95**: p. 395-403.
189. Cerro-Alarcón, M., et al., *Further insights into the Ru nanoparticles–carbon interactions and their role in the catalytic properties.* Carbon, 2005. **43**(13): p. 2711-2722.
190. García-García, F.R., et al., *Following the Evolution of Ru/Activated Carbon Catalysts during the Decomposition–Reduction of the Ru(NO)(NO3)3 Precursor.* ChemCatChem, 2013. **5**(8): p. 2446-2452.
191. Bachiller-Baeza, B., et al., *Hydrogenation of Citral on Activated Carbon and High-Surface-Area Graphite-Supported Ruthenium Catalysts Modified with Iron.* Journal of Catalysis, 2001. **204**(2): p. 450-459.
192. Koopman, P.G.J., et al., *Preparation and high temperature activation of ruthenium on carbon hydrogenation catalysts.* Carbon, 1979. **17**(5): p. 399-402.
193. Tavasoli, A., et al., *Cobalt supported on carbon nanotubes — A promising novel Fischer–Tropsch synthesis catalyst.* Fuel Processing Technology, 2008. **89**(5): p. 491-498.
194. Taylor, K.C., *Determination of ruthenium surface areas by hydrogen and oxygen chemisorption.* Journal of Catalysis, 1975. **38**(1-3): p. 299-306.
195. Dalla Betta, R.A., *Carbon monoxide adsorption on supported ruthenium.* The Journal of Physical Chemistry, 1975. **79**(23): p. 2519-2525.
196. Uchida, M. and A.T. Bell, *A study of NO reduction by H2 over an alumina-supported ruthenium catalyst.* Journal of Catalysis, 1979. **60**(2): p. 204-215.
197. Fu, T., J. Lv, and Z. Li, *Effect of Carbon Porosity and Cobalt Particle Size on the Catalytic Performance of Carbon Supported Cobalt Fischer–Tropsch Catalysts.* Industrial & Engineering Chemistry Research, 2014. **53**(4): p. 1342-1350.
198. Iqbal, S., et al., *Ruthenium Nanoparticles Supported on Carbon: An Active Catalyst for the Hydrogenation of Lactic Acid to 1,2-Propanediol.* ACS Catalysis, 2015. **5**(9): p. 5047-5059.
199. Miao, S., et al., *Ru Nanoparticles Immobilized on Montmorillonite by Ionic Liquids: A Highly Efficient Heterogeneous Catalyst for the Hydrogenation of Benzene.* Angewandte Chemie International Edition, 2006. **45**(2): p. 266-269.
200. Mai, E.F., et al., *Molybdenum carbide nanoparticles within carbon nanotubes as superior catalysts for γ-valerolactone production via levulinic acid hydrogenation.* Green Chemistry, 2014. **16**(9): p. 4092-4097.
201. Lin, G., et al., *Multi-walled carbon nanotubes as novel promoter of catalysts for certain hydrogenation and dehydrogenation reactions.* Science China Chemistry, 2015. **58**(1): p. 47-59.
202. Sun, Z., et al., *Selective hydrogenation of cinnamaldehyde over Pt nanoparticles deposited on reduced graphene oxide.* RSC Advances, 2014. **4**(4): p. 1874-1878.
203. Kukushkin, R.G., et al., *Influence of Mo on catalytic activity of Ni-based catalysts in hydrodeoxygenation of esters.* Applied Catalysis B: Environmental, 2015. **163**(0): p. 531-538.
204. Murzin, D.Y. and T. Salmi, *2.3 Catalysis by Transition Metals*, in *Catalytic Kinetics*. Elsevier.
205. Tao, F., *5. Nickel Nanoparticles in the Transfer Hydrogenation of Functional Groups*, in *Metal Nanoparticles for Catalysis - Advances and Applications*. Royal Society of Chemistry.
206. Twigg, M.V. and M.S. Spencer, *Deactivation of supported copper metal catalysts for hydrogenation reactions.* Applied Catalysis A: General, 2001. **212**(1): p. 161-174.
207. Kong, X., et al., *Switchable synthesis of 2, 5-dimethylfuran and 2, 5-dihydroxymethyltetrahydrofuran from 5-hydroxymethylfurfural over Raney Ni catalyst.* RSC Advances, 2014. **4**(105): p. 60467-60472.

208. Romano, P.N., et al., *Microwave-Assisted Selective Hydrogenation of Furfural to Furfuryl Alcohol Employing a Green and Noble Metal-Free Copper Catalyst.* ChemSusChem, 2016. **9**(24): p. 3387-3392.
209. Zhu, Y., et al., *Efficient synthesis of 2, 5-dihydroxymethylfuran and 2, 5-dimethylfuran from 5-hydroxymethylfurfural using mineral-derived Cu catalysts as versatile catalysts.* Catalysis Science & Technology, 2015. **5**(8): p. 4208-4217.
210. Guerrero-Ruiz, A. and I. Rodriguez-Ramos, *Spillover and Mobility of Species on Solid Surfaces*. 2001: Elsevier Science.
211. Di, X., et al., *Hydrogenation of succinic acid over supported rhenium catalysts prepared by the microwave-assisted thermolytic method.* Catalysis Science & Technology, 2015. **5**(4): p. 2441-2448.
212. Crisafulli, C., et al., *Ni–Ru bimetallic catalysts for the CO2 reforming of methane.* Applied Catalysis A: General, 2002. **225**(1–2): p. 1-9.
213. Tsubaki, N., S. Sun, and K. Fujimoto, *Different Functions of the Noble Metals Added to Cobalt Catalysts for Fischer–Tropsch Synthesis.* Journal of Catalysis, 2001. **199**(2): p. 236-246.
214. Guerrero-Ruiz, A., A. Sepu, and I. Rodri, *Carbon monoxide hydrogenation over carbon supported cobalt or ruthenium catalysts. Promoting effects of magnesium, vanadium and cerium oxides.* Applied Catalysis A: General, 1994. **120**(1): p. 71-83.
215. Portnoi, V.K., et al., *Formation of nickel carbide in the course of deformation treatment of Ni-C mixtures.* The Physics of Metals and Metallography, 2010. **109**(2): p. 153-161.
216. Chen, L., et al., *Aqueous-phase hydrodeoxygenation of carboxylic acids to alcohols or alkanes over supported Ru catalysts.* Journal of Molecular Catalysis A: Chemical, 2011. **351**: p. 217-227.
217. Miyazawa, T., et al., *Development of a Ru/C catalyst for glycerol hydrogenolysis in combination with an ion-exchange resin.* Applied Catalysis A: General, 2007. **318**: p. 244-251.
218. Bond, G.C., *Heterogeneous catalysis.* 1987.
219. Dimitratos, N., F. Porta, and L. Prati, *Au, Pd (mono and bimetallic) catalysts supported on graphite using the immobilisation method: Synthesis and catalytic testing for liquid phase oxidation of glycerol.* Applied Catalysis A: General, 2005. **291**(1–2): p. 210-214.
220. Comotti, M., C.D. Pina, and M. Rossi, *Mono- and bimetallic catalysts for glucose oxidation.* Journal of Molecular Catalysis A: Chemical, 2006. **251**(1–2): p. 89-92.
221. Verdeguer, P., N. Merat, and A. Gaset, *Oxydation catalytique du HMF en acide 2,5-furane dicarboxylique.* Journal of Molecular Catalysis, 1993. **85**(3): p. 327-344.
222. Lu, S., et al., *Low temperature hydrogenation of benzene and cyclohexene: A comparative study between γ-Al2O3 supported PtCo and PtNi bimetallic catalysts.* Journal of Catalysis, 2008. **259**(2): p. 260-268.
223. Anderson, J.R., *Structure of metallic catalysts.* Academic Press, ix+ 469, 24 x 16 cm, illustrated(<-> 16. 50, 1975.
224. Park, K.-W., et al., *Chemical and Electronic Effects of Ni in Pt/Ni and Pt/Ru/Ni Alloy Nanoparticles in Methanol Electrooxidation.* The Journal of Physical Chemistry B, 2002. **106**(8): p. 1869-1877.
225. Khromova, S.A., et al., *Anisole hydrodeoxygenation over Ni–Cu bimetallic catalysts: The effect of Ni/Cu ratio on selectivity.* Applied Catalysis A: General, 2014. **470**: p. 261-270.
226. Tavasoli, A., et al., *Enhancement of ruthenium-promoted Co/CNT nanocatalyst performance using microemulsion technique.* International Journal of Industrial Chemistry, 2014. **5**(1): p. 1.
227. Zhang, Y.J., et al., *Synthesis and characterization of carbon black supported Pt–Ru alloy as a model catalyst for fuel cells.* Catalysis Today, 2004. **93–95**(0): p. 619-626.
228. Ferrando, R., J. Jellinek, and R.L. Johnston, *Nanoalloys: From Theory to Applications of Alloy Clusters and Nanoparticles.* Chemical Reviews, 2008. **108**(3): p. 845-910.

229. Luo, J., et al., *Mechanisms for High Selectivity in the Hydrodeoxygenation of 5-Hydroxymethylfurfural over PtCo Nanocrystals.* ACS Catalysis, 2016. **6**(7): p. 4095-4104.
230. Sitthisa, S., W. An, and D.E. Resasco, *Selective conversion of furfural to methylfuran over silica-supported NiFe bimetallic catalysts.* Journal of Catalysis, 2011. **284**(1): p. 90-101.
231. Bailón-García, E., et al., *Catalysts Supported on Carbon Materials for the Selective Hydrogenation of Citral.* Catalysts, 2013. **3**(4): p. 853-877.
232. Titirici, M.-M. and M. Antonietti, *Chemistry and materials options of sustainable carbon materials made by hydrothermal carbonization.* Chemical Society Reviews, 2010. **39**(1): p. 103-116.
233. Cui, X., M. Antonietti, and S.H. Yu, *Structural effects of iron oxide nanoparticles and iron ions on the hydrothermal carbonization of starch and rice carbohydrates.* Small, 2006. **2**(6): p. 756-759.
234. Zheng, M., et al., *Alcohol-assisted hydrothermal carbonization to fabricate spheroidal carbons with a tunable shape and aspect ratio.* Carbon, 2010. **48**(4): p. 1224-1233.
235. Qian, H.-S., et al., *Synthesis of uniform Te@ carbon-rich composite nanocables with photoluminescence properties and carbonaceous nanofibers by the hydrothermal carbonization of glucose.* Chemistry of Materials, 2006. **18**(8): p. 2102-2108.
236. Titirici, M.M., et al., *A direct synthesis of mesoporous carbons with bicontinuous pore morphology from crude plant material by hydrothermal carbonization.* Chemistry of Materials, 2007. **19**(17): p. 4205-4212.
237. Budarin, V., et al., *Starbons: New Starch-Derived Mesoporous Carbonaceous Materials with Tunable Properties.* Angewandte Chemie, 2006. **118**(23): p. 3866-3870.
238. Yao, C., et al., *Hydrothermal dehydration of aqueous fructose solutions in a closed system.* The Journal of Physical Chemistry C, 2007. **111**(42): p. 15141-15145.
239. Cheng, F., et al., *Biomass waste-derived microporous carbons with controlled texture and enhanced hydrogen uptake.* Chemistry of Materials, 2008. **20**(5): p. 1889-1895.
240. Wang, Q., et al., *Monodispersed hard carbon spherules with uniform nanopores.* Carbon, 2001. **39**(14): p. 2211-2214.
241. Sun, X. and Y. Li, *Colloidal Carbon Spheres and Their Core/Shell Structures with Noble-Metal Nanoparticles.* Angewandte Chemie International Edition, 2004. **43**(5): p. 597-601.
242. Baccile, N., et al., *Structural Characterization of Hydrothermal Carbon Spheres by Advanced Solid-State MAS 13C NMR Investigations.* The Journal of Physical Chemistry C, 2009. **113**(22): p. 9644-9654.
243. Menéndez, J.A., et al., *Microwave heating processes involving carbon materials.* Fuel Processing Technology, 2010. **91**(1): p. 1-8.
244. Titirici, M.-M., et al., *Sustainable carbon materials.* Chemical Society Reviews, 2015. **44**(1): p. 250-290.
245. Yu, S.H., et al., *From Starch to Metal/Carbon Hybrid Nanostructures: Hydrothermal Metal-Catalyzed Carbonization.* Advanced Materials, 2004. **16**(18): p. 1636-1640.
246. Yu, J.C., et al., *Synthesis and Characterization of Core-Shell Selenium/Carbon Colloids and Hollow Carbon Capsules.* Chemistry – A European Journal, 2006. **12**(2): p. 548-552.
247. Zhang, F., et al., *Understanding effect of wall structure on the hydrothermal stability of mesostructured silica SBA-15.* The Journal of Physical Chemistry B, 2005. **109**(18): p. 8723-8732.

Appendix

A.1GC calibration plots for the reactant and the products in HMF hydrogeantion.

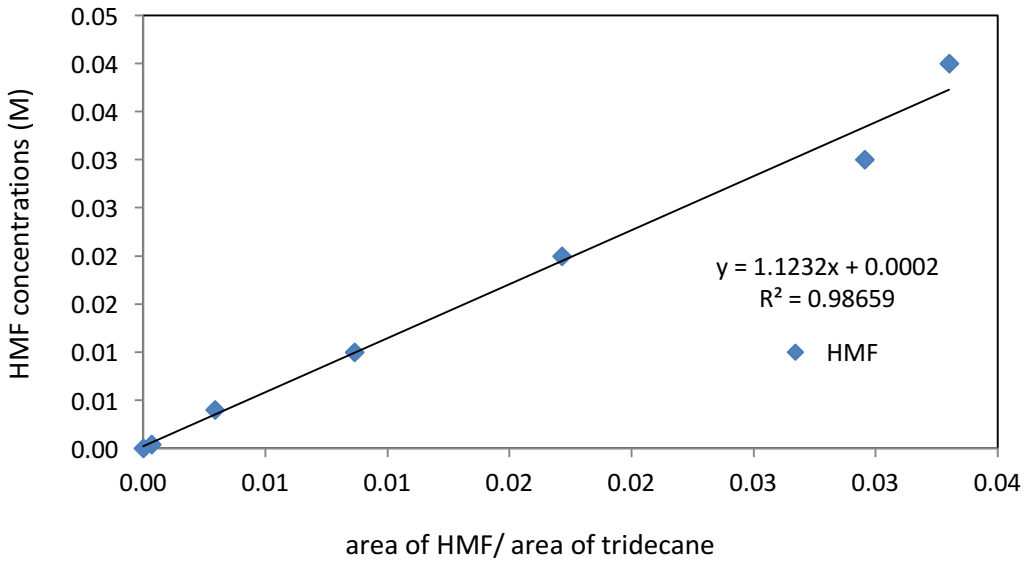

Appendix 1 Calibration plot of 5-hydroxymethylfurfural (HMF)

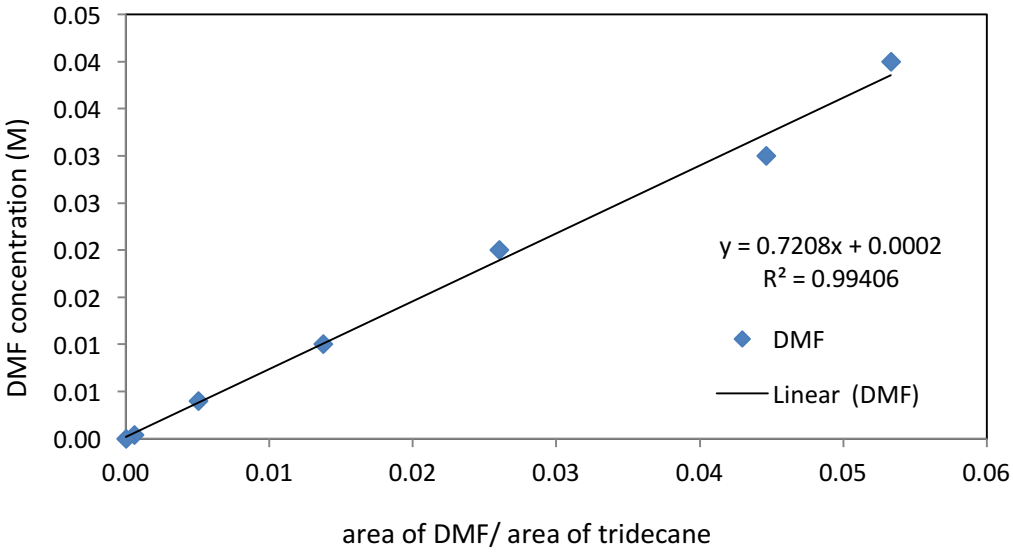

Appendix 2 Calibration plot of 2,5-dimethylfuran (DM

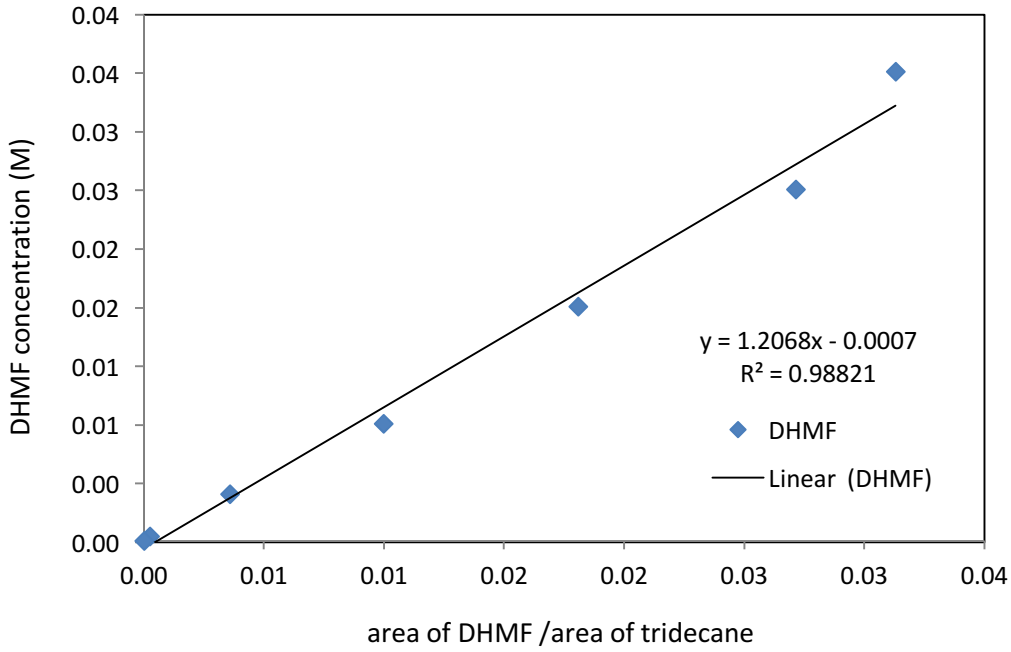

Appendix 3 Calibration plot of 2,5- dihydroxymethylfurrural (DHMF)

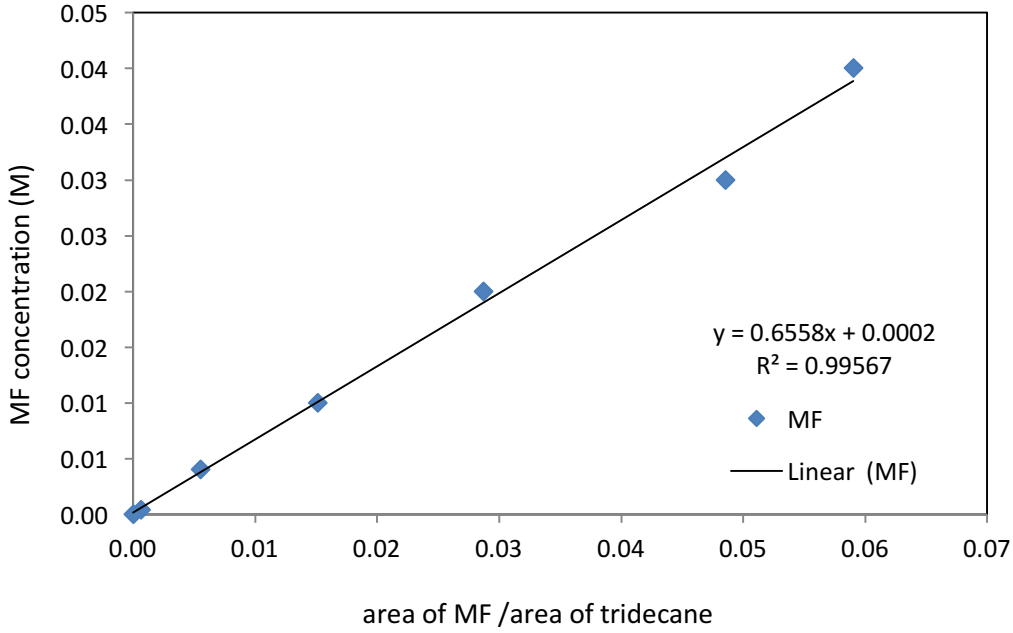

Appendix 4 Calibration plot of MF

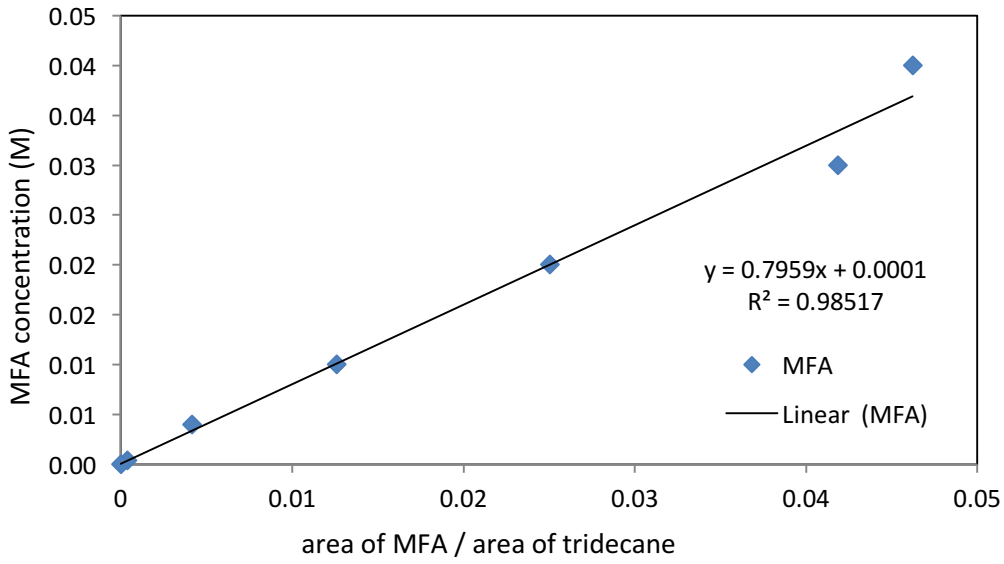

Appendix 5 Calibration plot of 5-methylfurfuryl alcohol (MFA)

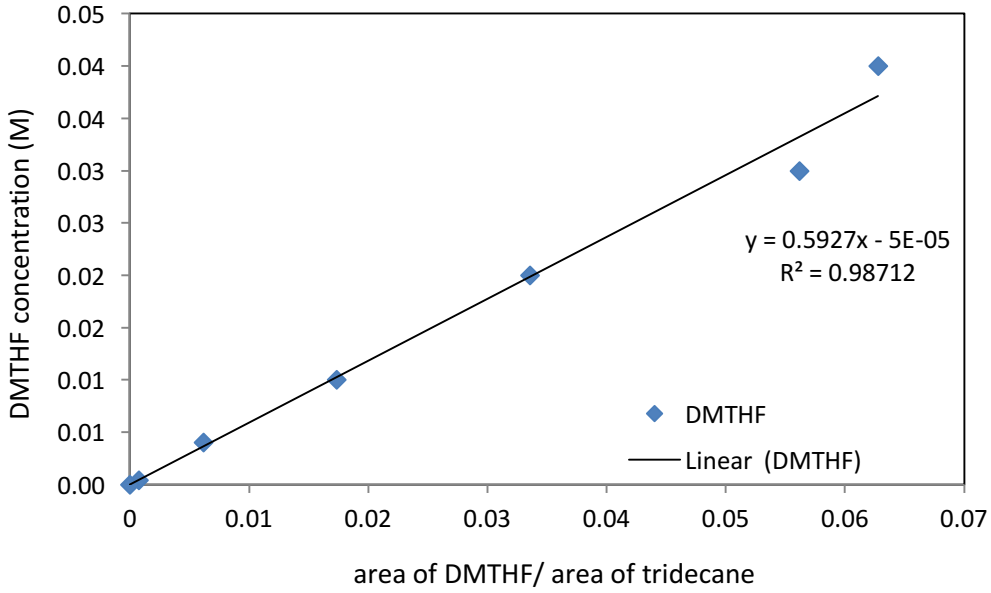

Appendix 6 calibration plot of 2,5-dimethyltetrahydrofuran (DMTHF)

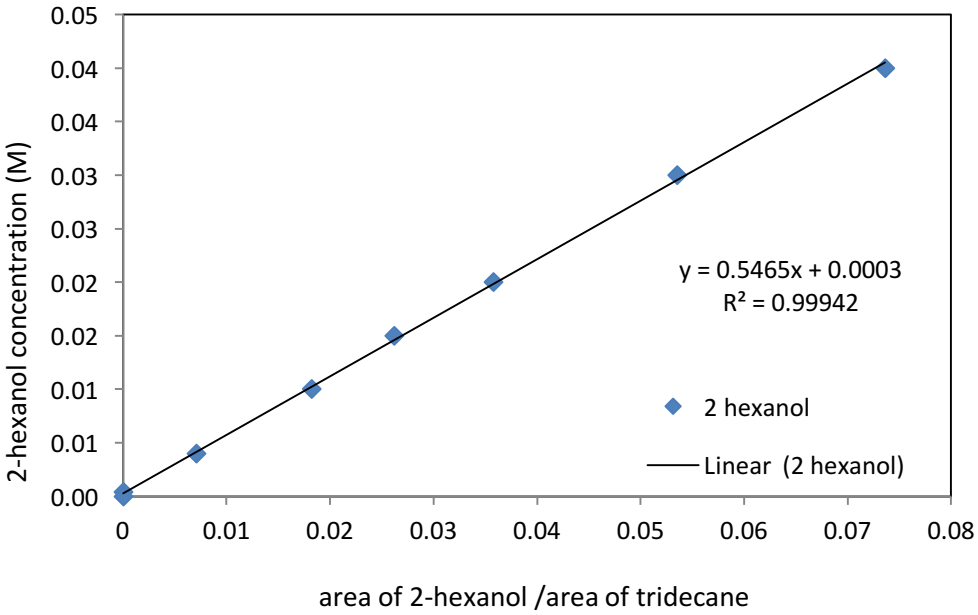

Appendix 7 calibration plot of 2-hexanol

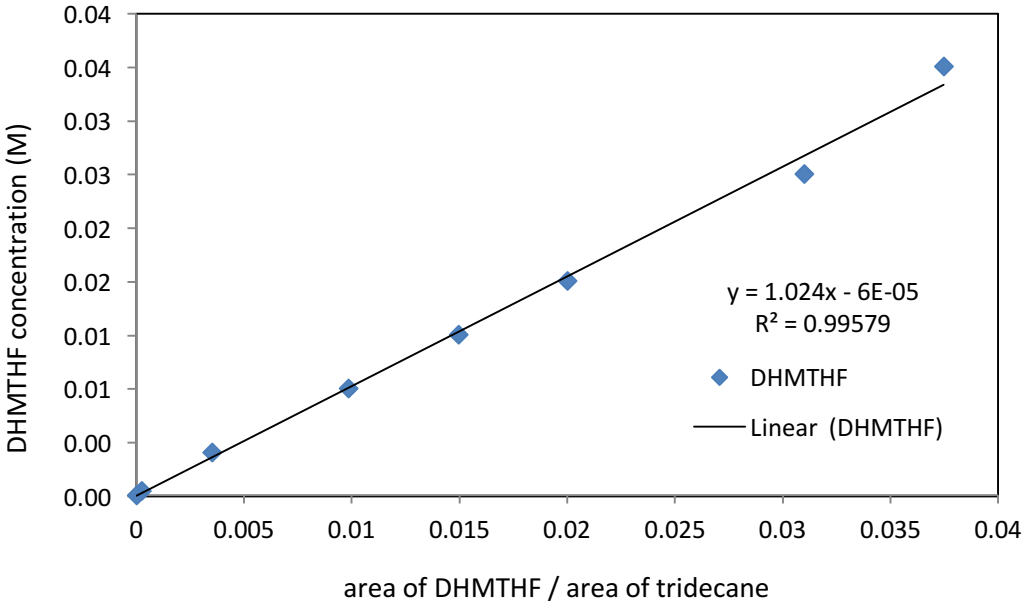

Appendix 8 calibration plot of 2,5-dihydroxymethyltetrahydrofuran (DHMTHF)

A.2 GC-MS spectrums and mass fraction of reactant and hydrogenation products of HMF.

File :C:\msdchem\1\data\AZAM\AZMHMF.D
Operator :
Acquired : 26 Nov 2015 12:43 using AcqMethod PP201115TEST V1.M
Instrument : GCMS
Sample Name: AZM HMF 46mM
Misc Info :
Vial Number: 3

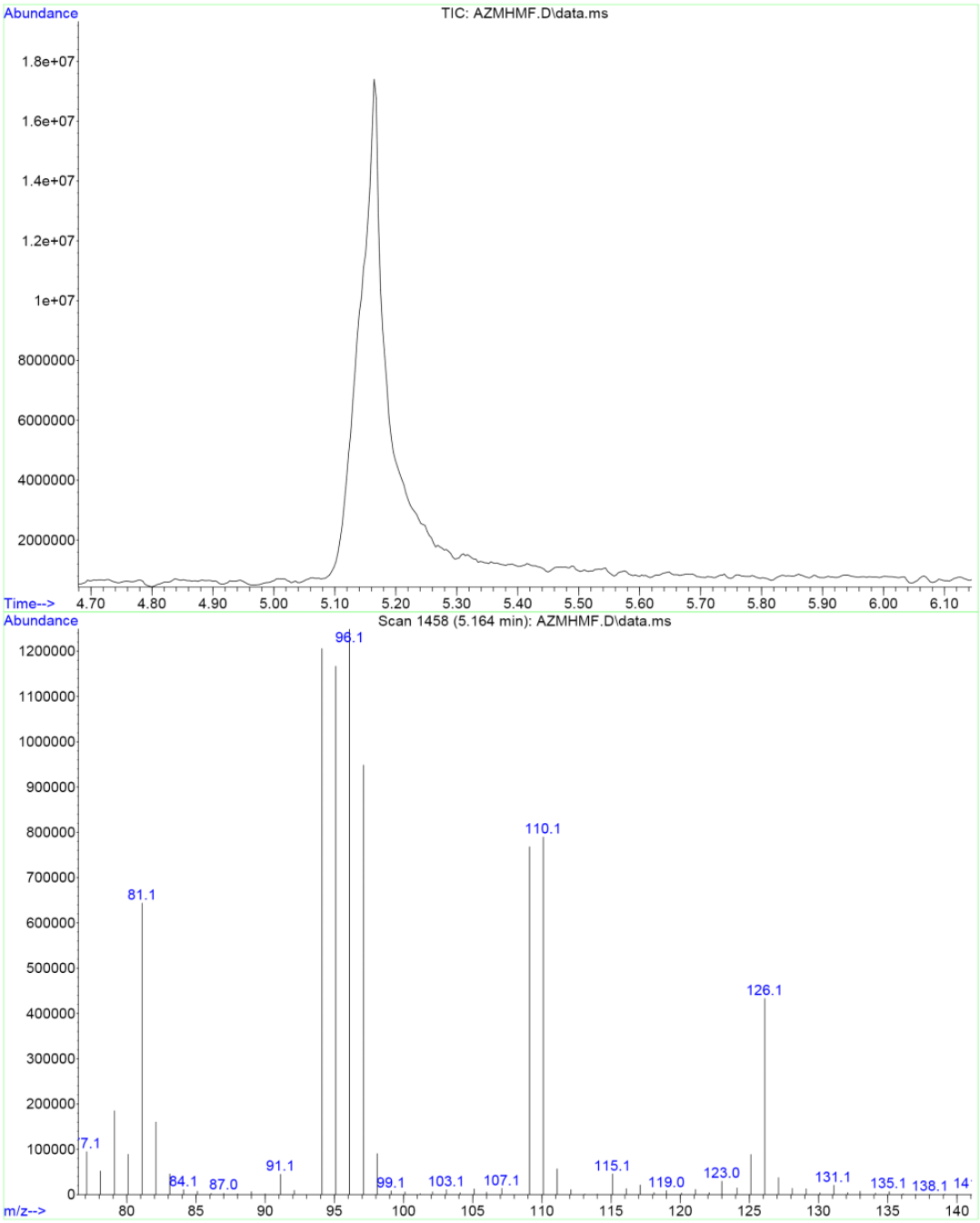

Appendix 9 Mass fraction of HMF

File :C:\msdchem\1\data\AZAM\AZMMF.D
Operator :
Acquired : 25 Nov 2015 19:00 using AcqMethod PP201115test v1.M
Instrument : GCMS
Sample Name: 40mM MF 231115
Misc Info :
Vial Number: 6

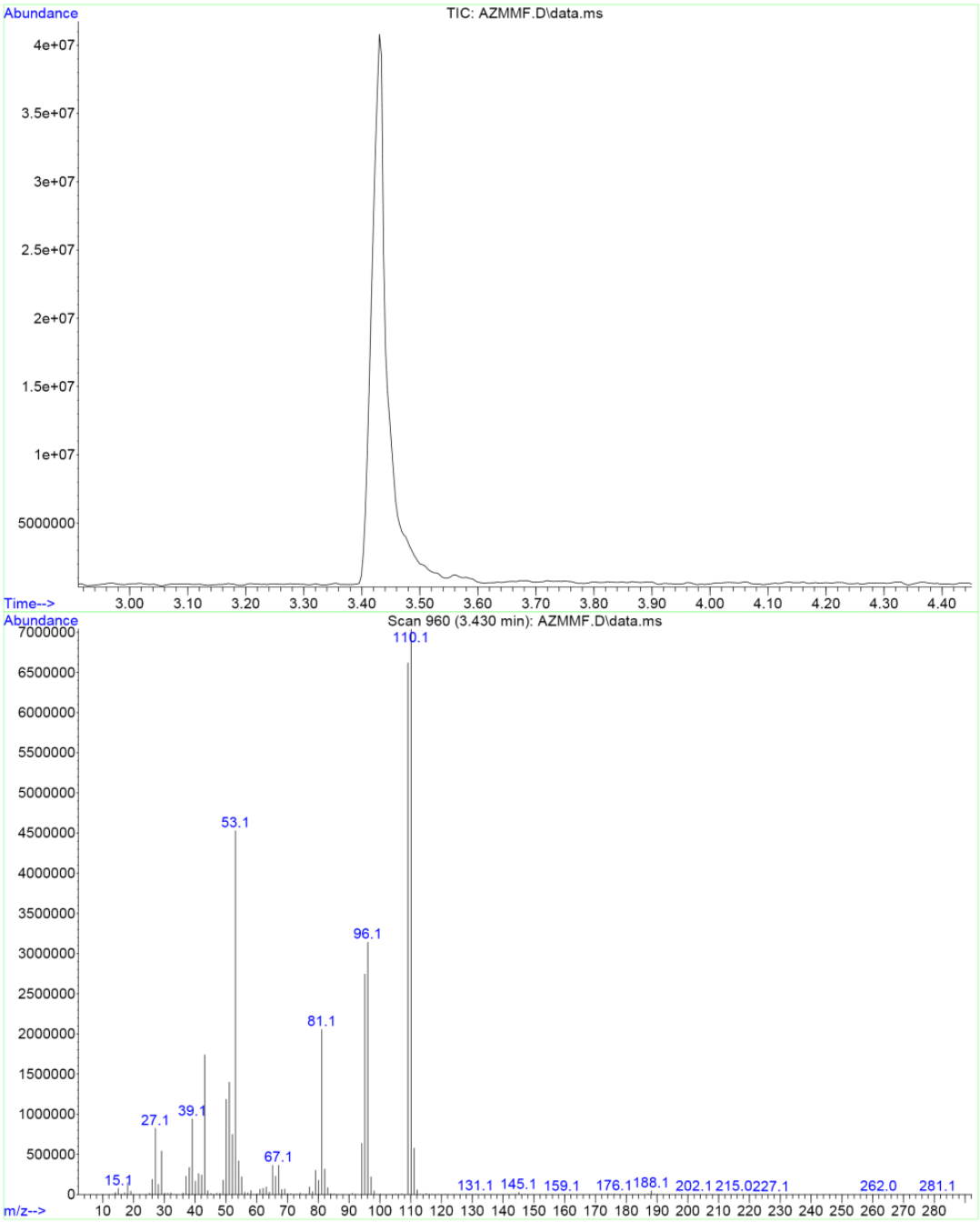

Appendix 10 Mass fraction of MF

File :C:\msdchem\1\data\AZAM\AZMMFA.D
Operator :
Acquired : 25 Nov 2015 18:39 using AcqMethod PP201115test v1.M
Instrument : GCMS
Sample Name: 40mM MFA 231115
Misc Info :
Vial Number: 5

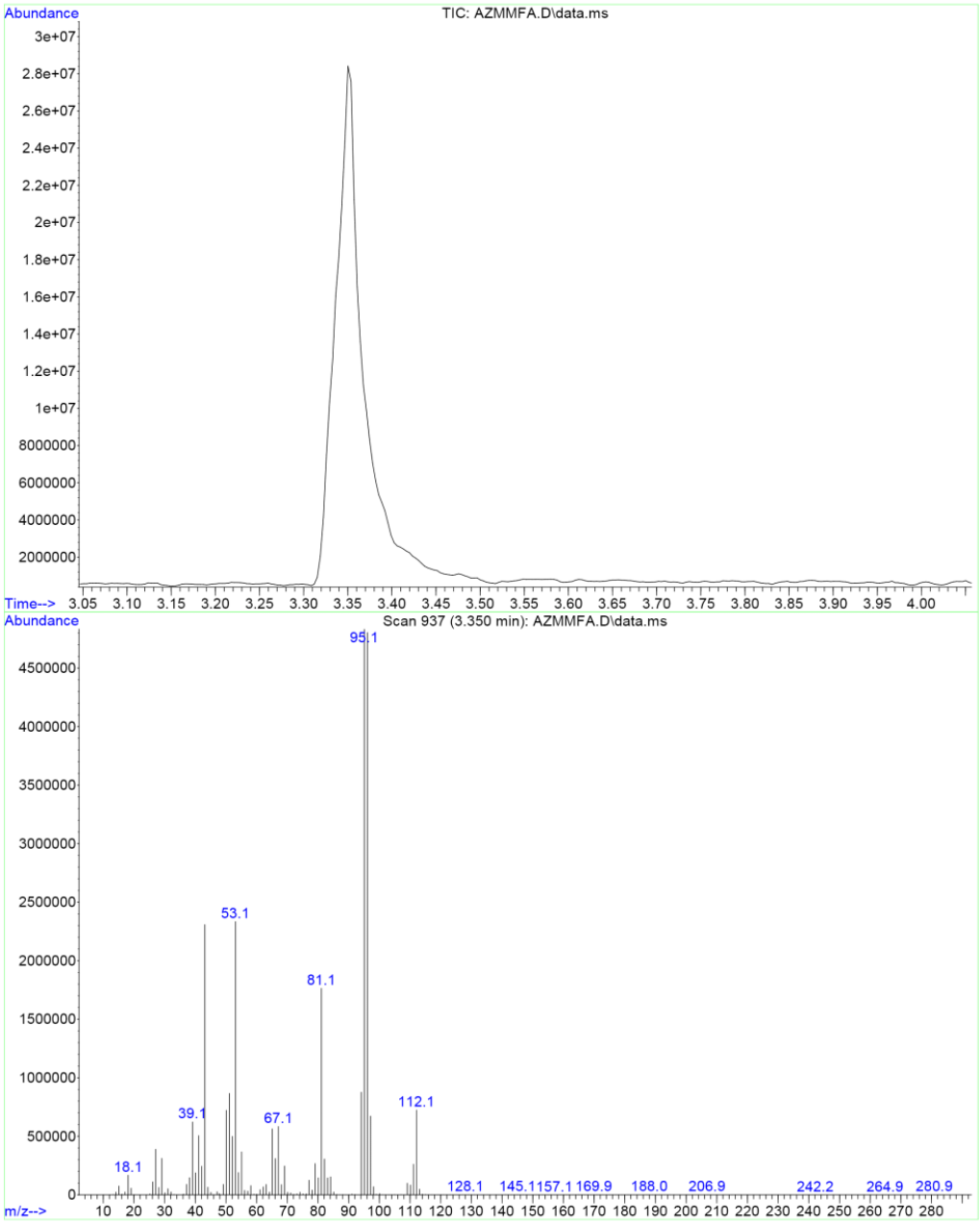

Appendix 11 Mass Fraction of MFA

File :C:\msdchem\1\data\AZAM\AZM DMF PURE.D
Operator :
Acquired : 26 Nov 2015 15:52 using AcqMethod PP201115TEST V1.M
Instrument : GCMS
Sample Name: AZM DMF NO SOLVENT
Misc Info :
Vial Number: 3

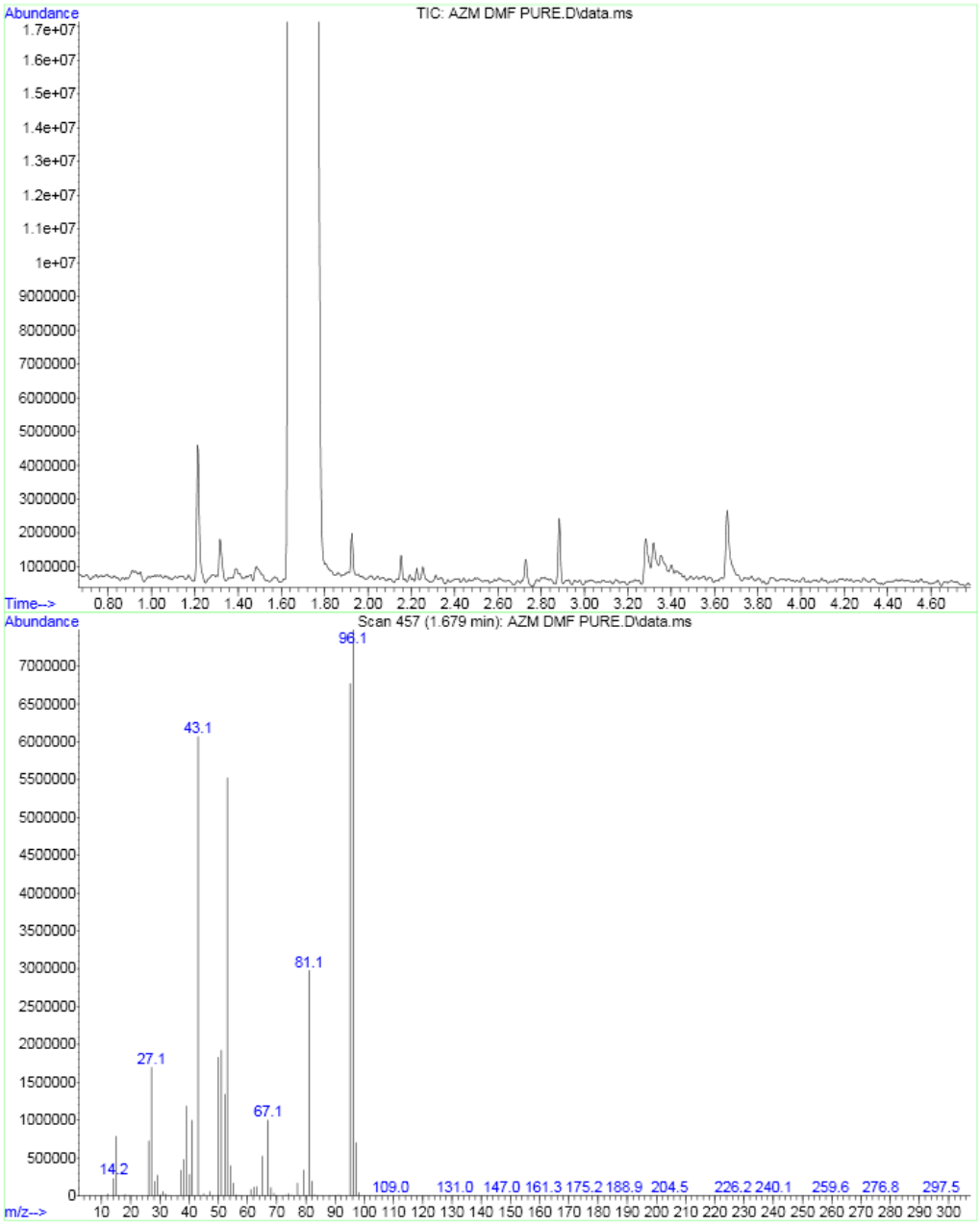

Appendix 12 Mass fraction of DMF

File :C:\msdchem\1\data\AZAM\AZMDMTHF.D
Operator :
Acquired : 25 Nov 2015 18:09 using AcqMethod PP201115test v1.M
Instrument : GCMS
Sample Name: 40mM DMTHF 231115
Misc Info :
Vial Number: 4

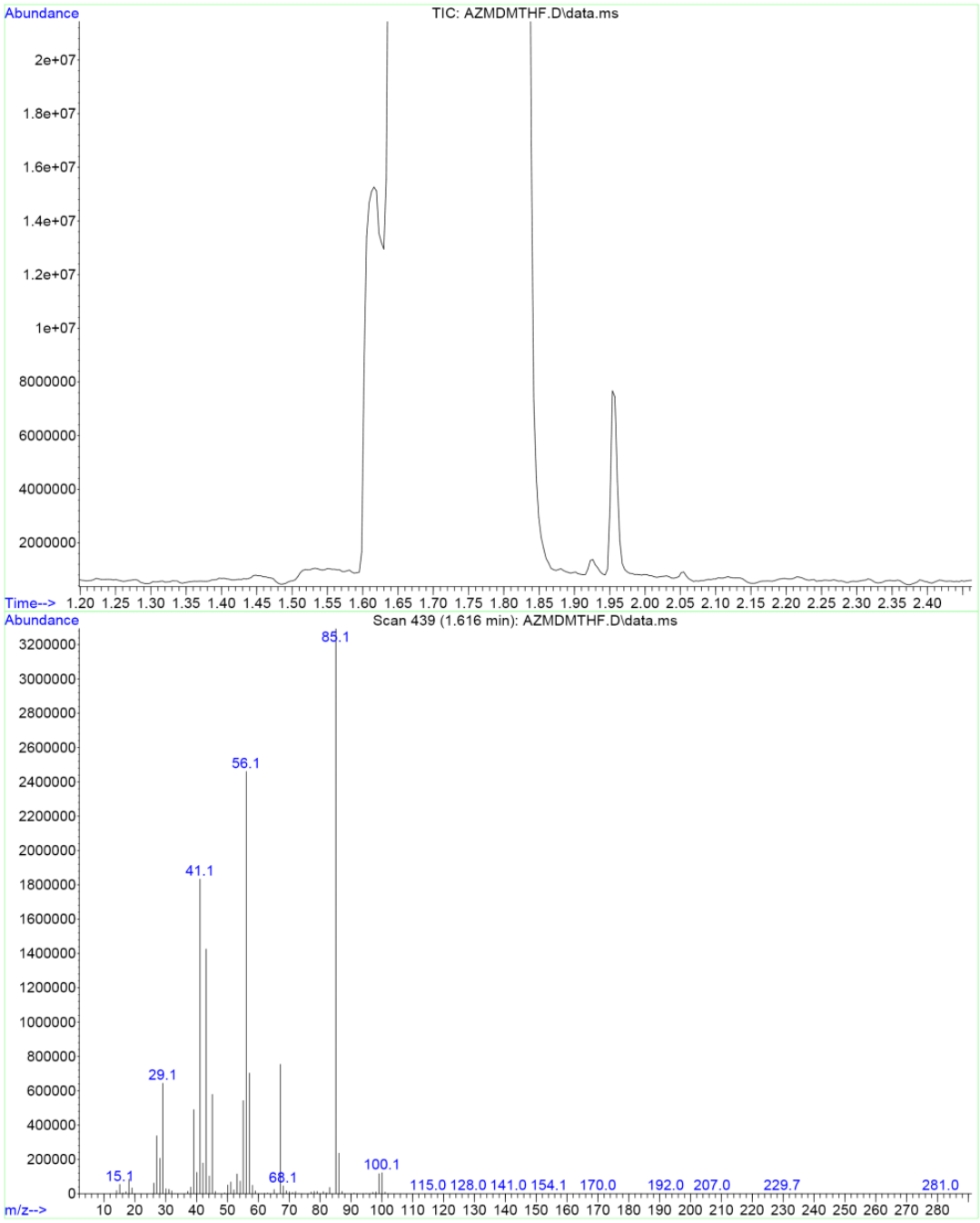

Appendix 13 Mass Fraction of DMTHF

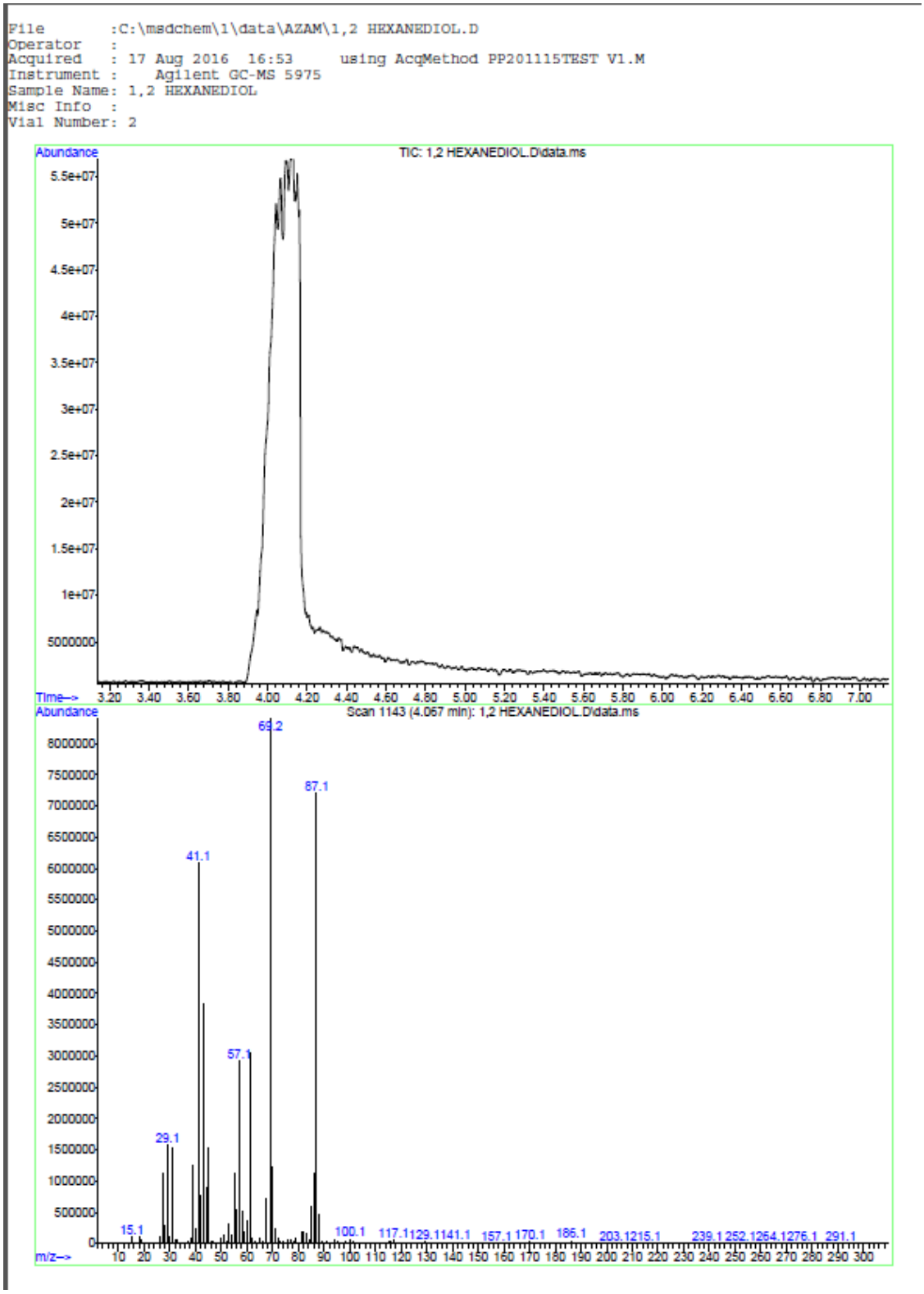

Appendix 14 Mass Fraction of 2 hexanol

A.3 TOL products distribution of bimetallic catalysts

Reaction conditions: HMF, 40 mM; catalyst, 60 mg; solvent, Dioxane; pressure, 20 bar H_2; temperature 150 °C, stirring, 1100 rpm

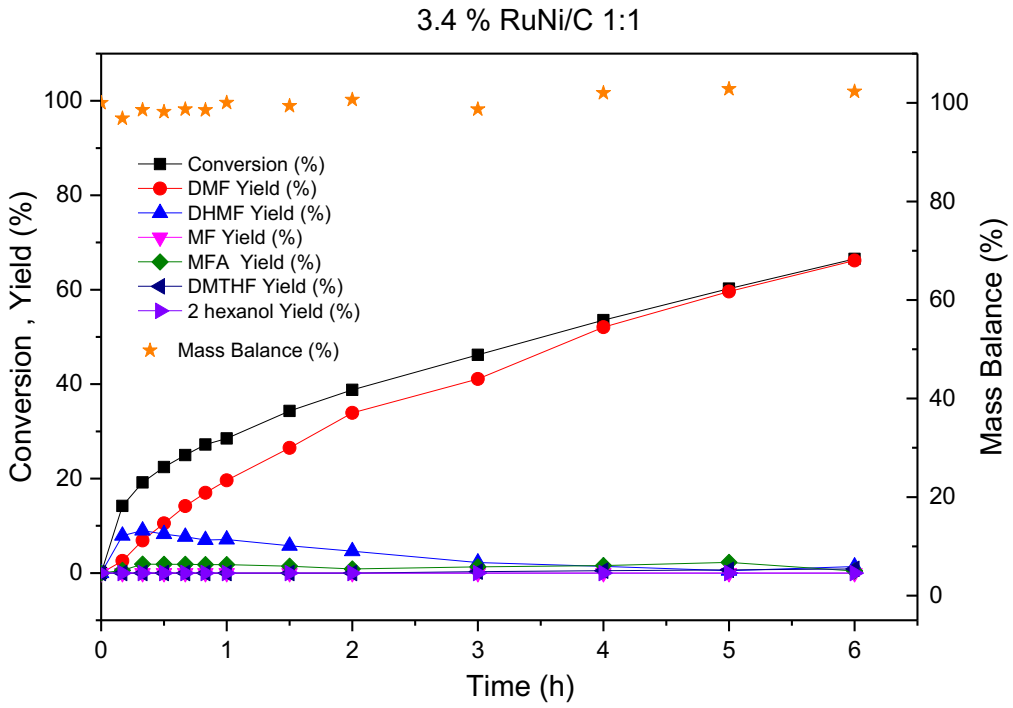

Appendix 15 TOL of product distribution of HMF hydrogenation over 3.4 % RuNi/C 1:1.

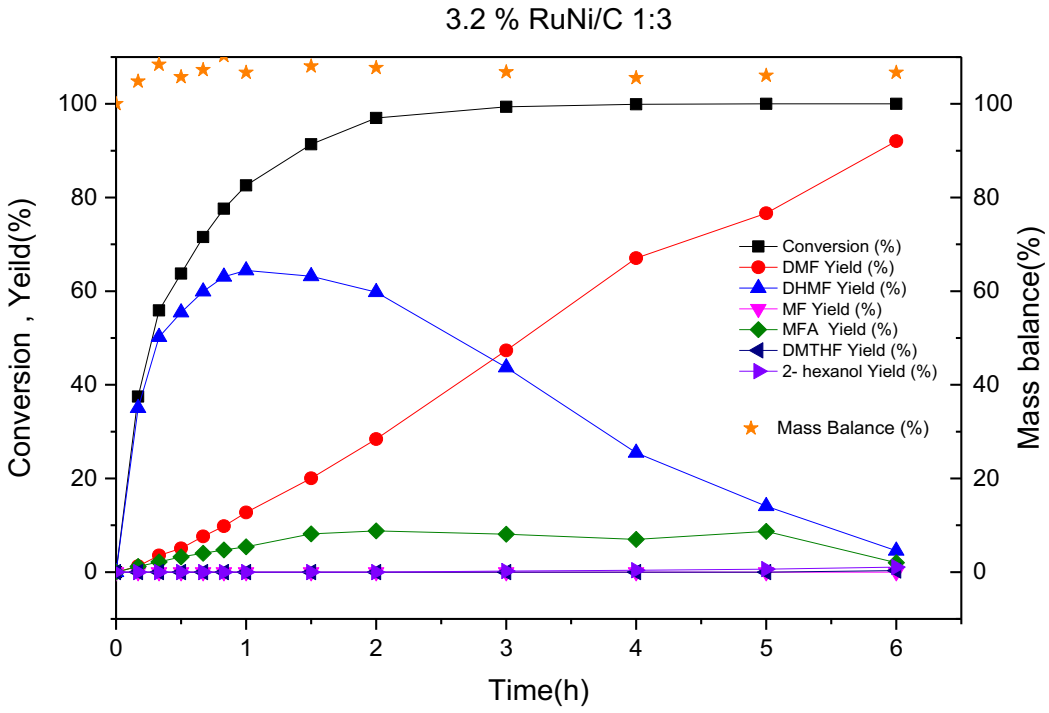

Appendix 16 TOL of product distribution of HMF hydrogenation over 3.4 % RuNi/C 1:3.

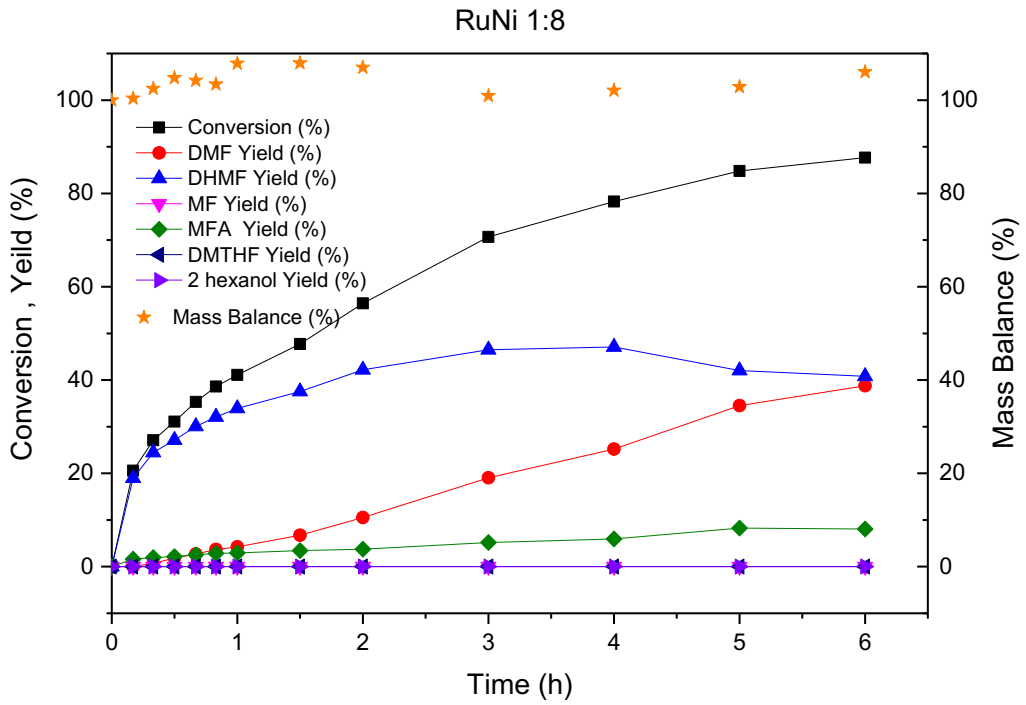

Appendix 17 TOL of product distribution of HMF hydrogenation over 3.4 % RuNi/C 1:8.

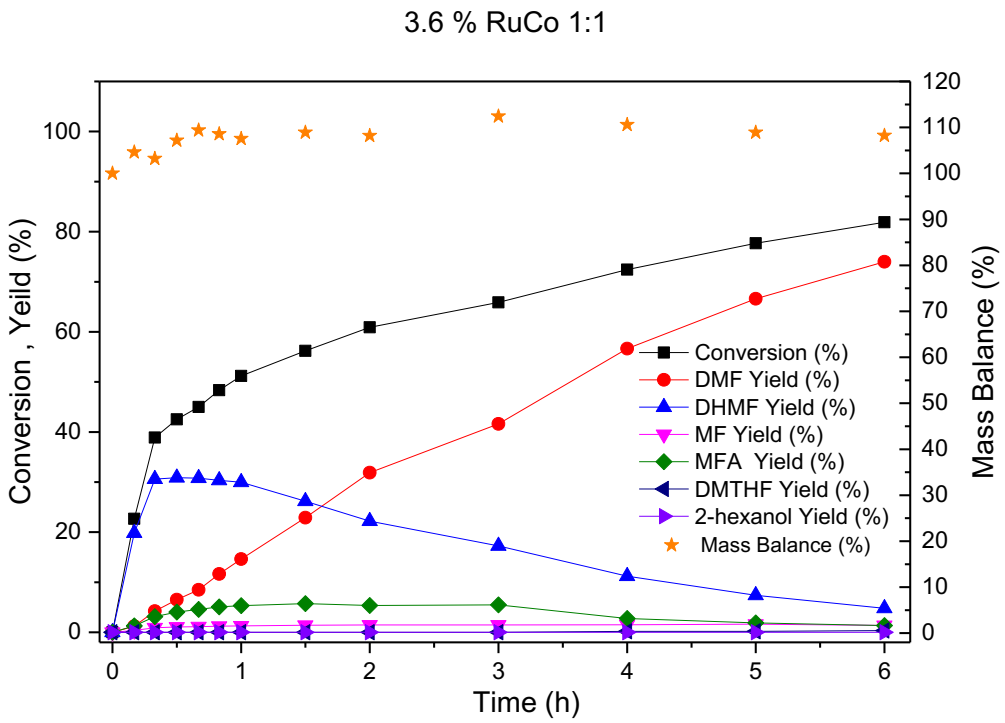

Appendix 18 TOL of product distribution of HMF hydrogenation over 3.6 % RuCo/C 1:1.

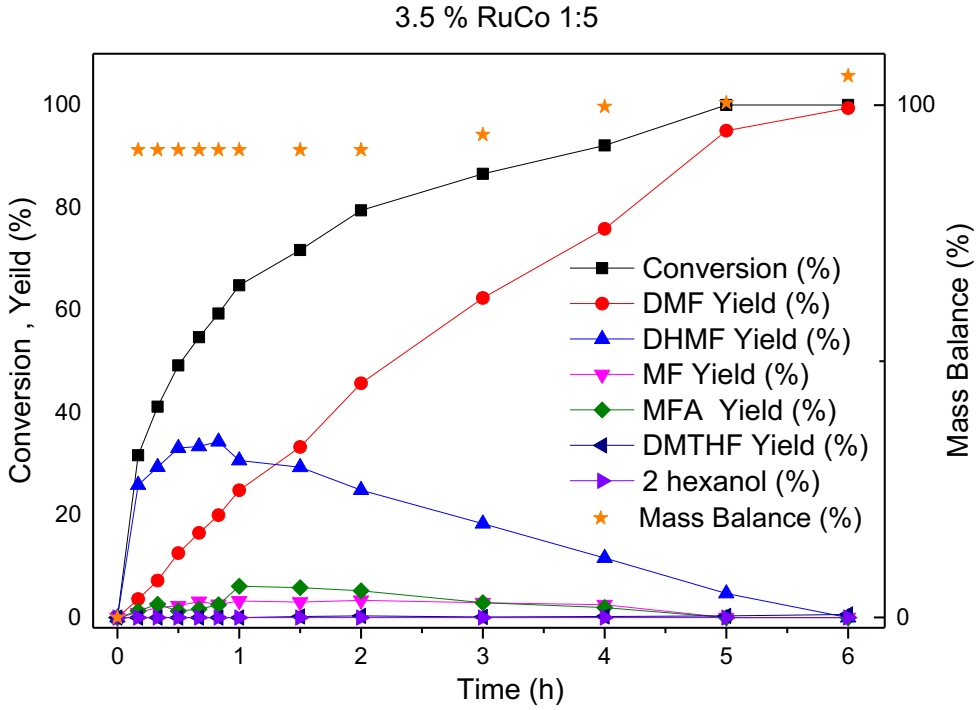

Appendix 19 TOL of product distribution of HMF hydrogenation over 3.5 % RuCo/C 1:5.

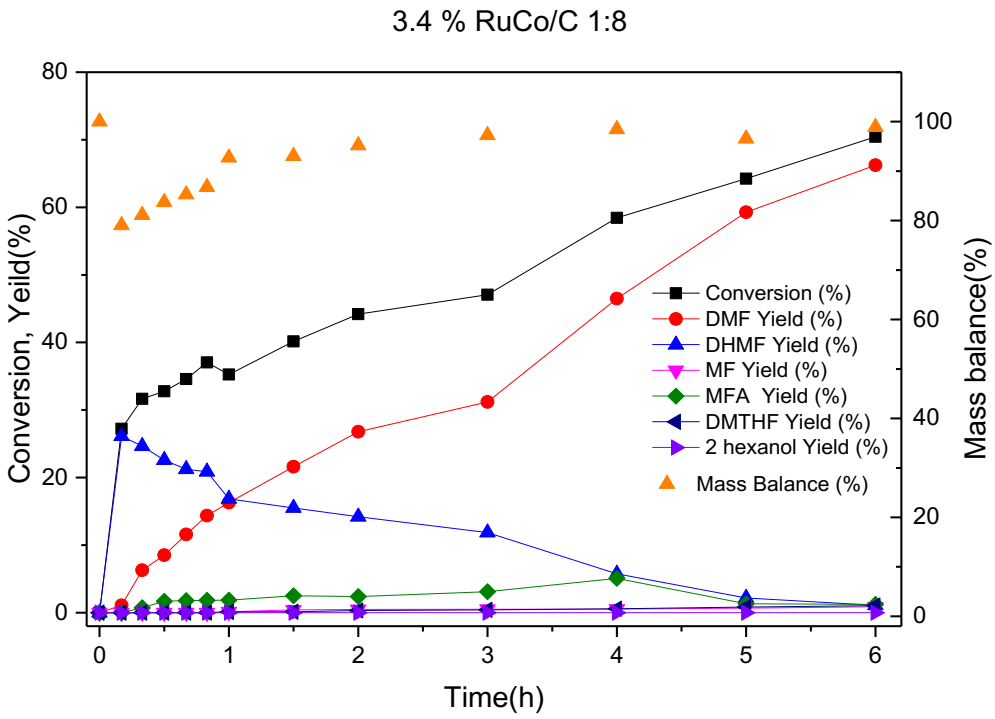

Appendix 20 TOL of product distribution of HMF hydrogenation over 3.4 % RuCo/C 1:3.

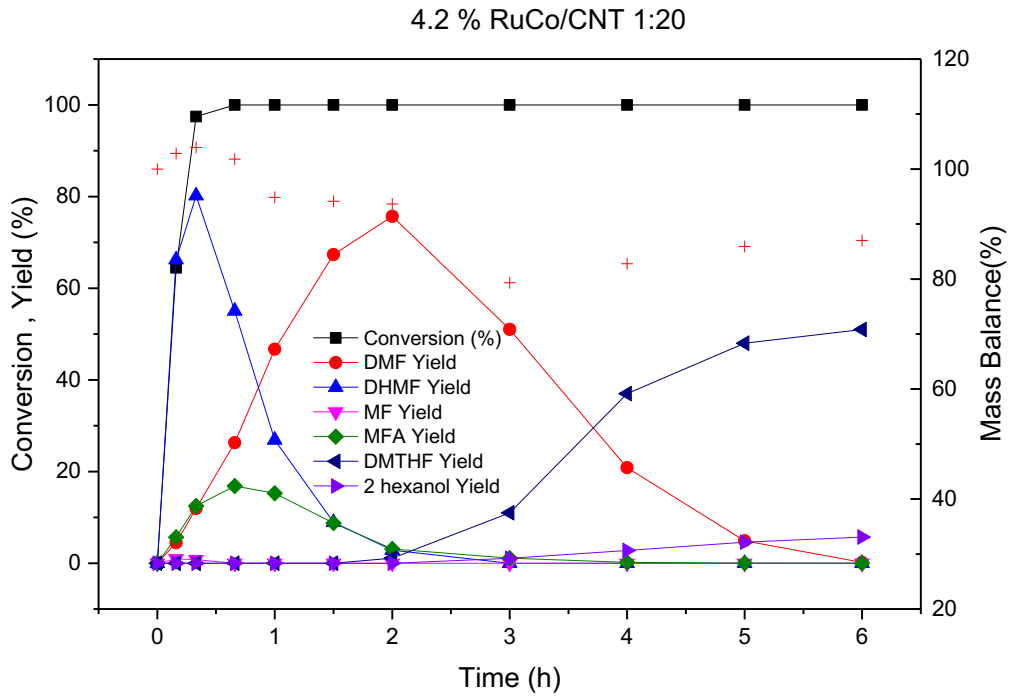

Appendix 21 TOL of product distribution of HMF hydrogenation over 4.2 % RuCo/CNT 1:20.

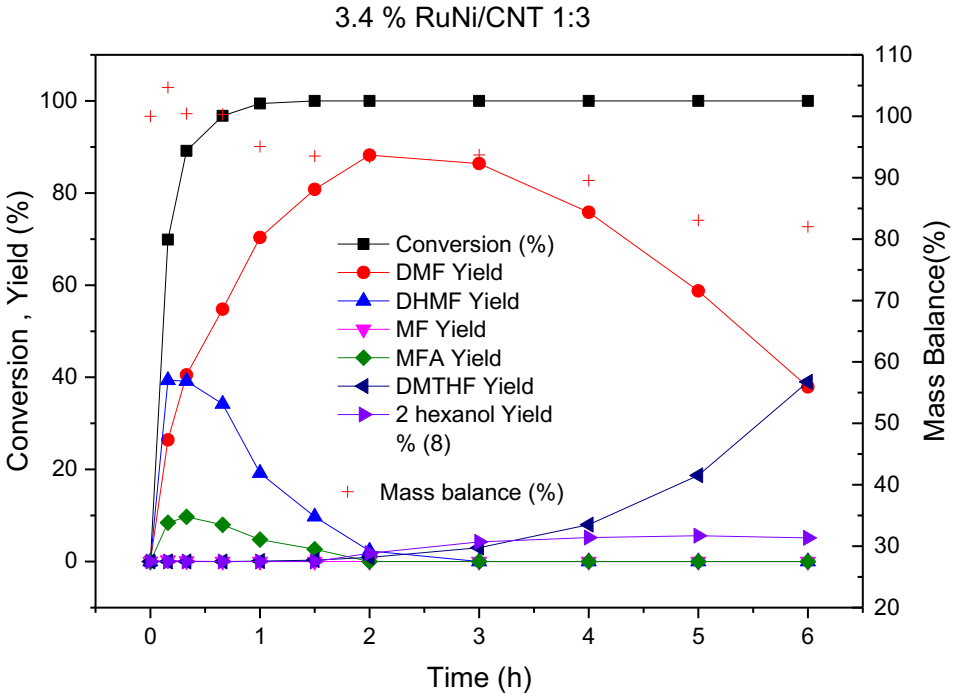

Appendix 22 TOL of product distribution of HMF hydrogenation over 3.4 % RuNi/CNT 1:3.